Fundamental Study on Thermally Robust Molecular Recognition Surface of Nanoscale Metal Oxides for Electrical Molecular Sensing and Discrimination

劉, 江洋

Fundamental Study on Thermally Robust Molecular Recognition Surface of Nanoscale Metal Oxides for Electrical Molecular Sensing and Discrimination

A DISSERTATION SUBMITTED TO

INTERDISCIPLINARY GRADUATE SCHOOL
OF ENGINEERING SCIENCE,
KYUSHU UNIVERSITY

IN PARTIAL FULFILLMENT OF REQUIREMENTS FOR THE DEGREE OF

DOCTOR OF PHILOSOPHY IN ENGINEERING

LIU JIANGYANG

Acknowledgements

This thesis was accomplished during 2017-2020 at the Department of Molecular and Material Sciences in Interdisciplinary Graduate School of Engineering Sciences, Kyushu University. I would like to thank the Ministry of Education, Culture, Sports, Science and Technology (MEXT) for financial support.

I would like to express my special thanks to my supervisor, Prof. Takeshi Yanagida, who providing me the opportunity to undertake the Ph.D research program. His continuous encouragement, invaluable supports and stimulating discussions were inestimable for my study.

I also would like to express my sincere gratitude to Prof. Kazuki Nagashima for his encyclopedic knowledge, perspectives and keen interests in scientific research. I learned not only the knowledge of scientific research, but also the rules of becoming a researcher from him. I wish to thank the other staffs in our Laboratory, Prof. Tsunaki Takahashi, Prof. Guozhu Zhang, Prof. Takuro Hosomi, Dr. Masaki Kanai, Dr. Masaru Suzuki and Dr. Benjarong Samransuksamer for their constructive advices and technical supports of various experiments for my research. I really thank to the secretary in our Laboratory, Ms. Hiroko, Imaizumi for her kind help in my daily life and study.

I would like to take this opportunity to thank several former staffs, Prof. Yong He, Prof. Gang Meng, Dr. Yosuke Hanai, Dr. Atsuo Nakao for their insightful advices and constructive discussions.

I would like to extend my sincere gratitude to our excellent collaborators, including Prof. Takehiro Tamaoka, Prof. Hideto Yoshida and Prof. Seiji Takeda from Osaka University, Prof. Nobutaka Shioya, Prof. Takafumi Shimoaka and Prof. Takeshi Hasegawa from Kyoto University, Prof. Takao Yasui and Prof. Yoshinobu Baba from Nagoya University, Prof. Jun Terao from The University of Tokyo, as well as Prof. Wataru Mizukami and Prof. Yuriko Aoki from Kyushu University.

In addition, I thank all current members in our Laboratory: Mr. Hiroshi Anzai, Mr. Hao Zeng, Ms. Wenjun Li, Ms. Ruolin Yan, Mr. Chaiyanut Jirayupat, Ms. Xixi Zhao, Mr. Ryoma Kamei,

Mr. Masahiro Shimuzu, Mr. Satoru Shiraishi, Mr. Mizuki Matsui, Mr. Shojiro Hayata, Mr. Haruka Honda, and Mr. Rimon Yamaguchi. They were good supporters in my research and daily life. And, I acknowledge all alumni in our Laboratory: Dr. Zetao Zhu, Mr. Hiroki Yamashita, Mr. Yuki Nagamatsu, Mr. Kentaro Nakabayashi, Mr. Yuya Akihiro, Mr. Junxion Zhang, Ms. Mengke Pei, Mr. Sameh Okasha, Mr. Akihide Inoue, Ms. Chie Nakamura.

Finally, I specially appreciate the support of my family and friends. It is exactly their encouragement and accompany making me accomplish the Ph.D study.

Liu Jiangyang

Abstract

This thesis is organized by a fundamental study for molecular recognition surface of nanoscale metal oxides, consequently aiming at improving the molecular detection performance of electronic devices whose directly molecular contact section is based on semiconductor metal oxide. As the increasing strictly demand for molecular detection in many fields, e.g., industry control, fuel emission control, human exhaust, household security, and environmental pollution monitoring, promoting the most promising detection devices, metal-oxide based sensors, is urgently necessary. Even though many R&D demonstrated excellent sensing property by continuously designing and synthesizing nanoscale materials, as well as optimizing device construction, insufficient detection limit and selectivity towards aiming molecule still play as dominant obstacles for accomplishing the commercial application. Therefore, this thesis focus on deeply understanding molecule-to-surface reaction behavior and novel sensing device integration, in order to make breakthrough for molecule detection.

On account of the unique chemical/property which are quite adaptive for benefiting the molecule sensing performance, we investigated the impurity metal ions doping approach for controlling the morphology of hydrothermal zinc oxide nanowires. A rational growth mechanism is proposed that face-selective behaviors of tungstate ions significantly enhances a nucleation at sidewall plane, while the dopant incorporation occurs only at (0001) plane. The inhomogeneous dopant distribution in an individual ZnO nanowire is unveiled for the first time, but such ion dopant nanowire failed to design the surface because most ion is doping at core part. Therefore we employ a metal modified nanowire surface and mixed the cations by a simple thermal treatment, molecule adsorption and transformation behavior on a gradual modulation of cation composition in heterostructured $(Cu_x,Zn_{1-x})O$ nanowires was investigated for a better understanding of molecule-to-surface reaction. A novel discovery that increasing Cu/Zn ratio on the nanowire surface systematically suppresses the aldol condensation reaction of nonanal, lead obviously durability and the recovery time improved. We also discovered a facile methodology to create zinc titanate nanotubes via reaction-byproduct etching, it created a mix cations surface on nanotube with lower thermal annealing temperature than solid-phase

diffusion method. In addition to surface cation modification, we also revealed a simple surface treatment using strong acids to elicit surface water on WO_3 nanowire to enhance the electrical molecular sensing of nonanal. The directly molecule-to-atom connection contributes to both sensitivity and recovery time enhancement. Those surface modification/treatment surface show their potential to be utilizing onto sensing devices merit from enhanced sensing properties such as recovery time and duration, but they can't contribute towards the tiny, selectively molecule detection, other surface functionalized method is in demand.

For achieving the aiming molecule detection from mixture volatiles, a "molecular fingerprinted" concept was designed. Prior to the device application, its molecular discrimination ability was optimized by control its formation temperature. Molecular fingerprinted nanowire formation mechanism was revealed by investigate the atomic-diffusion of zinc into the titanium oxide cross-link layer because the stronger bonding its provided for stabilizing template molecule during formation procedure. The excellent thermal robustness confirmed they can be fabricated onto sensing device operated at relative high temperature. A nanowire-chemosensor hybrid devises is carried out for the first time, nanowire play as pre-selector with its surface functionalized by as mentioned molecular fingerprinted strategy. The selectively detected of benzaldehyde, even from imbalanced molecular ratio of tiny benzaldehyde ratio show the potential of molecule detection from complex realistic application. Furthermore, such molecular fingerprinted nanowire as preconcerted platform integrated with sensor can reach ultralow detection by concentrated nonanal on the surface and thermally desorb into a small chamber. Obviously sensing response can be observed even to sub-ppb level nonanal (500 ppt), which could be detected by currently sensing device. Except the effort for promoting the discrimination adsorption of nanowire surface, we devoted to manipulating molecules discrimination at desorption procedure utilizing nanowire-sensor hybrid device, which could separate molecule sensing by controlling the desorption temperature and heating time. The successful discriminated sensing signal from co-adsorbed nonanal and its condensation product demonstrated its feasibility. We believe simultaneously utilizing molecular discriminate adsorption and desorption, more accuracy detection can be achieved in the near future.

The researches organized for this thesis already achieved staged results, we believe that based on these fundamental studies towards sensing material and novel sensor design, there will be breakthrough progress in the molecular detection sensor field.

CONTENTS

CHAPTER I
GENERAL INTRODUCTION

1.1 Introduction

1.1.1 Importance of molecule detection in modern society

Our living world is full of enormous species of molecules produced by nature or artificial. Some among them could directly reflect important information for human beings to deeply understand themselves and surroundings. Especially in modern society, scientific development as well as adoption of advanced technology have made the industry development extremely rapidly, means while greatly improved people's living standards. However, air pollution emerges and is getting worse, which led to a continuous increase in demand for air quality testing. For example, if industrial gas production is not properly monitored, it will cause serious impact on the environment, including the destruction of the ecological environment, even more serious issue plagues people's lives. Once harmful substances in industrial exhausted gases enter the human body through the respiratory tract and skin, they can cause temporary and permanent lesions on human breathing, blood, liver and other systems and organs, particularly carcinogen like benzopyrene-based polycyclic aromatic hydrocarbons. The flammable and explosive gases (methane, hydrogen etc.) used in industrial production are also a major hidden danger that threatens the safety of people's lives and property. Their volume ratio to air must below 20%, otherwise weak open flame can cause an explosion. Except the demand in industrial aspect, indoor air quality assessment is also imminent due to the harmful volatile organic compounds (VOCs) released by interior decoration. The main compounds of monitoring interest consist of aromatics such as benzene, toluene, xylene, and ethylbenzene. World Health Organization (WHO) Air Quality Guideline for Europe [1] establishes guidelines values for toluene, 260 $\mu g/m^3$ over 1 week, for formaldehyde, 100 $\mu g/m^3$ over 30 min and for tetrachloroethylene, 250 $\mu g/m^3$ over 1 year. Additionally, it sets the guideline values for benzene corresponding to the concentration's levels associated with an excess lifetime risk of 1/10,000, 1/100,000 and 1/1,000,000 equal to 17, 1.7 and 0.17 $\mu g/m^3$, respectively. Keeping the risk in controllable ranges are necessary.

In addition, disease-related biomarkers are usually VOCs, which indicate the presence or severity of a particular disease state or some abnormal physiological condition of an organism. A biomarker may be a chemical substance introduced into an organism (exogenous) or produced within the body (endogenous), which can be detected and measured in the blood, bodily fluids, tissues or human breath, and serves as an indicator of either normal or disease processes in the body. Realizing real-time and accurate biomarker molecule detection is useful

in early disease detection and diagnosis, disease prevention, drug target identification, drug response, determining probable effects of treatments on a patient.

What's more, as the popular Internet of Things (IoT) technique extends internet connectivity into physical devices and everyday objects, bringing new challenge and opportunity to develop and innovate molecular detection techniques due to their indispensable roles as connective bridge.

1.1.2 Application of metal oxides onto sensors for molecule detection

The initial discovery of semiconductor metal oxides as sensing material was conducted by Seiyama in 1962, he found a dramatically electric conductivity change when zinc oxide exposed to reduction gas atmosphere. [2] Soon after, the first industrial metal oxide gas sensor devices were fabricated and commercialized by T. Taguchi. [3] Since then, a lot of efforts have been addressed to improve sensing properties by developing novel wide-gap semiconductor oxides. Thousands of results have been reported about the characteristics and performance of sensors based on different materials, mainly including SnO_2, WO_3, In_2O_3, Fe_2O_3, NiO, Co_3O_4, CuO, etc. [5-15] They predominant domestic, commercial and industrial applications of solid-state gas detecting devices for a long time, even until now, the gas-sensitive components people are using are still made by them because of many advantages such as low cost; flexibility associated to their production; simplicity of their use and large number of detectable gases/possible application fields.[16-18] In recent decades, as nanotechnology arose, take the development of metal-oxide sensor in to a brand new world due to the performance of such sensors is significantly influenced by the morphology and structure of sensing materials, resulting in a great promoted the further improvement of metal oxide-based sensors by nanostructure designed. However, excellent individual gas sensing performance mainly obtained by measuring the signals of laboratory samples. Realistic environments from sensors' working conditions would be much more complicated. Factors such as humidity, presence of interfering gases and surrounding temperature are also needed to be taken into consideration. In other words, sensors must have strong anti-interference ability. Metal oxides as the defectively contact body with target, anonymous chemical/physical property will lead to same electric conductivity change phenomenon, which is still a main hindrance to a reliable application, especially when target concentration is relatively low. At present, certain molecular sensitively detection has not been identified yet via select a specific material. Moreover, for the purpose of fast responses and short recovery times, this type of sensor often operating under high

temperatures, thus the stabilization of the sensor electrical properties is of the utmost importance, to avoid changes while working [19-22]. In addition, the promising wearable molecular sensors request low power consumption, small size, and simple signal visible system. That's why wearable molecular detection devices based on metal oxides have rarely been used in real applications in spite of so many excellent laboratory results had been achieved. Molecular detection by metal oxide-based sensors is still in its infancy.

1.1.3 Objective and approach of this thesis

As opposed to the often employed expensive, bulky and complicated instrumental molecule detection methods, there is a need for inexpensive, low-power, simple, sensitive and stable electronic sensors suited for trace molecules detection in a wide spectrum of applications ranging from laboratory sensing devices to realistic environmental molecule monitoring, biomarker detection from breath and numerous of other detection requirements. Towards currently the main problems metal oxides sensor faced, our objective and approach are listed in the following:

1. Insufficient molecule detection limitation:

Chose nanowire nanostructure metal-oxide as sensing material to utilizing its large surface-to-volume area to improve molecules' adsorption/desorption, further conducted surface modification to promote its sensing performance.

2. Bad recovery character

Controlling molecular surface transformation by additional component ratio on nanowire surface to reduce the generation of molecules that are not easily desorbed, promoting recovery character become possible.

3. Poor aiming molecular selectivity

Develop a novel nanowire platform as preconcentrator utilizing prior to sensor, such preconcentrator should be able to recognize specific molecules and trapped them, even in mixtures, then release in a short time and small space for sensor to detect. This design might not only realize the selectively detection, but also achieve the detection of ultralow concentration molecules.

1.2 Framework of This Dissertation

This dissertation consists of ten chapters, which are presented as follows:

- Chapter I is a general introduction about the motivation and organization for this dissertation, including the facing issues remained that limited sensing technique's further evolution and promising methods to overcome. The framework of this thesis is also listed.
- Chapter II give an overview about the development of gas molecular detection techniques by metal-oxide semiconductor, comprising the literature reviews current and new strategies for realizing portable high-performance application. Especially emphasized the nanowires utilizing as essential section for facilitating the improvement of sensors.
- Chapter III is aiming at design molecular sensing surface by traditional method as metal ion doping, surface modification and treatment. First section of this chapter presents W-doped ZnO nanowire, element distribution was unveiled. Second section reports a novel way to design the ZnO nanowire sensor surface via inorganic (CuO) modification approach for further enhancing stability and the recovery time of nanowire sensor based on suppressing surface condensation reaction. Third section provide a facile methodology to create zinc titanate nanotubes via reaction-byproduct etching. And forth section shows a simple acid treatment on WO_3 nanowire surfaces for the catalytic aldehydes molecule (nonanal) sensing via both the oxidization and desorption procedures at room temperature.
- Chapter IV designed a molecular recognition surface named "molecular fingerprinted" and realized target molecule discrimination from mixture volatiles based on molecular adsorption procedure. The optimized material formation condition was confirmed via various pre-heating temperature treatment. The formation mechanism of functionalized recognition property is also discussed. An excellent discriminative sensing of benzaldehyde from mixture volatiles strategy by utilizing robust molecular fingerprinting of metal oxide nanowires as a "pre-selector" integrated with sensor was achieved for the first time. Furthermore, ultra-low (500 ppt) nonanal molecules detection was accomplished using fingerprinted nanowire as pre-concentrator foe nonanal molecule collection with a sensitive gas sensor in a package together.

- Chapter V provides a molecular discriminate platform by nanowire-sensor hybrid device through molecule desorption procedure for electrical separately detecting the co-exist molecules on metal oxide nanowire surface via thermally manipulated desorption.
- Chapter VI finally gives an overall conclusion of this thesis and the perspective for possible future work.

1.3 References

[1]. World Health Organization. Air Quality Guidelines for Europe, 2nd ed.; WHO regional publications; World Health Organization, Regional Office for Europe: Copenhagen, Denmark, 2000.

[2]. T. Seiyama, A. Kato, K. Fulishi and M. Nagatani, Anal. Chem., 34, 1502 (1962).

[3]. N. Taguchi, Jpn Pat. S45-38200 (1970).

[4]. Y. Okayama, H. Fulaya, K. Kojima, Y. Terasawa and T. Handa, in ‘‘Proceedings of the International Meeting on Chemical Sensors’’, edited by T. Seiyama, K. Fueki, J. Shiokawa and S. Suzuki, Fukuoka, Japan, September 1983, (Elsevier, Amsterdam—Oxford—New York—Tokyo, 1983) pp. 29—34

[5]. T. Kobayashi, M. Haruta, H. Sano and M. Natane, Sensors and Actuators, 13, 339 (1988).

[6]. N. Hykaway, W.M. Sears, R.F. Frindt and S. R. Morrison, Sensors and Actuators, 15, 105 (1988).

[7]. S.R. Morrison, Sensors and Actuators, 2, 329 (1982).

[8]. G. Heiland, Sensors and Actuators, 2, 343 (1982).

[9]. P. T. Moseley, Sensors and Actuators B, 6, 149 (1992). A4.6.10

[10]. Y. Matsuura, S. Matsushima, M. Sakamoto, and Y. Sadaoka, J. Mater. Chem. 3, 767 (1993).

[11]. J. Tamaki, Z, Zhang, K. Fujimori, M. Akiyama, T. Harada, N. Miura, N. Yamazoe, J. Electrochem. Soc., 141, 2207 (1994).

[12]. M.C. Carotta, M. Ferroni, V. Guidi, G. Martinelli, Advanced Materials, 11, 943 (1999).

[13]. Williams D.E., Sensors and Actuators B, 57, 1 (1999)

[14]. M. Ivanovskaya, D. Kotsikau, G. Faglia, P. Nelli, Sensors and Actuators B, 96(3), 498 (2003).

[15]. T. Maekawa, J. Tamaki, N. Miura, N. Yamazoe, Chemistry Letters, 4, 639 (1992).

[16]. Korotcenkov G. Gas response control through structural and chemical modification of metal oxide films: state of the art and approaches[J]. Sensors and Actuators B: Chemical, 2005, 107(1): 209-232.

[17]. Williams D E. Semiconducting oxides as gas-sensitive resistors[J]. Sensors and Actuators B: Chemical, 1999, 57(1-3): 1-16.

[18]. Barsan N, Schweizer-Berberich M, Göpel W. Fundamental and practical aspects in the design of nanoscaled SnO_2 gas sensors: a status report[J]. Fresenius' journal of analytical chemistry, 1999, 365(4): 287-304.

[19]. E. Traversa, P. Nunziante, M. Sakamoto, Y. Sadaoka, M.C. Carotta and G. Martinelli,Journal of Material Research, 13, 5, 1335 (1998).

[20]. E. Comini, G. Faglia, G. Sberveglieri, Zhengwei Pan, and Zhong L. Wang, Applied Physics Letters, 81(10), 1869 (2002). A4.6.11

[21]. V. Guidi, M.C. Carotta, M. Ferroni, G. Martinelli, M. Sacerdoti, Journal of Physical Chemistry B, 107,120 (2003).

[22]. A.M. Ruiz, G. Dezanneau, J. Arbiol, A. Cornet, J.R. Morante, Chem. Mater., 16, 862 (2004).

CHAPTER II
LITERATURE REVIEW

2.1 Introduction

Based on the demand towards volatiles molecule detection described in the chapter I, tremendous efforts had been paid by researchers to satisfy people's increasing requirement. To get a better understanding of research status and objective set up above, a comprehensive review related to this thesis is carried out in this chapter. First, several molecular detection techniques are basically introduced, including large-scale precision testing instruments and small-scale portable gas sensors. The advantage and disadvantage are also discussed according to their working principle, suitable utilized conditions and detection results. Then, we focus on the most widely used, portable semiconductor metal-oxide gas sensors. Their molecule detection performance can be controlled through designing sensor device configuration as well as the sensing material nanostructure. One of the potential nanostructure, nanowire, attracted our attention due to their unique chemical/physical properties as major sensing material. Next, we reviewed enormous nanowire sensors, multi-nanowires sensor and single nanowire sensor are introduced in detail. A novel concept of nanowire preconcentration platform also plays a role for assisting sensing performance. Finally, nanowire surface functionalization is considered as an effective way to improve the drawback of current nanowire sensors, versatile specific sensing properties become possible by certain receptor modification.

2.2 Volatile molecule detection methods

2.2.1 Molecule detection instruments

Several precious instruments take researcher's fancy due to their eligibility to achieve tiny molecule detection and complex compounds separation. But disadvantage comes along that long time consumptive and expensive machine expended, result in the limitation of application outside the laboratory.[1-2] Commonly these instruments assembled relying on the principle of various molecule behavior or features from gas chromatograph, mass spectroscopy and optical spectroscopy. Recent years the combination of multi-technic further improved the identification accuracy for tracing molecules. For example, gas chromatograph-mass spectroscopy (GC-MS) and gas chromatograph-infrared spectroscopy (GC-IR) have been extensively utilized as standard for molecules analysis.[3] Next, general working principles of these instruments are introduced.

Gas chromatograph (GC) instrument with column equipped can be normally utilized for volatiles mixture compounds separating and analyzing. Volatility of compounds is necessary

for completely vapored without decomposed. In gas chromatography, volatiles usually obtained from instantaneously heating inlet port that contained injected compounds, carrier gas (unreactive gas, helium is the most commonly used) is the mobile phase, takes volatiles molecule along to the stationary phase, column, which is consists of liquid or polymer microscopic layer inside a piece of glass or metal tubing. During the analysis procedure, each compound being eluted by column according to the various interaction property with wall of column between molecules, lead to the difference of retention time. Therefore, molecules separated from mixture compounds can be obtained by different retention time determined by stationary phase function, which means column selection is the most important factor for fully separating target mixture compounds. The analyte molecules forces with stationary phase material dominates the mixture compounds identification and separation. Van der Waals, hydrogen bonding and dipole-dipole intermolecular forces can be manipulated by alternatively chose column.

Mass spectrometry (MS) provides a mass spectrum consists of mass-to-charge ratio of ions signal, the varsity, sensitivity for molecules analyzing and remarkable specificity unknow molecules make itself an excellent resolver for gas chromatograph. In a typical MS procedure, typically analytical molecules are ionized by electrons bombarding for getting charged fragments. According to their mass-to-charge ratio, separation among these ions is feasible by accelerating them under high voltage and subjecting them in magnetic field. Detector of ions will present a signal intensity spectrum as function of the mass-to-charge ratio undergo the same amount of deflection. Ions amount is linear with the peak area from obtained spectra. The performance of mass spectrometry is strongly related with detector type and molecular ionization method. Combines the features of gas chromatography and mass spectrometry (GC-MS) to identify molecules species and amount is wild-spread applicated in identifying unknow molecules from environment analyzation [4-5], drug discovery [6-7] and explosive investigation [8-9] because of its 100% specific test. Researchers also called this analytical technical “golden standard” for species identification. Figure 1a presents the mainly detection procedure schematic illumination of GC-MS combined instrument. Accurately particular molecule identification by neither gas chromatography nor mass spectrometry respectively is impossible. Combine these two components allows a much degree of accuracy improvement than separately.

Optical spectroscopy is defined as the instrument used to identify material components, the amount of active ingredient or the color of a sample by measure properties of light interacts with electromagnetic radiation. Wavenumber of light usually be regarded as the measure units for representing photon energy because of the directly proportion property, other units has a reciprocal relationship to wavelength is also acceptable, such as reciprocal centimeters or electron volts. Spectral lines describing proton energy adsorption intensity various with wavenumbers can be operated at a wide rage, from gamma rays and X-rays into the far infrared. Spectral regions near visible spectrum is commonly used for molecules identification. Typically, infrared spectroscopy (IR spectroscopy) are powerful optical spectroscopy for confirming molecules species and structures based on vibrational-rotational transitions behavior of chemical bonds or functional groups in the molecules.[10-12] Organics molecules in majority degree show their absorption bands at near and mid-infrared region (wavenumber from 500 to 4000 cm^{-1}). Functional group region is defined based on the association between the stretching vibrations and functional groups, usually it located at high wavenumber region (>1450 cm^{-1}). For example, C=O (1660-1760 cm^{-1}). [13-14] Benzene skeleton (1450-1620 cm^{-1}) and OH (3300-3800 cm^{-1}). [15-17] Fingerprint region (500-1450 cm^{-1}) contains all manner of chemical bending vibrations within the molecule. Complex adsorption peak shapes and overlap phenomenon result in its negligible.[18-19] The most

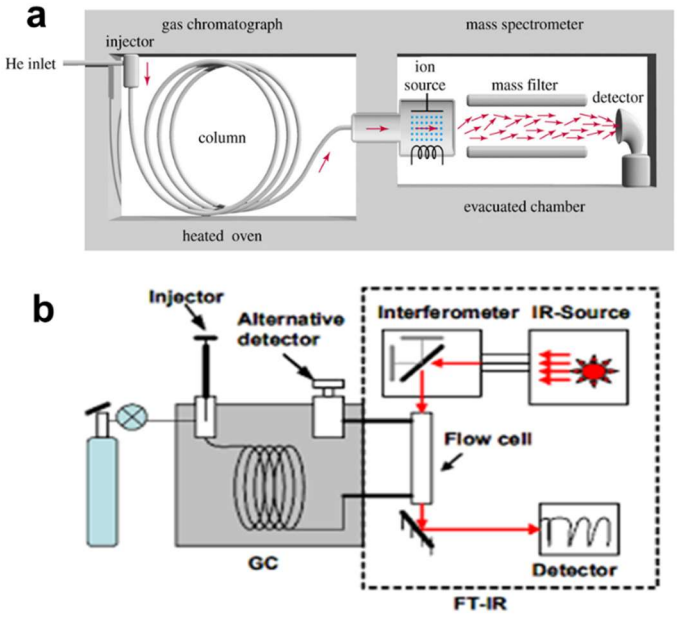

Figure 1. *Operating principle schematic of (a) gas chromatography and mass spectrometry (GC-MS) combination instrument. (b) gas chromatography and infrared spectroscopy (GC-IR) instrument.*

disadvantage of IR spectroscopy is the impossibility to distinguish molecule with same functional group due to anonymous it presents. Even so, the fast measurement speed and low detection limit give it competitive in molecule detection. Combine IR with GC technical mention above (as schematic in Figure 1b), real-time molecule analysis, complicated products of a reaction can be analyzed quantitatively and qualitatively. From the analysis of the products, the reaction process and its mechanism can be elucidated. [20-22]

In terms of ultraviolet–visible spectroscopy (UV-vis spectroscopy), its spectrum comes from energy absorption of electrons transition from ground to higher anti-bonding molecular orbitals under ultraviolet or visible light exciting. Wavenumber of light adsorbed by electrons is negative relation with electrons jumping ability. However, the detected information only represents the characteristic of chromophore and autochrome groups in molecules rather than specific functional group, which limits the application to unknown molecule identification. Other optical spectroscopy technical such as Raman spectroscopy, fluorescence spectroscopy and nuclear magnetic resonance (NMR) are also effective instrument for molecule detection and identification, alternatively combination between them can also obtain higher identification level, such GC-UV, GC-MS-NMR. However, high cost and complex operation these systems limit them in usual applications.[23-25]

2.2.2 Portable volatile organic molecule (VOCs) sensor

The concept of chemical sensors origins from a signal transfer from general analytical systems to dedicated systems. Real time detection and presentation bring them preponderation in the molecule detection field. Their operating procedure can be divided into two-steps: target recognition and signal transducer. The interaction between target molecules or ions in the sample with chemical sensor takes place at recognition part. In cases where the chemical molecule interaction in the recognition part does not directly modify an electrical property, such as resistance, current and potential, but rather other properties like strength, heat, mass, or light changes, some kinds of transducing converts part is required to get an electrical signal compatible with the electronic circuits. Currently, based on the working principle, chemical sensor can be divided into semiconductor gas sensor[26-27], electrochemistry gas sensor[28-29], optical gas sensor [30-31], PID (Photo Ionization Detector) VOCs sensor [32-33] and contact/catalytic combustion gas sensor[34-35]. Their ease of use and self-contained devices property merits the exceptionally attractivity and compatibility for target molecule detection application. To meet the portability demand, their development tendency mainly towards

miniaturization, intelligentlization and multi-functionalization. The successful application of nanomaterials, thin film technology and other new material preparation technologies provides conditions for gas sensors to realize new functions. Using MEMS technology to help achieving the miniaturization of sensor size, and then study the integration of multi-gas sensors to realize multi-function.[36-38] The integration of gas sensors and digital circuits will become an inevitable way to pursue intelligenlization.

As for the application in volatile organic compounds (VOCs) detection, the semiconductor gas sensor is the most widely used variety of gas sensors due to their simplicity of operator, stable detection and low production cost. Many commercialized products currently are in using in household gas detection, gifts, smart home appliances and other fields. Electrochemical gas sensors are very suitable for the detection of low concentration toxic gases, as well as the detection of non-toxic gases such as oxygen and alcohol, are currently mainly used in various industrial fields and road traffic safety detection fields. Catalytic combustion gas sensor is suitable for combustible gas detection, mainly used in coal mine gas detection. Infrared gas sensors are suitable for detecting methane, carbon dioxide and other gases. In current practical applications, carbon dioxide products dominate the detection, mainly applied to HVAC system and indoor air quality monitoring, industrial process and safety protection monitoring, agricultural and livestock production process monitoring and other fields. PID sensor is most suitable for very low concentration of volatile gas detection (VOCs).

2.3 Metal-oxide semiconductor gas sensor

2.3.1 Primary sensing mechanism

Since the advent of semiconductor metal-oxide semiconductor gas sensors in 1962, [39] semiconductor gas sensors have become the most commonly used and most practical type of gas sensors. According to their gas sensing mechanism, they can be divided into non-resistive and resistive types.

Non-resistive semiconductor gas sensors are diode-type and field-effect tube (MOSFET) semiconductor gas sensors.[40-42] Its working based on current or voltage changing with the gas content, and mainly detects combustible gases such as hydrogen and natural gas. Among them, the working principle of MOSFET gas sensor is that VOCs reacts with catalytic metal (such as button), the reaction product diffuses to the gate of MOSFET, which changes the performance of the device. Figure 2a presents the MOSFET structure and manner of working.

Identify VOCs by analyzing the changes in device performance. The sensitivity and selectivity can be optimized by changing the type and thickness of the catalytic metal, and the operating temperature can also devote to excellent sensing performance. MOSFET gas sensor has high sensitivity, but the manufacturing process is more complicated, alone with high cost. Therefore, the following mainly introduce the resistance-type semiconductor gas sensor.

The resistance type semiconductor gas sensor refers to semiconductor metal oxide ceramic gas sensor, which is an impedance device made of a metal oxide film (for example: SnO_2, ZnO, Fe_2O_3, TiO_2, etc.), and its resistance changes with different gas content. Sensitivity of resistance type sensor most common defined as R_a/R_g for reducing gases and R_g/R_a for oxidizing gases, where R_a is the resistance of the sensor in air or other background gas; R_g is the resistance when exposed to target contained gas atmosphere. Selectivity is one other crucial judgement criteria for sensing property that explained as the target discrimination ability of the sensor. Response and recovery time are the time consumption of sensor resistance reaching to their 90% of the total response, respectively. Although disadvantages exist that resistance type gas sensor must work at high temperature, poor selectivity to odor or gas, component parameter dispersion and high-power requirements, the superiority of low cost, simple manufacturing, high sensitivity, fast response speed, long life, low sensitivity to humidity and simple circuit attracts much attention. Considering the existence of the grain boundary contact barrier between the grains of semiconductor oxide sensitive materials layer in the existence of oxygen and target molecules, the sensitivity mechanism of the gas sensor during operation can be explained by the model of the sensitivity mechanism proposed by Yamazoe, which is based on the mutually charge transportation[27]. Taking n-type semiconductor oxide gas sensor contacting with reducing gas as an example, the schematic diagram of the sensing mechanism is shown in Figure 2b.When the gas sensor is placed in the air atmosphere, the oxygen molecules in the air will adsorb on the surface of the sensitive material by capturing the electrons in the conduction band of the sensitive material, forming a chemically adsorbed oxygen ion, which includes O^{2-}, O^- and O^{2-}. Barson et al.'s research indicates that the specific existence of adsorbed oxygen is determined by the operating temperature of the gas sensor [43]. An electron depletion layer is formed at surface, the contact barrier is relatively high, migration of electrons at the barrier is restricted, and the gas sensor exhibits a high resistance state. When exposing gas sensor in a reducing gas environment (taking ethanol gas as an example), the ethanol gas molecules react chemically with the adsorbed oxygen ions on sensing material surface. The electrons bound to the adsorbed oxygen molecules are released back into the conduction band of the sensitive material, the

electron concentration increases, width of the depletion layer will decrease, lead to the height of the contact barrier decreases significantly. At this condition, the gas sensor exhibits a low resistance state. The obvious changes make the gas sensor show higher sensitivity [44-50]. However, in the actual application process, the sensitive mechanism is more complicated because of many factors that affect the resistivity of the semiconductor oxide gas sensor, and its exploration and research are still in progress.

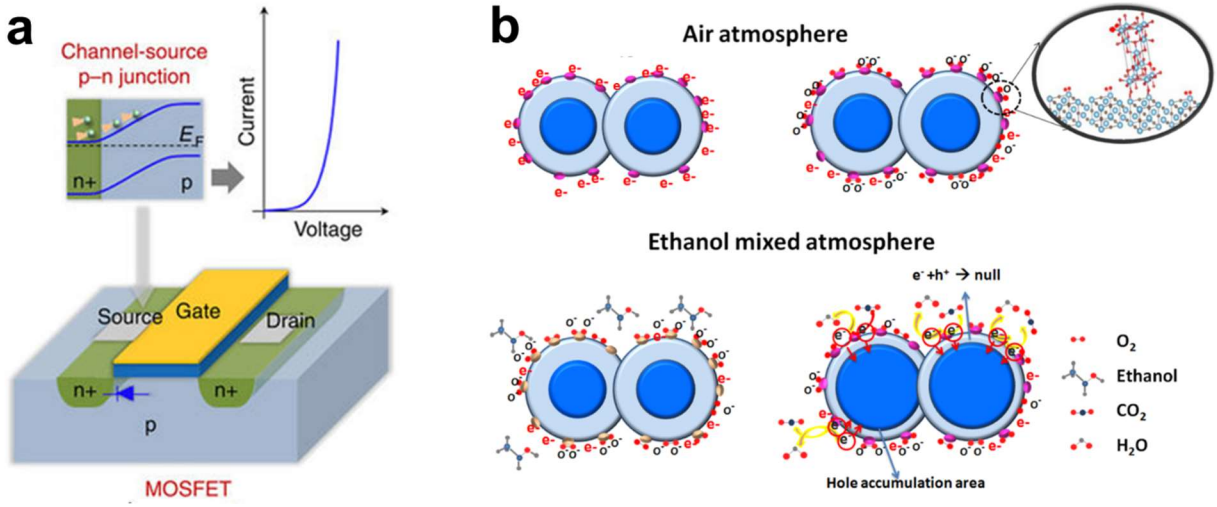

Figure 2. Sensing mechanism schematic illumination of (a) MOSFET gas sensor and (b) semiconductor-resistance gas sensor.

2.3.2 Design of sensor structure

In the previous section, we introduced the basic sensing mechanism of semiconductor gas sensor. Configuration of sensing device as the principle part for determining the sensing performance based on the manner of heating and interact between sensing material. In Figure 3, several sensor structures are presented. Basically they are consist of heating-plate, electrode, sensing materials and senor substrate. The side-heating device refers to a gas-sensitive element prepared by sintering a sensitive material coated on a ceramic tube and a heating wire passing through the ceramic tube. (schematic shown in Figure 3a). The characteristic of this device is that the heating wire does not directly contact sensitive materials, the measurement circuit and the heating circuit do not affect each other, result in high consistency. It is the most widely used type among thin-film sensor. The direct-heating device (Figure 3b) is fabricated by directly coating the gas-sensitive material on the platinum wire coil used for heating, and then conduct electricity after sintering to test the resistance change degree of the sensor device in the target

molecule contained environment. This type of sensor is regnant from simply manufactured process and low power consumption, but its easily affected by the environment greatly decrease the reliability of devices.

In general cases, the thin-film type sensing material always has high resistivity, so the method of reducing the resistance value of the sensitive film is to increase the thickness of the sensitive film or increase the width-to-length ratio of the sensitive film. However, if the thickness of the sensitive film is too large, the response time of the gas sensitive sensor will be reduced. Therefore, considering the response time and signal-to-noise ratio, it is necessary to design and optimize the thickness and aspect ratio of the microelectrode in gas sensor. A designed electrode configuration named “interdigitated finger” in Figure 3c provides a width-to-length ratio manipulatable sensor

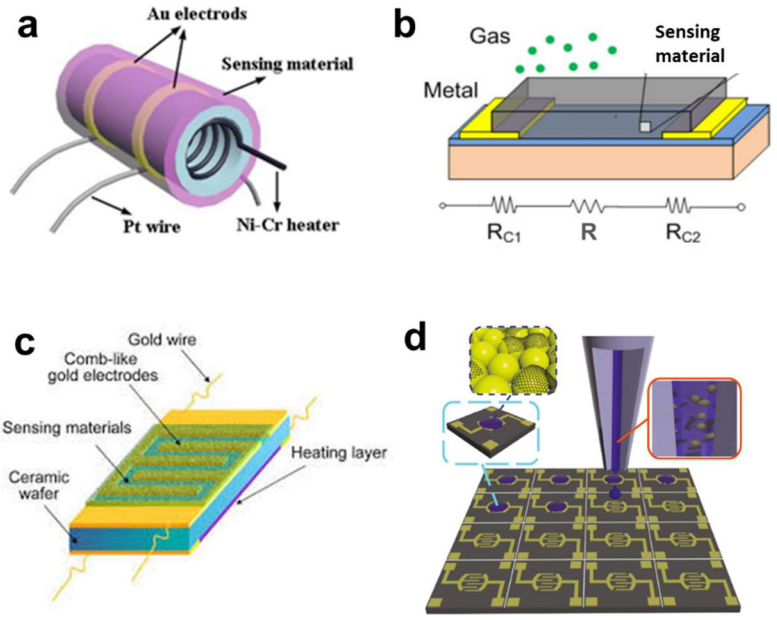

Figure 3. Semiconductor gas sensor structure of (a) heater type thin-film sensor; (b) directly heated type gas sensor; (c) interdigital finger electrode gas sensor; (d) sensor array [51].

substrate. The greater the length-width ratio and density of the interdigitated fingers, the lower the initial resistance of the interdigitated electrodes, thus the higher the sensitivity and response speed of the sensor. When the size of the interdigitated electrode structure is reduced to the order of micrometers, the weak resistance change between the interdigitated electrode structures can be sensitively detected, and the sensitivity of the interdigitated electrode sensor can be significantly improved.

By design an integrated sensor array (Figure 3d as an example for sensor array), which refers to a set of gas sensors group with different functional or selectivity, one of the main drawbacks that low molecule discrimination ability of semiconductor gas sensor can be significantly improved. Usually, sensor array deployed in a certain geometry pattern, used for collecting chemical information and processing sensing signals from the particular object. In a specify measurement procedure, each sensor exposed to one sample chamber contains multi-component gas mixtures simultaneously, utilized given functional property to convert chemical information of each molecule species independently. The mutually exclusivity of sensors guarantees multivariate response can be generated by gas sensor array from the same environment for gas mixture analysis accordance with the selectivity and sensitivity. Compare with using a single sensor, sensor array takes the advantage of adding new dimensions to the observation, which is meaningful to estimate more parameters simultaneously. But meanwhile raising the production cost and complexing the process. The application of array-based sensing concepts by Suslick, [52-53] Lavigne [54-55] and Anslyn [56] has provided material systems that recognize complex mixtures of similar compounds with surprising selectivity.

2.3.3 Hierarchical metal-oxide sensing material structure

Sensing material of semiconductor metal-oxide gas sensor as the main part to contact with detective gas molecules, its constituents and nanostructures determine the sensing performance. High surface area and full electron depletion are merit in term of enhancing the gas sensitivity.[57-58] During the design of sensing materials, nanostructures with higher dimension are advantageous, which are stacked by many low dimensional, nano-building blocks, usually researchers named those nanostructures as ‘hierarchical structure’. Low dimensional can be classified as: 0D (zero dimension) if all three spatial dimensions are in the nanometric range (<100 nm), for example, nanoparticles or clusters; 1D (one dimension) means two dimensions are in the nanometric range, like nanotubes, nanorods and nanowires; 2D (two dimensions) has only one spatial dimension within nanometric, thin films or nanosheets are typical instances. 3D (three dimensional) materials implies that the 0D, 1D and 2D elements are in close contact forming interfaces, hollow nanostructure or porous nanostructure. In recent years, various chemical routes have been developed for synthesis hierarchical nanostructures based on the primary mechanisms of Kirkendall effect, galvanic replacement, chemical etching, Ostwald ripening and self-templating manufacturing [59-64]. Above all, successful attainment

of either high gas response and rapid response and recovery speed by using various hierarchical structures in many literatures support the meaning of nanostructure design.

H. Kim et. al reported the significant sensitivity enhancement to 50 ppm C_2H_5OH and ultra-fast response (~1 s) performance by 2-3 flower-like SnO_2 hierarchical microspheres self-assembled from nanosheets that synthesized by hydrothermal method. [65] They explained the

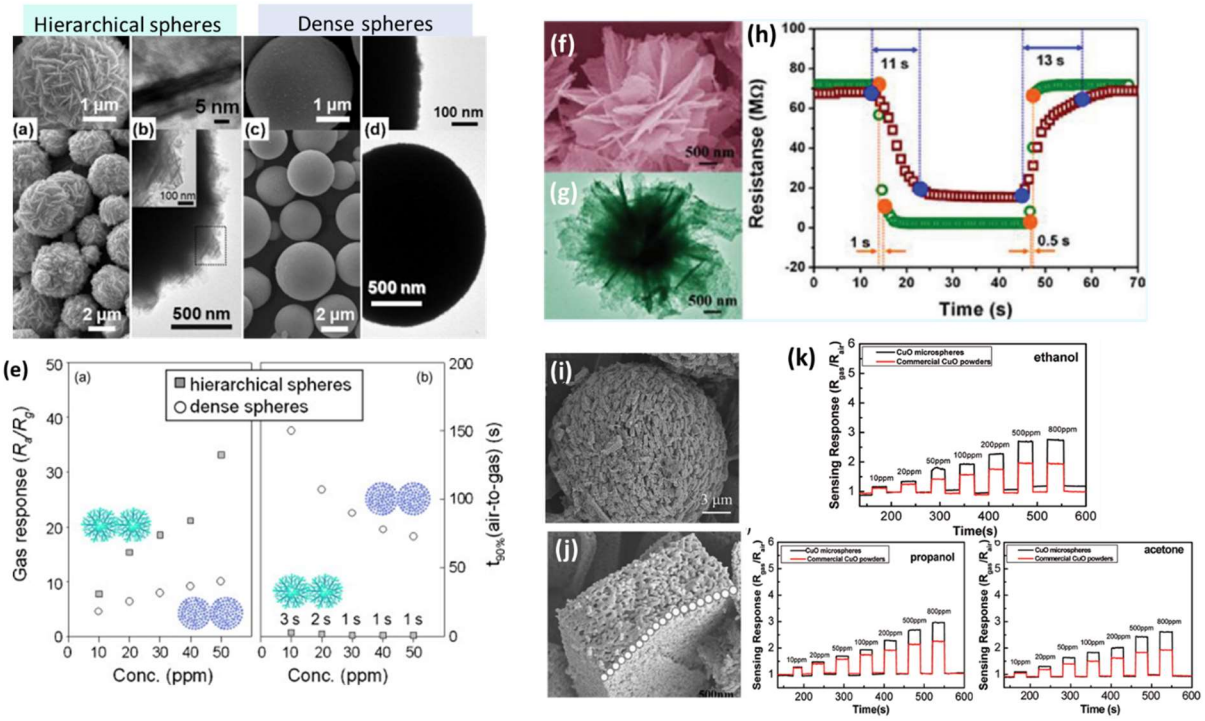

Figure 4. *VOCs sensing performance by hierarchical semiconductor material. (a-e) Ethanol sensing property comparison between hierarchical spheres and dense spheres of tin oxide. [65] (f-g) acetone sensing performances by hierarchical α-Fe_2O_3 sensor comparing with the compact α-Fe_2O_3 structures; [66] (i-k) Hierarchically porous CuO architecture sensing to ethanol, propanol and acetone, commercial CuO powder as comparison. [67]*

dramatic ethanol sensing improvement by the rapid diffusion of the target molecules onto the entire sensing materials surface through the nano-porous network of nanosheets. Their explanation was demonstrated via sensing performance comparison with dense spheres (Figure 4a-e). By controlling the composition of stock solution for hydrothermal synthesis, building blocks unit can be manipulated from 2D nanosheets into 0D nanoparticles, result in converting hierarchical SnO_2 nanoflower into dense spheres. 2-3 flower-like hierarchical SnO_2 microspheres has a larger specific surface area (46.4 m^2/g) than dense SnO_2 spheres (34.7 m^2/g). The exist of micropores and sub-micropores ranging within size from 4.5 to 20 nm and 33 to 100 nm, respectively. This clearly demonstrates that the hierarchical nanostructures provide a

high surface area for molecule sensing reaction happen without sacrificing the porosity for effective molecule diffusion. Results from other researchers, such as Wang et. al prepared hierarchical α-Fe_2O_3 as sensor material [66] in Figure 4f-h and p-type semiconductor porous CuO from the study of Zhu et.al [67] in Figure 4i-k gave strong evidence to support this explanation.

2.4 Nanowire based sensing devices

2.4.1 Development of metal-oxide nanowire

As an typical 1D nanomaterial, nanowires (defined as only one spatial dimension within nanometric) attracted substantial effort by researchers, especially in the late 1990s, a significant and rapidly application expansion happened due to their potential as building blocks for electronic devices—such as field-effect transistors (FET)—that could replace conventional silicon transistors in hybrid electronics or lead to stand-alone nano-systems based on their remarkable physical or chemical properties result from the nanoscale size in two dimensions confined carriers only conducted in one dimension, became one of the most active research areas within the nanoscience and nanotechnology community. [68-69] It is expected that the nanowire nanostructure based quasi one-dimensional materials would become the focus of the next decade of nanomaterials research.[70]

Until today, the synthesis of nanowire has already been quite mature owing to researchers' tremendous amount of effort for precisely control the nanowire growth dimensions at atomic level, means while closely related to the investigation towards intrinsic nanowire growth mechanism. Normal nanowire synthesis techniques can be divided into two categories according to their growth environments: vapor growth and solution growth manners.[71]

Vapor growth nanowires: this kind of growth technical can be described as vapor-liquid-solid (VLS) growth or vapor-solid (VS) based on the mechanism proposed by Wagner and Ellis in 1964 during their observing the growth of Si whisker. [72-73] The typical VLS nanowire growth process can be described as following: the solid powder precursor vaporized at a high temperature, will dissolve in a metal catalyst that has been melted into nanocrystals at a certain temperature. Crystallized and nucleation will happen after reaching the saturation of precursor. Further precursor dissolved in the metal catalyst to form an alloy under the transport of carrier gas, which is then continuously precipitated in a solid state, providing a continuous source of

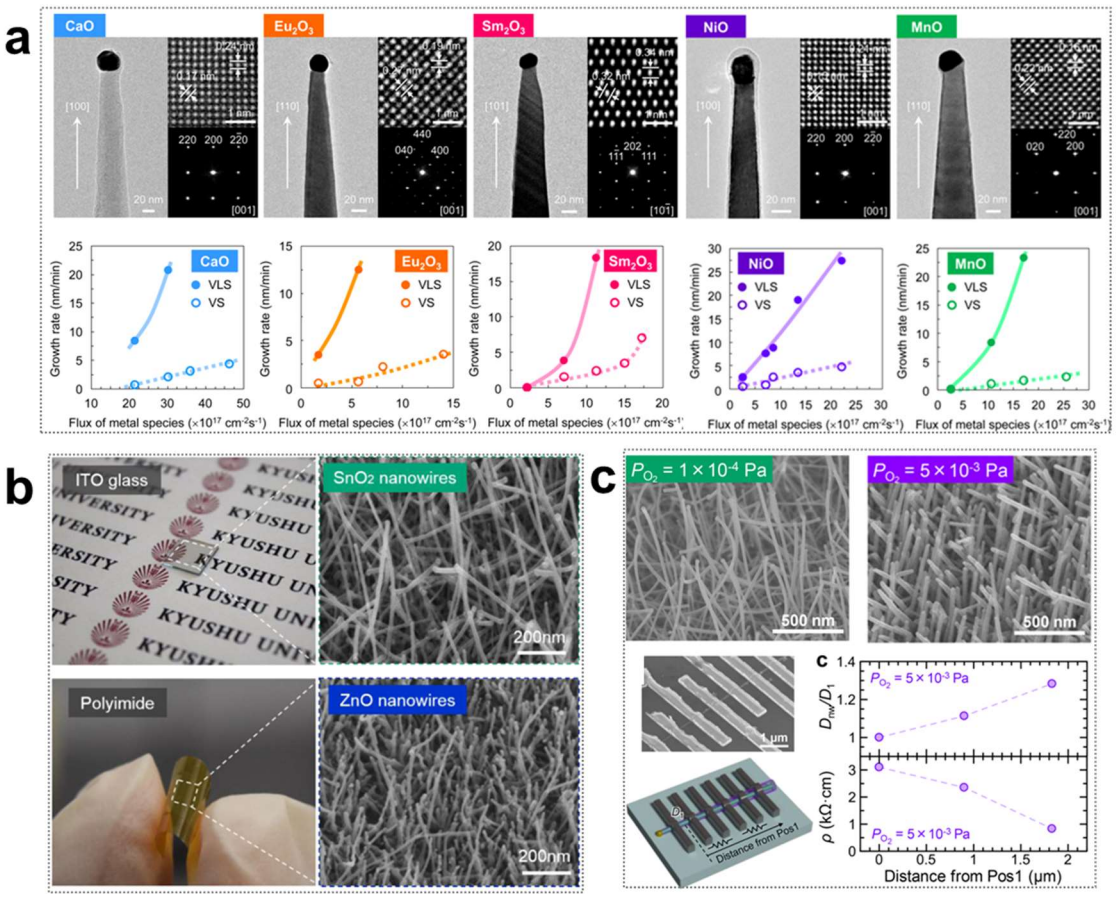

Figure 5. *Nanowire growth by PLD via VLS routine based on the concept of "material flux window". (a) Novel nanowires compose of MnO, CaO, Sm_2O_3, NiO and Eu_2O_3; [77] (b)Low temperature growth of SnO_2 and ZnO nanowires on ITO glass and PI substrates; [78] (c) Oxygen partial pressure dependence the electrical conductivities of SnO_2 nanowire.[79]*

power for the growth of nanowires. During this technical, the unique and fascinating features is nanowires size and spatial position are readily controllable by adjusting the size and spatial position of the metal catalyst, they are not attainable by other nanowire growth methods. Various nanowire growth methods, including pulsed laser deposition (PLD), molecular beam epitaxy (MBE) and chemical vapor deposition (CVD) are invented on the primary of VLS mechanism. [74-76] Among them, our group devoted much efforts to PLD growth, and also proposed a concept of "material flux window" for providing a better understanding of nanowire growth principle by VLS. [77] This concept raised that nucleation preferentially occurs only at a liquid−solid interface, in other words, VLS nanowire growth can proceed within a limited material flux range. This concept was demonstrated by several novel metal oxide nanowires, including MnO, CaO, Sm_2O_3, NiO and Eu_2O_3, all of them had never been successful synthesized by VLS route. Afterwards, Zhu et. al developed a rational pathway for VLS growth

metal-oxide nanowire process to reduce its temperature according to the concept of material flux window, the successfully prepared nanowires onto low growth temperatures required tin-doped indium oxide (ITO) glass and polyimide (PI) substrates (Figure 5b) shows its application potential.[78] What's more, an unusual oxygen partial pressure dependence of the electrical conductivity of VLS growth single-crystalline SnO_2 nanowires reported by H. Anzai et. al presented in Figure 5c, they pave the way for wide functionality synthesizing and real-life application of metal oxide nanowires. [79]

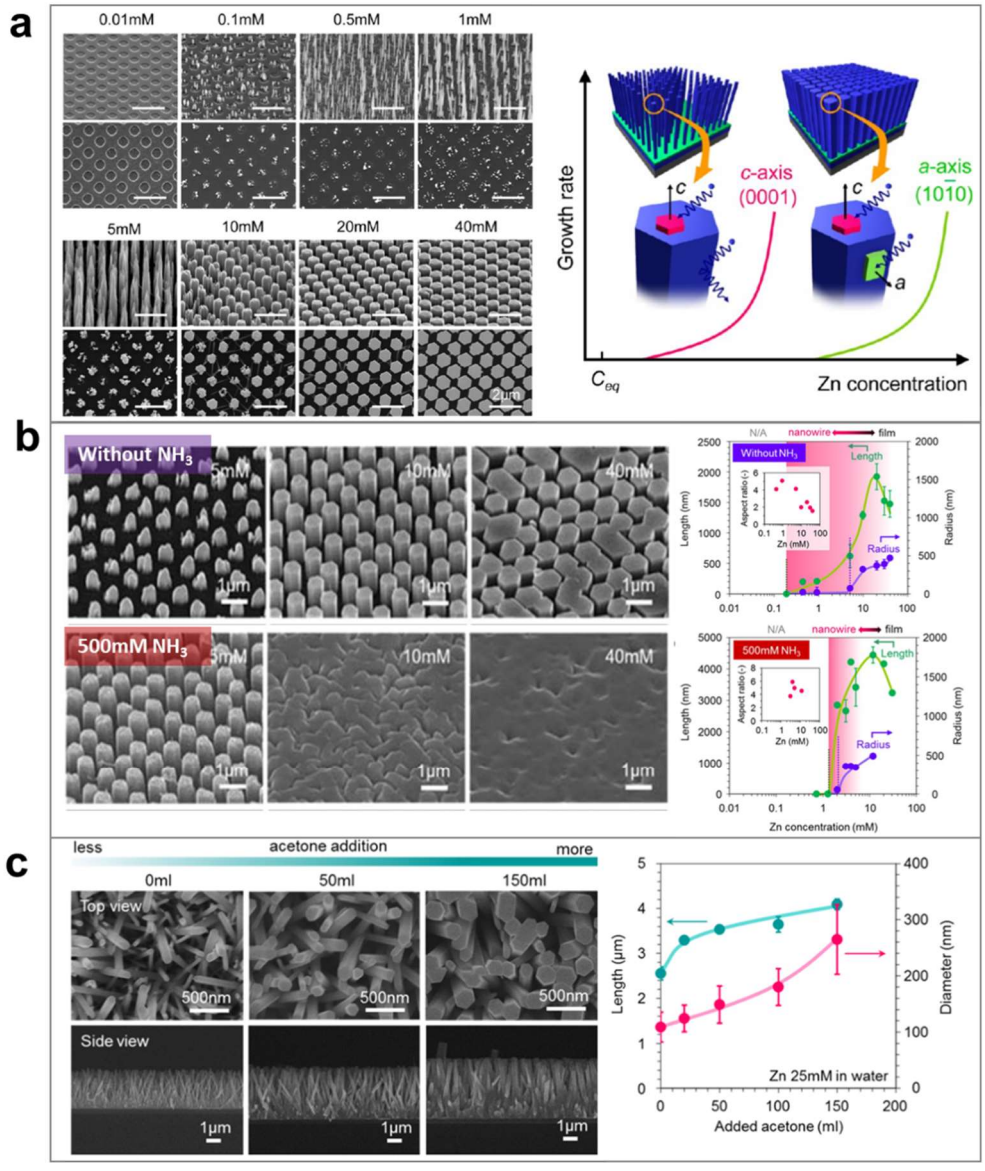

***Figure 6**. Investigation of hydrothermal ZnO nanowire growth mechanism. (a) Concentration dependence on a crystal growth of hydrothermal ZnO nanowires; [89] (b) "Concentration window" for hydrothermal ZnO nanowires relays on PH value in alkaline growth solution; [90] (c) Water−organic cosolvents as solution for on nucleation and anisotropic crystal ZnO nanowires growth.[91]*

Solution growth nanowires: Traditional vapor phase growth nanowire always suffers from the necessarily of high precursor vaporization temperature ranged from 600 to 1000 °C [80-85], which directly raised the requirement of instrument as well as synthesis cost. Even our group had reduced this temperature to 400 °C, when compared with conventional liquid methods, it still a main disadvantage for wide-range application. Contrarily, the solution nanowire growth method just advantage from its growth processes can be performed under a relatively low-temperature, in terms of hydrothermal method, the growth temperature of zinc oxide nanowire can be even less than 100 °C, [86-88] makes this method become so attractive in nanowire field. Those years our group also devoted much effort to investigate the hydrothermal ZnO nanowire growth principle in addition to VLS method. The Zn precursor concentration dependence the nanowire growth direction was confirmed by Y. He et. al by using a regular array structure. They proved the selective anisotropic growth on (0001) plane of ZnO emerged within a certain concentration Zn ion range. When beyond this range, a crystal growth on $(10\bar{1}0)$ plane tends to simultaneously occur. [89] Based on their result, D. Sakai et. al came up with an idea named "concentration window", which means anisotropic crystal growth of ZnO nanowires preferentially occurs under this condition. They found that the substantially addition of ammonia can narrow the width of "concentration window", significantly increased of ZnO nanowire growth rate within the narrow range of zinc ion concentration [90]. The addition of organic solution will promote the crystal growth of both length and diameter of the nanowires.[91] Such founding provides a foundation to synthesize novel inorganic−organic hybrid functional nanowires by simultaneously using water-compatible and organic-compatible chemical reagents.

2.4.2 Integrated metal-oxide nanowire onto sensing device

Metal-oxide nanowires have a broad application in the field of developing nanoelectronics, nanomechanics, and nanophotonics. [92-96] Their high surface-to-volume ratio, quantum confinement and ballistic carrier transport effects are important features to create integrated circuits with improved performance and configuration, especially for chemo-sensor development and field-effect transistor, single-electron transistor applications. [97-99] In the last two decades, extensive research has been dedicated to integrated metal-oxide nanowires onto nanoelectrons sensing functional substrates for fully being given play from the interesting nanowire features we motioned above. Achievements of high sensitivity performance and new mechanisms to transduce the binding or action of gas analytes proved the uniquely develop

prospection act as major sensing material architecture. In this section, typical integrated nanowire sensing devices will be reviewed.

Multi-nanowires sensing devices contains resistance-type and field effect transistors (FETs) type. They have emerged as a promising label-free ultrasensitive gas sensing platform not only in light of nanowire's intrinsically merits, interwire junctions also devoted for the good sensing behavior. Normally nanowires were fabricated directly onto the substrate that has a manipulatable heater for optimizing their operating temperature. Nanowires in resistance-type sensing device provide a pathway for current flowing from positive to negative electrodes at each side of multi-nanowires, in the meantime recording the resistance change with surrounding gas molecules. FETs-type devices basically convert the signals of molecules' surface reaction by the various of current through source to drain, which can be acted by two electrodes. In this case, current origins from applying gate voltage (located at the insulation layer) and influences by the density of charge carrier, this is the so-called "field effect". Many techniques have already successfully integrated multi-nanowires onto sensing devices, for example, chemical vapor deposition (CVD), hydrothermal methods and top down lithography, they are famous for capability to produce nanowires with small radial size, great accuracy, uniformity, and patterning flexibility. [100-103] T. V. Dang et. al fabricated ZnO_2, WO_3, and SnO_2 multi-nanowires sensors using on-chip growth through CVD method and compared their Cl_2 gas-sensing characteristics, [104] a brief schematic of this work is presented in Figure 7a. Their nanowires possessed an average diameter of approximately 350 nm and a length of several micrometers. Good sensing performance, such as high sensitivity and good stability can be got from as mentioned nanowires based sensor. However, there is a major drawback stands out, the relative high working temperature. For pursuing excellent sensing behaviors, heated those nanowires to above 200 °C is necessary. This is also the common defect of other semiconductor metal-oxide sensor types. In this year, Incheol Cho et. al developed a gas-sensitive zinc oxide (ZnO) nanowires synthesized directly on top of the μLED through a hydrothermal reaction. [105] Sensor device and its working performance show in Figure 7b. The direct contact between the sensing component and μLED sensor platform leads to high light coupling efficiency, minimizing power consumption of the sensor. Excellent NO_2 sensitivity ($\Delta R/R_0$ = 60.5% to 1 ppm NO_2) at the optimal operating power (~184 μW) demonstrate its potential for practical applications in mobile internet of things (IoT) devices. In addition to those tradition multi-nanowires integrated methods, a novel route reported by Javey et al. named "contact printing" from microfluidic channel method is also an easy way to get nanowires aligned with sensing

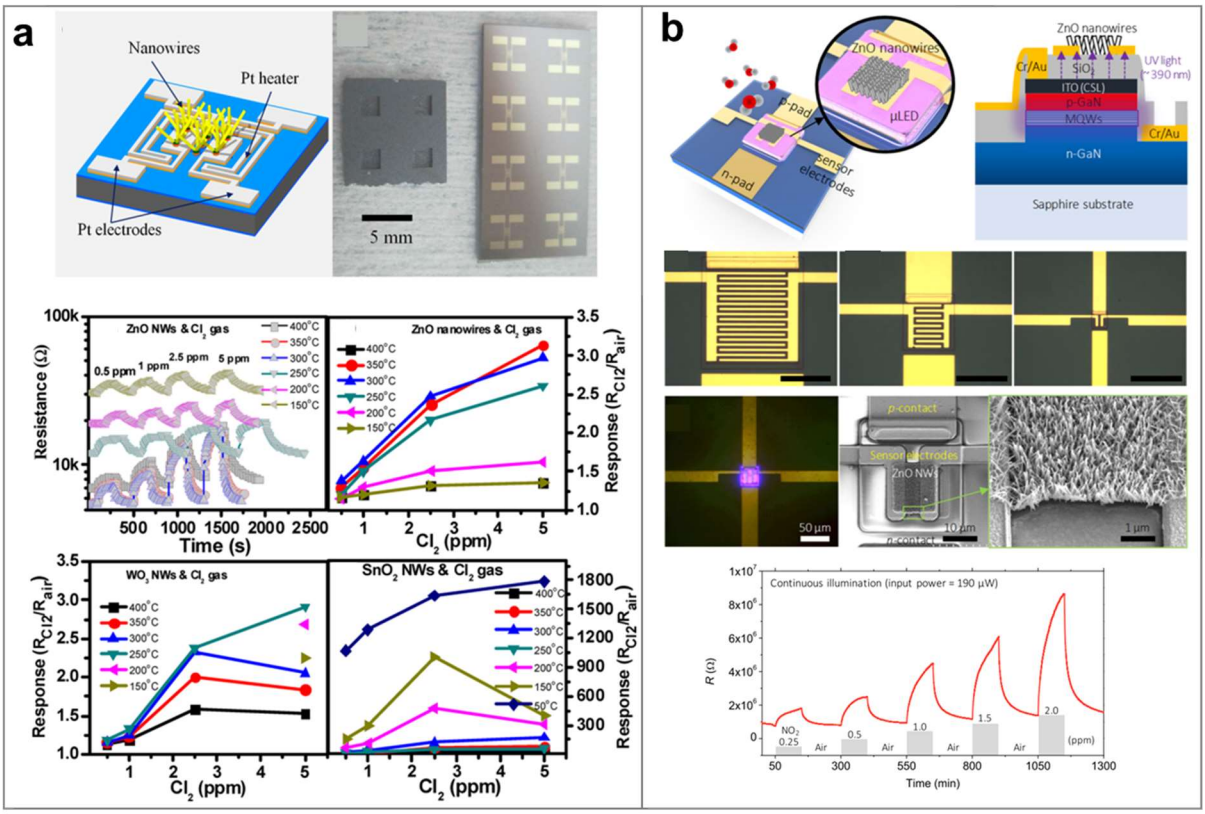

Figure 7. *Multi-nanowires sensing device. (a) Schematic and sensing property of resistance-type Cl_2 sensors integrated by ZnO_2, WO_3, and SnO_2 nanowires; [104] (b) Schematic of FETs-type ZnO nanowire NO_2 sensor actuated by μLED and its dynamic sensing response curve. [105]*

device via vander Waals interaction. [106-108]. What's more interesting is the nanowires are distributed along the sliding direction on the substrate after fabricated elsewhere, means complex functionalization process onto nanowire surface is available.

Single nanowire sensing devices: Due to the high-power consumption by multi-nanowires sensing devices we described above, researchers try to improve this defect by minimizing effective sensing area as well as heater size. Gradually manipulating a single nanowire becomes possible benefited from the spring up of nanotechnology and lithography technique, fabricating single nanowire devices on micro-heater would reduce power consumption at a certain degree. The working principle of single nanowire sensing device is same as multi-nanowires described in above paragraph. To researchers' surprise, self-heating effects caused by power dissipating within small dimensions will happen during the working of electrical devices. Applying well-controlled current values through individual nanowires at relative lower value could obtain the effective sensing compares with their counterparts made of nanocrystalline thin films, signify lowered the power consumption by single nanowire devices.[109] The concept of utilizing self-

Joule-heating to integrated low power consumption single nanowire senor had already been demonstrated by much studies. Take F. Yang et. al' research as an illustration, their senor structure and hydrogen sensing performance show in Figure 8a. [110] A single heated palladium (Pd) nanowire presents dramatic reductions of response and recovery time (less than 3 sec) by imparting Joule heating, as well as present the new ability for the smallest Pd nanowires to respond to >1% H_2 while dissipating just 4 mW of power. Recent years our group also continuously engaged in designing and integrating single nanowire sensing device with low power consumption and cost by utilizing semiconductor as major sensing material. Meng et. al in our group invented a suspended single SnO_2 nanowire sensor that applied pulsed self-Joule-heating method for saving powder consumption, means while remaining the sensitivity to NO_2. [111] Their results of tremendous down power consumption to 10^2 pJ/s and the higher sensitivity compared with continuous heating condition give a strong demonstration to the possibility of solving power consumption problems of traditional metal-oxide sensor by single nanowire sensing devices.

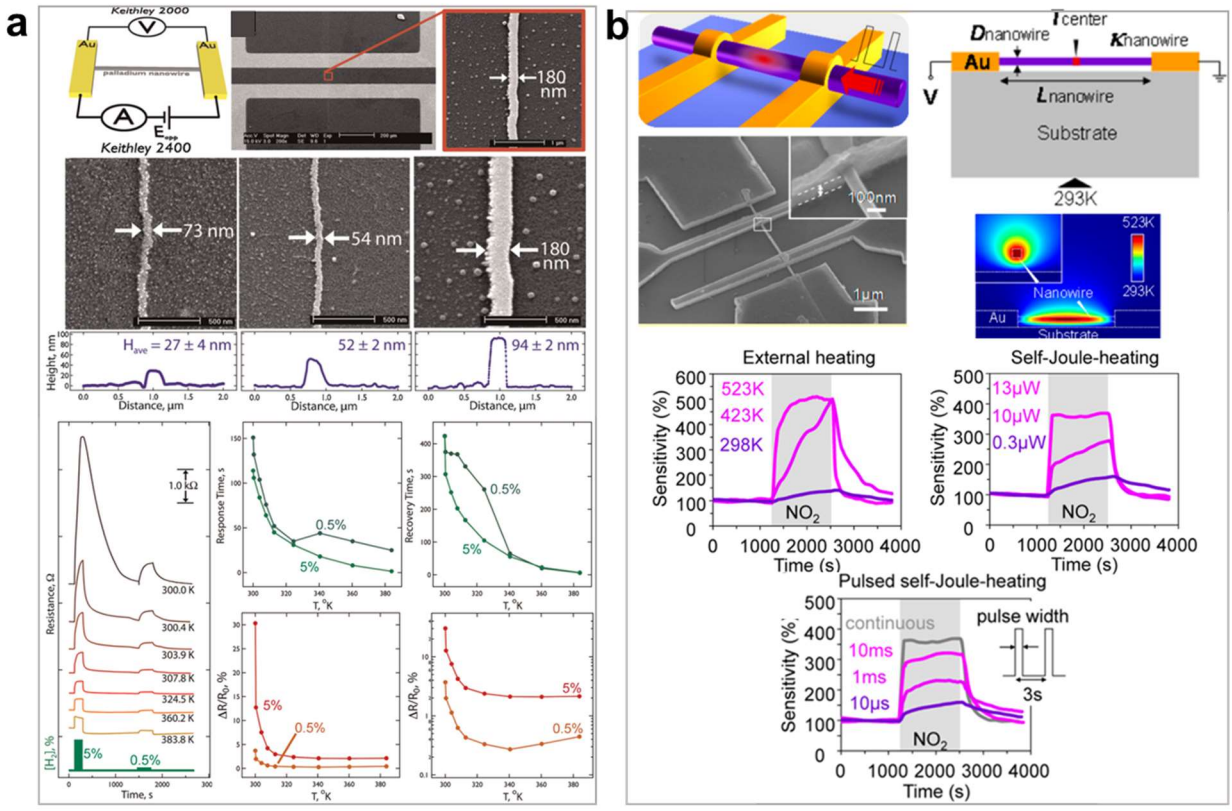

Figure 8. *Single nanowire sensing device. (a) SEM images of Pd nanowire sensor structure and Joule heating influenced on the response to hydrogen gas; [110] (b) Pulsed self-Joule-heating SnO_2 single nanowire sensor for NO_2 detection.[111]*

Nanowire preconcentration platform: In addition to the nanowire sensors that taking semiconductor metal-oxide as directly contacted section with target contained atmosphere, preconcentration platform also a suitable field for nanowire materials unleash their potential. Such preconcentration platform is a designed unit with functional target capture characters utilized prior to the detection equipment or devices for assisting improving the limitation of detection ability, such as unable to rule out interference and difficulty of tracing. In general condition, it is fabricated in a certain volume that overflow with transmit carries (reference gas or liquid buffer) allows collected matters to reach the detection section. Nowadays preconcentration platform has been successfully practiced toward classes of analytical, biological, organic, materials, and supramolecular chemistry for enhancing gas, VOCs molecules, DNA and protein recognition. [112-114] In terms of nanowire pre-concentrator, its high surface area adsorptive medium intrinsically endows capability of rapid and precise target storage/release. As a typical demonstration, the first-time separation of required protein analytes from raw bio-samples (whole blood) reported by V. Krivitsky et. al using an antibody-modified roughness-controlled silicon nanowires being performed as preconcentration platform, target proteins release in the subsequent step by liquid media swashing, their following detection was operated by anther silicon nanowire-based FETs sensing arrays with supersensitive performance. Figure 9a-b display their platform designed schematic and real-time ultrasensitive detection of protein biomarkers directly from blood samples [115]. Whole assay by such device can be rapidly performed at a time consumption around of 10 min, provides an upstream means for the analysis of proteins. Furthermore, vapor compounds preconcentrated by nanowire material would advantage from analyte vapor thermal desorption being controllable by Joule heating, as well as easy functionalization for specific recognition. These superiorities directly address a more competitive way to enhance both the sensitivity and selectivity of vapor molecule detection systems compare with previous porous analyte trapping bed and chromatography delayed separation method. B. C. Giordano's research realized the preconcentration and separation of trace nitroaromatic compounds by silicon nanowire arrays via Joule heating desorption process, can also prove the feasibility of nanowire preconcentration platform for vaporable molecules' application. Desorption temperature determination procedure (Figure 9c-f) and compounds separation analysis by mass spectrometry (Figure 9g) present the detail parameters for achieving ppt level compounds detection. [116] Even though currently few nanowire preconcentration platform integrated by metal-oxide semiconductors

has been reported, the good thermally stability and pass-through barrier-free characters reveal its worthy for further development.

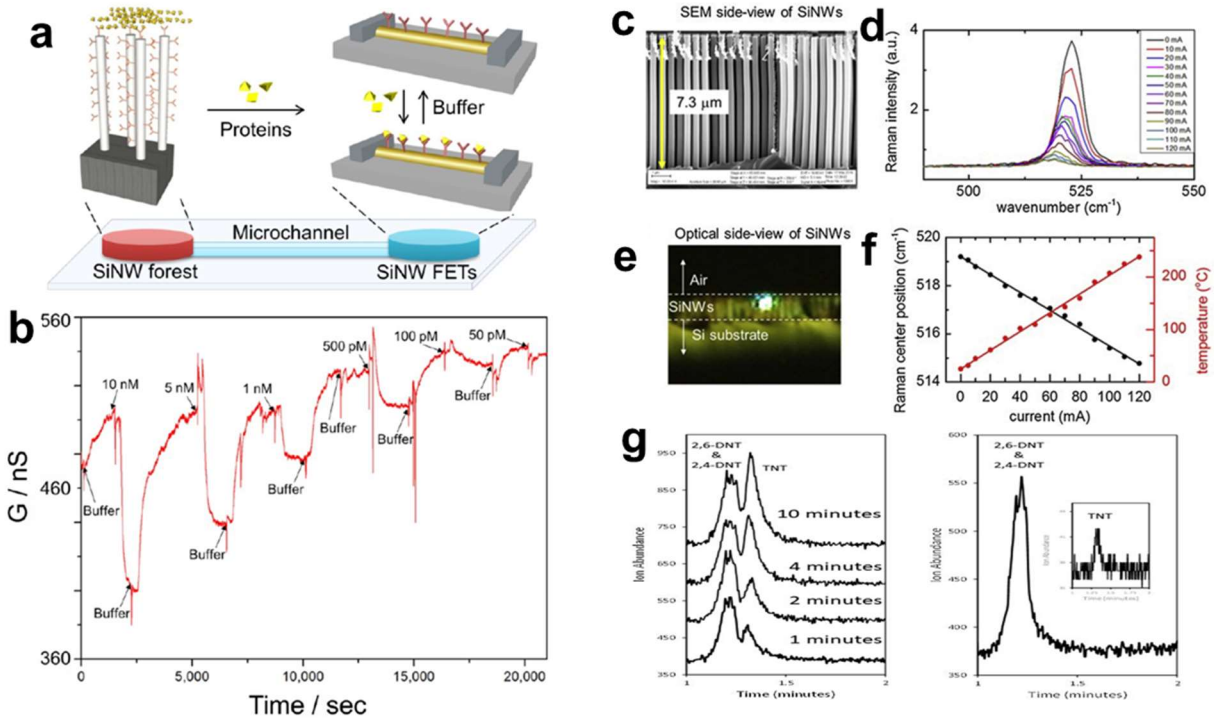

Figure 9. *(a) Schematic representation of a single chip platform integrated by silicon nanowire preconcentrator with FET nanowire detection device; (b) Real-time detection at different concentrations of the antigen; [115] (c) SEM image of silicon nanowire for fabricated vapor compounds preconcentration platform; (d-f) Raman spectra and summarized center position under different current flow; (g) Mass spectrometry by utilizing such platform for compounds concentration and separation. [116]*

2.4.3 Sensing functionalization on nanowire surface

As the ongoing raising requirement of modern society, promoting nanowire sensing property become essential for more precise and accurate detection. The impressive surface-to-volume ratio and uniformly vertical distribution on substrate of nanowire array fabricated by chemical deposition or solvent growth prompt the nanowire surface to be available to be functionalized. Nanowire based sensing devices modified with specific surface receptors have a number of key features, not only the intrinsically of direct, label-free, real-time electrical signal transduction, and addressable integrated, also ultrahigh sensitivity with exquisite selectivity improved via specific modification, bring their such an unique position among a broad range of fields that can't be cough up by currently most other types of sensing devices. C. M. Lieber with F.

Patolsky reviewed several typical nanowire FET sensors with specific functional modification on sensing material surface to illustrate them as powerful detection platform for aiming biological and chemical species in both commercial and research applications.[117-118] A pH nanowire FET sensor was first designed principled from 3-aminopropyltriethoxysilane yielding amino groups together with silanol moieties function as receptors for hydrogen ions to be captured and taken reaction into occurring by silicon nanowire surface modification manner.[119] Where after this, protein streptavidin was selectively detected through molecule biotin modified nanowire sensor, as well as virus bind with antibody evidenced the advances of surface functionalization method for particularly detecting capability. [120] However, as far to our knowledge, direct at functionalization for specific small molecules detection (gas and short-chain organic molecules) has not been achieved so far because of the similar surface reaction mechanism. Once this problem is solved, gas sensor will enter a brand-new space. Therefore, many researches endeavor to develop novel material as modifying receptor take advantage of unique characters. For example, cerium oxide (CeO_2) is discovered as a potential receptor based on the reversible valence states transition between Ce^{4+} and Ce^{3+} when exposed to oxidation/reduction gas atmosphere. In account of this principle, CeO_2 nanodot-decorated WO_3 nanowires are successfully synthesized by K. Yuan. [121] Sensor structure, nanowire morphology and acetone sensing property are shown in Figure 10 (a-h) in detail. nanowires exhibited a remarkable enhancement in acetone-sensing performance and superior selectivity. Except metal oxide modification, metal catalyst decoration is also an effective way to obtain excellent nanowire sensing material. Y. Qin et. al formed a needle-like, rough silicon nanowires with firm attachment of tiny Ag NPs, its TEM images shown in Figure 10i. [122] Comparative investigations for NH_3 sensing properties indicate that the Ag@silicon-nanowire displayed an ~3-fold enhancement in gas response and ultra-fast response and recovery characters at room temperature compared with pristine Si nanowires (Figure 10j and k), thus provides a new approach for development of ultrasensitive Si-nanowire-based gas sensors. A resistance effect model was further suggested to clarify the underlying mechanism which is favorable for further understanding and investigating modified nanowires. A mass of similar studies has proved that surface functionalization by specific modification is an easy and effective manner to obtained desired sensing material, with the merits of nanowire, a broad research space is waiting to be reached.

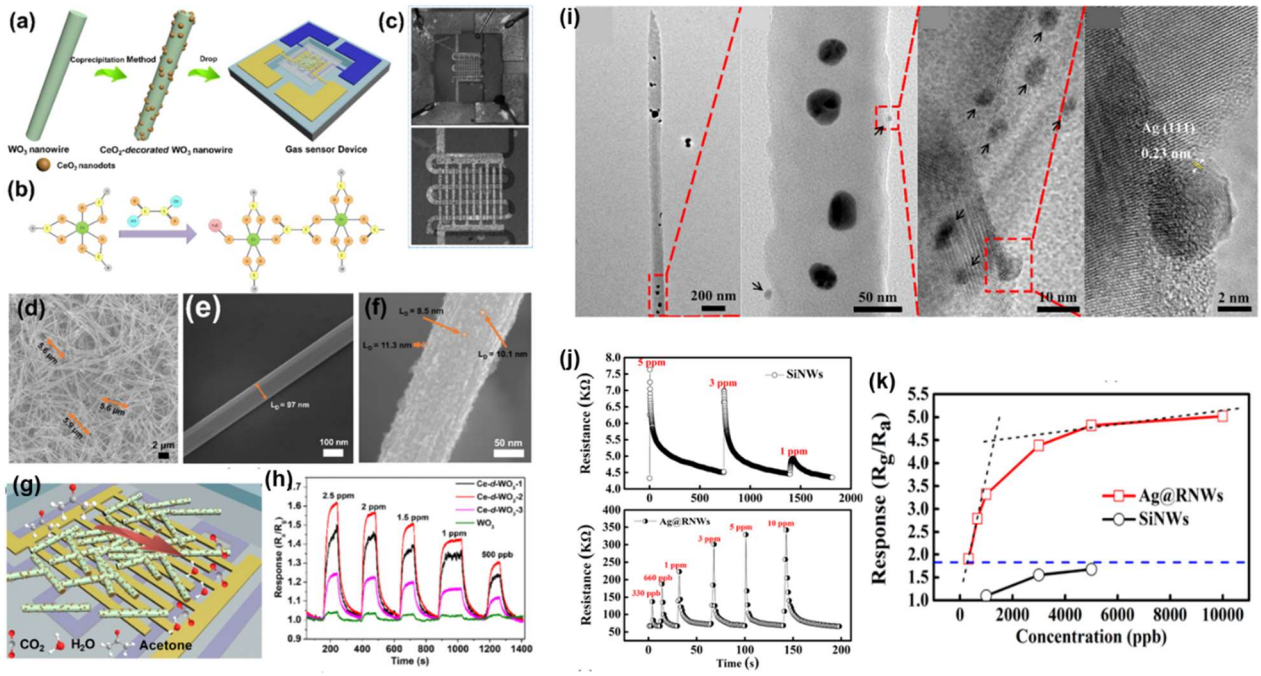

Figure 10. *(a-h) CeO_2 nanodot-decorated WO_3 nanowires acetone sensor. (a) Sensor fabricated procedure; (b)Valence state transition illumination; (c)SEM images of fabricated sensor. (d-f) SEM images of CeO_2 nanodot-decorated WO_3 nanowires; (g) Schematic of acetone sensing principle; (h) Acetone sensing property by CeO_2 nanodot-decorated WO_3 nanowires. (i-k) Ag modified silicon nanowire NH_3 sensor. (i) TEM images of Ag modified silicon nanowire; (j) Sensing performance towards several concentration NH_3;(k) Sensing response summarized from j.*

2.5 Summary

In this chapter, literatures reported about gas molecules detection techniques were generally reviewed, they can be divided into two spices: laboratorial instruments and portable gas sensor. Laboratory instruments always employ mass spectrometry and optical spectroscopy as molecular analyzation skills, which can provide accurate chemical species analysis results. But at the mean time greatly enlarged the bulk, as well as rouse the cost up, limited their application in laboratory range. On the contrary to those instruments, portable gas sensors take the advantages of small size, low power consumption and availability for real-time detection, but lack of precise detection. Semiconductor metal-oxide based sensors are regarded as the most potential portable kind origin from their flexible fabricated and stable sensing performance.

Then the discussion went to the most accepted sensing mechanism, design of sensor configuration and nanomaterial structure effected to sensing performance. Surface adsorbed and ionized oxygen species take the crucial position for the resistance type sensors, where

located the majority molecule to surface reaction. Hierarchical nanostructure sensing materials with high surface area and good porosity performed supersensitive than normal nanoparticles or thin-film. Among mass of structures, nanowire as a typical one-dimension nanostructure presents considerable sensing property due to its well-confined and uniformly controllable characters.

Subsequently, metal oxide nanowires were emphasizing introduced from the synthesis methods to sensing device application. Currently VLS deposition and hydrothermal methods dominate the nanowire synthesis. Both methods can easily obtain desired radio and length single crystal nanowires on the substrate. Integrated nanowires array on to sensor devices would fabricate multi-nanowires sensor, even though excellent sensitivity is achievable, this kind od sensor always suffered from high operating temperature, which means high power consumption. Manipulate a single nanowire to integrate a sensor device can greatly reduced temperature requirement. Nanowires could also perform as preconcentrating platform, assisting the sensor to reach low molecular detection limit and discriminate from complex surroundings.

Finally, for achieving nanowire sensing device with specific recognition function, surface receptor modification become a suitable manner. Despite obvious gas sensitivity enhancement by surface functionalization, the low selectivity is still a drawback limited their development. Further investigation towards concentrated and uninterpreted sensing functionalization would be attractive in the following decades.

2.6 REFERENCE

[1]. Reynolds J H. High sensitivity mass spectrometer for noble gas analysis[J]. Review of Scientific Instruments, 1956, 27(11): 928-934.

[2]. Pavia, D. L.; Lampman, G. M.; Kritz, G. S.; Engel, R. G. Introduction to Organic Laboratory Techniques (4th Ed.). Thomson Brooks/Cole., 2006.

[3]. Materazzi S, Curini R. On-line evolved gas analysis by infrared spectroscopy coupled to thermoanalytical instruments[J]. Applied Spectroscopy Reviews, 2001, 36(1): 1-9.

[4]. Cullen W R, Eigendorf G K, Nwata B U, et al. The quantitation of butyltin and cyclohexyltin compounds in the marine environment of British Columbia[J]. Applied organometallic chemistry, 1990, 4(6): 581-590.

[5]. Ramaswamy B R, Shanmugam G, Velu G, et al. GC–MS analysis and ecotoxicological risk assessment of triclosan, carbamazepine and parabens in Indian rivers[J]. Journal of hazardous materials, 2011, 186(2-3): 1586-1593.

[6]. Sermakkani M, Thangapandian V. GC-MS analysis of Cassia italica leaf methanol extract[J]. Asian J Pharm Clin Res, 2012, 5(2): 90-94.

[7]. Styczynski M P, Moxley J F, Tong L V, et al. Systematic identification of conserved metabolites in GC/MS data for metabolomics and biomarker discovery[J]. Analytical chemistry, 2007, 79(3): 966-973.

[8]. Tamiri T, Zitrin S. Capillary column gas chromatography/mass spectrometry of explosives[J]. Journal of energetic materials, 1986, 4(1-4): 215-237.

[9]. Stambouli A, El Bouri A, Bouayoun T, et al. Headspace-GC/MS detection of TATP traces in post-explosion debris[J]. Forensic science international, 2004, 146: S191-S194.

[10]. Günzler H, Gremlich H U. IR spectroscopy. An introduction[J]. 2002.

[11]. Noda I. Two-dimensional infrared (2D IR) spectroscopy: theory and applications[J]. Applied Spectroscopy, 1990, 44(4): 550-561.

[12]. Ferrari M, Quaresima V. A brief review on the history of human functional near-infrared spectroscopy (fNIRS) development and fields of application[J]. Neuroimage, 2012, 63(2): 921-935.

[13]. Suggs J W. Isolation of a stable acylrhodium (III) hydride intermediate formed during aldehyde decarbonylation. Hydroacylation[J]. Journal of the American Chemical Society, 1978, 100(2): 640-641.

[14]. Rauchfuss T B. Transition metal activation of aldehydes: platinum metal derivatives of o-diphenylphosphinobenzaldehyde[J]. Journal of the American Chemical Society, 1979, 101(4): 1045-1047.

[15]. Yee A, Morrison S J, Idriss H. A study of ethanol reactions over Pt/CeO2 by temperature-programmed desorption and in situ FT-IR spectroscopy: evidence of benzene formation[J]. Journal of Catalysis, 2000, 191(1): 30-45.

[16]. Solcà N, Dopfer O. Protonated benzene: IR spectrum and structure of C6H7+[J]. Angewandte Chemie International Edition, 2002, 41(19): 3628-3631.

[17]. Bell D R, Ihinger P D, Rossman G R. Quantitative analysis of trace OH in garnet and pyroxenes[J]. American Mineralogist, 1995, 80(5-6): 465-474.

[18]. Guillen M D, Cabo N. Characterization of edible oils and lard by Fourier transform infrared spectroscopy. Relationships between composition and frequency of concrete bands in the fingerprint region[J]. Journal of the American Oil Chemists' Society, 1997, 74(10): 1281-1286.

[19]. Baker M J, Trevisan J, Bassan P, et al. Using Fourier transform IR spectroscopy to analyze biological materials[J]. Nature protocols, 2014, 9(8): 1771.

[20]. Stuart B. Infrared spectroscopy[J]. Kirk-Othmer Encyclopedia of Chemical Technology, 2000.

[21]. Hanna A, Marshall J C, Isenhour T L. A GC/FT-IR Compound Identification System[J]. Journal of Chromatographic Science, 1979, 17(8): 434-440.

[22]. Ragunathan N, Krock K A, Klawun C, et al. Gas chromatography with spectroscopic detectors[J]. Journal of Chromatography A, 1999, 856(1-2): 349-397.

[23]. Andrasko J, Lagesson-Andrasko L, Dahlén J, et al. Analysis of Explosives by GC-UV[J]. Journal of forensic sciences, 2017, 62(4): 1022-1027.

[24]. Moy F J, Haraki K, Mobilio D, et al. MS/NMR: a structure-based approach for discovering protein ligands and for drug design by coupling size exclusion chromatography, mass spectrometry, and nuclear magnetic resonance spectroscopy[J]. Analytical chemistry, 2001, 73(3): 571-581.

[25]. Kühnle M, Holtin K, Albert K. Capillary NMR detection in separation science[J]. Journal of separation science, 2009, 32(5-6): 719-726.

[26]. Yamazoe N. New approaches for improving semiconductor gas sensors[J]. Sensors and Actuators B: Chemical, 1991, 5(1-4): 7-19.

[27]. Yamazoe N, Sakai G, Shimanoe K. Oxide semiconductor gas sensors[J]. Catalysis Surveys from Asia, 2003, 7(1): 63-75.

[28]. Goto K S. Solid state electrochemistry and its applications to sensors and electronic devices[M]. Elsevier, 2013.

[29]. Rajeshwar K, Ibanez J G. Environmental electrochemistry: Fundamentals and applications in pollution sensors and abatement[M]. Elsevier, 1997.

[30]. Levitsky I A. Porous silicon structures as optical gas sensors[J]. Sensors, 2015, 15(8): 19968-19991.

[31]. Hodgkinson J, Tatam R P. Optical gas sensing: a review[J]. Measurement Science and Technology, 2012, 24(1): 012004.

[32]. Barrettino D, Graf M, Taschini S, et al. CMOS monolithic metal–oxide gas sensor microsystems[J]. IEEE Sensors Journal, 2006, 6(2): 276-286.

[33]. Itoh T, Matsubara I, Nishibori M, et al. Calibration gas preparation for non-disposable portable MOx, PID, and IER VOC detectors[J]. Sensor Letters, 2012, 10(3-4): 985-992.

[34]. Xu D, Zhang Z, Yu Z. Analysis on thermal balance and design principles of catalytic combustion gas sensor[C]//2009 4th IEEE International Conference on Nano/Micro Engineered and Molecular Systems. IEEE, 2009: 898-903.

[35]. Lee E B, Hwang I S, Cha J H, et al. Micromachined catalytic combustible hydrogen gas sensor[J]. Sensors and Actuators B: Chemical, 2011, 153(2): 392-397.

[36]. Du H, Bogue R. MEMS sensors: past, present and future[J]. Sensor Review, 2007.

[37]. Nguyen N T, Huang X, Chuan T K. MEMS-micropumps: a review[J]. J. Fluids Eng., 2002, 124(2): 384-392.

[38]. Zhang W M, Yan H, Peng Z K, et al. Electrostatic pull-in instability in MEMS/NEMS: A review[J]. Sensors and Actuators A: Physical, 2014, 214: 187-218.

[39]. Japanese Patent Application No. 45-38200 (1962); Y. Shimizu, Y. Nakamura, and M. Egashira

[40]. Hydrogen-sensitive Schottky barrier diodes Surface Sci., 86 (1979), pp. 345-352.

[41]. Briand D, van der Schoot B, de Rooij N F, et al. A low-power micromachined MOSFET gas sensor[J]. Journal of microelectromechanical systems, 2000, 9(3): 303-308.

[42]. Seo H, Endoh T, Fukuda H, et al. Highly sensitive MOSFET gas sensors with porous platinum gate electrode[J]. Electronics letters, 1997, 33(6): 535-536.

[43]. Barsan, N., Simion, C., Heine, T, et al. Modeling of sensing and transduction for p-type semiconductor metal oxide based gas sensors [J]. Journal of Electroceramics, 2009,25:11-19

[44]. Min, Y., Tuller, H.L., Palzer, S., Wölenstein, J., Bötner, H., Gas response of reactively sputtered ZnO films on Si-based micro-array [J]. Sens. Actuators B 2003, 93: 435-441

[45]. Gong, H., Wang, Y.J., Teo, S.C., Huang, L., Interaction between thin-film tin oxide gas sensor and five organic vapors [J]. Sens. Actuators B 1999, 54: 232-235

[46]. Gergintschew, Z., Förster, H., Kositza, J., Schipanski, D., Two-dimensional numerical simulation of semiconductor gas sensor [J]. Sens. Actuators B 1995, 25: 170-173

[47]. Zhang, J., Wang, S.R., Wang, Y., Zhu, B.L., Zhang, S.M., Huang, W.P., Wu, S.H., Hierarchically porous ZnO architectures for gas sensor application [J]. Cryst. Growth Des., 2009, 9: 3532-3537

[48]. Law, M., Kind, H., Messe, B., Kim, F., Yang, P. Angew. Photochemical sensing of NO2 with SnO2 nanoribbon nanosensors at room temperature [J]. Chem., Int. Ed. 2002, 41: 2405−2408

[49]. Li, X.W., Zhou, X., Guo, H., Wang, C., Liu, J.Y., Sun, P., Liu, F., Lu, G. Design of Au@ZnO yolk−shell nanospheres with enhanced gas sensing properties. [J]ACS Appl. Mater. Interfaces. 2014, 6: 18661−18667.

[50]. Seiyama, T., A new detector for gases components using semiconductive thin film [J]. Anl. Chem., 1962, 34: 1502-1503

[51]. Wu T C, De Luca A, Zhong Q, et al. Inkjet-printed CMOS-integrated graphene–metal oxide sensors for breath analysis[J]. npj 2D Materials and Applications, 2019, 3(1): 1-10.

[52]. Rakow N A, Suslick K S. A colorimetric sensor array for odour visualization[J]. Nature, 2000, 406(6797): 710-713.

[53]. Lin H, Suslick K S. A colorimetric sensor array for detection of triacetone triperoxide vapor[J]. Journal of the American Chemical Society, 2010, 132(44): 15519-15521.

[54]. Lavigne J J. Tastes good to me[J]. Nature materials, 2007, 6(8): 548-549.

[55]. Nelson, T. L.; O'Sullivan, C.; Greene, N. T.; Maynor, M. S.; Lavigne, J. J. J. Am. Chem. Soc. 2006, 128, 5640–5641.

[56]. Snowden, T. S.; Anslyn, E. V. Curr. Opin. Chem. Biol. 1999, 3, 740–746.

[57]. Y. Takezawa, H. Imai, Bottom-up synthesis of titanate nanosheets with hierarchical structures and a high specific surface area, Small 3 (2006) 390–393.

[58]. X.-J. Huang, Y.-K. Choi, Chemical sensors based on nanostructured materials, Sens. Actuators B 122 (2007) 659–671.

[59]. Yin Y, Rioux R M, Erdonmez C K, et al. Formation of hollow nanocrystals through the nanoscale Kirkendall effect[J]. Science, 2004, 304(5671): 711-714.

[60]. Sun Y, Mayers B T, Xia Y. Template-engaged replacement reaction: a one-step approach to the large-scale synthesis of metal nanostructures with hollow interiors[J]. Nano Letters, 2002, 2(5): 481-485.

[61]. Wang Z, Luan D, Boey F Y C, et al. Fast formation of SnO_2 nanoboxes with enhanced lithium storage capability[J]. Journal of the American Chemical Society, 2011, 133(13): 4738-4741.

[62]. Wang L, Tang F, Ozawa K, et al. A general single-source route for the preparation of hollow nanoporous metal oxide structures[J]. Angewandte Chemie International Edition, 2009, 48(38): 7048-7051.

[63]. He T, Chen D, Jiao X, et al. Co_3O_4 Nanoboxes: Surfactant-Templated Fabrication and Microstructure Characterization[J]. Advanced Materials, 2006, 18(8): 1078-1082.

[64]. Wang Z, Zhou L, Lou X W. Metal oxide hollow nanostructures for lithium-ion batteries[J]. Advanced materials, 2012, 24(14): 1903-1911.

[65]. Kim H R, Choi K I, Lee J H, et al. Highly sensitive and ultra-fast responding gas sensors using self-assembled hierarchical SnO2 spheres[J]. Sensors and Actuators B: Chemical, 2009, 136(1): 138-143.

[66]. Wang L L, Fei T, Lou Z, et al. Three-dimensional hierarchical flowerlike α-Fe2O3 nanostructures: synthesis and ethanol-sensing properties[J]. ACS applied materials & interfaces, 2011, 3(12): 4689-4694.

[67]. Zhu G, Xu H, Xiao Y, et al. Facile fabrication and enhanced sensing properties of hierarchically porous CuO architectures[J]. ACS applied materials & interfaces, 2012, 4(2): 744-751.

[68]. Bennewitz, R. Aligned Carbon Nanotubes; 2004.

[69]. Wang, Z. L. ZnO Nanowire and Nanobelt Platform for Nanotechnology. Mater. Sci. Eng. R: Reports 2009, 64, 33–71

[70]. Z.L. Wang (Ed.), Nanowires and Nanobelts—Materials, Properties and Devices, Kluwer Academic Publishers, Boston (2003)

[71]. Ra, H. W.; Choi, K. S.; Kim, J. H.; Hahn, Y. B.; Im, Y. H. Fabrication of ZnO Nanowires Using Nanoscale Spacer Lithography for Gas Sensors. Small 2008, 4, 1105–1109.

[72]. Jain, S. K.; Bhardwaj, B. R.; Ault, S. Impact of Intelligence Dissemination on New Business Creation. Singapore Manag. Rev. 2011, 33, 29–41.

[73]. Wagner, R. S.; Ellis, W. C.; Jackson, K. A.; Arnold, S. M. Study of the Filamentary Growth of Silicon Crystals from the Vapor. J. Appl. Phys. 1964, 35, 2993–3000.

[74]. Morber J R, Ding Y, Haluska M S, et al. PLD-assisted VLS growth of aligned ferrite nanorods, nanowires, and nanobelts synthesis, and properties[J]. The Journal of Physical Chemistry B, 2006, 110(43): 21672-21679.

[75]. Paek J H, Nishiwaki T, Yamaguchi M, et al. Catalyst free MBE-VLS growth of GaAs nanowires on (111) Si substrate[J]. physica status solidi c, 2009, 6(6): 1436-1440.

[76]. Givargizov E I. Fundamental aspects of VLS growth[M]//Vapour Growth and Epitaxy. Elsevier, 1975: 20-30.

[77]. Klamchuen A, Suzuki M, Nagashima K, et al. Rational concept for designing vapor–liquid–solid growth of single crystalline metal oxide nanowires[J]. Nano letters, 2015, 15(10): 6406-6412.

[78]. Zhu Z, Suzuki M, Nagashima K, et al. Rational Concept for Reducing Growth Temperature in Vapor–Liquid–Solid Process of Metal Oxide Nanowires[J]. Nano letters, 2016, 16(12): 7495-7502.

[79]. Anzai H, Takahashi T, Suzuki M, et al. Unusual Oxygen Partial Pressure Dependence of Electrical Transport of Single-Crystalline Metal Oxide Nanowires Grown by the Vapor–Liquid–Solid Process[J]. Nano letters, 2019, 19(3): 1675-1681.

[80]. Ng, H. T.; Li, J.; Smith, M. K.; Nguyen, P.; Cassell, A.; Han, J.; Meyyappan, M. Growth of epitaxial nanowires at the junctions of nanowalls. Science 2003, 300, 1249−1249.

[81]. Kuang, Q.; Lao, C.; Wang, Z. L.; Xie, Z.; Zheng, L. High- sensitivity humidity sensor based on a single SnO 2 nanowire. J. Am. Chem. Soc. 2007, 129, 6070−6071.

[82]. Yanagida, T.; Marcu, A.; Matsui, M.; Nagashima, K.; Oka, K.; Yokota, K.; Taniguchi, M.; Kawai, T. Enhancement of oxide VLS growth by carbon on substrate surface. J. Phys. Chem. C 2008, 112, 18923−18926.

[83]. Yanagida, T.; Nagashima, K.; Tanaka, H.; Kawai, T. Mechanism of catalyst diffusion on magnesium oxide nanowire growth. Appl. Phys. Lett. 2007, 91, 061502.

[84]. Nagashima, K.; Yanagida, T.; Tanaka, H.; Kawai, T. Epitaxial growth of MgO nanowires by pulsed laser deposition. J. Appl. Phys. 2007, 101, 124304.

[85]. Meng, G.; Yanagida, T.; Nagashima, K.; Yoshida, H.; Kanai, M.; Klamchuen, A.; Zhuge, F. W.; He, Y.; Rahong, S.; Fang, X.; Takeda, S.; Kawai, T. Impact of Preferential Indium Nucleation on Electrical Conductivity of Vapor-Liquid-Solid Grown Indium-Tin Oxide Nanowires. J. Am. Chem. Soc. 2013, 135, 7033−7038.

[86]. Vayssieres L. Growth of arrayed nanorods and nanowires of ZnO from aqueous solutions[J]. Advanced Materials, 2003, 15(5): 464-466.

[87]. Greene L E, Law M, Goldberger J, et al. Low-temperature wafer-scale production of ZnO nanowire arrays[J]. Angewandte Chemie International Edition, 2003, 42(26): 3031-3034.

[88]. Greene L E, Law M, Tan D H, et al. General route to vertical ZnO nanowire arrays using textured ZnO seeds[J]. Nano letters, 2005, 5(7): 1231-1236.

[89]. He Y, Yanagida T, Nagashima K, et al. Crystal-plane dependence of critical concentration for nucleation on hydrothermal ZnO nanowires[J]. The Journal of Physical Chemistry C, 2013, 117(2): 1197-1203.

[90]. Sakai D, Nagashima K, Yoshida H, et al. Substantial narrowing on the Width of “concentration Window” of Hydrothermal Zno nanowires via Ammonia Addition[J]. Scientific reports, 2019, 9(1): 1-10.

[91]. Akihiro Y, Nagashima K, Hosomi T, et al. Water–Organic Cosolvent Effect on Nucleation of Solution-Synthesized ZnO Nanowires[J]. ACS omega, 2019, 4(5): 8299-8304.

[92]. Gudiksen, M. S.; Lauhon, L. J.; Wang, J.; Smith, D. C.; Lieber, C. M. Growth of Nanowire Superlattice Structures for Nanoscale Photonics and Electronics. Nature 2002, 415, 617−620.

[93]. Jibril, L.; Ramírez, J.; Zaretski, A. V.; Lipomi, D. J. SingleNanowire Strain Sensors Fabricated by Nanoskiving. Sens. Actuators, A 2017, 263, 702−706.

[94]. Johnson, J. C.; Yan, H.; Schaller, R. D.; Haber, L. H.; Saykally, R. J.; Yang, P. Single Nanowire Lasers. J. Phys. Chem. B 2001, 105, 11387−11390.

[95]. Tian, B.; Kempa, T. J.; Lieber, C. M. Single Nanowire Photovoltaics. Chem. Soc. Rev. 2009, 38, 16−24.

[96]. Su, Y.; Liu, C.; Brittman, S.; Tang, J.; Fu, A.; Kornienko, N.; Kong, Q.; Yang, P. Single-Nanowire Photoelectrochemistry. Nat. Nanotechnol. 2016, 11, 609−612

[97]. Huang, Y.-L.; Chou, M. H.; Wu, S. Y.; Cheng, C.-L. Investigation of Quantum-Confinement Effect in a Single CuO Nanowire. Jpn. J. Appl. Phys. 2008, 47, 703−705.

[98]. Kobayashi, M.; Hiramoto, T. Experimental Study on Quantum Confinement Effects in Silicon Nanowire Metal-Oxide-Semiconductor Field-Effect Transistors and Single-Electron Transistors. J. Appl. Phys. 2008, 103, 053709.

[99]. Colinge, J.-P.; Lee, C.-W.; Afzalian, A.; Akhavan, N. D.; Yan, R.; Ferain, I.; Razavi, P.; O’Neill, B.; Blake, A.; White, M.; et al. Nanowire Transistors without Junctions. Nat. Nanotechnol. 2010, 5, 225−229.

[100]. Cui Y, Wei Q, Park H, et al. Nanowire nanosensors for highly sensitive and selective detection of biological and chemical species[J]. science, 2001, 293(5533): 1289-1292.

[101]. Chen Y, Zhu C, Wang T. The enhanced ethanol sensing properties of multi-walled carbon nanotubes/SnO2 core/shell nanostructures[J]. Nanotechnology, 2006, 17(12): 3012.

[102]. Elibol O H, Morisette D, Akin D, et al. Integrated nanoscale silicon sensors using top-down fabrication[J]. Applied Physics Letters, 2003, 83(22): 4613-4615.

[103]. Engström D, Trivedi R P, Persson M, et al. Three-dimensional imaging of liquid crystal structures and defects by means of holographic manipulation of colloidal nanowires with faceted sidewalls[J]. Soft Matter, 2011, 7(13): 6304-6312.

[104]. Van Dang T, Duc Hoa N, Van Duy N, et al. Chlorine gas sensing performance of on-chip grown ZnO, WO3, and SnO2 nanowire sensors[J]. ACS applied materials & interfaces, 2016, 8(7): 4828-4837.

[105]. Cho I, Sim Y, Cho M, et al. Monolithic Micro LED/Metal Oxide Nanowire Gas Sensor with Microwatt-Level Power Consumption[J]. ACS sensors, 2020.

[106]. Javey, A.; Nam, S. W.; Friedman, R. S.; Yan, H.; Lieber, C. M. Nano Lett. 7, 773-777.

[107]. Fan, Z.; Ho, J. C.; Jacobson, Z. A.; Yerushalmi, R.; Alley, R. L.; R, H.; Javey, A. Nano Lett. 2008, 8, 20-25.

[108]. Takahashi, T.; Takei, K.; Ho, J. C.; Chueh, Y.-L.; Fan, Z.; Javey, A. J. Am. Chem. Soc. 2009, 131, 2102-2103.

[109]. Prades J D, Jimenez-Diaz R, Hernandez-Ramirez F, et al. Ultralow power consumption gas sensors based on self-heated individual nanowires[J]. Applied Physics Letters, 2008, 93(12): 123110.

[110]. Yang F, Taggart D K, Penner R M. Joule heating a palladium nanowire sensor for accelerated response and recovery to hydrogen gas[J]. small, 2010, 6(13): 1422-1429.

[111]. Meng G, Zhuge F, Nagashima K, et al. Nanoscale thermal management of single SnO2 nanowire: pico-Joule energy consumed molecule sensor[J]. ACS sensors, 2016, 1(8): 997-1002.

[112]. Xu X Y, Yan B. Eu (III)-functionalized ZnO@ MOF heterostructures: integration of pre-concentration and efficient charge transfer for the fabrication of a ppb-level sensing platform for volatile aldehyde gases in vehicles[J]. Journal of Materials Chemistry A, 2017, 5(5): 2215-2223.

[113]. Abbas A, Brimer A, Slocik J M, et al. Multifunctional analytical platform on a paper strip: separation, preconcentration, and subattomolar detection[J]. Analytical chemistry, 2013, 85(8): 3977-3983.

[114]. Romero V, Costas-Mora I, Lavilla I, et al. Graphene membranes as novel preconcentration platforms for chromium speciation by total reflection X-ray fluorescence[J]. Rsc Advances, 2016, 6(1): 669-676.

[115]. Krivitsky V, Hsiung L C, Lichtenstein A, et al. Si nanowires forest-based on-chip biomolecular filtering, separation and preconcentration devices: nanowires do it all[J]. Nano letters, 2012, 12(9): 4748-4756.

[116]. Giordano B C, Ratchford D C, Johnson K J, et al. Silicon nanowire arrays for the preconcentration and separation of trace explosives vapors[J]. Journal of Chromatography A, 2019, 1597: 54-62.

[117]. Patolsky F, Zheng G, Hayden O, et al. Electrical detection of single viruses[J]. Proceedings of the National Academy of Sciences, 2004, 101(39): 14017-14022.

[118]. Patolsky F, Zheng G, Lieber C M. Nanowire sensors for medicine and the life sciences[J]. 2006.

[119]. Cui Y, Wei Q, Park H, et al. Nanowire nanosensors for highly sensitive and selective detection of biological and chemical species[J]. science, 2001, 293(5533): 1289-1292.

[120]. Patolsky F, Zheng G, Hayden O, et al. Electrical detection of single viruses[J]. Proceedings of the National Academy of Sciences, 2004, 101(39): 14017-14022.

[121]. Yuan K, Wang C Y, Zhu L Y, et al. Fabrication of a Micro-Electromechanical System-Based Acetone Gas Sensor Using CeO2 Nanodot-Decorated WO3 Nanowires[J]. ACS Applied Materials & Interfaces, 2020, 12(12): 14095-14104.

[122]. Qin Y, Liu D, Zhang T, et al. Ultrasensitive silicon nanowire sensor developed by a special Ag modification process for rapid NH3 detection[J]. ACS applied materials & interfaces, 2017, 9(34): 28766-28773.

CHAPTER III

DESIGNED SYNTHESIS OF METAL OXIDE NANOWIRE AND THEIR SURFACE CHEMICAL PROPERTY

3.1 Elemental doping on Hydrothermal Metal Oxide Nanowire Synthesis

3.1.1 ABSTRACT

Rationally designing morphology and elemental doping of inorganic nanomaterials is the most fundamental and important challenge for developing bottom-up nanodevice applications. Here we demonstrate that coordination structure of impurity metal ions on nanowire surface critically determines the morphology and the dopant distribution of hydrothermal zinc oxide (ZnO) nanowires. Introduction of tungstate ions (WO_4^{2-}) significantly enhances a nucleation at sidewall $(10\bar{1}0)$ plane, while the dopant incorporation occurs only at (0001) plane unexpectedly. These conflicted face-selective behaviors lead to inhomogeneous dopant distribution in an individual ZnO nanowire. Density functional theory (DFT) calculations reveal that such face-selective behaviors are interpreted in terms of the coordination structure of WO_4^{2-} ions on each ZnO crystal plane. WO_4^{2-} ions coordinated on $(10\bar{1}0)$ plane with unipodal or bipodal bonds serve as surfactant for attracting Zn ion species, whereas those coordinated on (0001) plane with tripodal bonds are easily incorporated into nanowire as dopant. Upon our findings, we successfully demonstrate the rational control over the morphology and the elemental doping of W-doped ZnO nanowire via modulating nucleation events and WO_4^{2-} ion adsorption with a recently developed concentration window principle. This study clearly highlights the essential importance to understand the coordination structure of metal ions for designing the hydrothermal metal oxide nanowire synthesis.

KEYWORDS

Elemental doping, face-selective event, nucleation, dopant distribution, hydrothermal growth, ZnO nanowires

3.1.2 INTRODUCTION

Hydrothermal synthesis of inorganic nanomaterials[1-4] offers wide range of applications[5-11] due to the scalability and the compatibility with various substrates and material processes[12-14] originating from its low process temperature which is not available by vapor-phase synthesis[15-18]. The functions of inorganic nanomaterials strongly depends on their geometry. Therefore, most of previous researches have been devoted to establishing predictable models and strategies for controlling the morphology of nanomaterials. As for the hydrothermally synthesized zinc oxide (ZnO) nanowires, the strategies based on the electrostatic interaction between metal ions and crystals[19], the organic ligand based surface capping[20], the ligand-exchange effect[21] and the difference in critical nucleation concentrations on crystal planes so-called "concentration window"[22-24] have been demonstrated and successfully manipulated the nanowire morphology.

On the other hand, elemental doping is a typical approach for aggressively tuning the functions of inorganic nanomaterials. The elemental doping to nanowires has been intensively investigated in vapor-phase synthesis[25,26]. The feasibility of elemental doping for hydrothermal ZnO nanowires has been also demonstrated together with successful modifications of electrical, optical and surface chemical properties[27-30]. However, there still remains much room for investigating the elemental doping in hydrothermal nanowire synthesis. For example, the doping often accompanies the variations of anisotropic crystal growth of ZnO nanowires[31-34] and in other case, the metal impurities solely serve as counter ions rather than being incorporated into the nanowires[19,35]. These results plausibly originate from the variety of chemical reactions and electrostatic effects in the hydrothermal system[19,36-38], which are not seen in vapor-phase synthesis. Furthermore, the dopant distribution in an individual hydrothermal nanowire has not been discussed so far, while its importance has been highlighted in a vapor-liquid-solid (VLS) nanowire[25]. As such, the elemental doping in hydrothermal synthesis is far from comprehensive understanding and controlling over the morphology and the dopant distribution of hydrothermal nanowire is a challenging issue.

In the present research, we report the critical role of coordination structure of impurity metal ions on nanowire surface for controlling over the morphology and the dopant distribution of hydrothermal ZnO nanowires. Systematic experiments and simulations reveal that tungstate ions (WO_4^{2-}) face-selectively act as surfactant and dopant on different crystal planes according to their coordination structure. Furthermore, the dopant distribution in an individual

hydrothermal ZnO nanowire is unveiled for the first time by means of three-dimensional atom probe (3DAP) measurement. Based on above results, a predictable model and a rational strategy to control over the morphology and the dopant distribution of hydrothermal ZnO nanowires are demonstrated.

3.1.3 EXPERIMENTAL

W-doped ZnO nanostructures/nanowires were fabricated by a seed layer assisted hydrothermal method under atmospheric pressure. Prior to the growth, a 50 nm thick ZnO seed layer was deposited onto a 100 nm thick SiO_2 coated Si (100) substrate with a 1 nm thick Ti adhesion layer by radio frequency (RF) sputtering. The growth solution was prepared at room temperature by mixing zinc nitrate hexahydrate ($Zn(NO_3)_2 \cdot 6H_2O$, Wako 99.0 %), hexamethylenetetramine (HMTA, $(CH_2)_6N_4$ Wako 99.0 %), polyethyleneimine (PEI, number average m.w. 1800, ALDRICH 50 wt.% in H_2O) and sodium tungstate dehydrate ($Na_2WO_4 \cdot 2H_2O$, ALDRICH ≥99 %) in deionized (DI) water with varying their concentrations. Then the hydrothermal reaction was conducted at 95 ºC and 75 ºC for 5 hours by immersing the seed layer coated substrate into the growth solution in a manner of upside down. After the growth, the samples were rinsed in DI water and dried by N_2 blow at room temperature. The equilibrium concentrations of ionic species in the growth solution was calculated by Visual MINTEQ 3.1. The DFT calculations for the coordinated structures of WO_4^{2-} ion and Zn ion species on ZnO surface were performed by VASP 5.4.4 using implicit water solvation model. The resident time of WO_4^{2-} ion on ZnO crystals was estimated by using the Frenkel equation. The morphology, composition and crystal structure of fabricated nanostructures were characterized by field effect scanning electron microscopy (FESEM, JEOL JSM-7610F) equipped with energy dispersive x-ray spectroscopy (EDS), transmission electron microscopy (TEM, JEOL JEM-2100F), x-ray photoelectron spectroscopy (XPS, Kratos AXIS-ULTRA) and x-ray diffraction (XRD, Philips X'Pert MRD), respectively. High angle annular dark field scanning transmission electron microscopy (HAADF-STEM) and EDS analyses in figure 5 and figure S7 were performed by FEI Titan G2 80-200. Three-dimensional atom probe (3DAP) measurement was carried out using CAMECA LEAP5000XS in a laser mode at specimen temperature of 30 K and the laser pulse energy and pulse rate were 30 pJ and 250 kHz, respectively. Samples for STEM and 3DAP measurement were prepared by focused ion beam (FIB) with dual beam system (FEI Helios G4UX).

3.1.4 RESULTS AND DISCUSSION

Tungsten is an appropriate dopant species for ZnO in terms of the ionic radius (Zn^{2+} 60pm, W^{6+} 42 pm) and the coordination number (Zn^{2+}(IV) and W^{6+}(IV)). In fact, the improvement of molecular sensing property of ZnO thin film was previously demonstrated by W doping.[39,40] Figure 1 (a) shows side view and top view scanning electron microscopy (SEM) images of ZnO nanowires when varying Na_2WO_4 concentration (C_W) under the constant $Zn(NO_3)_2$ concentration (C_{Zn}) 25 mM. The details of growth conditions are shown in Experimental Section and figure S1-S2. When increasing C_W, the nanowire tends to be a platelet form. The statistic nanowire length and diameter in figure 1 (b) show that the diameter exceeds the length above C_W 0.25 mM. This indicates that the preferential growth direction of ZnO nanowires changes from [0001] to $[10\bar{1}0]$ just by adding 1 % of impurity in the growth solution. Figure 1 (c) shows the low and high magnification transmission electron microscopy (TEM) images and the electron diffraction patterns for both nanowire (C_W 0 mM) and nanoplatelet (C_W 0.125 mM) structures. Both samples show single crystallinity and hexagonal wurtzite structure, indicating that the crystallographic features of ZnO nanostructure are not varied by the W addition. Figure 1 (d) and (e) show the x-ray photoelectron spectroscopy (XPS) spectra (Zn 2p and W 4f) and the estimated W concentration (at%) of ZnO nanostructures synthesized with various C_W. When increasing C_W, W 4f peaks tend to be larger while Zn 2p peaks remains almost unchanged, leading to the systematic increase of W concentration. Figure 1 (f) and (g) show the x-ray diffraction (XRD) patterns and the calculated *d*-values of ZnO nanostructures synthesized with various C_W. The ZnO (0004) peak shifts to be higher angle and the *d*-value decreases with increasing C_W, which is plausibly due to the substitution of Zn^{2+} with W^{6+}. The results of XPS and XRD show that W is incorporated into ZnO nanostructures. Alternatively, these results represent that controlling morphology and W doping of hydrothermal ZnO nanowires is quite difficult.

For exploring a way to overcome above dilemma between the dopant incorporation and the morphological variation, we first consider why the preferential growth direction of nanowires is changed by W addition. In previous studies, the formation of nanoplatelet structure was interpreted in terms of the growth inhibition by the electrostatic adsorption of counter ions[19] and/or the chemisorption of inorganic and organic ligands[20,35] on ZnO (0001) plane. In order to specify the possible metal counter ion species, we performed thermodynamic calculation of equilibrium concentration of ionic species under the given growth condition. We found that

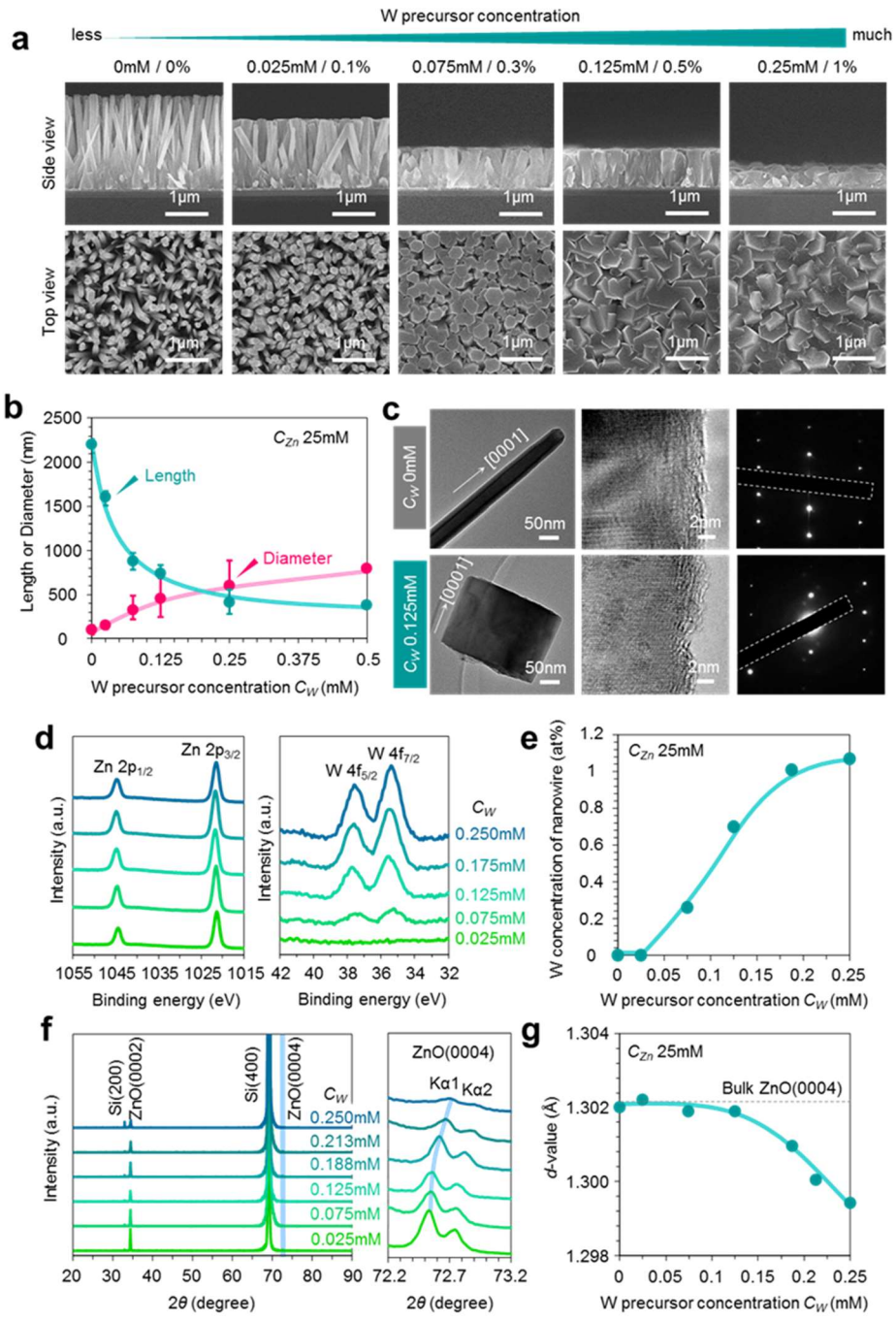

Figure 1. *(a) SEM images and (b) statistic length and diameter data of ZnO nanowires grown with varying CW. CZn is kept to be 25 mM. (c) TEM images and selected area electron diffraction (SAED) patterns of both nanowire and nanoplate grown with CW 0 mM and CW 0.125 mM, respectively. (d) Zn 2p and W 4f XPS spectra and (e) W concentration of ZnO nanowires grown with various CW. (f) XRD patterns and (g) d-value of ZnO nanowires grown with various CW.*

WO_4^{2-} ion is the most plausible adsorption species for the growth inhibition (Figure S3). To understand the contribution of WO_4^{2-} ions for the growth inhibition, next we examine the Zn

precursor concentration dependence on ZnO nanowire growth with various C_W. Previous our study demonstrated that there exist two threshold concentrations corresponding to the critical concentrations for nucleation on (0001) plane and $(10\bar{1}0)$ plane[22-24]. By evaluating the shifts of critical concentrations by varying C_W, the influence of WO_4^{2-} ions for the nucleation events on ZnO crystal planes can be identified. Figure 2 (a) and (b) show the Zn precursor concentration dependences on length and diameter of ZnO nanowires with various C_W. The SEM images for the series of C_{Zn} are shown in Figure S4. The triangle marks in the graphs represent the critical concentration for nucleation. These results are summarized in figure 2 (c). The critical concentration on $(10\bar{1}0)$ plane (i.e. sidewall) tends to be lower while that on (0001) plane (i.e. nanowire top) is almost unchanged with increasing C_W. This indicates that WO_4^{2-} ions rather enhance the nucleation on $(10\bar{1}0)$ plane than suppress the nucleation on (0001) plane. Note that the growth inhibition on (0001) plane seems to be negligible at lower C_W range, but it becomes significant by increasing C_W to 0.25 mM. We found that the nucleation on (0001) would be enhanced with decreasing C_{Zn} below the critical concentration on $(10\bar{1}0)$ plane although the W/Zn ratio in precursor becomes higher. Thus, above results indicate that the variation of preferential growth direction of ZnO nanowires by W addition cannot be explained by the existing growth inhibition model and rather suggest the selective nucleation enhancement on $(10\bar{1}0)$ plane.

In general, dopant incorporation event is accompanied with crystal growth. Therefore we assume that W incorporation mainly occurs through $(10\bar{1}0)$ plane. In fact, the results of XPS analysis in figure 2 (d) and (e) support this model, i.e. the W concentration of ZnO nanowires increases with increasing C_{Zn} above the critical concentration for nucleation on $(10\bar{1}0)$ plane. However, the following XRD results show more complicated situation for the W incorporation. Figure 2 (f) and (g) show the XRD pattern of ZnO (0002) peak and the *d*-value for the W-doped ZnO nanowires when varying C_{Zn}. We found that there are two components in (0002) peak and among the one is consistent with bulk ZnO, implying the coexistence of non-doped part and W-doped part in an individual ZnO nanowire. Furthermore, there are two inconsistencies between the results of XPS and XRD. First, the XRD peak associated with W-doped ZnO still remains when completely suppressing the nucleation on $(10\bar{1}0)$ plane. Second, in XRD result, W incorporation seems to be promoted by decreasing C_{Zn} as can be seen in the decreasing trend of *d*-value for W-doped ZnO in figure 2 (g). These two features are contradictive to the results of XPS. Considering the difference of surface sensitive XPS and bulk sensitive XRD, such

contradictive features can be interpreted by that ZnO nanowires are composed of W-doped core and non-dope shell. Also this suggests that W incorporation unexpectedly occurs on (0001) plane even though W addition enhances the nucleation on $(10\bar{1}0)$ plane.

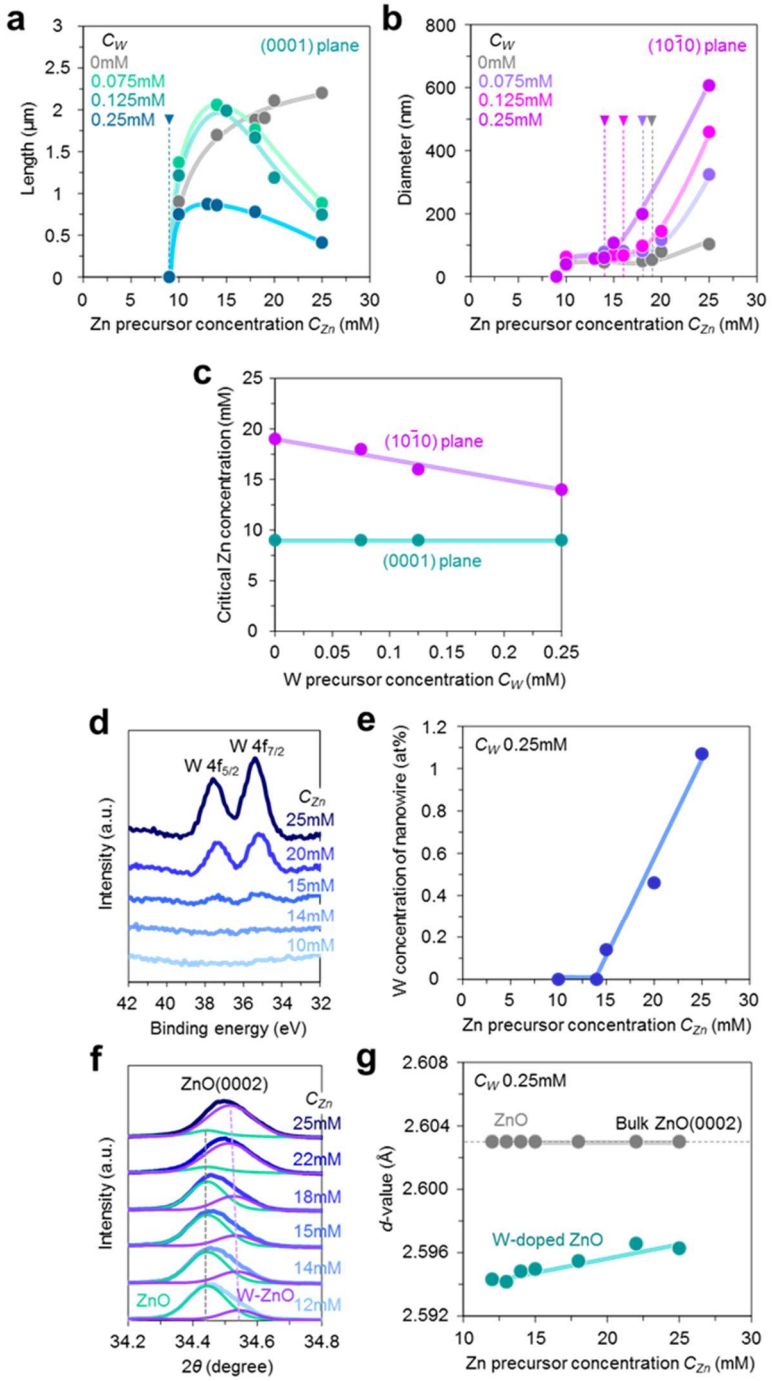

Figure 2. *Zn concentration dependences on (a) length and (b) diameter of ZnO nanowires grown with various C_W. (c) Critical Zn concentration for nucleation on (0001) plane and* $(10\bar{1}0)$ *plane as a function of C_W. (d) W 4f XPS spectra and (e) W concentration of ZnO nanowires when varying C_{Zn}. (f) XRD patterns and (g) d-value of ZnO nanowires when varying C_{Zn}.*

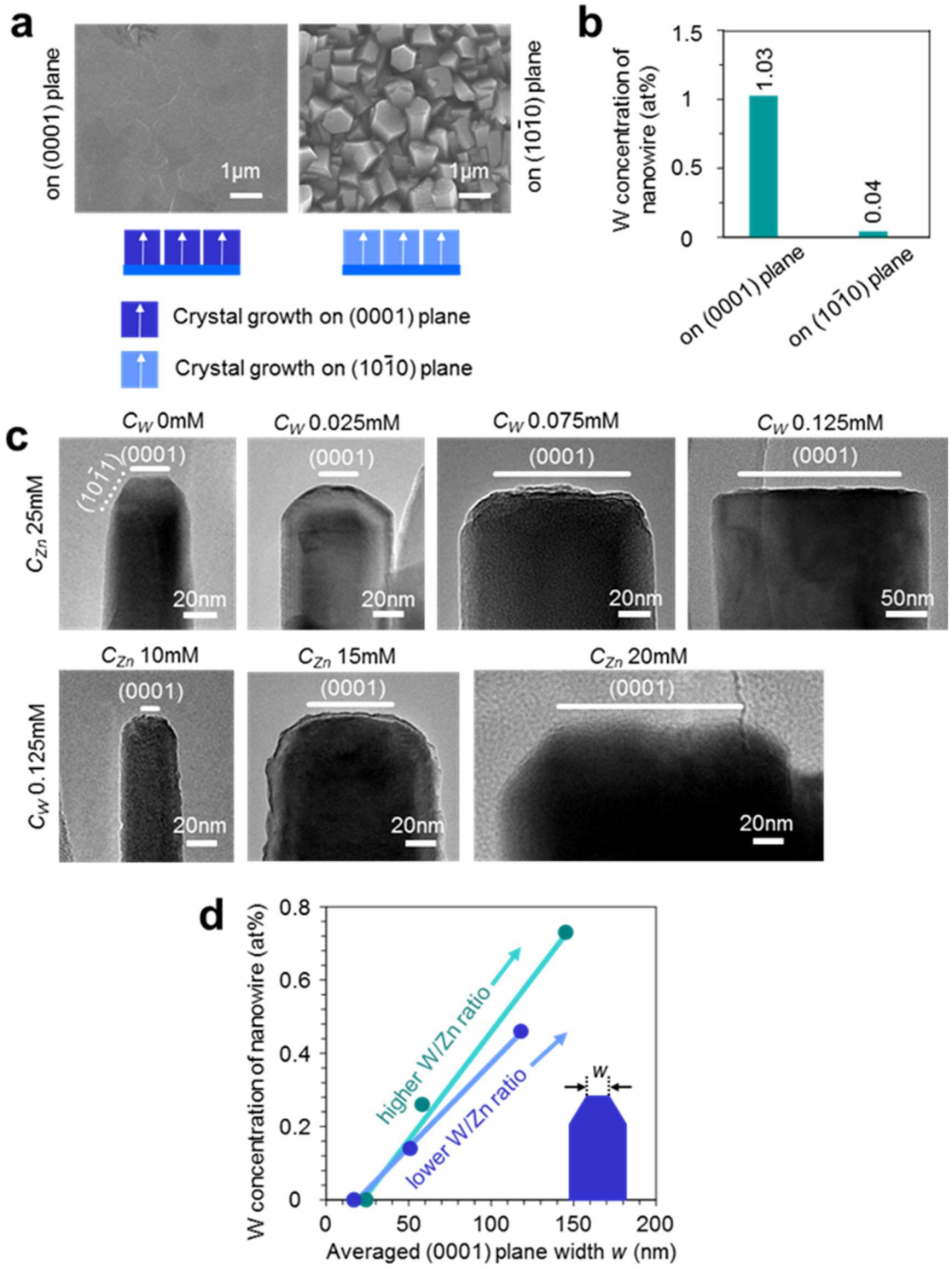

Figure 3. *(a) SEM images and (b) W concentration of ZnO nanowires grown on (0001)-oriented and* (10$\bar{1}$0)*-oriented single crystalline ZnO substrates. The nanowires are grown by* C_{Zn} *25 mM and* C_W *0.25 mM. (c) TEM images of ZnO nanowires grown with various* C_{Zn} *and* C_W*. (d) W concentration of ZnO nanowires as a function of averaged (0001) plane width. The width of (0001) plane is evaluated by TEM images.*

In order to clarify the dopant incorporation pathway, we examine the feasibility of W incorporation via the crystal growth on $(10\bar{1}0)$-oriented and (0001)-oriented single crystalline ZnO substrates as shown in figure 3 (a) and (b). In these experiments, C_{Zn} and C_W are 25 mM and 0.25 mM. The W concentration of ZnO structures grown on (0001)-oriented and $(10\bar{1}0)$-oriented substrates are 1.03 at% and 0.04 at%, respectively, supporting that W is mainly incorporated through (0001) plane. This is further confirmed via the compositional analysis using 2 step grown nanowires (see Figure S5). According to the face-selective W incorporation on (0001) plane, the result in figure 2 (e) can be interpreted in terms of an expansion of (0001) plane size followed by the sidewall growth. Therefore, we perform the TEM observation and analyze the correlation between the (0001) plane size and the W concentration of ZnO nanowires. Figure 3 (c) shows the TEM images of ZnO nanowires grown with various C_{Zn} and C_W. The (0001) plane tends to be larger with increasing C_{Zn} and/or C_W, which is associated with the nucleation enhancement on $(10\bar{1}0)$ plane discussed above. The relationship between (0001) plane width and W concentration is summarized in figure 3 (d). There is a strong correlation between them, and the W concentration is irrelevant to W/Zn ratio in precursors, clearly evidencing that W incorporation selectively occurs on (0001) plane. The TEM observation also reveals the presence of $(10\bar{1}1)$ plane at the tip of nanowires. Note that the $(10\bar{1}1)$ plane exists even suppressing the sidewall growth. The W concentration becomes almost zero when the $(10\bar{1}1)$ plane dominates the nanowire tip with decreasing the diameter. This suggests that W is not incorporated on $(10\bar{1}1)$ plane.

To confirm the hypothesis as to the face-selective dopant incorporation, we directly identify the dopant distribution in an individual ZnO nanowire. It should be described that the dopant distribution in hydrothermal ZnO nanowire has not been discussed before unlike that in VLS nanowire[16-18,25]. This might be due to that the impinging rate of impurity metal ions on each crystal plane of nanowire is equal in hydrothermal synthesis, but those on liquid-solid interface and vapor-solid interface in VLS synthesis are supposed to be different. In high angle annular dark field scanning transmission electron microscopy (HAADF-STEM) image of figure 4 (a), the clear contrast with darker core and brighter shell is seen. For this experiment, the nanowires are grown with C_{Zn} 15 mM and C_W 0.125 mM (W concentration in precursor: 0.83 %) and we chose a nanowire with sidewall growth. We found that the darker area, which is associated with W-doped part, tends to be larger along the nanowire growth direction. This is well consistent with the model of face-selective W incorporation on (0001) plane discussed above. The

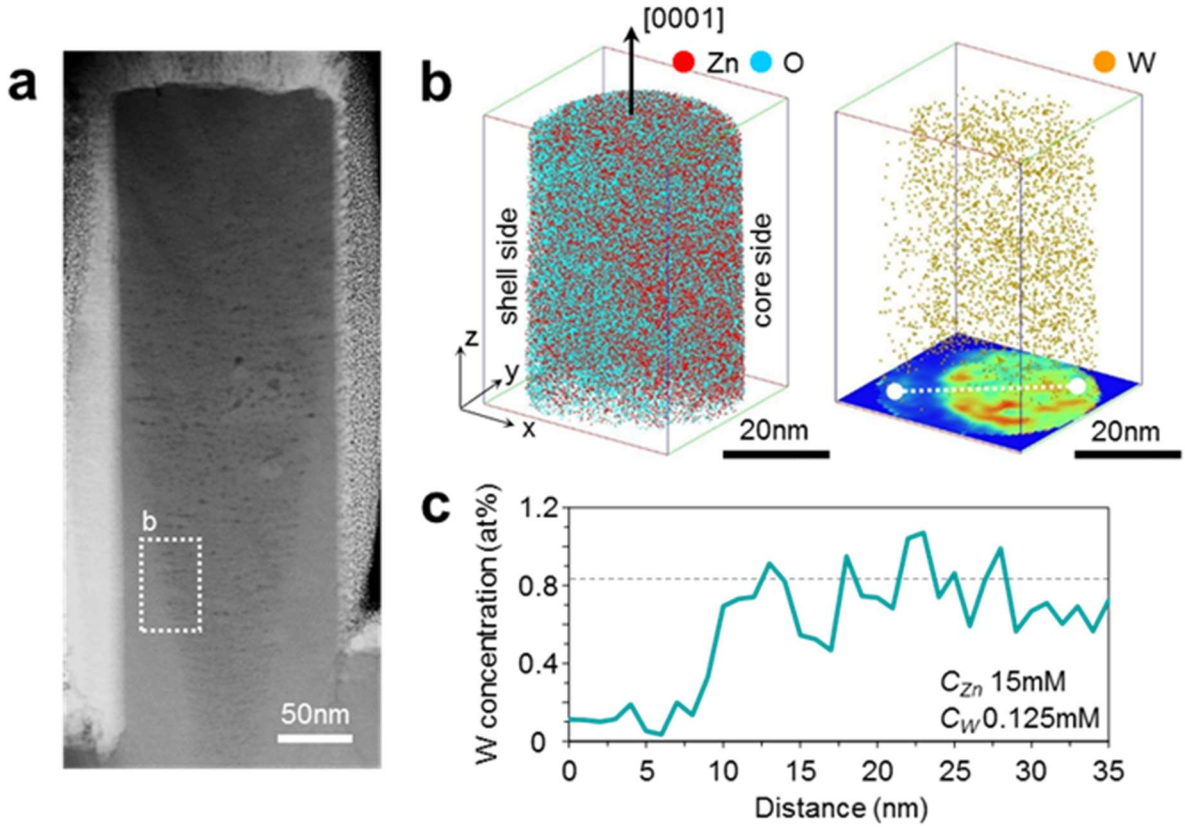

Figure 4. *(a) HAADF-STEM image of ZnO nanowire grown with C_{Zn} 15 mM and C_W 0.125 mM. (b) 3D elemental maps for Zn, O (left), and W (right) taken around the projected area in (a). 2D W concentration plot in z direction is shown at the bottom of 3D W map. (e) Line profile of W concentration along the dotted line in 2D W concetration plot of (b). The dotted line is W concentration in precursor*

qualitative analysis of dopant distribution by energy dispersive spectroscopy (EDS) shows that the darker area has higher W concentration and in this area dopant seems to be homogeneously distributed as shown in figure S6. In addition, the dopant distribution in an individual ZnO nanowire is quantitatively analyzed by 3DAP measurement as details can be seen in figure S7. Figure 4 (b) shows 3D elemental maps for Zn, O (left), and W (right) taken around the projected area in figure 4 (a). W atoms are more densely distributed in core side than shell side. This is also confirmed by 2D concentration plot shown at the bottom of 3D map and line profile in figure 4 (c). Note that avaeraged W concentrations in core area is 0.66 at%, indicating that 80% of WO_4^{2-} ions impinged on (0001) plane are incorporated into nanowires. On the other hand, W concentration in shell area is limited to 0.11 at%, which corresponds to 13% of WO_4^{2-} ions impinged on $(10\bar{1}0)$ plane. These results highlight the inhomogeneous dopant distribution in

an individual hydrothermal ZnO nanowire, resulting from the face-selective dopant incorporation.

To gain the theoretical insight as to the conflicted face-selective behaviors of WO_4^{2-} ions on nucleation and dopant incorporation, we performed density functional theory (DFT) calculations. The details of calculation are shown in Figure S8. Figure 5 (a) shows the most stable coordination structure of WO_4^{2-} ion on ZnO $(10\bar{1}0)$ plane, (0001) plane and $(10\bar{1}1)$ plane. WO_4^{2-} ion is coordinated with tripodal bonds on (0001) and $(10\bar{1}1)$ planes, and with unipodal or bipodal bonds on $(10\bar{1}0)$ plane. Here we discuss the WO_4^{2-} ion-induced nucleation enhancement on $(10\bar{1}0)$ plane by examining the various coordination of WO_4^{2-} ion and Zn species (Zn^{2+}, $[ZnOH]^+$ and $Zn(OH)_2$) on $(10\bar{1}0)$ plane in the presence of water solvent (Figure 5 (b)). The calculated interaction energies between WO_4^{2-} ion and various Zn species are summarized in Table I. The results demonstrate that the sufficient energy gain are obtained for the examined all coordination structures. The coordination is further stabilized by incorporating Zn species into ZnO crystal as shown in figure 5 (c) and (d), highlighting the surfactant role of WO_4^{2-} ions for enhancing the nucleation. Such surfactant effect of WO_4^{2-} ion must be more significant on $(10\bar{1}0)$ plane than on (0001) plane in terms of the number of unsaturated bonds of WO_4^{2-} ion for coordinating with Zn ions (i.e. 2 or 3 bonds on $(10\bar{1}0)$ plane and 1 bond on (0001) plane). Thus WO_4^{2-} ions selectively enhance the nucleation on $(10\bar{1}0)$ plane as experimentally shown above. Next we consider the face-selective dopant incorporation on (0001) plane, which must be correlated with the stability of coordinated WO_4^{2-} ions. We calculated the adsorption energies of WO_4^{2-} ions on ZnO $(10\bar{1}0)$ plane, (0001) plane and $(10\bar{1}1)$ plane, as summarized in Table II. Note that in the simulation, the WO_4^{2-} ions are not adsorbed on O-terminated (0001) and $(10\bar{1}1)$ planes, therefore, we calculated the adsorption energies on Zn-terminated planes. The adsorption energies of WO_4^{2-} ions on ZnO crystal planes become higher in the following order $(10\bar{1}1) < (10\bar{1}0) <$ (0001). This indicates that the WO_4^{2-} ion is preferentially adsorbed on (0001) plane followed by being incorporated into nanowire. Although the stable adsorption of WO_4^{2-} ions with tripodal bonds is also available on $(10\bar{1}1)$ plane, it is destabilized on $(10\bar{1}1)$ plane by the hydration effect. Thus our calculation clearly explain that the coordination structure of WO_4^{2-} ion on ZnO crystal surface critically determines the morphology and the dopant distribution of hydrothermal ZnO nanowire.

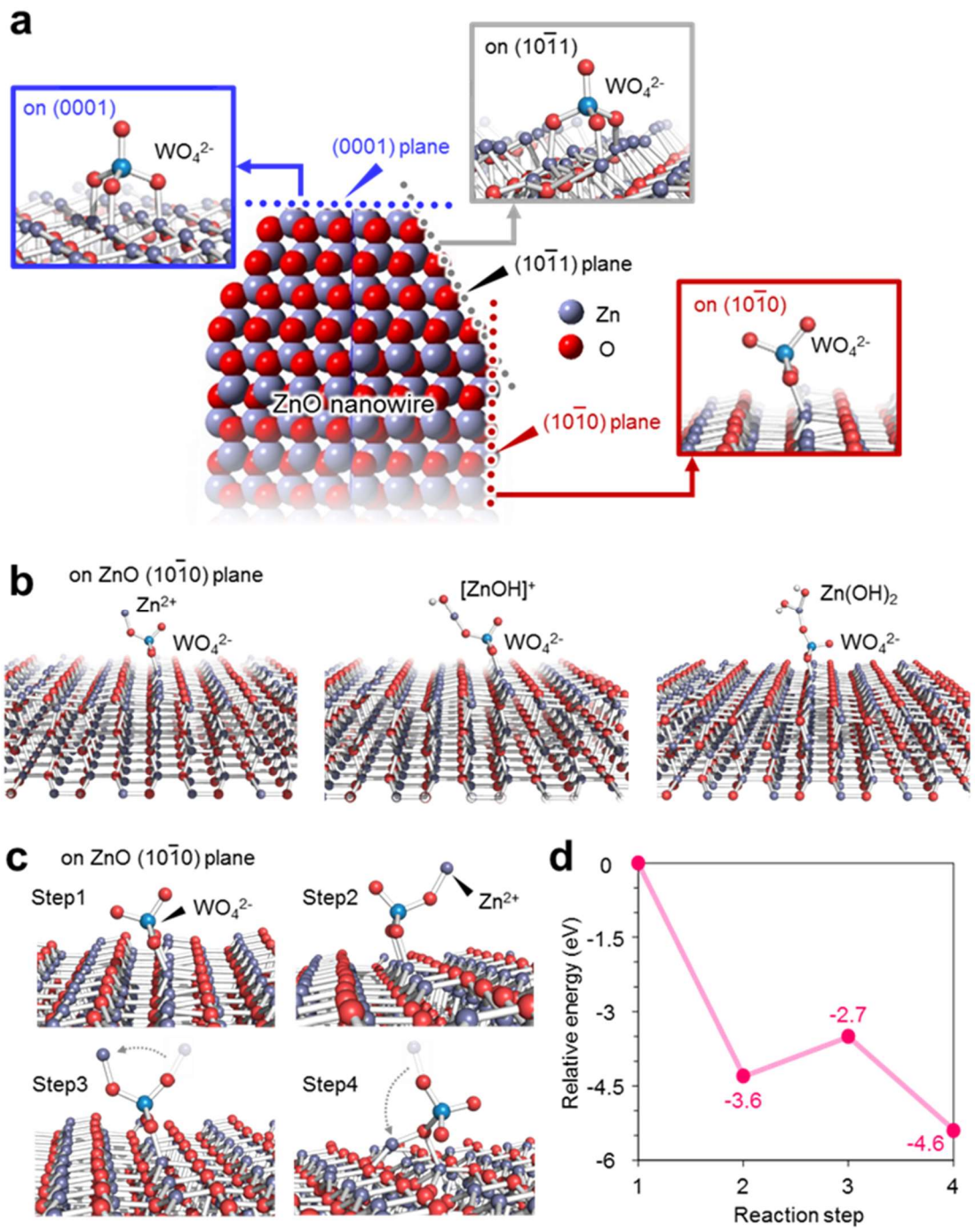

Figure 5. *(a) The coordination structures of adsorbed WO_4^{2-} ion on ZnO* (10$\bar{1}$0) *plane, (0001) plane and* (10$\bar{1}$1) *plane, respectively. (b) The coordination structures of WO_4^{2-} ion and various Zn species (Zn^{2+}, $[ZnOH]^+$ and $Zn(OH)_2$) on ZnO* (10$\bar{1}$0) *plane (b) The coodination structures and (c) Relative interaction energies of WO_4^{2-}-Zn^{2+}ions on ZnO* (10$\bar{1}$0) *plane during the Zn incorporation process. The coordination structures are simulated by DFT calculation in the presence of water solvent.*

Table I. Calculated interaction energy between Zn ion species (Zn^{2+}, $[ZnOH]^{+}$, $Zn(OH)_2$) and WO_4^{2-} ions adsorbed on ZnO $(10\bar{1}0)$ plane in kcal/mol.

Zn species	Zn^{2+}	$[ZnOH]^{+}$	$Zn(OH)_2$
Interaction Energy with WO_4^{2-} (kcal/mol)	63.4	41.8	1.0

Table II. Calculated adsorption energy of WO_4^{2-} ion on ZnO $(10\bar{1}0)$ plane, (0001) plane and $(10\bar{1}1)$ plane in vacuum and water conditions.

Crystal planes	$(10\bar{1}0)$	Zn-terminated (0001)	Zn-terminated $(10\bar{1}1)$	O-terminated (0001), $(10\bar{1}1)$
Adsorption energy (kcal/mol) in vacuum	36.6	121.3	73.1	Not adsorbed
Adsorption energy (kcal/mol) in water	13.9	20.4	-29.8	—

Table III. The average surface resident time of WO_4^{2-} ion on (0001) plane at 75 ºC and 95 ºC, estimated from the Frenkel equation using a typical molecular vibrational period 1.0×10^{-13} sec.

Growth temperature	95 ºC	75 ºC
Average resident time on (0001) plane (sec)	$1.2\text{x}10^{-1}$	$7.2\text{x}10^{-1}$

On the basis of suggested model, finally we control over the morphology and the elemental doping of ZnO nanowires. To best of our knowledge, the well-defined synthesis of W-doped hydrothermal ZnO nanowire has not been achieved so far because the W addition seriously causes the nanowire morphology[33,34]. In principle, there are two possible approaches for modulating the dopant incorporation, i.e. a control of W precursor concentration and a control of dopant adsorption on nanowire surface. On the other hand, the morphology can be manipulated by controlling C_{Zn} according the critical concentration for nucleation on ZnO crystal planes, which is so-called as "concentration window principle" [22-24]. However, as shown in figure 2 (c), W addition substantially narrows the concentration window for enhancing the anisotropic nanowire growth. Therefore further increase of C_W is not practical

for enhancing W incorporation. Here, we control the adsorption of WO_4^{2-} ions on nanowire surface by varying the thermodynamic parameter. The DFT calculation revealed that the resident time of WO_4^{2-} ions on (0001) plane becomes longer by decreasing the temperature, as shown in Table III. Figure S9 (a) and (b) show the TEM images and XRD patterns of W-doped ZnO nanowires grown at 95 ºC and 75 ºC, respectively. In this experiment, the sidewall growth i.e. nucleation on $(10\bar{1}0)$ plane of each sample is perfectly suppressed by controlling C_{Zn} below the critical nucleation concentration. We found that (0002) peak of W-doped ZnO shifts to higher angle (i.e. smaller *d*-value) by decreasing the growth temperature, meaning that more W is incorporated into nanowires. Thus we successfully demonstrated the controlled morphology and elemental doping of W-doped ZnO nanowires for the first time by the predictable model based on coordination structure of impurity metal ions.

3.1.5 CONCLUSION

In conclusion, we demonstrated the unexpected face-selective behaviors of WO_4^{2-} ions on nucleation and dopant incorporation in hydrothermal ZnO nanowire synthesis. Introduction of WO_4^{2-} ions significantly enhanced a nucleation at sidewall $(10\bar{1}0)$ plane, while the dopant incorporation occurred only at (0001) plane unexpectedly. We found that these conflicted face-selective behaviors led to inhomogeneous dopant distribution in an individual hydrothermal ZnO nanowire, as demonstrated for the first time by 3DAP measurement. DFT calculations revealed that these conflicted face-selective behaviors of WO_4^{2-} ions can be interpreted in terms of the coordination structure of WO_4^{2-} ions on each ZnO crystal plane. WO_4^{2-} ions coordinated on $(10\bar{1}0)$ plane with unipodal or bipodal bonds serve as surfactant for attracting Zn ion species, whereas those coordinated on (0001) plane with tripodal bonds are easily incorporated into nanowire as dopant. Furthermore, we successfully demonstrated the rational control over the morphology and the elemental doping of W-doped ZnO nanowire via modulating nucleation events and impurity adsorption with concentration window principle. This study clearly highlights the essential importance to understand the coordination structure of metal ions for designing the hydrothermal metal oxide nanowire synthesis and the resultant functions of metal oxide nanowire-based device applications.

3.1.6 REFERENCES

[1]. Xu, S.; Wang, Z. L. One-Dimensional ZnO Nanostructures: Solution Growth and Functional Properties. Nano Res. 2011, 4, 1013-1098. DOI: 10.1007/s12274-011-0160-7

[2]. Greene, L. E.; Low, M.; Goldberger, J.; Kim, F.; Johnson, J. C.; Zhang, Y.; Saykally, R. J.; Yang, P. Low-Temperature Wafer-Scale Production of ZnO Nanowire Arrays. Angew. Chem. Int. Ed. 2003, 42, 3031-3034. DOI: 10.1002/anie.200351461

[3]. Liu, C.; Tang, J.; Chen, H. M.; Liu, B.; Yang, P. A Fully Integrated Nanosystem of Semiconductor Nanowires for Direct Solar Water Splitting. Nano Lett. 2013, 13, 2989-2992. DOI: 10.1021/nl401615t

[4]. Navarro, J. R. G.; Mayence, A.; Andrade, J.; Lerouge, F.; Chaput, F.; Oleynikov, P.; Bergström, L.; Parola, S.; Pawlicka, A. WO_3 Nanorods Created by Self-Assembly of Highly Crystalline Nanowires under Hydrothermal Conditions. Langmuir 2014, 30, 10487-10492. DOI: 10.1021/la5025907

[5]. Qin, Y.; Wang, X.; Wang, Z. L. Microfibre-nanowire hybrid structure for energy scavenging. Nature 2008, 451, 809-813. DOI: 10.1038/nature06601

[6]. Fan, F. R.; Tang, W.; Wang, Z. L. Flexible Nanogenerators for Energy Harvesting and Self-Powered Electronics. Adv. Mater. 2016, 28, 4283-4305. DOI: 10.1002/adma.201504299

[7]. Law, M.; Greene, L. E.; Johnson, J. C.; Saykally, R.; Yang, P. Nanowire dye-sensitized solar cells. Nat. Mater. 2005, 4, 455-459. DOI: 10.1038/nmat1387

[8]. Katwal, G.; Paulose, M.; Rusakova, I. A.; Martinez, J. E.; Varghese, O. K. Rapid Growth of Zinc Oxide Nanotube-Nanowire Hybrid Architectures and Their Use in Breast Cancer-Related Volatile Organics Detection. Nano Lett. 2016, 16, 3014-3021. DOI: 10.1021/acs.nanolett.5b05280

[9]. Kang, Z.; Gu, Y.; Yan, X.; Bai, Z.; Liu, Y.; Liu, S.; Zhang, X.; Zhang, Z.; Zhang, X.; Zhang, Y. Enhanced photoelectrochemical property of ZnO nanorods array synthesized on reduced graphene oxide for self-powered biosensing application. Biosens. Bioelectron. 2015, 64, 499-504. DOI: 10.1016/j.bios.2014.09.055

[10]. Wang, T.; Lv, R.; Zhang, P.; Li, C.; Gong, J. Au nanoparticle sensitized ZnO nanopencil arrays for photoelectrochemical water splitting. Nanoscale 2015, 7, 77-81. DOI: 10.1039/c4nr03735a

[11]. Yasui, T.; Yanagida, T.; Ito, S.; Konakade, Y.; Takeshita, D.; Naganawa, T.; Nagashima, K.; Shimada, T.; Kaji, N.; Nakamura, Y.; Thiodorus, I. A.; He, Y.; Rahong, S.; Kanai, M.; Yukawa, H.; Ochiya, T.; Kawai, T.; Baba, Y. Unveiling massive numbers of cancer-related urinary-microRNA candidates via nanowires. Sci. Adv. 2017, 3, e1701133. DOI: 10.1126/sciadv.1701133

[12]. Zhao, L.; Chen, Y.; Liu, Y.; Zhang, G.; She, J.; Deng, S.; Xu, N.; Chen, J. Integration of ZnO nanowires in gated field emitter arrays for large-area vacuum microelectronics applications. Curr. Appl. Phys. 2017, 17, 85-91. DOI: 10.1016/j.cap.2016.11.004

[13]. Santra, S.; Guha, P. K.; Ali, S. Z.; Hiralal, P.; Unalan, H. E.; Convington, J. A.; Amaratunga, G. A. J.; Milne, W. I.; Gardner, J. W.; Udrea, F. ZnO nanowires grown on SOI CMOS substrate for ethanol sensing. Sens. Act. B: Chem. 2010, 146, 559-565. DOI: 10.1016/j.snb.2010.01.009

[14]. Alenezi, M. R.; Henley, S. J.; Silva, S. R. P. On-chip Fabrication of High Performance Nanostructured ZnO UV Detectors. Sci. Rep. 2015, 5, 8516. DOI: 10.1038/srep08516

[15]. Klamchuen, A.; Suzuki, M.; Nagashima, K.; Yoshida, H.; Kanai, M.; Zhuge, F. W.; He, Y.; Meng, G.; Kai, S.; Takeda, S.; Kawai, T.; Yanagida, T. Rational Concept for Designing Vapor-Liquid-Solid Growth of Single Crystalline Metal Oxide Nanowires. Nano Lett. 2015, 15, 6406-6412. DOI: 10.1021/acs.nanolett.5b01604

[16]. Klamchuen, A.; Yanagida, T.; Kanai, M.; Nagashima, K.; Oka, K.; Seki, S.; Suzuki, M.; Hidaka, Y.; Kai, S.; Kawai, T. Dopant homogeneity and transport properties of impurity-doped oxide nanowires. Appl. Phys. Lett. 2011, 98, 053107. DOI: 10.1063/1.3549703

[17]. Anzai, H.; Suzuki, M.; Nagashima, K.; Kanai, M.; Zhu, Z.; He, Y.; Boudot, M.; Zhang, G.; Takahashi, T.; Kanemoto, K.; Seki, T.; Shibata, N.; Yanagida, T. True Vapor-Liquid-Solid Process Suppresses Unintentional Carrier Doping of Single Crystalline Metal Oxide Nanowires. Nano Lett. 2017, 17, 4698-4705. DOI: 10.1021/acs.nanolett.7b01362

[18]. Anzai, H.; Takahashi, T.; Suzuki, M.; Kanai, M.; Zhang, G.; Hosomi, T.; Seki, T.; Nagashima, K.; Shibata, N.; Yanagida, T. Unusual Oxygen Partial Pressure Dependence of Electrical Transport of Single-Crystalline Metal Oxide Nanowires Grown by the Vapor-Liquid-Solid Process. Nano Lett. 2019, 19, 1675-1681. DOI: 10.1021/acs.nanolett.8b04668

[19]. Joo, J.; Chow, B. Y.; Prakash, M.; Boyden, E. S.; Jacobson, J. M. Face-selective electrostatic control of hydrothermal zinc oxide nanowire synthesis. Nat. Mater. 2011, 10, 596-601. DOI: 10.1038/NMAT3069

[20]. Tian, Z. R.; Voigt, J. A.; Liu, J.; Mckenzie, B.; Mcdermott, M. J.; Rodriguez, M. A.; Konishi, H.; Xu, H. Complex and oriented ZnO nanostructures. Nat. Mater. 2003, 2, 821-826. DOI: 10.1038/nmat1014

[21]. Sakai, D.; Nagashima, K.; Yoshida, H.; Kanai, M.; He, Y.; Zhang, G.; Zhao, X.; Takahashi, T.; Yasui, T.; Hosomi, T.; Uchida, Y.; Takeda, S.; Baba, Y.; Yanagida, T. Substantial Narrowing on the Width of "Concentration Window" of Hydrothermal ZnO Nanowires via Ammonia Addition. Sci. Rep. 2019, 9, 14160. DOI: 10.1038/s41598-019-50641-y

[22]. He, Y.; Yanagida, T.; Nagashima, K.; Zhuge, F. W.; Meng, G.; Xu, B.; Klamchuen, A.; Rahong, S.; Kanai, M.; Li, X. M.; Suzuki, M.; Kai, S.; Kawai, T. Crystal-Plane Dependence of Critical

Concentration for Nucleation on Hydrothermal ZnO Nanowires. J. Phys. Chem. C 2013, 117, 1197-1203. DOI: 10.1021/jp3113232

[23]. Akihiro, Y.; Nagashima, K.; Hosomi, T.; Kanai, M.; Anzai, H.; Takahashi, T.; Zhang, G.; Yasui, T.; Baba, Y.; Yanagida, T. Water−Organic Cosolvent Effect on Nucleation of Solution-Synthesized ZnO Nanowires. ACS Omega 2019, 4, 8299-8304. DOI: 10.1021/acsomega.9b00945

[24]. Zhao, X.; Nagashima, K.; Zhang, G.; Hosomi, T.; Yoshida, H.; Akihiro, Y.; Kanai, M.; Mizukami, W.; Zhu, Z.; Takahashi, T.; Suzuki, M.; Samransuksamer, B.; Meng, G.; Yasui, T.; Aoki, Y.; Baba, Y.; Yanagida, T. Synthesis of Monodispersedly Sized ZnO Nanowires from Randomly Sized Seeds. Nano Lett. 2020, 20, 599-605. DOI: 10.1021/acs.nanolett.9b04367

[25]. Perea, D. E.; Hemesath, E. R.; Schwalbach, E. J.; Lensch-Falk, J. L.; Voorhees, P. W.; Lauhon, L. J. Direct measurement of dopant distribution in an individual vapour-liquid-solid nanowire. Nat. Nanotechnol. 2009, 4, 315-319. DOI: 10.1038/NNANO.2009.51

[26]. Gudiksen, M. S.; Lauhon, L. J.; Wang, Jianfang, Smith, D. C.; Lieber, C. M. Growth of nanowire superlattice structures for nanoscale photonics and electronics. Nature 2002, 415, 617-620. DOI: 10.1038/415617a

[27]. Lupan, O.; Chow, L.; Ono, L. K.; Cuenya, B. R.; Chai, G.; Khallaf, H.; Park, S.; Schulte, A. Synthesis and Characterization of Ag- or Sb-Doped ZnO Nanorods by a Facile Hydrothermal Route. J. Phys. Chem. C 2010, 114, 12401-12408. DOI: 10.1021/jp910263n

[28]. Chen, J. T.; Wang, J.; Zhuo, R. F.; Yan, D.; Feng, J. J.; Zhang, F.; Yan, P. X. The effect of Al doping on the morphology and optical property of ZnO nanostructures prepared by hydrothermal process. Appl. Surf. Sci. 2009, 255, 3959-3964.

[29]. Wang, Z.-H.; Yu, H.-C.; Yang, C.-C.; Yeh, H.-T.; Su, Y.-K. Low-Frequency Noise Performance of Al-Doped ZnO Nanorod Photosensors by a Low-Temperature Hydrothermal Method. IEEE Trans. Electron Dev. 2017, 64, 3206-3212. DOI: 10.1109/TED.2017.2706320

[30]. Panda, J.; Sasmal, I.; Nath, T. K. Magnetic and optical properties of Mn-doped ZnO vertically aligned nanorods synthesized by hydrothermal technique. AIP Adv. 2016, 6, 035118. DOI: 10.1063/1.4944837

[31]. Thirumalai, K.; Shanthi, M.; Swaminathan, M. Hydrothermal fabrication of natural sun light active Dy2WO6 doped ZnO and its enhanced photoelectrocatalytic activity and self-cleaning properties. RSC Adv. 2017, 7, 7509-7518. DOI: 10.1039/c6ra24843h

[32]. Goris, L.; Noriega, R.; Donovan, M.; Jokisaari, J.; Kusinski, G.: Salleo, A. Intrinsic and Doped Zinc Oxide Nanowires for Transparent Electrode Fabrication via Low-Temperature Solution Synthesis. J. Electron. Mater. 2009, 38, 586-595.

[33]. Adhyapak, P. V.; Meshram, S. P.; Pawar, A. A.; Amalnerkar, D. P.; Mulik, U. P.; Mulla, I. S. Synthesis of burger/donut like V and W doped ZnO and study of their optical and gas sensing properties. Ceram. Int. 2014, 40, 12105-12115.

[34]. Shirini, F.; Abedini, M.; Zamani, S.; Moafi, H. F. Introduction of W-doped ZnO nanocomposite as a new and efficient nanocatalyst for the synthesis of biscoumarins in water. J. Nanostruct. Chem. 2015, 5, 123-130.

[35]. Gautam, K.; Singh, I.; Bhatnagar, P. K.; Peta, K. R. Role of Cl doping on the growth and relaxation dynamics of ZnO nanorods synthesized by hydrothermal method. Chem. Phys. Lett. 2016, 662, 196-200. DOI: 10.1016/j.cplett.2016.09.026

[36]. Byrappa, K. Novel hydrothermal solution routes of advanced high melting nanomaterials processing. J. Ceram. Soc. Jpn. 2009, 117, 236-244. DOI: 10.2109/jcersj2.117.236

[37]. Kawska, A.; Duchstein, P.; Hochrein, O.; Zahn, D. Atomistic Mechanisms of ZnO Aggregation from Ethanolic Solution: Ion Association, Proton Transfer, and Self-Organization. Nano Lett. 2008, 8, 2336-2340. DOI: 10.1021/nl801169x

[38]. Belghiti, H. E.; Paurporté, T.; Lincot, D. Mechanistic study of ZnO nanorod array electrodeposition. Phys. Stat. Sol. A 2008, 205, 2360-2364. DOI: 10.1002/pssa.200879443

[39]. Adachi, Y.; Saito, N.; Hashiguchi, M.; Sakaguchi, I.; Suzuki, T.; Ohashi, N.; Hishita, S. Electrical and optical properties of W-doped ZnO films grown on (11-20) sapphire substrates using pulsed laser deposition. J. Ceram. Soc. Jpn. 2014, 122, 908-913. DOI: 10.2109/jcersj2.122.908

[40]. Fukami, S.; Taguchi, M.; Adachi, Y.; Sakaguchi, I.; Watanabe, K.; Kinoshita, T.; Muro, T.; Matsushita, T.; Matsui, F.; Daimon, H.; Suzuki, T. T. Correlation Between High Gas Sensitivity and Dopant Structure in W-doped ZnO. Phys. Rev. Appl. 2017, 7, 064029.

3.1.7 Supporting Information

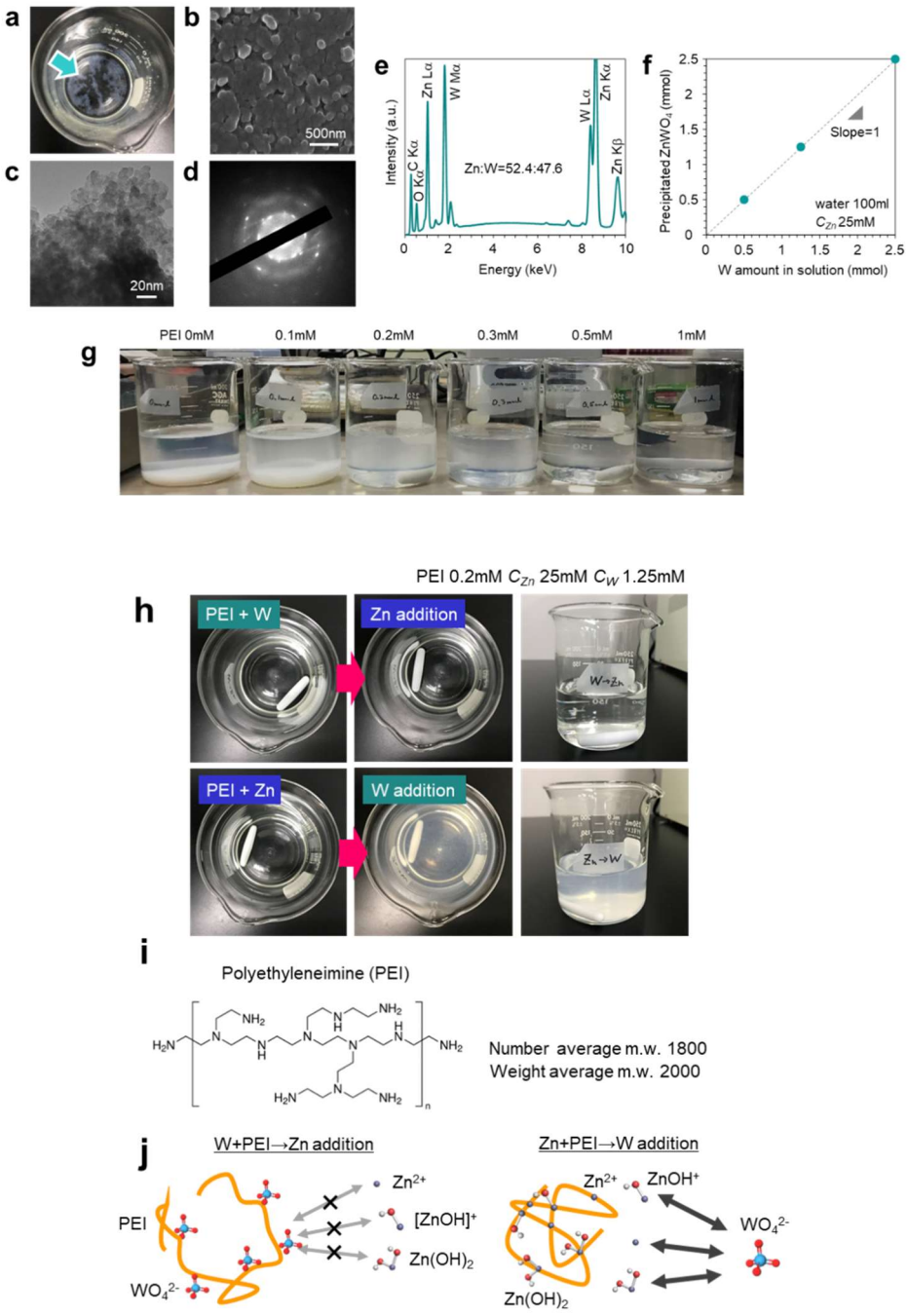

Figure S1. *Structural and compositional analysis of $ZnWO_4$ complex salt, and an approach to suppress the formation of complex salt. (a) Snapshot, (b) SEM image, (c) TEM image, (d) SAED pattern and (e) EDS spectrum of $ZnWO_4$ complex salt, precipitated by mixing $Zn(NO_3)_2$ 25 mM and Na_2WO_4 0.25 mM in 100 ml deionized (DI) water without polyethyleneimine (PEI) addition. (f) Precipitated amount of $ZnWO_4$ complex salt when varying the amount of W precursor. In this experiment, Zn precursor concentration (C_{Zn}) and volume of DI water are kept to be 25 mM and 100 ml, respectively. (g) Snapshots of the nanowire growth solution with varying the PEI concentration in the range of 0-1 mM. In this*

experiments, C_{Zn}, and C_W are 25 mM and 1.25 mM. (h) Snapshots of the nanowire growth solution with varying the sequence of reagent addition. In this experiment, the concentrations of Zn precursor C_{Zn}, W precursor C_W and PEI are 25 mM, 1.25 mM and 0.2 mM, respectively. (i) Molecular structure and detailed information of PEI employed in this study. (j) Schematic images for the interactions between WO_4^{2-} ion and various Zn ion species, which are coordinated with PEI.

In this study, polyethyleneimine (PEI) is utilized as a dispersant. As shown in figure S1(a), we found that white precipitate is readily formed when mixing $Zn(NO_3)_2$ 25 mM with Na_2WO_4 0.25 mM in DI water 100 ml without PEI. In this case, W precursor in growth solution is almost exhausted prior to the nanowire growth. The white precipitate has a granular structure and is partially crystalline as shown in SEM image of figure S1 (b)-(d). EDS analysis shows that the precipitate is mainly composed of Zn, W and O with the ratio of Zn : W = 52.4 : 47.6, implying that the precipitate is $ZnWO_4$ complex salt (Figure S1 (e)). When we assume the formation of $ZnWO_4$, the weight of precipitate linearly increases with slope=1 by increasing the amount of W precursor in figure S1 (f). This clearly confirms that the precipitate is $ZnWO_4$ complex salt. The formation of $ZnWO_4$ complex salt is gradually suppressed by adding PEI prior to mixing $Zn(NO_3)_2$ and Na_2WO_4 as seen in figure S1 (g) that the solution becomes transparent with increasing PEI concentration. Since the pH values of growth solution changes from 6.6 to 6.7 with adding PEI, the variation of pH value is not a main factor for suppressing the precipitate.

We found that the precipitate formation is suppressed only when the addition of Zn precursor is following the W precursor addition. When the Zn precursor is added prior to the W precursor addition, as shown in figure S1 (h). The mechanism of this reagent addition sequence dependence can be interpreted in terms of the coordination of Zn ion species and W ion species. Based on the calculation for the equilibrium concentrations of ionic species (Figure S3), positively charged and neutral Zn species (e.g. Zn^{2+}, $[ZnOH]^+$, $[Zn(NH_3)_4]^{2+}$, $Zn(OH)_2$) and negatively charged W species (e.g. WO_4^{2-}, HWO_4^-) exist in the growth solution. These Zn and W species can coordinate with PEI (Figure S1 (i)). Although the formation of $ZnWO_4$ complex salt is based on the electrostatic interaction between Zn species and W species, and the following aggregation of Zn-W complex ions, the coordination of W species with PEI substantially suppresses them. When the W precursor is added first, all W species are coordinated with PEI and no extra W species exist for interacting with the subsequently added Zn species. This may lead to the suppression of the $ZnWO_4$ complex salt formation. On the other hand, the situation is different when the Zn precursor is added prior to the W precursor addition. Since the concentration of Zn precursor is much higher than that of W precursor in

this study, Zn species are partly coordinated with PEI and extra Zn species remains in the solution. The extra Zn species must interact with the subsequently added W species, resulting in the formation of $ZnWO_4$ complex salt. Note that the number of coordination point in PEI is more than the amount of Zn species. Therefore, only the concentration difference between Zn species and W species cannot explain the obtained result. Since the Zn species is known to form a chelating structure with PEI via bipodal bonds [Ref 1], the coordination of Zn species and PEI may shrink PEI structure as shown in figure S1 (j), which plausibly suppresses the further coordination with Zn species and increases the remaining Zn species in the solution. These results highlight that PEI serves as a dispersant for the nanowire growth solution and the PEI addition with W precursor is of crucial importance to suppress the complex salt formation.

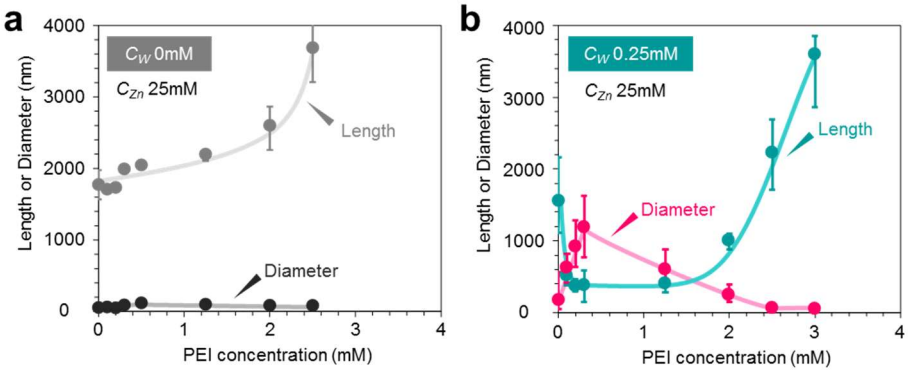

Figure S2. *PEI concentration dependence on the length and diameter of ZnO nanostructures grown with (a) C_W 0 mM and (b) C_W 0.25 mM. In these experiments, C_{Zn} is kept to be 25 mM.*

Here we discuss the effect of PEI addition on the anisotropic crystal growth of ZnO nanowires. PEI is well-known surfactant for promoting the crystal growth on (0001) plane by capping on $(10\bar{1}0)$ plane [Ref 2]. In fact, the promotion of longitudinal nanowire growth and the decrease of diameter by PEI addition is seen in figure S2 (a). On the other hand, when the W species is added, the crystal growth is promoted on $(10\bar{1}0)$ plane as shown in figure 1 and figure 2. We assume that the observed face-selective promotion of crystal growth is associated with the increase of local Zn precursor concentration near $(10\bar{1}0)$ plane, which is induced by the weak coordination of Zn ions to WO_4^{2-} ions. As discussed in figure S1, WO_4^{2-} ions preferentially coordinate with PEI and the formation of Zn-W complex salt is interrupted by suppressing the interaction between Zn ions (e.g. Zn^{2+}, $Zn(OH)^{+}$, $[Zn(NH_3)_4]^{2+}$) and WO_4^{2-} ions. Although the Zn-W complex salt formation is interrupted by PEI, the coordination between Zn ions and WO_4^{2-} ions must still exist. Since PEI preferentially caps on $(10\bar{1}0)$ plane as

confirmed in figure S2 (a), weakly coordinated Zn ions with WO_4^{2-} ions on PEI may increase the local Zn precursor concentration near $(10\bar{1}0)$ plane. This plausibly leads to the face-selective enhancement of nucleation on $(10\bar{1}0)$ plane. In fact, the increasing trend of nanowire diameter is seen when increasing PEI at low concentration range in figure S2 (b), strongly supporting our model.

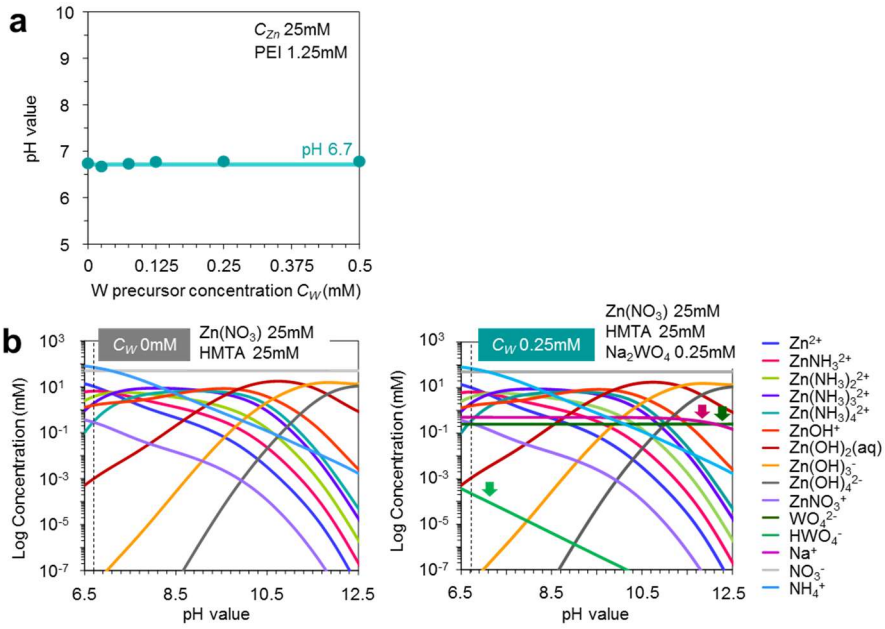

Figure S3. *(a) pH value of growth solution with various C_W. In this experiment, C_{Zn} and PEI concentration are kept to be 25 mM and 1.25 mM, respectively. (b) Thermodynamically calculated equilibrium ion concentrations in growth solution for C_W 0 mM (left) and C_W 0.25 mM (right). $Zn(NO_3)$ 25 mM and hexamethylenetetramine (HMTA) 25 mM are utilized for the calculation. The dot lines represent the measured pH value in growth solution at these conditions. The arrows represent the supplemented ion species via the addition of Na_2WO_4.*

In order to identify the possible adsorption species on ZnO nanowires, we measure the pH value and calculate the equilibrium concentrations of ionic species in growth solution. When adding Na_2WO_4, the pH value of 6.7 remains almost constant and the equilibrium concentrations of each Zn species are not influenced while Na^+, WO_4^{2-}, HWO_4^- ions are supplemented. Since the both $(10\bar{1}0)$ and (0001) planes of ZnO nanowires, where their isoelectric points (IEPs) are 10.2±0.2 and 8.7±0.2 respectively [Ref 3,4], must be positively charged at pH=6.7 and its equilibrium concentration of WO_4^{2-} ion is much higher than HWO_4^- ions, WO_4^{2-} ions are the most plausible species for the electrostatic adsorption or the chemisorption on ZnO nanowire surface.

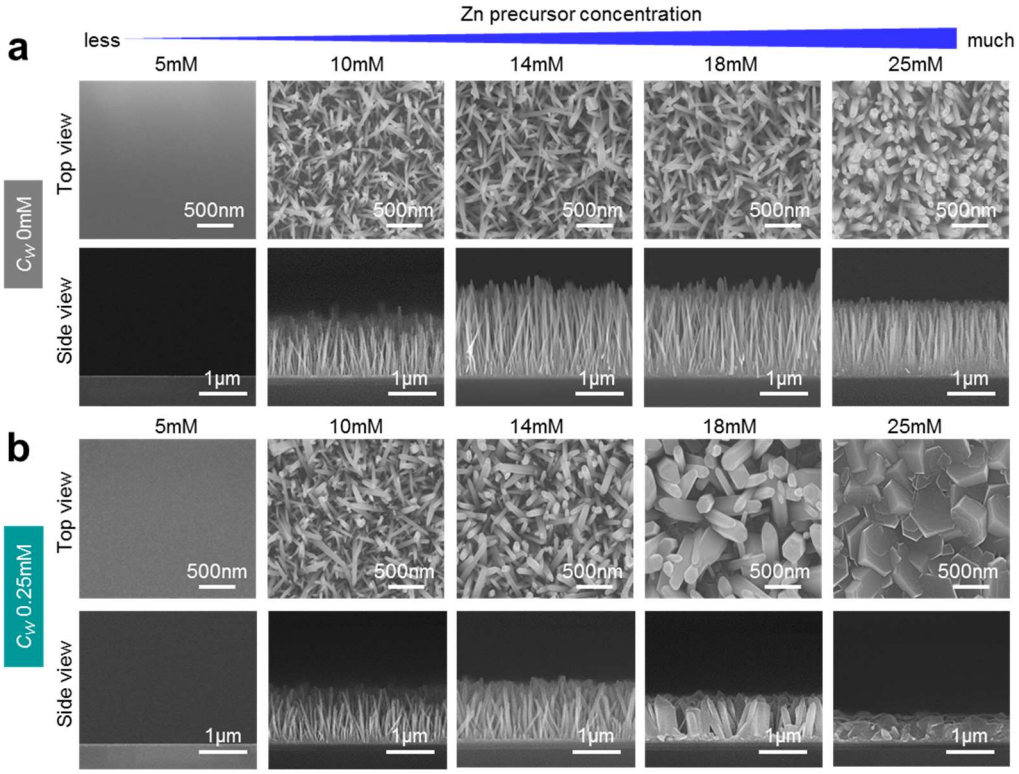

Figure S4. *Side view and top view SEM images of ZnO nanostructures /nanowires grown with (a) C_W 0 mM and (b) C_W 0.25 mM, respectively, when varying C_{Zn}.*

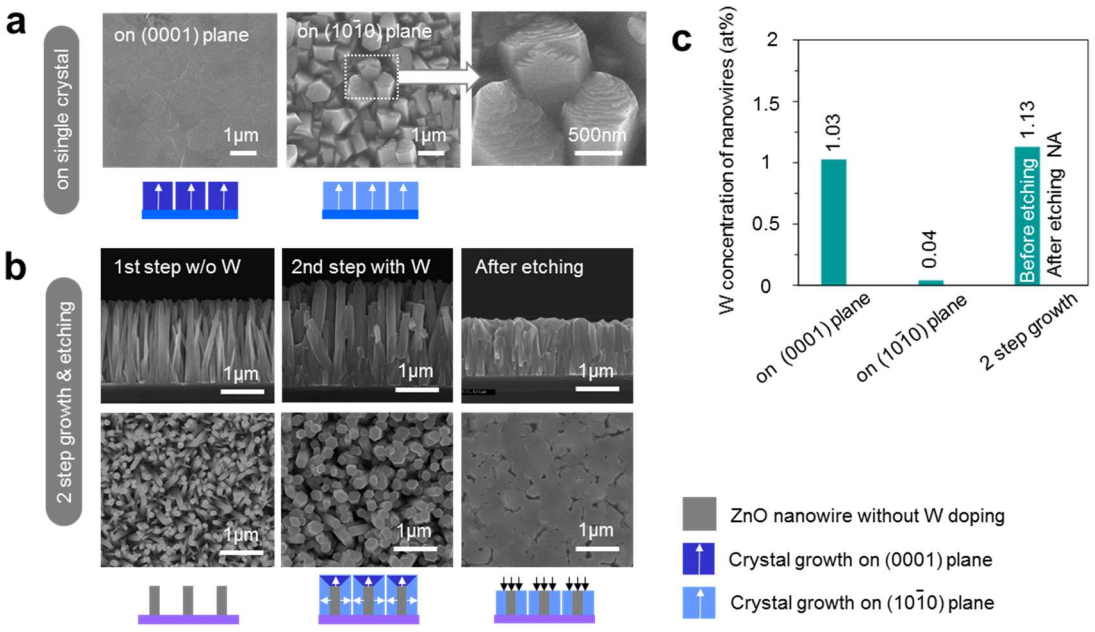

Figure S5. *(a) Top view SEM images of ZnO nanostructures grown on (0001) and* $(10\bar{1}0)$ *oriented single crystalline ZnO substrates. In this experiment, C_{Zn} and C_W are 25 mM and 0.25 mM, respectively. (b) Side view and top view SEM images of 2 step grown ZnO nanowires. In this experiment, non-dope ZnO nanowires are grown on a Si substrate with C_{Zn} 25 mM (step 1) and W-doped ZnO shell is then*

grown with C_{Zn} 25 mM and C_W 0.25 mM (step 2). The images are taken after step 1, step 2 and dry etching process, respectively. The etching depth is about 150 nm. Schematic illustrations represent the non-dope ZnO crystal (grey), the W-doped ZnO crystals grown on (0001) plane (blue) and $(10\bar{1}0)$ *plane (light blue), respectively. (c) W concentration of ZnO nanostructures grown on (0001) and* $(10\bar{1}0)$ *oriented single crystalline ZnO substrates and of 2 step grown ZnO nanowires before and after dry etching.*

In order to confirm the hypothesis for the dopant incorporation pathway, we examine the composition analysis of the nanostructures grown on $(10\bar{1}0)$ and (0001) oriented single crystalline ZnO substrates. Figure S5 (a) shows the SEM images of ZnO nanostructures grown on single crystalline ZnO substrates with W addition. The film with smooth surface is formed on (0001) oriented substrate while the nanostructure with rough surface is formed on $(10\bar{1}0)$ oriented substrate. The measured W concentration of ZnO structures grown on (0001) and $(10\bar{1}0)$ substrates are 1.03 % and 0.04 %, respectively, supporting that W is mainly incorporated on (0001) plane. This result is further confirmed by using the 2 step grown nanowires. The 2 step growth is conducted by the initial growth of non-dope ZnO nanowires (step 1) and the subsequent growth of W-doped ZnO shell (step 2). By removing the top part of 2 step grown nanowires with a dry etching, only the shell layer grown on $(10\bar{1}0)$ plane of non-dope ZnO nanowires remains. Figure S5 (b) shows the SEM images of 2 step grown nanowires observed after step 1, step 2 and dry-etching. We found that the W concentration becomes undetectable level after the etching, clearly confirming that W is incorporated on (0001) plane rather than $(10\bar{1}0)$ plane (Figure S5 (c)).

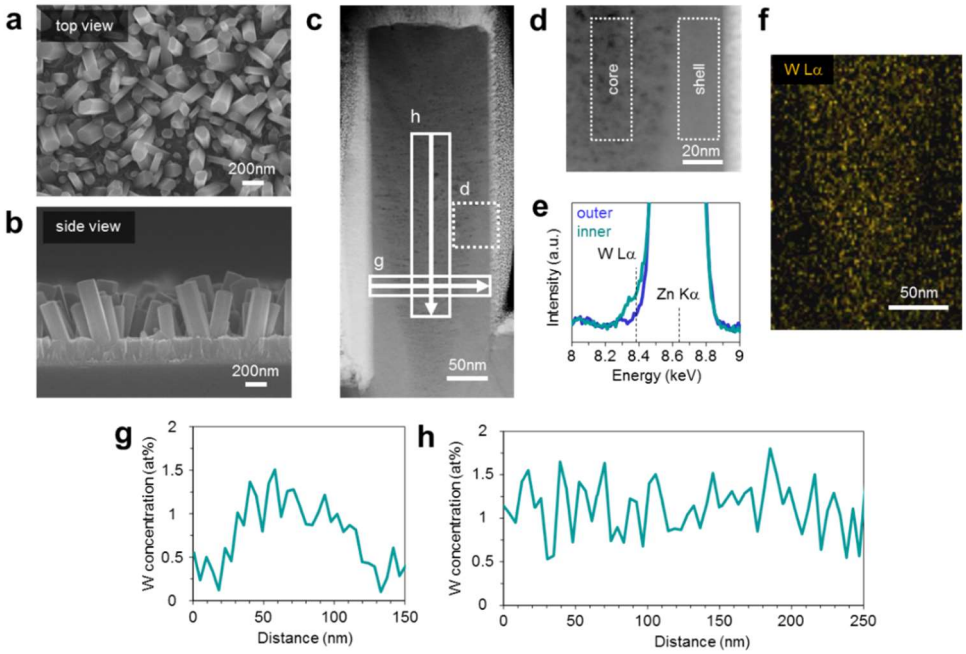

Figure S6. *(a) Top view and (b) side view SEM images of ZnO nanowires grown with C_{Zn} 15 mM and C_W 0.125 mM. (c) HAADF-STEM image of single nanowire sliced by FIB technique. (d) Magnified HAADF-STEM image in the projected area in (c). (e) EDS spectra of outer region and inner region, which are projected in (d). (f) Elemental map of W L taken at bottom part in (c). (g) Lateral and (h) longitudinal line profiles of W concentration in the projected area in (c).*

Spatial distribution of incorporated W in ZnO nanowire was evaluated by HAADF-STEM observation and EDS analysis. We selected a nanowire with ca. 150 nm diameter as a specimen, in which there is the sidewall growth i.e. nucleation on $(10\bar{1}0)$ plane. In the HAAD-STEM image, we found that the shell region has relatively brighter contrast while the core region has darker contrast (figure S6 (d)). In the EDS spectra, the weak shoulder peak associated with W L was seen only at the darker region. Elemental map of W L at the bottom part of nanowire confirmed that dopant is mainly distributed in the core region (figure S6 (f)). Note that the quantitatively analyzing the W ratio in ZnO nanowire is rather difficult by EDS because Zn K□ peak (8.629 keV) and W L peak (8.392 keV) are relatively close and hardly separated. Therefore the dopant distribution was qualitatively analyzed here. The EDS line profile in figure S6 (g) and (h) showed that the dopant distribution of nanowire is inhomogeneous in radial direction while that in longitudinal direction is relatively homogeneous.

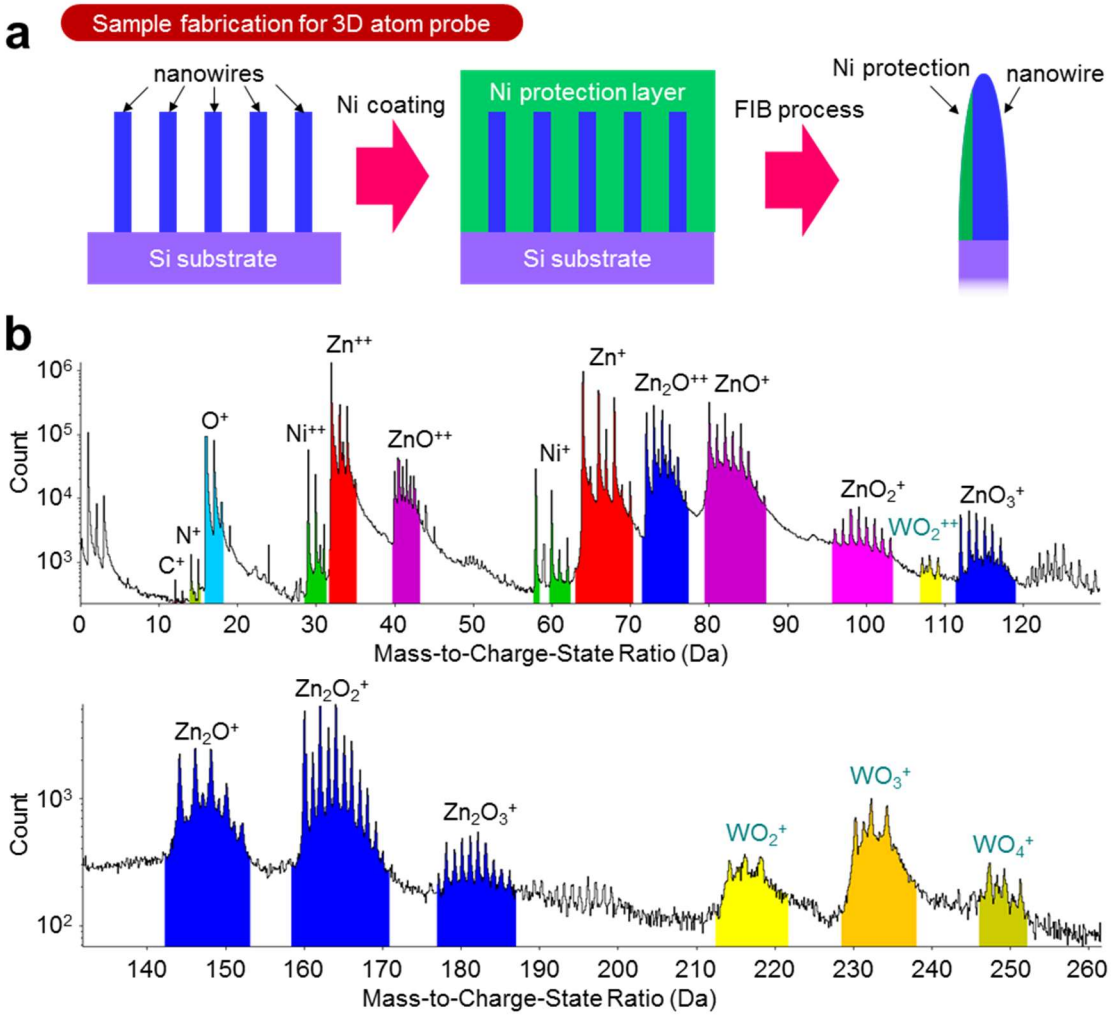

Figure S7. *(a) Fabrication procedure for a sample of 3D atom probe (3DAP) measurement. (b) Mass spectrum of ZnO nanowire obtained in 3DAP measurement. The ZnO nanowires were grown with* C_{Zn} *15 mM and* C_W *0.125 mM.*

3DAP sample was fabricated by the process shown in figure S7 (a). Firstly, Ni protection layer was deposited on nanowires in order to support the nanowires in the following focused ion beam (FIB) etching process and 3DAP measurement. Then FIB etching was performed to make a specimen composed of a single ZnO nanowire. Mass spectrum of ZnO nanowire obtained by 3DAP measurement (figure S7 (b)) clearly evidenced the existence of W dopant in nanowires.

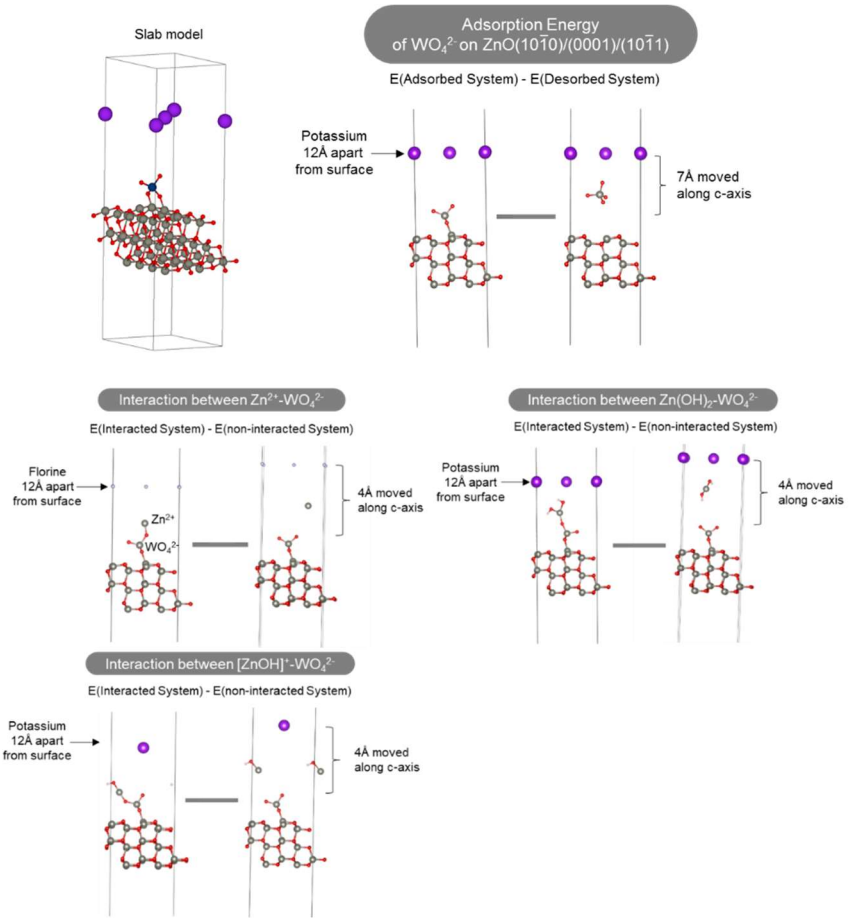

Figure S8. *Slab model used in this work to perform DFT calculations. An example is shown for ZnO* (10$\bar{1}$0) *surface with* WO_4^{2-} *ion and counter cations* K^+. *The methods for calculating the adsorption energy and interaction energy of various coordinated structures are shown.*

Computational Details

We used density functional theory (DFT) to estimate adsorption energies of WO_4^{2-} on ZnO (10$\bar{1}$0), Zn-terminated (0001) or (10$\bar{1}$1) surfaces, and interaction energies between Zn species (i.e. Zn^{2+}, $Zn(OH)_2$, $[ZnOH]^+$) and WO_4^{2-} on ZnO (10$\bar{1}$0). Vienna Ab initio Simulation Package (VASP) version 5.4.4 was employed to perform DFT calculations [Ref 5-8]. We chose RPBE for the exchange-correlation functional [Ref 9]. The projector-augmented wave (PAW) approach was used to describe core electrons [Ref 10]. We adopted the Gaussian smearing method with the width of 0.05 eV and the gamma point approximation. The cut-off energies were 400 and 520 eV for geometry optimizations and subsequent interaction/adsorption energy calculations, respectively. The convergence criterion for geometry optimizations was 0.01 eV/Å. Interaction/adsorption energy calculations were performed by considering water solvation effects using an implicit water solvation model implemented as an extension to the VASP code by Mathew and Hennig [Ref 11,12].

The slab model for the ZnO $(10\bar{1}0)$ surface consists of a (4×2)-supercell (a=12.85Å, b=10.31Å) and three ZnO atomic layers as shown in figure S8, while that for ZnO (0001) consisted of a (3×3)-supercell and four ZnO atomic layers (a=b=9.64Å, γ=120.0º). The ZnO $(10\bar{1}1)$ surface was described by a (2×4) four-layer slab model (a= 12.15 Å, b= 12.86 Å, γ=74.7 º). We applied the 20 Å vacuum region to the slab models. The bottom layers were kept fixed during the optimizations. The bottom layers of ZnO (0001) and $(10\bar{1}1)$ were passivated by hydrogen atoms, as their surfaces are not symmetric. Potassium or fluorine atoms were introduced as counter ions to maintain cell's charge neutrality. They were put at least 12Å apart from the adsorbed layer of ZnO.

The adsorption energies of WO_4^{2-} were estimated as the energy difference between a surface with an adsorbed WO_4^{2-} molecule and that with a desorbed WO_4^{2-} in aqueous phase. In the desorbed state, we positioned a WO_4^{2-} ion 7 Å above the topmost surface layer. The coordinate of the tungsten atom of the desorbed ion was frozen during geometry optimization. The average resident time of WO_4^{2-} ion on ZnO surface was estimated by using the Frenkel equation with the adsorption energies. We tentatively set a molecular vibration period along with the surface normal to be 1.0×10^{-13} seconds.

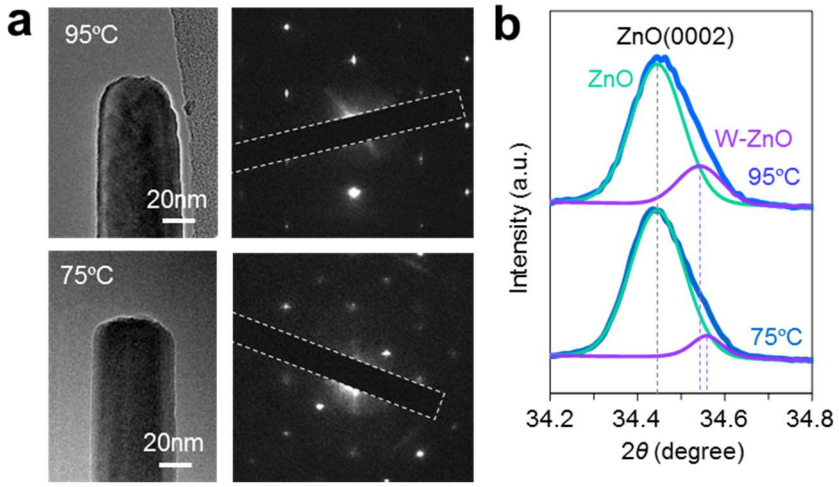

Figure S9. *(a) TEM iamges, SAED patterns and (b) XRD patters of ZnO nanowires grown with C_W 0.25 mM at 95 ºC and 75 ºC, respectively*

SI-References

[Ref 1] Soyekwo, F.; Zhang, Q.; Gao, R.; Qu, Y.; Lv, R.; Chen, M.; Zhu, A.; Liu, Q. Metal *in situ* surface functionalization of polymer-grafted-carbon nanotube composite membranes for fast efficient nanofiltration. *J. Mater. Chem. A* **2017**, *5*, 583-592. DOI: 10.1039/C6TA07567C

[Ref 2] Qiu, J.; Li, X.; Zhuge, F.; Gan, X.; Gao, X.; He, W.; Park, S.-J.; Kim, H.-K.; Hwang, Y.-H. Solution-derived 40 μm vertically aligned ZnO nanowire arrays as photoelectrodes in dye-sensitized solar cells. *Nanotechnology* **2010**, *21*, 195602. DOI: 10.1088/0957-4484/21/19/195602

[Ref 3] Valtiner, M.; Borodin, S.; Grundmeier, G. Stabilization and Acidic Dissolution Mechanism of Single-Crystalline ZnO(0001) Surfaces in Electrolytes Studied by *In-Situ* AFM Imaging and *Ex-Situ* LEED. *Langmuir* **2008**, *24*, 5350-5358. DOI: 10.1021/la7037697

[Ref 4] Kunze, C.; Valtiner, M.; Michels, R.; Huber, K.; Grundmeier, G. Self-localization of polyacrylic acid molecules on polar ZnO(0001)-Zn surfaces. *Phys. Chem. Chem. Phys.* **2011**, *13*, 12959-12967. DOI: 10.1039/C1CP20913B

[Ref 5] Kresse, G.; Hafner, J. *Ab initio* molecular dynamics for liquid metals. *Phys. Rev. B* **1993**, *47*, 558. DOI: 10.1103/PhysRevB.47.558

[Ref 6] Kresse, G.; Hafner, J. *Ab initio* molecular-dynamics simulation of the liquid-metal–amorphous-semiconductor transition in germanium. *Phys. Rev. B* **1994**, *49*, 14251. DOI: 10.1103/PhysRevB.49.14251

[Ref 7] Kresse, G.; Furthmüller, J. Efficiency of ab-initio total energy calculations for metals and semiconductors using a plane-wave basis set. *Comp. Mater. Sci.* **1996**, *6*, 15-50. DOI: 10.1016/0927-0256(96)00008-0

[Ref 8] Kresse, G.; Furthmüller, J. Efficient iterative schemes for *ab initio* total-energy calculations using a plane-wave basis set. *Phys. Rev. B* **1996**, *54*, 11169. DOI: 10.1103/PhysRevB.54.11169

[Ref 9] Krasse, G.; Joubert, D. From ultrasoft pseudopotentials to the projector augmented-wave method. *Phys. Rev. B* **1999**, *59*, 1758. DOI: 10.1103/PhysRevB.59.1758

[Ref 10] Hammer, B.; Hansen, L. B.; Nørskov, J. K. Improved adsorption energetics within density-functional theory using revised Perdew-Burke-Ernzerhof functionals. *Phys. Rev. B* **1999**, *59*, 7413. DOI: 10.1103/PhysRevB.59.7413

[Ref 11] Fishman, M.; Zhuang, H. L.; Mathew, K.; Dirschka, W.; Henning, R. G. Accuracy of exchange-correlation functionals and effect of solvation on the surface energy of copper. *Phys. Rev. B* **2013**, *87*, 245402. DOI:10.1103/PhysRevB.87.245402

[Ref 12] Mathew, K.; Sundararaman, R.; Letchworth-Weaver, K.; Arias, T. A.; Henning, R. G. Implicit solvation model for density-functional study of nanocrystal surfaces and reaction pathways. *J. Chem. Phys.* **2014**, *140*, 084106. D

3.2 Surface copper impact to molecular adsorption and transformation on $(Cu_xZn_{1-x})O$ nanowire

3.2.1 ABSTRACT

Surface cation composition of nanoscale metal oxides critically determines the properties of various functional chemical processes including inhomogeneous catalysts and molecular sensors. Here we employ a gradual modulation of cation composition in heterostructured $(Cu_x,Zn_{1-x})O$ nanowires to study the effect of surface cation composition (Cu/Zn) on the adsorption and chemical transformation behaviors of volatile carbonyl compounds (nonanal: biomarker). Controlling a cation diffusion of ZnO(core)/CuO(shell) nanowires allows us to continuously manipulate the surface cation composition of heterostructured $(Cu_x,Zn_{1-x})O$ nanowires while keeping the macroscopic morphology. We found that a surface exposed copper significantly supresses the adsorption of nonanal, which is not consistent with our initial expectation since the Lewis acidity of Cu^{2+} is strong enough and comparable to Zn^{2+}. In addition, increasing Cu/Zn ratio on the nanowire surface systematically suppresses the aldol condensation reaction of nonanal. Surface spectroscopic analysis and theoretical simulations reveal that the nonanal molecules adsorbed at surface Cu^{2+} site are not activated, and a coordination-saturated in-plane square geometry of surface Cu^{2+} is responsible for observed weak molecular adsorption behaviors. This inactive surface Cu^{2+} site well explains the mechanism of suppressed surface aldol condensation reactions in terms of preventing the neighboring of activated nonanal molecules. We apply this tailored mixed cation composition surface for electrical molecular sensing of nonanal, where the durability and the recovery time of molecular sensing are improved.

KEYWORDS: Metal oxide nanowire, copper oxide, surface cation composition, volatile carbonyl compounds, molecular sensing

3.2.2 INTRODUCTION

Surface cation composition of nanoscale metal oxides is well known to significantly affect the molecular transformation behaviors on the surface for various applications including inhomogeneous catalysts, molecular sensing, and others.[1-5] This is solely because the surface cation variation induces various molecular reaction pathways via interacting sequentially or simultaneously with different cation species on the surface.[6-9] Thus, investigating the effect of surface cation composition on the surface molecular behaviors is important but frequently challenging issue because it is difficult to alter systematically and precisely only surface cation composition of nanoscale metal oxides without the macroscopic morphology change.10,11 A cation exchange or cation diffusion within nanoscale metal oxides is a promising way to create such tailored surface cation composition of oxides.[12-17] For example, the surface cation of Fe_3O_4 nanoparticle was exchanged by Co and Mn using a wet-process[12] and ZnO/$ZnCo_2O_4$ core/shell nanowires were synthesized from ZnO nanobelts via a cation-exchange in a dry-process.[13,14] The cation diffusion offers a facile and versatile approach for controlling the composition of nanoscale metal oxides, e.g. Mn-doped TiO_2 nanowire surface and ZnO/$InxZn_{1-x}O$ axial heteronanowires were successfully demonstrated.[15,17] These methodologies allow us to widely and systematically control the surface cation composition of nanoscale metal oxides while keeping their macroscopic morphology.

Here we demonstrate a gradual modulation of surface cation composition in heterostructured metal oxide nanowires via controlling a cation diffusion at core/shell interface. The heterostructured $(Cu_x,Zn_{1-x})O$ nanowire is employed as a model and the surface Cu/Zu ratio is continuously modulated to investigate the effect of surface cation ratio (Cu/Zn) on the molecular transformation behavior of volatile carbonyl compounds (nonanal: biomarker). Copper oxide (CuO), zinc oxide (ZnO) and their composite are abundant and often utilized for molecular sensing and catalyst of carbonyl compounds.[18-22] Carbonyl compounds are important as initiators for organic synthesis[23,24] and also as target molecules for environmental, industrial and biomedical sensing.[25-27] By continuously modulating the surface Cu/Zn ratio, we found the unexpected property of surface exposed Cu of the heterostrucured $(Cu_x,Zn_{1-x})O$ nanowires on the adsorption and chemical transformation behaviors of nonanal. Surface spectroscopic analysis and theoretical simulations provide the mechanistic understanding as to the role of surface exposed Cu on the nanowires. Furthermore, we demonstrate the applicability of the tailored mixed cation composition surface for electrical molecular sensing of nonanal.

3.2.3 EXPERIMENTAL

Preparation of nanowires samples. ZnO nanowires were grown on a 100 nm thick SiO_2 coated Si (100) substrate by hydrothermal synthesis.[40-43] A 5 nm thick Ti buffer layer and a 100 nm thick ZnO film were sequentially deposited on the substrate by radio frequency (RF) sputtering. The substrate was immersed into 150 ml aqueous solution containing 25 mM zinc nitrate hexahydrate ($Zn(NO_3)_2 \cdot 6H_2O$, Wako 99.0%) and 25 mM hexamethylenetetramine (HMTA, $(CH_2)_6N_4$ Wako 99.0%) in a manner of up-side-down. The ZnO nanowires were grown by keeping the solution at 95 ºC for 15 h in oven. After the growth, the samples were taken out from the solution and rinsed by water. The as-grown samples were thermally annealed at 500 ºC for 3 h in air for fully removing organic contaminant on nanowire surface and then ZnO nanowire samples were prepared. CuO/ZnO nanowires were fabricated by depositing CuO on the thermally annealed ZnO nanowires by means of pulsed laser deposition at room temperature in 1 Pa oxygen atmosphere. CuO (II) tablet was utilized as a target for PLD. The thickness of CuO shell was controlled by varying the deposition time. After depositing CuO layer, the oxygen plasma treatment was performed at 150 W in 1 Torr oxygen atmosphere. Cu-Zn-O heterocompositional nanowire surface (*i.e.* CuZnO nanowires) was formed by thermal treatment at 500 ºC for 3 h in air.

Characterization of nanowires. Morphology, crystal structure and composition of the samples were characterized by using scanning electron microscopy (SEM, JEOL JSM-7610F) at accelerating voltage of 15 kV, x-ray diffraction (XRD, Rigaku TTR-II) with Cu Kα radiation source at 50 kV and 300 mA, transmission electron microscopy (TEM, JEOL JEM-2100F) equipped with energy dispersive x-ray spectroscopy (EDS) at accelerating voltage of 200 kV and x-ray photoelectron spectroscopy (XPS, Kratos AXIS-ULTRA) with Al Kα radiation source. Fourier transform infrared spectroscopy (FTIR, Thermo Fisher Scientific Nicolet iS50) equipped with MCT (HgCdTe) detector was used to evaluate the adsorbed molecules on nanowires. For monitoring the temperature dependent variations of adsorbed state of molecules, the samples were heated at a given temperature for 5 min and immediately cooled down to room temperature in air. All FTIR measurements were performed at room temperature.

Analysis of desorbed molecules. For the desorbed molecule analysis, firstly nonanal was adsorbed to the nanowire surface. The nanowire samples were cut into a piece of 2 mm×20 mm. 2 μl liquid nonanal was placed at the bottom of 25 ml vial bottle, followed by closing the bottle

and keeping for 30 min to vaporize nonanal. The suspended samples were inserted in the bottle filled with nonanal vapor, kept for 30 sec and transferred to gas chromatograph mass spectrometry (GCMS, SHIMADZU GCMS-QP2020 Ultra) system. The desorbed compounds were analyzed by GCMS equipped with inlet temperature control unit (OPTIC4) using Supelco SLB-IL60 capillary column. During the measurement, inlet temperature was kept at 400 ºC. Desorption temperature of compounds was evaluated via temperature-programmed desorption mass spectrometry (TPDMS) measurements. A capillary column (length: 1 m, inner diameter: 0.1 mm) without stationary phases was utilized to connect between inlet and mass spectrometer unit. The inlet temperature was controlled from 35 ºC to 500 ºC by multi-shot pyrolyzer (FRONTIER LAB, EGA/PY-3030D) with a heating rate of 0.5 ºC/sec. The variations in total ion currents (TIC) were monitored during elevating the inlet temperature.

Computational details. We computed the vibrational frequencies of nonanal on ZnO $(10\bar{1}0)$ and CuO (111) surfaces using density functional theory (DFT) to assign the C=O stretch bands. Simplified cluster models were employed to consider the adsorbed ZnO $(10\bar{1}0)$ and CuO (111) surface approximately. These models were extracted from a Wurtzite ZnO crystal structure with a=b=3.25 Å and c=5.2 Å, or monoclinic CuO crystal structure with a=b=2.93 Å and c=5.15 Å. In order to mimic the above-mentioned surfaces, unsaturated MO bonds are capped and neutralized with protons placed at the position where neighboring Zn^{2+} or Cu^{2+} originally exist. The DFT calculations were carried out using the Gaussian 16 program suite Revision A03 with the B3LYP hybrid functional.[44] The basis sets employed were def2-SVP. All the cluster atoms were kept fixed during geometry optimizations. The obtained harmonic vibrational frequencies were shifted using a scale factor of 0.95 to incorporate anharmonic effects effectively.

Preparation of single nanowire sensor and molecular sensing measurement. Nanowire suspension was prepared by sonicating the fabricated nanowire samples in 2-propanol. The nanowire was transferred by dropping the suspension on a 100 nm thick SiO_2 coated Si (100) substrate with pre-patterned contact electrodes. Electron beam (EB) lithography (JEOL, JSM-7001F and SANYU electron, NANO PRINTER SPG-724) was performed at accelerating voltage of 30 kV to make the electrode patterns for bridging a single nanowire between them using ZEP520A-7 (ZEON) as a resist. For the electrical contact, Pt was deposited by RF sputtering with 300 nm thickness. After a lift-off process in *N,N*-dimethylformamide (DMF) and a rinse process in acetone, a single nanowire sensor device was obtained. The gap size of bridged nanowire was designed to be 500 nm and the nanowires with ca. 100 nm diameter were

chosen for all fabricated device to eliminate the variation of electrical properties caused by the device geometry. Molecular sensing measurement was conducted in the customized probe station (JANIS, ST-500) connected with a gas flow system and a semiconductor parameter analyzer (Tektronix, Keithley 4200-SCS). The variations of electrical signal under flowing N_2 or 2.48 ppm nonanal were monitored by applying voltage of 1 V to the electrodes. All measurements were performed at 200 ºC. The sensor response was defined as R_a/R_g, where R_a and R_g are the sensor resistance when exposed to N_2 and nonanal, respectively. The sensor recovery time was defined as the time for reaching 90 % of R_a after stopping the nonanal flow. We evaluated several nanowire sensor devices for reliability of results shown in this study.

3.2.4 RESULTS AND DISCUSSION

A cation diffusion in core/shell heterostructured nanowire is employed to gradually modulate the surface cation composition. Figure 1 (a) shows the schematic images for three types of nanowire samples utilized in this study; i) ZnO nanowires, ii) ZnO/CuO nanowires and iii) (Cu,Zn)O nanowires, where ZnO/CuO nanowires and (Cu,Zn)O nanowires represent CuO shell coated ZnO nanowires and their 500 ºC annealed sample, respectively (see details in figure S1-S5). A heterocompositional surface of $(Cu_x,Zn_{1-x})O$ nanowire is formed by a cation diffusion at ZnO(core)/CuO(shell) interface during thermal annealing[28-30] and controlled by a CuO thickness. In order to confirm the occurrence of cation diffusion, we performed structural and compositional analyses of the nanowires. Figure 1 (b) and (c) show the transmission electron microscopy (TEM) images of ZnO/CuO nanowire and (Cu,Zn)O nanowire, respectively. The polycrystalline nature of CuO shell layer with thickness of ca. 10 nm is observed in both samples, and the surface roughness of nanowires becomes smaller after annealing treatment. Figure 1 (d) and (e) show the energy dispersive x-ray spectroscopy (EDS) elemental mappings (Zn Kα, Cu Kα) and their radial line profiles for ZnO/CuO nanowire and (Cu,Zn)O nanowire, respectively. While a distinct core/shell interface is seen in a ZnO/CuO nanowire before annealing (figure 1(d)), it becomes unclear and homogeneously distributed Zn atoms in CuO shell are observed in a (Cu,Zn)O nanowire after annealing. X-ray photoemission spectroscopy (XPS) shows that the surface Zn ratio of nanowires increases from 2 % (in ZnO/CuO nanowires) to 17 % (in (Cu,Zn)O nanowires) by annealing. A few percent of zinc detected in ZnO/CuO nanowires is due to the imperfect coating of CuO layer at the bottom part of ZnO nanowires. As such, these results reveal the occurrence of cation diffusion in (Cu,Zn)O nanowire.

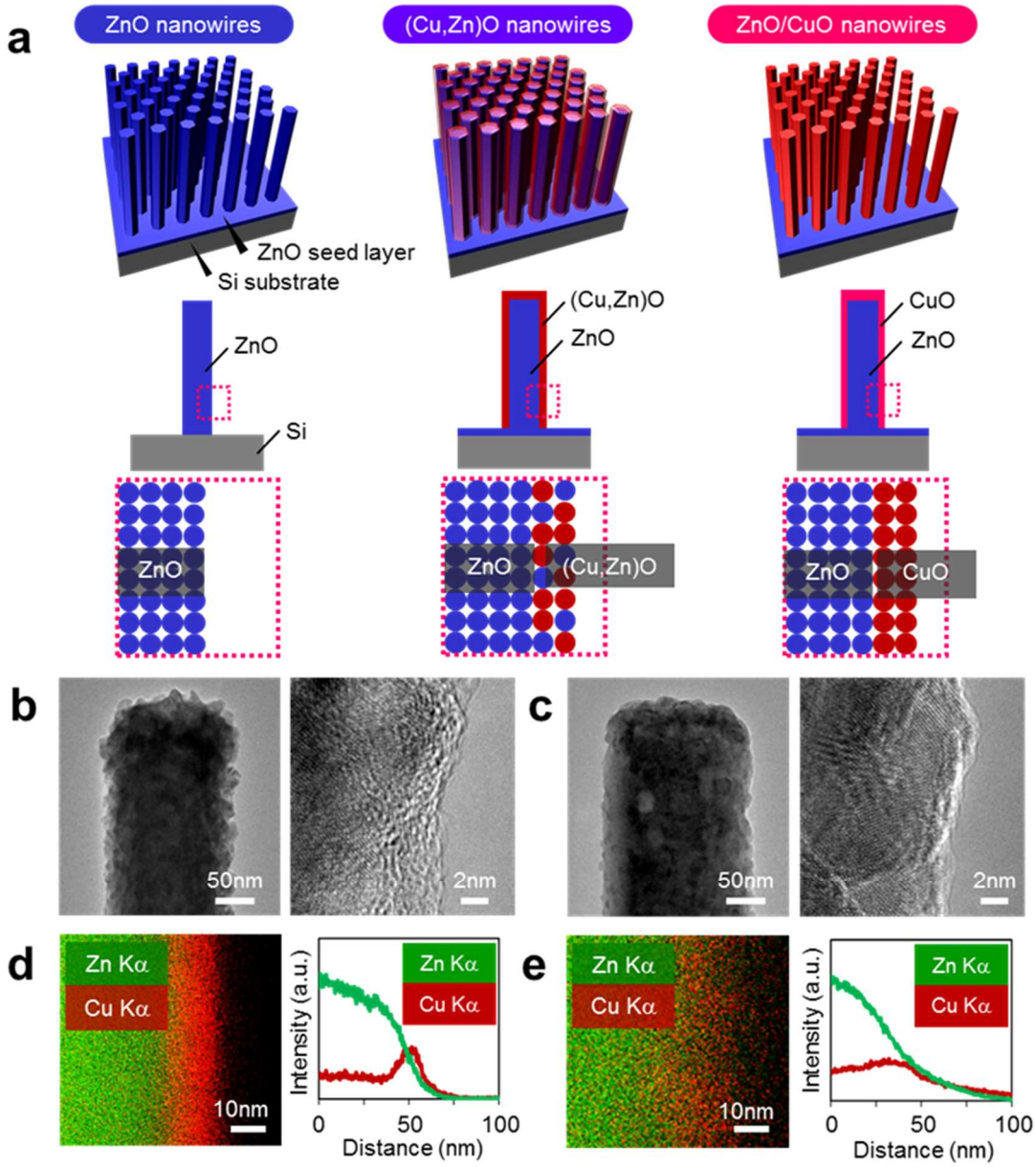

Figure 1. *(a) Schematic images of ZnO nanowires, (Cu,Zn)O nanowires and ZnO/CuO nanowires. ZnO/CuO nanowires and (Cu,Zn)O nanowires represent the CuO shell coated ZnO nanowires and their 500 ºC annealed sample, respectively. (b,c) TEM images, (d,e) EDS elemental mappings and line profiles of (b,d) ZnO/CuO nanowires and (c,e) (Cu,Zn)O nanowires, respectively.*

In addition, we found that the surface Zn ratio of (Cu,Zn)O nanowires is systematically modulated from 10 % to 43 % by varying the deposited CuO thickness from 20 nm to 3 nm (figure S4). The major valence state of Cu^{2+} and the macroscopic morphology of nanowires are preserved even varying the CuO thickness (figure S4-S5). Thus we successfully achieved the

gradual modulation of surface Cu/Zn ratio of the heterostructured (Cu_x,Zn_{1-x})O nanowires via the proposed approach.

Next we investigated the effect of Cu/Zn ratio of the heterostructured (Cu_x,Zn_{1-x})O nanowires on the adsorption and the chemical transformation of adsorbed molecules on the nanowire surface. Figure 2 (a) shows the gas chromatograph mass spectrometry (GCMS) spectra of desorbed compounds from the nonanal-adsorbed ZnO nanowires, (Cu,Zn)O nanowires and ZnO/CuO nanowires. Two distinct peaks which are assigned to nonanal and (*E*)-2-heptyl-2-undecenal are seen in the spectrum of ZnO nanowires. Our previous study revealed that nonanal transforms to (*E*)-hepthyl-2-undecenal via aldol condensation reaction on ZnO nanowire surface and such transformation ~~detrimentally~~ increases the desorption temperature of molecules.[31] Remarkably, the (*E*)-2-heptyl-2-undecenal peak becomes smaller in (Cu,Zn)O nanowires while the nonanal peak remains almost unchanged. Such effect tends to be more significant when increasing the CuO thickness. On the other hand, in ZnO/CuO nanowires, where the nanowire surface is almost fully covered by CuO, none of peaks are observable and hence it supposes that nonanal hardly adsorbs on the CuO surface. This is ~~quite~~ an interesting unexpected result because the Lewis acidity of Cu^{2+} is strong enough and comparable to that of Zn^{2+}.[32] Figure 2 (b) shows the conversion ratio of nonanal to (*E*)-2-hepthyl-2-undecenal on ZnO nanowires and (Cu,Zn)O nanowires. The conversion ratio decreases from 36.7 % to 9.0 % by increasing the CuO thickness from 0 nm to 20 nm, clearly showing that surface exposed copper suppresses the aldol condensation reaction. A linear relationship between the conversion ratio and the surface Zn ratio (inset of figure 2 (b)) indicates that the surface condensation reaction is governed by the surface Zn ratio and nonanal mainly adsorbs at Zn^{2+} site rather than Cu^{2+} site on (Cu,Zn)O nanowires. Figure 2 (c) shows the temperature-programmed desorption mass spectrometry (TPDMS) profiles of desorption compounds from the nonanal-adsorbed nanowires. Whereas there are no peak in ZnO/CuO nanowires, two peaks associated with nonanal (ca. 115 ºC) and (*E*)-2-hepthyl-2-undecenal (ca. 230 ºC) are seen in ZnO nanowires and (Cu,Zn)O nanowires. The higher temperature peak of (*E*)-2-hepthyl-2-undecenal is drastically suppressed in (Cu,Zn)O nanowires while maintaining the desorption temperature of nonanal. Thus, these results highlight the significant role of surface copper on the adsorption and the chemical transformation of nonanal.

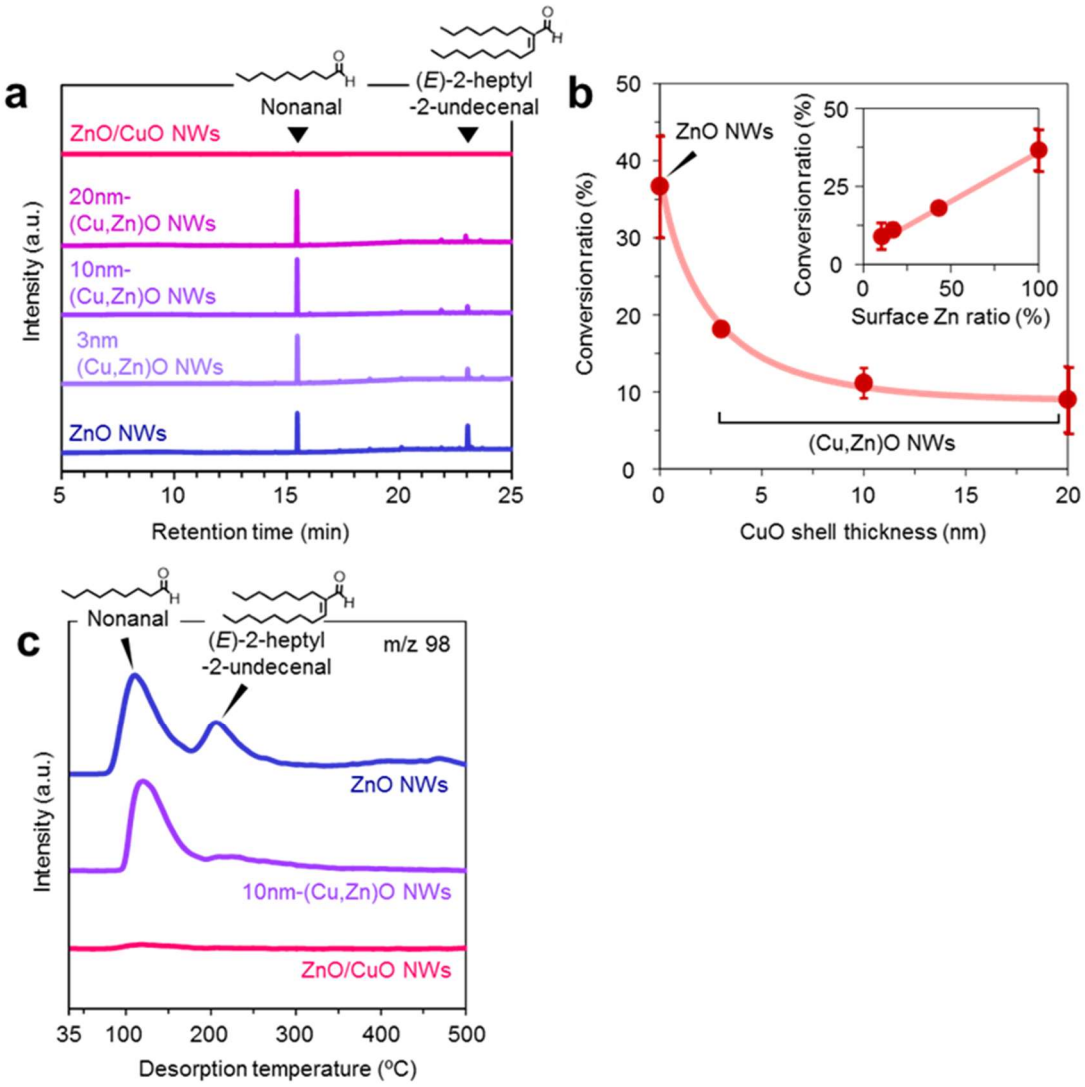

Figure 2. *(a) GCMS spectra for desorbed compounds on ZnO nanowires, (Cu,Zn)O nanowires and ZnO/CuO nanowires. For (Cu,Zn)O nanowires, CuO shell thickness is varied with 3-20 nm. (b) CuO shell thickness dependent conversion ratio of nonanal to (E)-2-hepthyl-2-undecenal. Inset shows its surface Zn ratio dependence. (c) TPDMS profiles of desorbed compounds on ZnO nanowires, (Cu,Zn)O nanowires and ZnO/CuO nanowires, which are evaluated with m/z 98. 'NWs' abbreviates 'nanowires'.*

Here we question why the surface copper significantly suppressed the adsorption and the chemical transformation of nonanal while the Lewis acidities of Cu^{2+} and Zn^{2+} are comparable.[32] We consider the effect of coordination degree of exposed surface metal ions, which should influence the adsorption of molecules. A coordination degree of surface metal ions is inherently complex, but in general depends on a crystal structure and a crystal plane.[33] On the CuO surface, CuO (111) plane, which has the lowest surface energy, is likely to be exposed via surface reconstruction during thermal annealing.[34,35] Cu^{2+} ion on CuO (111) plane

has the coordination-saturated in-plane square geometry while Zn^{2+} ion on ZnO $(10\bar{1}0)$ plane (*i.e.* sidewall plane) has the coordination-unsaturated tetrahedral geometry. To examine such effect of coordination degree of surface metal ions, we conducted the density functional theory (DFT) calculations for the nonanal molecules adsorbed on CuO (111) plane and ZnO $(10\bar{1}0)$ plane (figure 3 (a) and (b)). The

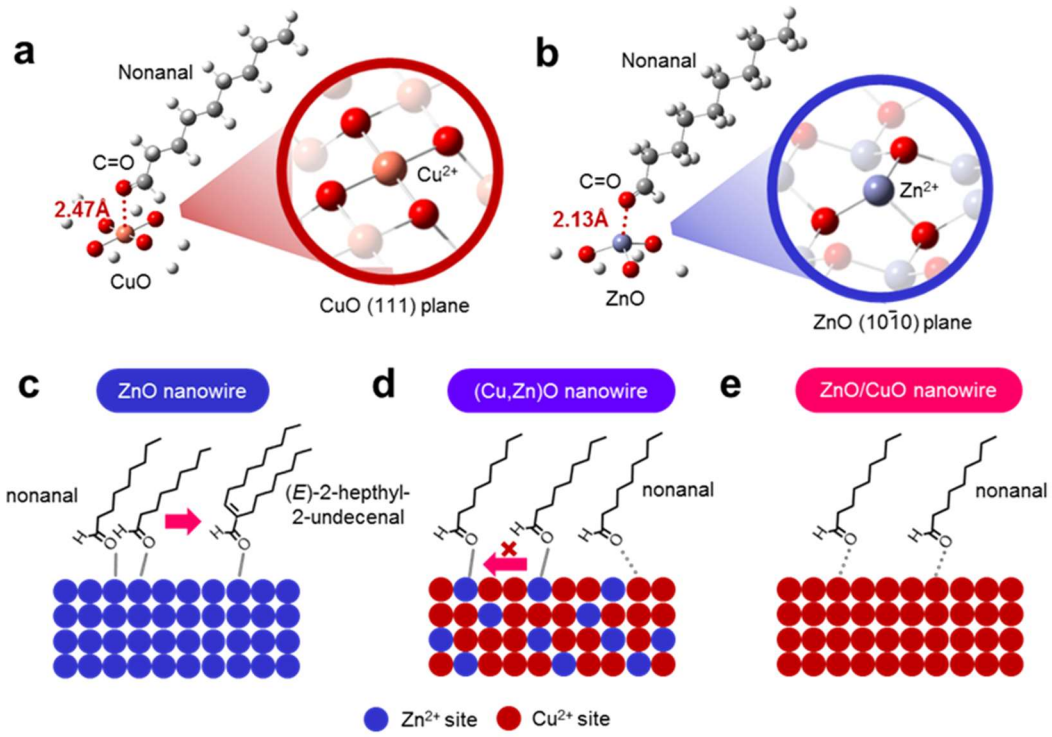

Figure 3. *(a,b) Computed structures and calculated bond lengths of nonanal C=O—metal ions on (a) CuO (111) plane and (b) ZnO* $(10\bar{1}0)$ *plane using cluster model (c-e) Schematic illustrations for nonanal adsorption and aldol condensation event on (c) ZnO nanowire surface, (d) (Cu,Zn)O nanowire surface and (e) ZnO/CuO nanowire surface.*

Table I. Simulated bond length of nonanal C=O—metal ions by cluster model and complex ion model.

model cluster	bond length (Å)	model ion	bond length (Å)
ZnO: $(10\bar{1}0)$ plane	2.13	Zn(II) ion	2.18
CuO: (111) plane	2.47	Cu(II) ion	2.03

estimated length of C=O—M^+ bonding is much longer on CuO (2.47 Å) than that on ZnO (2.13 Å) (Table I), indicating the weaker adsorption of nonanal on CuO (111) plane. It should be noted that the C=O—M^+ bonding length estimated using the coordination-unsaturated metal complex ions is similar in Cu (II) ion (2.03 Å) and Zn (II) ion (2.18 Å) (figure S6 and Table I). Thus, the coordination-saturated geometry of Cu^{2+} ion must be responsible for experimentally observed weak adsorption behaviors of nonanal on CuO surface.

Furthermore, above simulation results also well explain why the surface aldol condensation reaction was supressed when increasing surface Cu/Zn ratio on the $(Cu_x,Zn_{1-x})O$ nanowires. The weak C=O—Cu^{2+} bonding assumes that nonanal molecules are not activated at Cu^{2+} site of the $(Cu_x,Zn_{1-x})O$ nanowires. Since our previous study revealed that the aldol condensation reaction is triggered by two activated nonanal molecules adsorbed at neighboring Zn^{2+} Lewis acidic sites on ZnO nanowires (figure 3 (c)),[31] increasing the surface ratio of inactive Cu^{2+} site should suppress the surface aldol condensation reactions via preventing the neighboring of two activated nonanal molecules on the surface (figure 3 (d)). Note that the molecular behaviors on $(Cu_x,Zn_{1-x})O$ surface and CuO surface must be different; nonanal adsorption is not hindered on $(Cu_x,Zn_{1-x})O$ surface and nonanal coordinated at the isolated Zn^{2+} site remain without contributing to the condensation reaction (figure 3 (d)) whereas nonanal adsorption itself is suppressed on CuO surface (figure 3 (e)). These models are well consistent with the results of GCMS and TPDMS in figure 2. Thus, the weak adsorption of nonanal at surface Cu^{2+} site and the supressed aldol condensation reaction can be interpreted in terms of the saturated-coordination geometry of Cu^{2+} site on the surfaces of $(Cu_x,Zn_{1-x})O$ nanowires and ZnO/CuO nanowires.

In order to experimentally validate above simulated results, we analyzed the adsorption states of molecules on nanowire surfaces using Fourier transform infrared spectroscopy (FTIR). Figure 4 (a) shows the FTIR spectra for nonanal-adsorbed ZnO nanowires, ZnO/CuO nanowires and (Cu,Zn)O nanowires. Background signals from nanowires are subtracted in each spectrum. The spectra show three peaks in the 1650-1710 cm^{-1} region, which correspond to different ν(C=O) vibration modes of nonanal (ν_1: 1706-1708 cm^{-1}, ν_2: ~1700 cm^{-1}, ν_3: 1658-1666 cm^{-1}). Based on our DFT calculations, these peaks can be assigned to nonanal C=O coordinating to i) Cu^{2+} site (ν_1), ii) –OH (ν_2) and iii) Zn^{2+} site (ν_3), respectively (see details in Ref [31] and figure S6-7). We found that nonanal coordinates to both Cu^{2+} site and Zn^{2+} site on the $(Cu_x,Zn_{1-x})O$

nanowire surface. The presence of C=O—Cu^{2+} peak in ZnO/CuO nanowires seems to contradict the results of GCMS and TPDMS in figure 2, of which none of peaks associated with nonanal were observed. Two additional peaks around 1590 and 1550 cm^{-1} are observed in ZnO nanowires and 3 nm-thick (Cu,Zn)O nanowires, which are assigned to (*E*)-2-hepthyl-2-undecenal (ν_4) and their oxidized species (ν_{as}(COO)), respectively.[31] Note that ν_4 and ν_{as}(COO) peaks disappears when increasing the CuO shell thickness over 10 nm due to the suppressed aldol condensation reaction. We further investigate a variation of molecular adsorption state when increasing temperature in figure 4 (b). After a thermal treatment at 100 ºC (5 min in air), the ν_1(C=O) peak disappears while the ν_3(C=O) peak remains, validating our simulated model where the C=O—Cu^{2+} bonding is much weaker than the C=O—Zn^{2+} bonding. Also these results well explain the discrepancy between the results of ZnO/CuO nanowires in FTIR and GCMS/TPDMS, *i.e.* the nonanal adsorbed at Cu^{2+} site is removed in a flow of GCMS/TPDMS systems before conducting the measurements. Thus spectroscopic data consistently support our simulated model, giving further in-depth understanding as to complex molecular adsorption behaviors on the nanowire surface.

Finally we applied the $(Cu_x,Zn_{1-x})O$ mixed cation composition of heterostructured nanowire surface for the electrical molecular sensing of nonanal. In this experiment, ZnO nanowire and 10 nm-thick (Cu,Zn)O nanowire were examined in the form of single nanowire device as shown in figure 5 (a) and (b), respectively. All devices exhibit linear current-voltage (*I-V*) characteristics, representing Ohmic contact between the nanowires and the Pt electrodes (figure S8). The sensing measurements were conducted at 200 ºC with the readout voltage of 1 V. The resistance ratio R_a/R_g, where R_a and R_g are resistance values in N_2 flow and 2.48 ppm nonanal flow respectively, were monitored as a sensor response. Figure 5 (c) and (d) show the five successive sensor responses to nonanal in ZnO nanowire device and (Cu,Zn)O nanowire device, respectively. The sensor response of ZnO nanowire device tends to deteriorate when increasing the number of sensing cycles. The result can be interpreted by the existence of residual condensation product on the surface because the required temperature for fully desorbing (*E*)-2-hepthyl-2-undecenal (ca. 300-350 ºC, figure 2 (c)) is higher than the operation temperature of sensor. On the contrary, the sensor response of (Cu,Zn)O nanowire device is almost same even increasing the number of sensing cycles, reflecting the suppressed condensation reaction. The effect of suppressed molecular condensation was also found in the recovery response, in (e)-(g)). As such, the durability and the recovery time of nanowire sensor can be successfully

which the recovery time in ZnO nanowire device (992 s) becomes much shorter in (Cu,Zn)O nanowire device (245 s) (figure 5) improved by suppresing the detrimental aldol condensation reaction. It is worth describing that all these improvements in sensor performance of (Cu,Zn)O nanowire device were demonstrated by maintaining the sensitiviy (figure 5 (h)). This is well consistent with the resutls of spectrometric and spectroscopic analyses (figure 2 and figure 4),

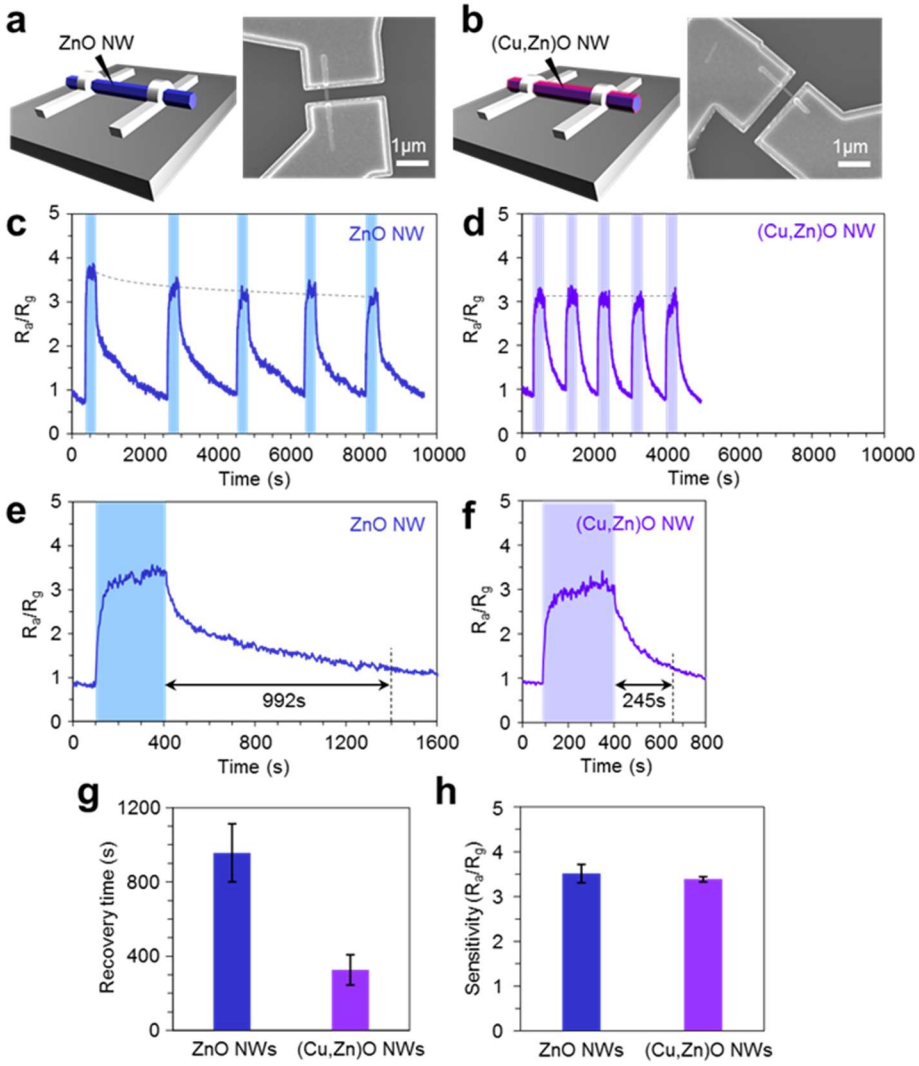

Figure 5. *(a,b) Schematic illustrations and SEM images of single nanowire sensor devices for (a) ZnO nanowire and (b) (Cu,Zn)O nanowire. The CuO thickness for (Cu,Zn)O nanowire is 10 nm. (c,d) Successive five sensor responses and (e,f) typical single sensor response to 2.48 ppm nonanal for (c,e) ZnO nanowire device and (d,f) (Cu,Zn)O nanowire device, respectively. All measurements were performed at 200 ºC with readout voltage of 1 V. (g) recovery time and (h) Sensitivity R_a/R_g for ZnO nanowire device and (Cu,Zn)O nanowire device. 'NWs' and 'NW' abbreviates 'nanowires' and 'nanowire', respectively.*

of which the amount of adsorbed nonanal is maintained as a consequence of controlled number of exposed Zn^{2+} adsorption site and suppressed molecular condensation. Such precise controllability in adsorption and chemical transformation of molecules are not available in the organic surface passivation by a self-assembled monolayer (SAM)[36,37] and the surface decoration by nanoparticles.[38,39] Thus a cation diffusion based coninuous modulation of surface cation composition revealed the unique property of surface exposed Cu in the heterostrucured $(Cu_x,Zn_{1-x})O$ nanowires and allows us to tailor the surface molecular behaviors. Since the proposed approach for modulating the surface cation composition can be extended to various metal oxides by varying their material combination, it paves a novel way to design the nanoscale metal oxide surface for further enhancing the performance of various applications such as molecular sensors and catalysts.

3.3.5 CONCLUSION

In conclusion, we demonstrated a gradual modulation of surface Cu/Zn ratio of heterostructured $(Cu_x,Zn_{1-x})O$ nanowires via a cation diffusion at core/shell interface and investigated its effect on the adsorption and chemical transformation behaviors of nonanal. The gradual modulation of surface Cu/Zn ratio was successfully achieved by preserving the macroscopic morphology and the major valence state of Cu^{2+}. We found that surface exposed copper significantly supresses the adsorption of nonanal and the increase of surface Cu/Zn ratio systematically suppresses the molecular condensation reaction, although the Lewis acidity of Cu^{2+} is strong enough and comparable to Zn^{2+}. Infrared spectroscopy analysis and theoretical simulation revealed that the nonanal molecules adsorbed at Cu^{2+} site are not activated due to its coordination-saturated in-plane square geometry and thus such inactive surface Cu^{2+} site is responsible for suppressing the molecular condensation. Our study also revealed the importance to control the density of exposed Zn^{2+} site for maintaining the amount of adsorbed nonanal. As a consequence of supressed condensation reaction and controlled Zn^{2+} site density, we successfully demonstrated the significant improvements in the durability and the recovery time of nanowire sensor while maintaining the sensitivity. The results highlighted a critical importance to continuously modulate the surface cation composition for understanding and tailoring the adsorption and chemical transformation behaviors on nanoscale metal oxide surface.

3.2.6 REFERENCES

[1]. Corberán, V. C.; Rives, V.; Stathopoulos, V. Recent Applications of Nanometal Oxide Catalysts in Oxidation Reactions. *Advanced Nanomaterials for Catalysis and Energy*; Sadykov. V. A., Eds.; Elsevier: Amsterdam, 2019; pp 227-293.

[2]. Krivetskiy, V; Rumyantseva, M.; Gaskov, A. Design, Synthesis and Application of Metal Oxide-Based Sensing Elements: A Chemical Principles Approach. *Metal Oxide Nanomaterials for Chemical Sensors*; Carpenter, M. A., Mathur, S., Kolmakov, A., Eds.; Springer: New York, 2013; pp 69-115.

[3]. Jeong, N. C.; Lee, J. S.; Tae, E. L.; Lee, Y. J.; Yoon, K. B. Acidity Scale for Metal Oxides and Sanderson's Electronegativities of Lanthanide Elements. *Angew. Chem. Int. Ed.* **2008**, 47, 10128 - 10132. DOI: 10.1002/anie.200803837

[4]. Degler, D.; Weimar, U.; Barsan, N. Current Understanding of the Fundamental Mechanisms of Dopedand Loaded Semiconducting Metal-Oxide-Based Gas Sensing Materials. *ACS Sens.***2019**, 4, 2228-2249. DOI:10.1021/acssensors.9b00975

[5]. Lupan, O.: Postica, V.; Gröttrup, J.; Mishra, A. K.; de Leeuw, N. H.; Carreira, J. F. C.; Rodrigues, J.; Sedrine, N. B.; Correia, M. R.; Monteiro, T.; Cretu, V.; Tiginyanu, I.; Smazna, D.; Mishra, Y. K.; Adelung, R. Hybridization of Zinc Oxide Tetrapods for Selective Gas Sensing Applications. *ACS Appl. Mater. Interfaces* **2017**, 9, 4084-4099. DOI:10.1021/acsami.6b11337

[6]. Metiu, H.; Chrétien, S.; Hu, Z.; Li, B.; S. X. Y. Chemistry of Lewis Acid-Base Pairs on Oxide Surfaces. *J. Phys. Chem. C* **2012**, 116, 10439-10450. DOI: 10.1021/jp301341t

[7]. Gawande, M. B.; Pandey, R. K.; Jayaram, R. V. Role of mixed metal oxides in catalysis science-versatile applications inorganic synthesis. *Catal. Sci. Technol.* **2012**, 2, 1113-1125. DOI: 10.1039/c2cy00490a

[8]. Ma, S.; Huang, S.-D.; Liu, Z.-P. Dynamic coordination of cations and catalytic selectivity on zinc-chromium oxide alloys during syngas conversion. *Nat. Catal.* **2019**, 2, 671-677. DOI: 10.1038/s41929-019-0293-8

[9]. Yan, T.; Bing, W.; Xu, M.; Li, Y.; Yang, Y.; Cui, G.; Yang, L.; Wei, M. Acid-base sites synergistic catalysis over Mg-Zr-Al mixed metal oxide toward synthesis of diethyl carbonate. *RSC Adv.* **2018**, 8, 4695-4702. DOI: 10.1039/c7ra13629c

[10]. Yamauchi, M.; Hata, S.; Eguchi, H.; Kitano, S.; Fukushima, T.; Higashi, M.; Sadakiyo, M.; Kato, K. Catalytic enhancement on Ti–Zr complex oxide particles for electrochemical hydrogenation of oxalic acid to produce an alcoholic compound by controlling electronic states and oxide structures. *Catal. Sci. Technol.* **2019**, 9, 6561-6565 DOI: 10.1039/c9cy01541h

[11]. Singh, P.; Kumar, R.; Singh, R. K. Progress on Transition Metal-Doped ZnO Nanoparticles and Its Application. *Ind. Eng. Chem. Res.* **2019**, 58, 17130-17163. DOI: 10.1021/acs.iecr.9b01561

[12]. Ling, T.; Da, P.; Zheng, X.; Ge, B.; Hu, Z.; Wu, M.; Du, X.-W.; Hu, W.-B.; Jaroniec, M.; Qiao, S.-

Z. Atomic-level structure engineering of metal oxides for high-rate oxygen intercalation pseudocapacitance. *Sci. Adv.* **2018**, 4, eaau6261. DOI: 10.1126/sciadv.aau6261

[13]. Lentijo-Mozo, S.; Deiana, D.; Sogne, E.; Casu, A.; Falqui, A. Unexpected Insights about Cation-Exchange on Metal Oxide Nanoparticles and Its Effect on Their Magnetic Behavior. *Chem. Mater.* **2018**, 30, 8099-8112. DOI: 10.1021/acs.chemmater.8b04331

[14]. Na, C. W.; Woo, H.-S.; Kim, H.-J.; Jeong, U.; Chung, J.-H.; Lee, J.-H. Controlled transformation of ZnO nanobelts into CoO/Co_3O_4 nanowires. *Cryst. Eng. Comm.* **2012**, 14, 3737-3741. DOI: 10.1039/c2ce06681e

[15]. Resasco, J.; Dasgupta, N. P.; Rosell, J. R.; Guo, J.; Yang, P. Uniform Doping of Metal Oxide Nanowires Using Solid State Diffusion. *J. Am. Chem. Soc.* **2014**, 136, 10521-10526. DOI: 10.1021/ja505734s

[16]. Chen, Y. H.; Huang, C. W.; Yeh, P. H.; Chen, J. Y.; Lin, T. Y.; Chang, C. F.; Wu, W. W. A solid-state cation exchange reaction to form multiple metal oxide heterostructure nanowires. *Nanoscale* **2016**, 8, 17039-17043. DOI: 10.1039/c6nr01287f

[17]. Wang, S.-C.; Lu, M.-Y.; Manekkathodi, A.; Liu, P.-H.; Lin, H.-C.; Li, W.-S.; Hou, T.-C.; Gwo, S.; Chen, L.-J. Complete Replacement of Metal in Metal Oxide Nanowires via Atomic Diffusion: In/ZnO Case Study. *Nano Lett.* **2014**, 14, 3241-3246. DOI: 10.1021/nl5006228

[18]. Tamuly, C.; Saikia, I.; Hazarika, M.; Das, M. R. Bio-derived CuO nanocatalyst for oxidation of aldehyde: a greener approach. *RSC Adv.* **2014**, 4, 20636-20640. DOI: 10.1039/c4ra01683a

[19]. Hu, J.; Li, D.; Lu, J. G.; Wu, R. Effects on Electronic Properties of Molecule Adsorption on CuO Surfaces and Nanowires. *J. Phys. Chem. C* **2010**, 114, 17120-17126. DOI: 10.1021/jp1039089

[20]. Tayebee, R.; Nasr, A. H.; Rabiee, S.; Adibi, E. Zinc Oxide as a Useful and Recyclable Catalyst for the One-Pot Synthesis of 2,4,6-Trisubstituted-1,3,5-trioxanes under Solvent-Free Conditions. *Ind. Eng. Chem. Res.* **2013**, 52, 9538-9543.

[21]. Yao, M.-S.; Tang, W.-X.; Wang, G.-E.; Nath, B.; Xu, G. MOF Thin Film-Coated Metal Oxide Nanowire Array: Significantly Improved Chemiresistor Sensor Performance. *Adv. Mater.* **2016***,* 28, 5229-5234.

[22]. Wang, C.; Zhu, J.; Liang, S.; Bi, H.; Han, Q.; Liu, X.; Wang, X. Reduced graphene oxide decorated with CuO-ZnO hetero-junctions: towards high selective gas sensing property to acetone. *J. Mater. Chem. A* **2014**, 2, 18635-18643.

[23]. Gawande, M. B.; Pandey, R. K.; Jayaram, R. V. Role of mixed metal oxides in catalysis science—versatile applications in organic synthesis. *Catal. Sci. Technol.* **2012**, 2, 1113-1125.

[24]. Chng, L. L.; Erathodiyil, N.; Ying, J. Y. Nanostructured Catalysts for Organic Transformations. *Acc. Chem. Res.* **2013**, 46, 1825-1837. DOI: 10.1021/ar300197s

[25]. Laghrib, F.; Lahrich, S.; Mhammedi, M. A. E. Review—Recent Advances in Direct and Indirect Methods for Sensing Carbonyl Compounds Aldehydes in Environment and Foodstuffs. *J.*

Electrochem. Soc. **2019**, 166, B1543-B1551. DOI: 10.1149/2.0761915jes

[26]. Li, M.; Li, Q.; Nantz, M. H.; Fu, X.-A. Analysis of Carbonyl Compounds in Ambient Air by a Microreactor Approach. *ACS Omega* **2018**, 3, 6764-6769. DOI: 10.1021/acsomega.8b00503

[27]. Nakhleh, M. K.; Amal, H.; Jeries, R.; Broza, Y. Y.; Aboud, M.; Gharra, A.; Ivgi, H.; Khatib, S.; Badarneh, S.; Har-Shai, L.; Glass-Marmor, L.; Lejbkowicz, I.; Miller, A.; Badarny, S.; Winer, R.; Finberg, J.; Cohen-Kaminsky, S.; Perros, F.; Montani, D.; Girerd, B.; Garcia, G.; Simonneau, G.; Nakhoul, F.; Baram, S.; Salim, R.; Hakim, M.; Gruber, M.; Rone, O.; Marshak, T.; Doweck, I.; Nativ, O.; Bahouth, Z.; Shi, D.-Y.; Zhang, W.; Hua, Q.-L.; Pan, Y.-Y.; Tao, L.; Liu, H.; Karban, A.; Koifman, E.; Rainis, T.; Skapars, R.; Sivins, A.; Ancans, G.; Liepniece-Karele, I.; Kikuste, I.; Lasina, I.; Tolmanis, I.; Johnson, D.; Millstone, S. Z.; Fulton, J.; Wells, J. W.; Wilf, L. H.; Humbert, M.; Leja, M.; Peled, N.; Haick, H. Diagnosis and Classification of 17 Diseases from 1404 Subjects via Pattern Analysis of Exhaled Molecules. *ACS Nano* **2017**, 11, 112-125. DOI: 10.1021/acsnano.6b04930

[28]. Fan, H. J.; Knez, M.; Scholz, R.; Nielsch, K.; Pippel, E.; Hesse, D.; Zacharias, M.; Gösele, U. Monocrystalline spinel nanotube fabrication based on the Kirkendall effect. *Nat. Mater.* **2006**, 5, 627-631. DOI: 10.1038/nmat1673

[29]. Nagashima, K.; Yanagida, T.; Tanaka, H.; Seki, S.; Saeki, A.; Tagawa, S.; Kawai, T. Effect of the Heterointerface on Transport Properties of in Situ Formed MgO/Titanate Heterostructured Nanowires. *J. Am. Chem. Soc.* **2008**, 130, 5378-5382. DOI: 10.1021/ja800367a

[30]. Marcu, A.; Yanagida, T.; Nagashima, K.; Oka, K.; Tanaka, H.; Kawai, T. Crucial role of interdiffusion on magnetic properties of *in situ* formed MgO/$Fe_{3-\delta}O_4$ heterostructured nanowires. *Appl. Phys. Lett.* **2008**, 92, 173119. DOI: 10.1063/1.2918132

[31]. Wang, C.; Hosomi, T.; Nagashima, K.; Takahashi, T.; Zhang, G.; Kanai, M.; Zeng, H.; Mizukami, W.; Shioya, N.; Shimoaka, T.; Tamaoka, T.; Yoshida, H.; Takeda, S.; Yasui, T.; Baba, Y.; Aoki, Y.; Terao, J.; Hasegawa, T.; Yanagida, T. Rational Method of Monitoring Molecular Transformations on Metal-Oxide Nanowire Surfaces. *Nano Lett.* **2019**, 19, 2443-2449. DOI: 10.1021/acs.nanolett.8b05180

[32]. Gagné O. C.; Hawthorne, C. H. Empirical Lewis acid strengths for 135 cations bonded to oxygen. *Acta Cryst.* **2017**, 956-961, B73. DOI: 10.1107/S2052520617010988

[33]. Huang, W.; Cao, T. Surface Chemistry and Catalytic Properties of Well-Defined Cu_2O Nanocrystals. *Catalysis by Materials with Well-Defined Structures*; Wu, Z., Overbury, S. H., Eds.; Elsevier: Amsterdam, 2015; pp 1-30.

[34]. Mishra, A. K.; Roldan, A.; de Leeuw, N. H. CuO Surfaces and CO_2 Activation: A Dispersion-Corrected DFT+U Study. *J. Phys. Chem. C* **2016**, 120, 1298-2214. DOI: 10.1021/acs.jpcc.5b10431

[35]. Gattinoni, C.; Michaelides, A. Atomistic details of oxide surfaces and surface oxidation: the example of copper and its oxides. *Surf. Sci. Rep.* **2015**, 70, 424-447. DOI:

10.1016/j.surfrep.2015.07.001

[36]. Song, S.; Hong, W.-K.; Kwon, S.-S.; Lee, T. Passivation effects on ZnO nanowire field effect transistors under oxygen, ambient, and vacuum environments. *Appl. Phys. Lett.* **2008**, 92, 263109. DOI: 10.1063/1.2955512

[37]. Nishitani, S.; Sakata, T. Enhancement of Signal-to-Noise Ratio for Serotonin Detection with Well-Designed Nanofilter-Coated Potentiometric Electrochemical Biosensor. *ACS Appl. Mater. Interfaces* **2020**, 12, 14761-14769. DOI: 10.1021/acsami.9b19309

[38]. Li, Z.; Jia, M.; Abraham, B.; Blake, J. C.; Bodine, D.; Newberg, J. T.; Cundlach, L. Synthesis and Characterization of ZnO/CuO Vertically Aligned Hierarchical Tree-like Nanostructure. *Langmuir* **2018**, 34, 961-969. DOI: 10.1021/acs.langmuir.7b02840

[39]. Vuong, N. M.; Chinh, N. D.; Huy, B. T.; Lee, Y.-I. CuO-Decorated ZnO Hierarchical Nanostructures as Efficient and Established Sensing Materials for H_2S Gas Sensors. *Sci. Rep.* **2016**, 6, 26736. DOI: 10.1038/srep26736

[40]. He, Y.; Yanagida, T.; Nagashima, K.; Zhuge, F. W.; Meng, G.; Xu, B.; Klamchuen, A.; Rahong, S.; Kanai, M.; Li, X. M.; Suzuki, M.; Kai, S.; Kawai, T. Crystal-Plane Dependence of Critical Concentration for Nucleation on Hydrothermal ZnO Nanowires. *J. Phys. Chem. C* **2013**, 117, 1197-1203.

[41]. Sakai, D.; Nagashima, K.; Yoshida, H.; Kanai, M.; He, Y.; Zhang, G.; Zhao, X.; Takahashi, T.; Yasui, T.; Hosomi, T.; Uchida, Y.; Takeda, S.; Baba, Y.; Yanagida, T. Substantial Narrowing on the Width of "Concentration Window" of Hydrothermal ZnO Nanowires via Ammonia Addition. *Sci. Rep.* **2019**, 9, 14160. DOI: 10.1038/s41598-019-50641-y

[42]. Akihiro, Y.; Nagashima, K.; Hosomi, T.; Kanai, M.; Anzai, H.; Takahashi, T.; Zhang, G.; Yasui, T.; Baba, Y.; Yanagida, T. Water-Organic Cosolvent Effect on Nucleation of Solution-Synthesized ZnO Nanowires. *ACS Omega* **2019**, 4, 8299-8304. DOI: 10.1021/acsomega.9b00945

[43]. Zhao, X.; Nagashima, K.; Zhang, G.; Hosomi, T.; Yoshida, H.; Akihiro, Y.; Kanai, M.; Mizukami, W.; Zhu, Z.; Takahashi, T.; Suzuki, M.; Samransuksamer, B.; Meng, G.; Yasui, T.; Aoki, Y.; Baba, Y.; Yanagida, T. Synthesis of Monodispersedly Sized ZnO Nanowires from Randomly Sized Seeds. *Nano Lett.* **2020**, 20, 599-605. DOI: 10.1021/acs.nanolett.9b04367

[44]. Gaussian 16, Revision A.03, M. J. Frisch, G. W. Trucks, H. B. Schlegel, G. E. Scuseria, M. A. Robb, J. R. Cheeseman, G. Scalmani, V. Barone, G. A. Petersson, H. Nakatsuji, X. Li, M. Caricato, A. V. Marenich, J. Bloino, B. G. Janesko, R. Gomperts, B. Mennucci, H. P. Hratchian, J. V. Ortiz, A. F. Izmaylov, J. L. Sonnenberg, D. Williams-Young, F. Ding, F. Lipparini, F. Egidi, J. Goings, B. Peng, A. Petrone, T. Henderson, D. Ranasinghe, V. G. Zakrzewski, J. Gao, N. Rega, G. Zheng, W. Liang, M. Hada, M. Ehara, K. Toyota, R. Fukuda, J. Hasegawa, M. Ishida, T. Nakajima, Y. Honda, O. Kitao, H. Nakai, T. Vreven, K. Throssell, J. A. Montgomery, Jr., J. E. Peralta, F. Ogliaro, M. J. Bearpark, J. J. Heyd, E. N. Brothers, K. N. Kudin, V. N. Staroverov, T. A. Keith, R. Kobayashi, J.

Normand, K. Raghavachari, A. P. Rendell, J. C. Burant, S. S. Iyengar, J. Tomasi, M. Cossi, J. M. Millam, M. Klene, C. Adamo, R. Cammi, J. W. Ochterski, R. L. Martin, K. Morokuma, O. Farkas, J. B. Foresman, and D. J. Fox, Gaussian, Inc., Wallingford CT, 2016. https://gaussian.com/citation_a03/

3.2.7 Supporting information

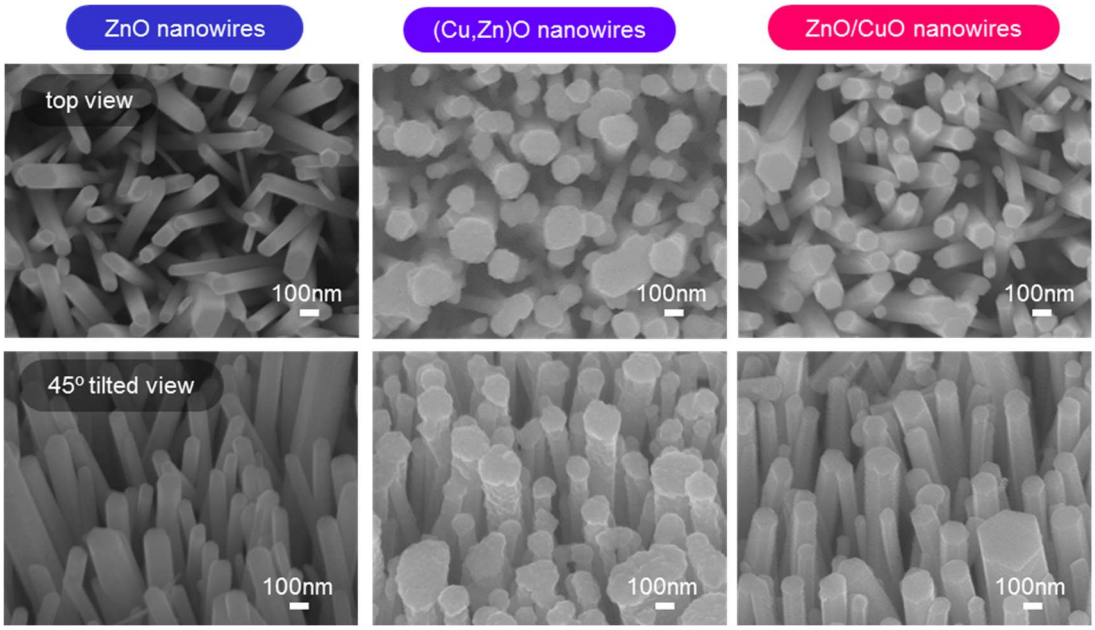

Figure S1. *Top view and 45° tilted SEM images of ZnO nanowires, (Cu,Zn)O nanowires and ZnO/CuO nanowires. CuO shell thickness is ca. 10 nm.*

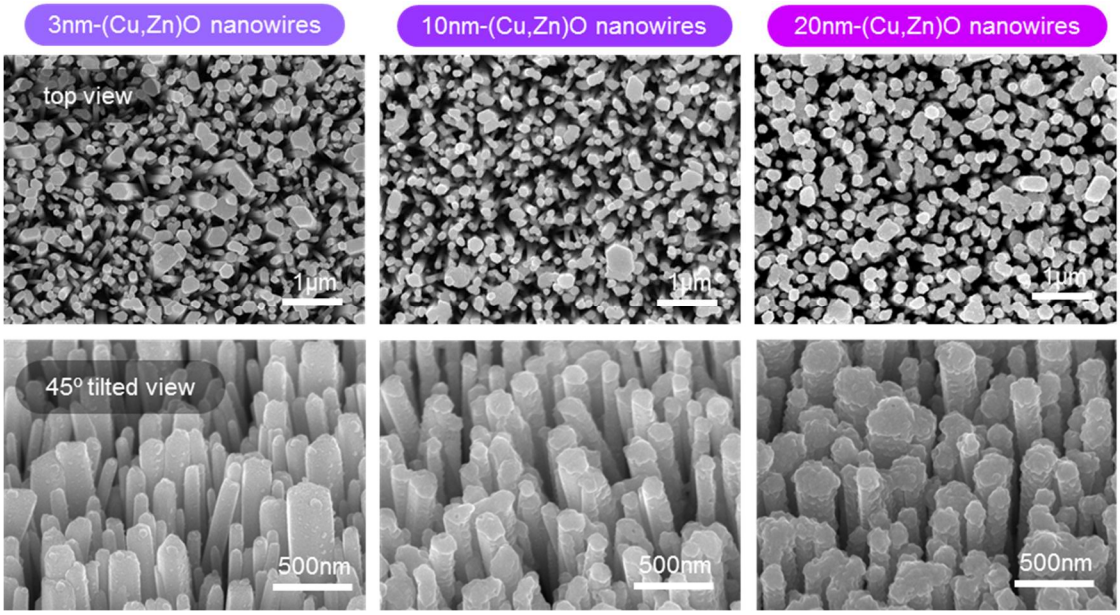

Figure S2. *Top view and 45° tilted SEM images of (Cu,Zn)O nanowires with various CuO shell thickness (3 nm, 10 nm, 20 nm).*

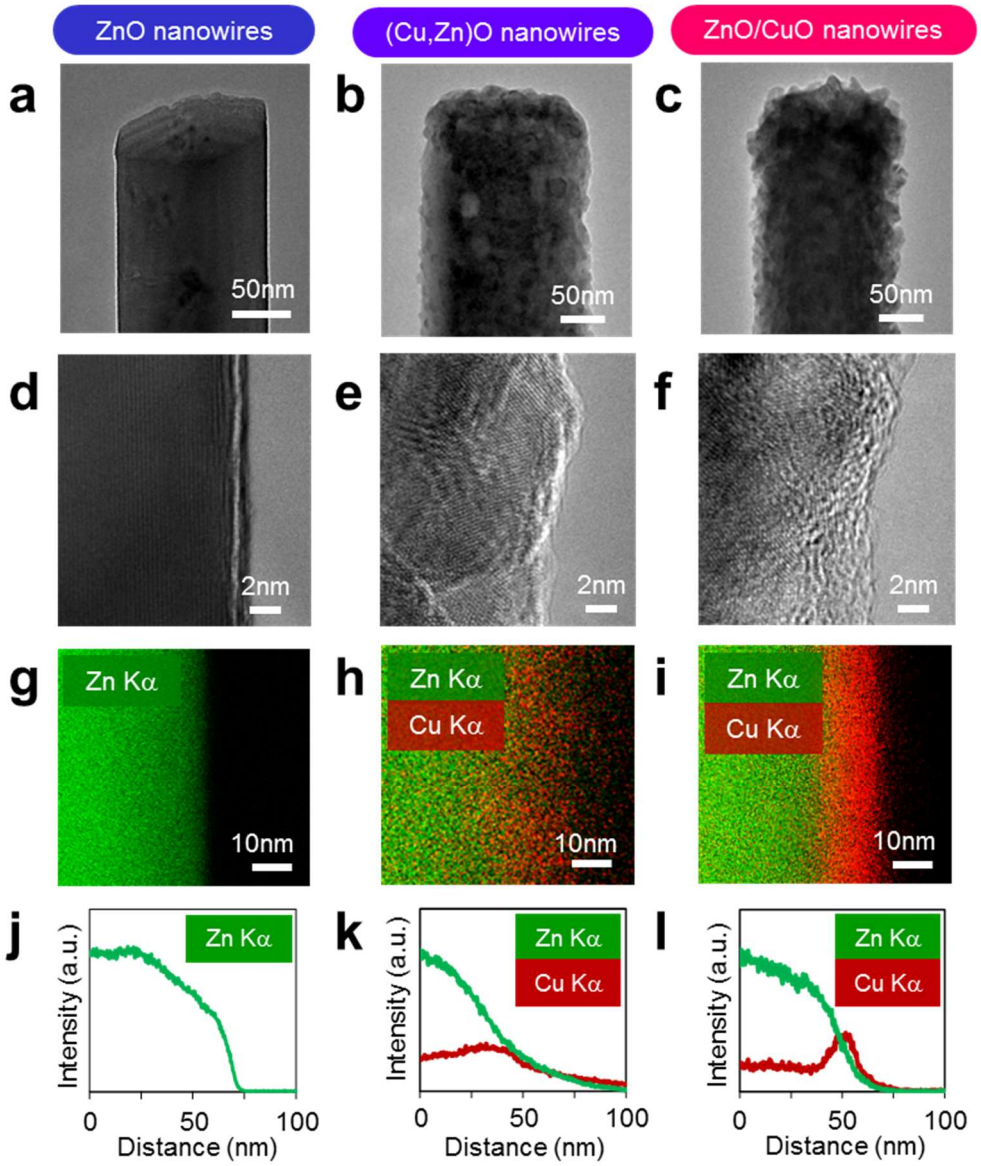

Figure S3. *(a-c) Low magnification and (d-f) high magnification TEM images, (g-i) EDS elemental mappings and (j-l) their line profiles of (a,d,g,j) ZnO nanowires, (b,e,h,k) (Cu,Zn)O nanowires and (c,f,i,l) ZnO/CuO nanowires, respectively.*

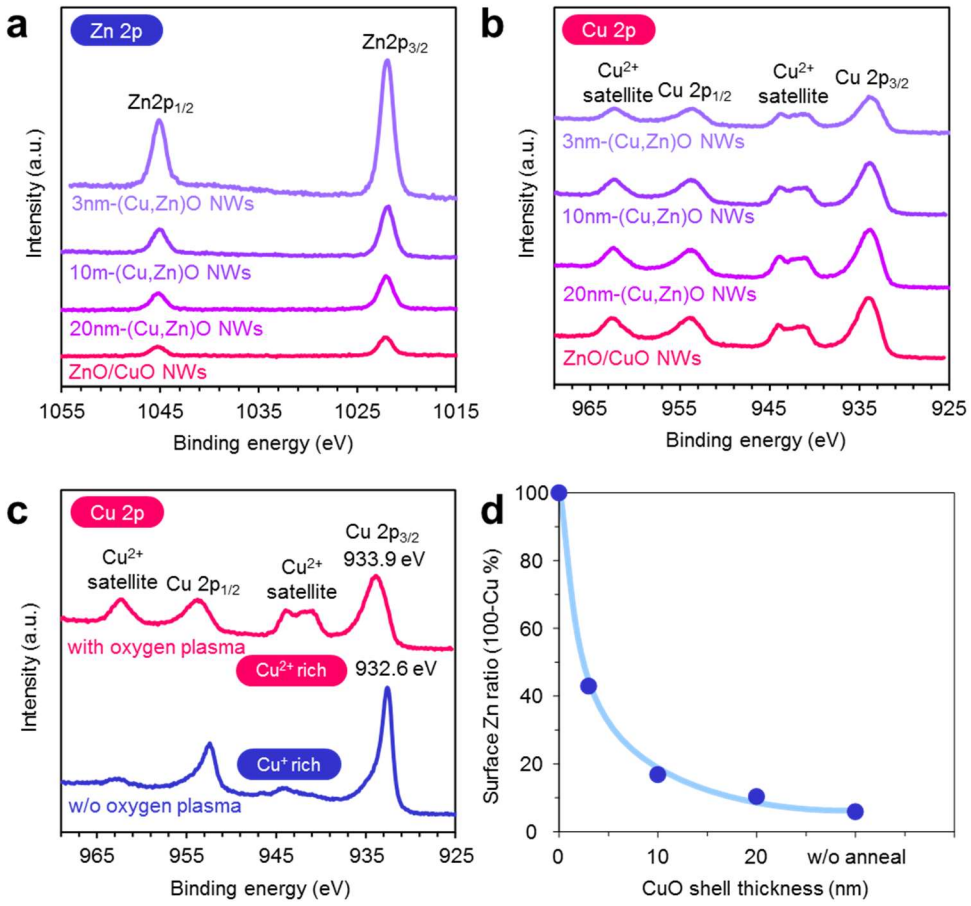

Figure S4. *(a) Zn 2p and (b) Cu 2p XPS spectra of (Cu,Zn)O nanowires and ZnO/CuO nanowires. For (Cu,Zn)O nanowires, CuO shell thickness is varied with 3-20 nm. For ZnO/CuO nanowires, oxygen plasma treatment is performed prior to measurement. (c) Cu 2p XPS spectra of ZnO/CuO nanowires before and after performing oxygen plasma treatment. (d) Surface Zn ratio as a function of CuO shell thickness.*

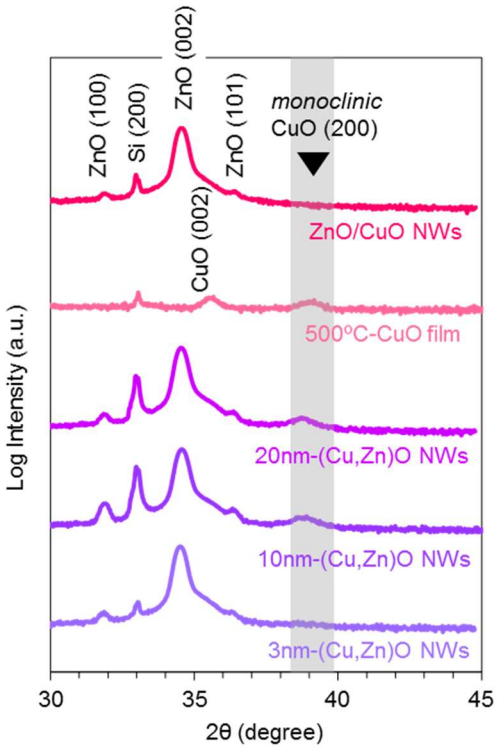

Figure S5. *XRD patterns of (Cu,Zn)O nanowires, CuO film and ZnO/CuO nanowires. For (Cu,Zn)O nanowires, CuO thickness is varied with 3-20 nm. CuO film with 200 nm thickness is annealed at 500 ºC for 1 h in air prior to measurement.*

Sample	2θ (degree)	*d* value (Å)
ZnO/CuO NWs	-	-
CuO film	39.167	2.299
20nm-(Cu,Zn)O NWs	38.807	2.319
10nm-(Cu,Zn)O NWs	38.757	2.322
3nm-(Cu,Zn)O NWs	-	-

Table I. *2θ values and d values of CuO (200) peaks.*

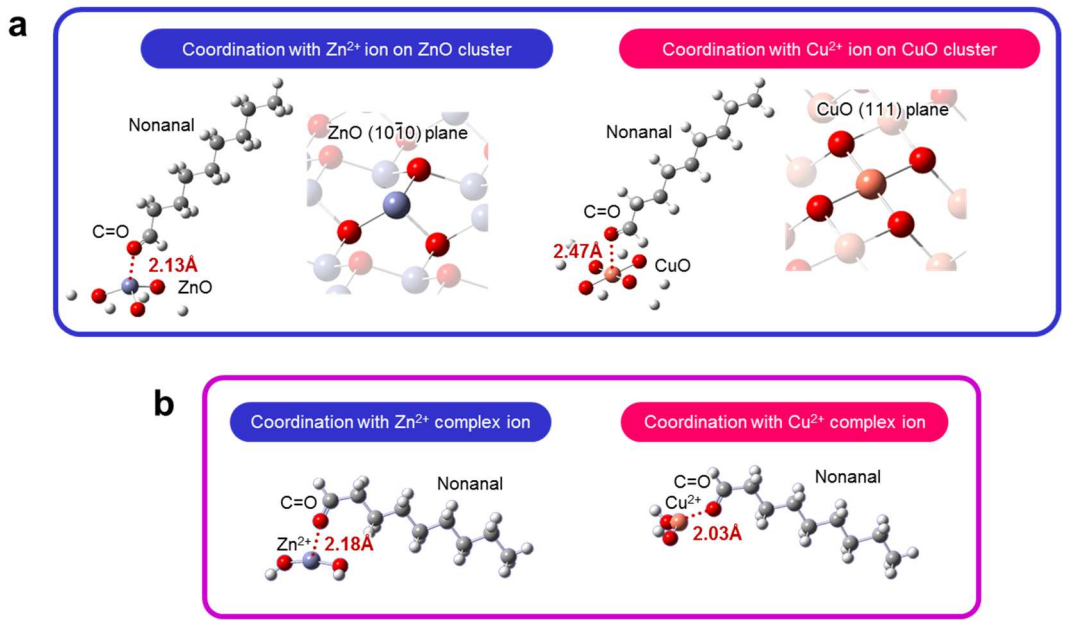

Figure S6. *Computed structures and calculated bond lengths of nonanal C=O—metal ions (Zn^{2+} and Cu^{2+}) using (a) cluster model and (b) complex ion model. For the cluster model, ZnO* (10$\bar{1}$0) *plane and CuO (111) plane are used as models in calculation.*

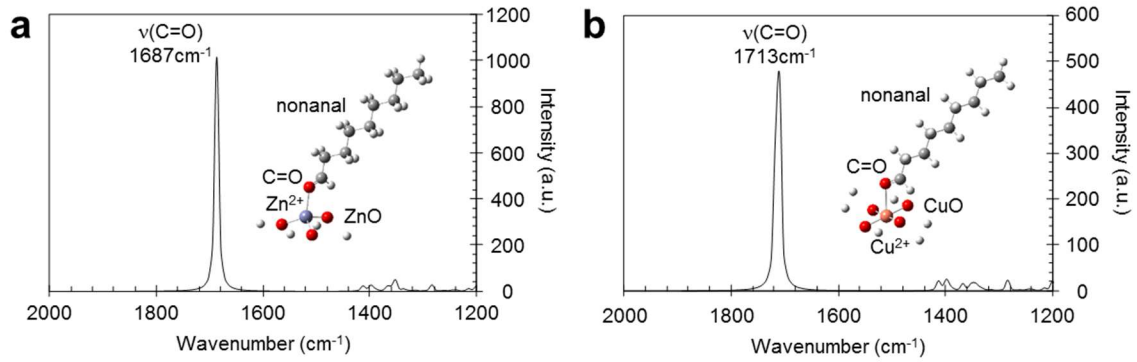

Figure S7. *Simulated infrared spectra for adsorbed nonanal on (a) ZnO* (10$\bar{1}$0) *and (b) CuO (111), respectively. The molecular geometries used to calculate these vibrational frequency calculations are summarized in the Table II.*

(a) C=O—ZnO $(10\bar{1}0)$ plane

element	x	y	z
O	5.733326	-1.03765	-0.3105
O	3.564471	1.016691	-1.62413
O	4.77038	1.636277	1.343851
Zn	4.193222	0.180518	0.095672
H	6.362091	-1.87434	1.407867
H	5.399155	0.79956	3.062199
H	3.74072	3.00653	-1.47025
H	4.703657	0.332624	-3.12459
O	2.320933	-0.75378	0.516432
C	1.384396	-0.61868	-0.2582
H	1.529191	0.003368	-1.17254
C	0.044175	-1.24137	-0.04674
C	-1.10277	-0.21623	-0.12478
H	0.050669	-1.78357	0.911475
H	-0.08471	-1.98686	-0.85617
C	-2.4859	-0.86124	0.004883
H	-0.97041	0.537038	0.671525
H	-1.03961	0.333732	-1.08094
C	-3.6373	0.14638	-0.05848
H	-2.61154	-1.61491	-0.79438
H	-2.53878	-1.4204	0.956727
H	-3.50705	0.899552	0.740443
H	-3.58024	0.706346	-1.01034
C	-5.02266	-0.4941	0.070228
C	-6.17694	0.510133	0.005097
H	-5.07835	-1.05318	1.022755
H	-5.15061	-1.24948	-0.72739
C	-7.56314	-0.12911	0.13419
H	-6.04872	1.266016	0.802425
H	-6.12106	1.069363	-0.94768
C	-8.71062	0.879596	0.067287
H	-7.68916	-0.88507	-0.66238
H	-7.61737	-0.68734	1.086672
H	-9.69047	0.385374	0.163525
H	-8.63491	1.627511	0.874449
H	-8.70751	1.427982	-0.88975

(b) C=O—CuO (111) plane

element	x	y	z
Cu	-4.00765	0.443732	-0.11721
O	-5.45393	-0.86967	-0.02243
O	-4.36306	1.322949	1.586082
O	-3.65279	-0.43615	-1.81849
O	-2.56155	1.757221	-0.20943
H	-4.172	0.112847	3.100572
H	-5.26287	-2.07977	1.492057
H	-3.84449	0.773723	-3.33224
H	-2.75324	2.967092	-1.72318
H	-2.91684	2.637454	1.492942
H	-5.09933	-1.74928	-1.72519
O	-2.15818	-0.94415	0.759274
C	-1.24089	-1.01979	-0.03343
H	-1.40667	-0.70294	-1.0902
C	0.13308	-1.51812	0.317603
C	1.228889	-0.49995	-0.04177
H	0.300765	-2.44813	-0.2596
H	0.151481	-1.77718	1.388164
C	2.644042	-1.00893	0.246797
H	1.14348	-0.2337	-1.11078
H	1.049747	0.435511	0.517037
C	3.741205	0.002676	-0.09694
H	2.721559	-1.28503	1.314486
H	2.81674	-1.94408	-0.31782
H	3.660342	0.279648	-1.16453
H	3.56514	0.936803	0.468001
C	5.158648	-0.50224	0.188942
C	6.257482	0.507806	-0.15389
H	5.333533	-1.43706	-0.37574
H	5.238272	-0.77952	1.256668
C	7.675716	0.003778	0.131386
H	6.177796	0.785588	-1.22171
H	6.082948	1.442839	0.410856
C	8.767109	1.018001	-0.21369
H	7.753863	-0.27367	1.198542
H	7.84858	-0.93076	-0.43314
H	9.772057	0.622382	0.004138
H	8.740607	1.287583	-1.28298
H	8.644856	1.950487	0.362736

Table II. *Optimized molecular geometries used for vibrational frequency calculations.*

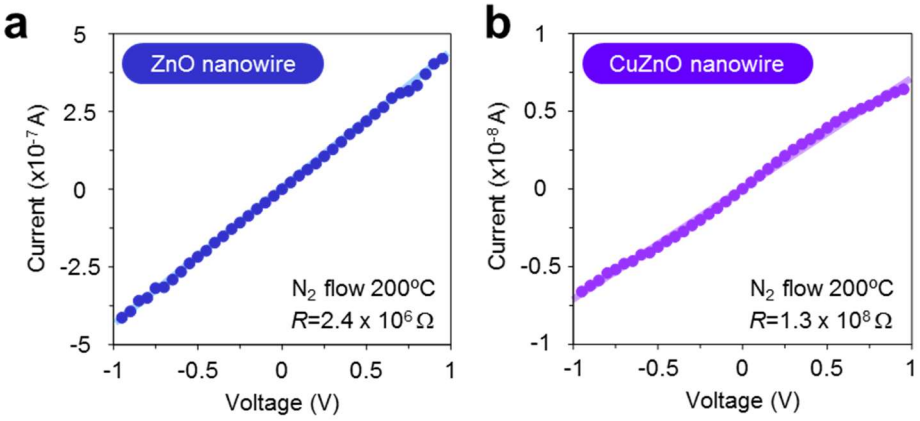

Figure S8. *Current-voltage (I-V) curves of single nanowire devices composed of (a) ZnO nanowire and (b) (Cu,Zn)O nanowire (CuO shell thickness: 10 nm), respectively. Measurements are performed at 200 ºC under N_2 flow.*

3.3 Facile synthesis of zinc titanate nanotubes via reaction-byproduct etching

3.3.1 ABSTRACT

A facile methodology to create zinc titanate nanotubes via reaction-byproduct etching is demonstrated. The chemical etching by the sol-gel reaction byproduct-hydrochloric acid (HCl) allows us to create the nanotube structure from the initial zinc oxide (ZnO)/titanium dioxide (TiO_2) core/shell nanowires. We found that TiO_2 shell layer plays the crucial roles on the nanotube formation as a support layer to maintain their structure during etching and as a permeable layer for HCl and Zn ions in their diffusion processes.

KEYWORDS: Zinc titanate nanotube, Chemical etching, Zn diffusion

3.3.2 INTRODUCTION

Inorganic nanotubes are interesting nanomaterials among various nanostructures. [1-2] This is because the nanotubes exhibit the inner confined nanospace, which is hardly attainable to other inorganic nanostructures including nanosheets, nanowires and nanoparticles. Carbon nanotube has been the most representative nanotube, since the discovery by Iijima. [3-4] Inspired by carbon nanotube, many inorganic nanotubes such as metal oxide nanotubes and group III-Nitride nanotubes have been numerously reported by various methods. [5-10] Recently, complex oxide nanotubes are emerging as new class of materials with unique functionalities. Thanks to their structural and material properties, various nanotube based applications including chemical sensors [11], molecular sieving [12], photo catalysis [13], energy storage [14-15] have been demonstrated using complex oxide nanotubes.

Major synthetic approaches for complex oxide nanotubes are categorized as follows: positive-template method using nanowires/nanofibers [16-17], negative-template method using anodic aluminum oxide (AAO) [18-19] and solid-phase diffusion with Kirkendall effect [20-21] and others [22]. For both positive- and negative-template methods, the template removal process by thermal calcination or chemical etching is necessary after the syntheses. The method using Kirkendall effect doesn't require the template removal process, however, it is applicable only to the material combination with good affinity and different diffusion coefficients. In fact, many metal oxide core/shell nanowires don't exhibit Kirkendall effect. [23-24] Therefore, complex oxide nanotubes still explore a versatile and facile synthetic approach.

Here we demonstrate a facile methodology to synthesize zinc titanate nanotubes via reaction-byproduct etching. Zinc titanates have been utilized in photocatalysis [25], microwave dielectrics [26], chemical sensor [27], Li-ion battery [28] and desulphurization [29]. In this study, surface sol-gel reaction on zinc oxide (ZnO)/titanium dioxide (TiO_2) core/shell nanowires is used for the nanotube formation. The chemical etching by the sol-gel reaction byproduct-hydrochloric acid (HCl) allows us to create the nanotube structure from the initial core/shell nanowires. We found the crucial role of TiO_2 shell layer on the nanotube formation, as a support layer to maintain their structure during etching and as a permeable layer for HCl and Zn ions in their diffusion processes. The proposed methodology allows us to form zinc titanate nanotubes at much lower temperature than the conventional solid-phase diffusion method.

3.3.3 EXPERIMENTAL

ZnO nanowire synthesis

ZnO nanowires were grown on a Si(100) substrate by a seed-assisted hydrothermal approach. First, 5 nm thick Ti adhesive layer and 100 nm thick ZnO seed layer were deposited on the substrate by radio frequency (RF) sputtering. Then the substrate was immersed in 100 ml aqueous solution containing 25 mM zinc nitrate hexahydrate $Zn(NO_3)_2 \cdot 6H_2O$, 25 mM hexamethylenetetramine $(CH_2)_6N_4$ (HMTA), 2.5 mM polyethyleneimine (PEI, number average m.w. 1800) in manner of upside-down. The hydrothermal process was conducted at 95 ºC for 24 h. After the growth, the samples were rinsed by water and dried by blowing nitrogen gas.

TiO_2 support layer deposition

For depositing the TiO_2 support layer, Ti film was deposited on the ZnO nanowires by RF sputtering (50 W, Ar 0.3 Pa) by controlling the thickness (3 nm, 10 nm). Then oxygen plasma treatment (150 W, O_2 1 Torr, 20 min) was performed to convert Ti to TiO_2.

Zinc titanate nanotube formation

Zinc titanate nanobutes were formed during the titania sol-gel process on ZnO/TiO_2 core-shell nanowires. For the sol preparation, 67µl titanium (IV) propoxide ($Ti(OBu)_4$) and 10µl titanium (IV) chloride ($TiCl_4$) were mixed and stirred in 970 µl 2-propanol at 60 ºC for 1 hr. All chemicals were analytical grade and utilized without further purification. The prepared sol was deposited on the ZnO/TiO_2 nanowires by spin-coating technique at 4000 rpm for 1 min, followed by annealing with at 400 ºC for 1 h in air. Finally, the zinc titanate nanotubes were obtained.

Characterization

The morphology and the composition of samples were characterized by using scanning electron microscopy (SEM, JEOL JSM-7610F) equipped with energy dispersive x-ray spectroscopy (EDS) and scanning transmission electron microscopy (STEM) mode at accelerating voltage of 15-30 kV. The crystal structure of samples was evaluated by transmission electron microscopy (TEM, JEOL ARM-200F) at accelerating voltage of 200 kV.

3.3.4 RESULTS AND DISCUSSION

The procedure of zinc titanate synthesis is schematically shown in Figure 1. First, ZnO nanowires are grown on a substrate via a seed-assisted hydrothermal synthesis. The growth mechanism and the strategies to control the morphology of hydrothermal ZnO nanowires are reported in our previous study. [30-33] A TiO_2 support layer is then deposited to maintain the free-standing nanowire structure during chemical etching. After that, titanium chloride ($TiCl_4$) contained sol, which byproduces HCl during the sol-gel process [34], is coated on the ZnO/TiO_2 core/shell nanowires. In the sol-gel process, the byproduct-HCl penetrates through TiO_2 support layer and reacts with the inner ZnO nanowires. Zn ions generated by the chemical etching of ZnO nanowires diffuse towards outside and are incorporated in titania layer during the sol-gel process. This leads to the formation of zinc titanate nanotubes.

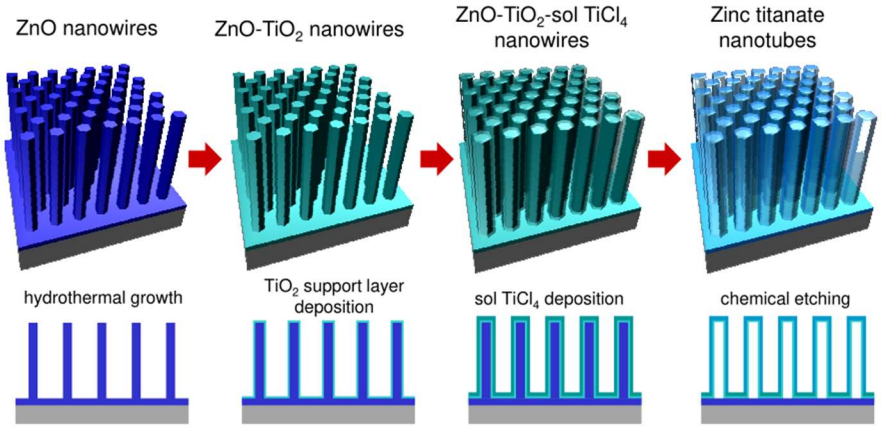

Figure 1. *Procedure of zinc titanate nanotube synthesis.*

Figure 2A, B show typical SEM images of the nanostructures synthesized by the procedure in Figure 1. For this sample, 3 nm thick support layer was utilized. The nanostructures are vertically grown on the substrate with free-standing shape. The diameter and the length of nanostructures are about 80-150 nm and 2.5-3 μm, respectively. Figure 2C, D show the SEM images of the nanostructures grown in the absence of TiO_2 support layer. The nanostructures are dissolved and collapsed by chemical etching, clearly showing the key role of TiO_2 support layer.

For more detailed structural analysis, Figure 3 shows TEM images and selected area diffraction (SAED) patterns of a nanostructure synthesized with 3 nm thick TiO_2 support layer. The hollow structure was observed at the top part of the nanostructure (Figure 3A, B), exhibiting

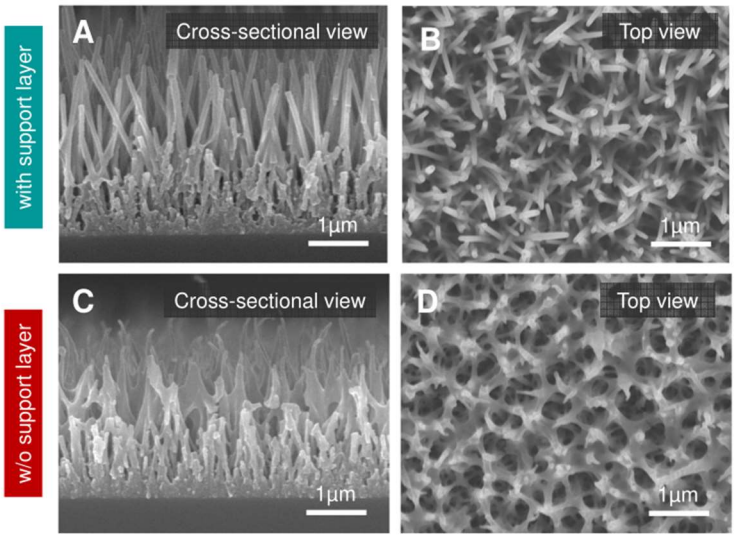

Figure 2. *(A) Cross-sectional view and (B) top view SEM images of samples fabricated with TiO_2 support layer. (C) Cross-sectional view and (D) top view SEM images of samples fabricated without TiO_2 support layer.*

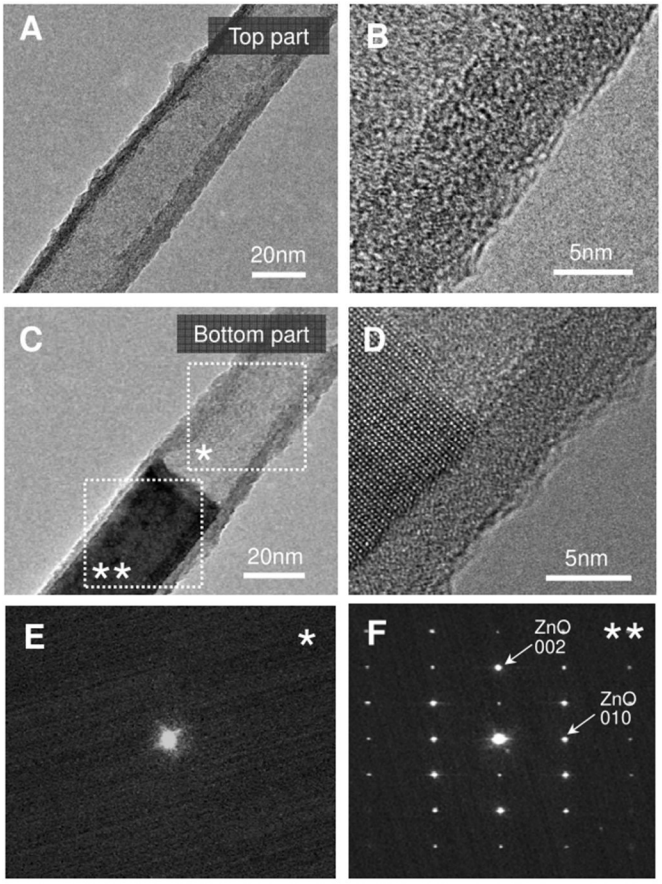

Figure 3. *(A) Low magnification and (B) high magnification TEM images of nanotube at top part. (C) Low magnification and (D) high magnification TEM images of nanotube at bottom part. (E,F) SAED pattern of (E) hollow part and (F) filled part in (C).*

the successful formation of nanotube structure. The thickness of the observed nanotube is about 5-10 nm. On the other hand, at the bottom part, the nanotube is partly filled with ZnO (Figure 3C, D, and Supporting Information Figure S1). The SAED patterns in Figure 3E, F identify that the nanotube and ZnO filled in the nanotube have amorphous structure and single crystalline nature, respectively. These results highlight that both the reaction byproduct-HCl and Zn ions generated by chemical etching diffuse through the TiO_2 support layer.

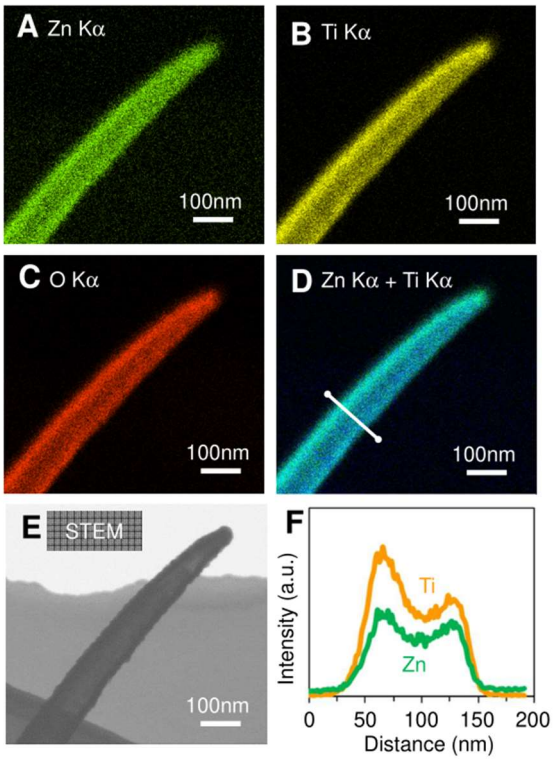

Figure 4*. (A-D) EDS mappings for (A) Zn Kα, (B) Ti Kα, (C) O Kα, (D) Zn Kα + Ti Kα, (E) bright-field STEM image and (F) EDS line profiles for a zinc titanate nanotube fabricated with 3 nm thick support layer. The line profiles are obtained from the area indicated in (D).*

The composition of the synthesized nanotubes was characterized by EDS as shown in Figure 4. Figure 4A-D show the EDS elemental mappings of Zn Kα, Ti Kα, O Kα, and overlaid Zn Kα + Ti Kα for the synthesized nanotube, respectively. The corresponding STEM image of nanotube is shown in Figure 4E. The nanotube is composed of Zn, Ti and O, and none of other elements were identified by EDS analysis. The Zn:Ti ratio of the nanotube is 43.5:56.5, indicating that the composition of the nanotube is in between $ZnTiO_3$ and $Zn_2Ti_3O_8$. [35] We found that all elements (Zn, Ti and O) are uniformly distributed in the nanotube without segregation. This is also confirmed by the line-profiles of Zn and Ti in Figure 4F. The profiles

of Zn and Ti show the similar trends i.e. weaker intensities at the inner part and stronger intensities at the outer shell part. This result highlights that Zn ions generated by chemical etching were diffused to the entire shell layer during the sol-gel process.

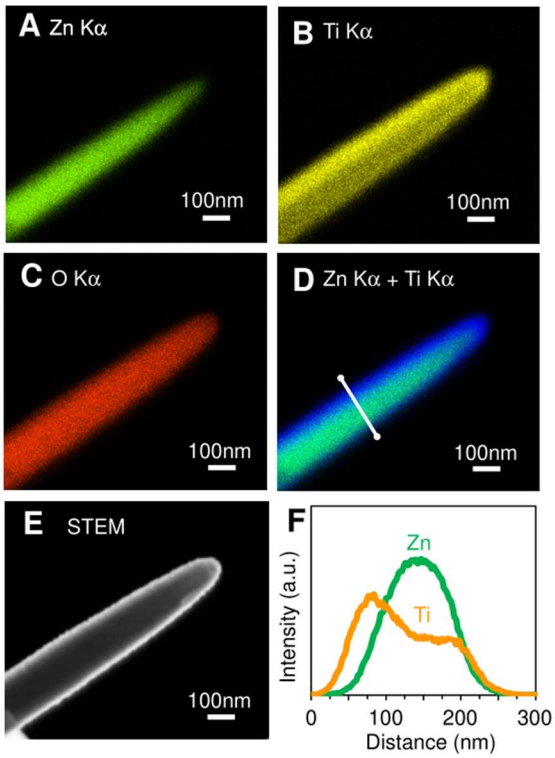

Figure 5. *(A-D) EDS mappings for (A) Zn Kα, (B) Ti Kα, (C) O Kα, (D) Zn Kα + Ti Kα, (E) dark-field STEM image and (F) EDS line profiles for a ZnO-titanate core-shell nanowire fabricated with 10 nm thick support layer. The line profiles are obtained from the area indicated in (D).*

Here we discuss the formation mechanism of zinc titanate nanotubes. The results imply that HCl passing thorough TiO_2 support layer react with ZnO nanowires. On the other hand, in our procedure, the thermal annealing treatment is performed at relatively high temperature condition of 400 ºC to conduct the sol-gel process and to fully desorb the residual contaminant molecules on the nanotube surface. Since previous report by Rashid *et al.* shows the occurrence of solid-phase atomic diffusion at ZnO/TiO_2 interface by thermal annealing treatment at 600 ºC, [36] one can consider that our zinc titanate nanotubes were formed by thermally driven atomic diffusion rather than the chemical etching based principle. To specify the nanotube formation mechanism, we examined the nanotube synthesis via increasing the TiO_2 support layer thickness. Figure 5A-D show the EDS elemental mappings of Zn Kα, Ti Kα, O Kα and overlaid Zn Kα + Ti Kα for the nanostructure obtained by employing 10 nm thick support layer, respectively. The corresponding STEM image of the nanostructure is shown in Figure 5E. Contrary to the result in Figure 4, the nanostructure has a filled nanowire form and Zn is mainly

located at the inner part, where it is different from the location of Ti. This trend is clearly seen in the line-profiles of Zn and Ti in Figure 5F. The results clearly evidence that the zinc titanate nanotubes were formed by chemical etching based atomic diffusion and also highlight the critical importance to control the thickness of TiO_2 support layer for the nanotube formation. Note that the chemical etching based atomic diffusion demonstrated here does not require high temperature for zinc titanate nanotube formation like a solid-phase diffusion (i.e. 700 ºC) [37], implying the zinc titanate nanotubes demonstrated here might be compatible to various device processes. In addition, the proposed approach allows us to design the various complex oxide nanotubes by alternating the combination of core and shell materials. These excellent features of proposed approach have a great potential to develop novel functional nanodevice applications based on metal oxide nanotubes.

3.3.5 CONCLUSION

In summary, we demonstrated a facile methodology to create zinc titanate nanotubes via reaction-byproduct etching. Surface sol-gel reaction on ZnO/TiO_2 core/shell nanowires was used for the nanotube formation. During the sol-gel reaction with $TiCl_4$-contained sol, byproduct-HCl was produced and etches ZnO nanowires. Zn atoms from the etched ZnO nanowires diffuse to outer layer and were incorporated in sol-gel titania, led to the formation of zinc titanate nanotubes. We found that TiO_2 shell layer plays the crucial roles on the nanotube formation as a support layer to maintain their structure during etching and as a permeable layer for HCl and Zn ions in their diffusion processes. Since this methodology doesn't require high temperature condition like a solid-phase diffusion process, the zinc titanate nanotubes demonstrated here might be compatible to various device processes.

3.3.6 REFERENCE

[1]. J. Goldberger, R. Fan, P. Yang, Acc. Chem. Res. **2006**, 39, 239.

[2]. M. Lee, T. W. Kim, C. Bae, H. Shin, J. Kim, JOM **2010**, 62, 44.

[3]. S. Iijima, Nature **1991**, 354, 56. 50

[4]. S. Iijima, T. Ichihashi, Nature **1993**, 363, 603. 51

[5]. R. Fan, R. Karnik, M. Yue, D. Li, A. Majumdar, P. Yang, Nano Lett. **2005**, 5, 1633.

[6]. Y. Li, X.-Y. Yang, Y. Feng, Z.-Y. Yuan, B.-L. Su, Crit. Rev. Solid State Mater. Sci. **2012**, 37, 1.

[7]. C. Bae, H. Yoo, S. Kim, K. Lee, J. Kim, M. M. Sung, H. Shin, Chem. Mater. **2008**, 20, 756.

[8]. D. Golberg, Y. Bando, Y. Huang, T. Terao, M. Mitome, C. Tang, C. Zhi, ACS Nano **2010**, 4, 2979

[9]. J. Goldberger, R. He, Y. Zhang, S. Lee, H. Yan, H.-J. Choi, P. Yang, Nature **2003**, 422, 599.

[10]. M. Noei, H. Soleymanabadi, A. A. Peyghan, Chem. Pap. **2017**, 71, 881.

[11]. G.-Y. Zhang, B. Guo, J. Chen, Sens. Actuators B **2006**, 114, 402.

[12]. M. S. Amara, E. Paineau, S. Rouzière, B. Guiose, M.-E. M. Krapf, O. Taché, P. Launois, A. Thill, Chem. Mater. **2015**, 27, 1488.

[13]. Y. Liu, L. Han, J. Zhang, R. Yao, H. Zhan, H. Yang, L. Bai, L. Yang, D. Wei, W. Wang, H. Chen, Ind. Eng. Chem. Res. **2020**, 59, 6488.

[14]. J. Meng, C. Niu, X. Liu, Z. Liu, H. Chen, X. Wang, J. Li, W. Chen, X. Guo, L. Mai, Nano Res. **2016**, 9, 2445.

[15]. C. Pan, Z. Liu, W. Li, Y. Zhuang, Q. Wang, S. Chen, J. Phys. Chem. C **2019**, 123, 25549.

[16]. C. Niu, J. Meng, X. Wang, C. Han, M. Yan, K. Zhao, X. Xu, W. Ren, Y. Zhao, L. Xu, Q. Zhang, D. Zhao, L. Mai, Nat. Commun. **2015**, 6, 7402.

[17]. H. Fan, M. Knez, R. Scholz, K. Nielsch, E. Pippel, D. Hesse, U. Gösele, M. Zacharias, Nanotechnology **2006**, 17, 5157.

[18]. M. D. Dickey, E. A. Weiss, E. J. Smythe, R. C. Chiechi, F. Capasso, C. M. Whitesides, ACS Nano **2008**, 2, 800.

[19]. C. Y. Li, B. Liu, J. P. Zhao, J. F. Wang, B. B. Hu, Z. L. Du, Chinese Sci. Bull. **2009**, 54, 719.

[20]. H. J. Fan, M. K. Roland Scholz, K. Nielsch, E. Pippel, D. Hesse, M. Zacharias, U. Gösele, Nat. Mater. **2006**, 5, 627.

[21]. A.-A. E. Mel, R. Nakamura, C. Bittencourt. Beilstein J. Nanotechnol. **2015**, 6, 1348.

[22]. G. R. Lima, W. F. Monteiro, B. O. Toledo, R. A. Ligabue, R. M. C. Santana, Macromol. Symp. **2019**, 383, 1800008.

[23]. K. Nagashima, T. Yanagida, H. Tanaka, S. Seki, A. Saeki, S. Tagawa, T. Kawai, J. Am. Chem. Soc. **2008**, 130, 5378.

[24]. A. Marcu, T. Yanagida, K. Nagashima, K. Oka, H. Tanaka, T. Kawai, Appl. Phys. Lett. **2008**, 92, 173119.

[25]. X. Yan, C.-L. Zhao, Y.-L. Zhou, Z.-J. Wu, J.-M. Yuan, W.-S. Li, Trans. Nonferrous Met. Soc. China **2015** 25, 2272.

[26]. C. F. Shih, W. M. Li, M. M. Lin, K. T. Hung, J. Electrochem. Soc. **2009**, 156, E13

[27]. B. C. Yadav, A. Yadav, S. Singh, K. Singh, Sens. Actuators B **2013**, 177, 605.

[28]. Z. Hong, M. Wei, Q. Deng, X. Ding, L. Jiang, K. Wei, Chem. Commun. **2010**, 46, 740. 100

[29]. S. Ozdemir, T. Bardakci, Sep. Purif. Technol. **1999**, 16, 225.

[30]. Y. He, T. Yanagida, K. Nagashima, F. W. Zhuge, G. Meng, B. Xu, A. Klamchuen, S. Rahong, M. Kanai, X. M. Li, M. Suzuki, S. Kai, T. Kawai, J. Phys. Chem. C **2013**, 117, 1197.

[31]. D. Sakai, K. Nagashima, H. Yoshida, M. Kanai, Y. He, G. Zhang, X. Zhao, T. Takahashi, T. Yasui, T. Hosomi, Y. Uchida, S. Takeda, Y. Baba, T. Yanagida, Sci. Rep. **2019**, 9, 14160.

[32]. Y. Akihiro, K. Nagashima, T. Hosomi, M. Kanai, H. Anzai, T. Takahashi, G. Zhang, T. Yasui, Y. Baba, T. Yanagida, ACS Omega **2019**, 4, 8299.

[33]. X. Zhao, K. Nagashima, G. Zhang, T. Hosomi, H. Yoshida, Y. Akihiro, M. Kanai, W. Mizukami, Z. Zhu, T. Takahashi, M. Suzuki, B. Samransuksamer, G. Meng, T. Yasui, Y. Aoki, Y. Baba, T. Yanagida, Nano Lett. **2020**, 20, 599.

[34]. E. Y. C. Yang, S. Zakaria, C. H. Chia, AIP Conf. Proc. **2014**, 1614, 122.

[35]. H. T. Kim, Y. Kim, M. Valant, D. Suvorov, J. Am. Ceram. Soc. **2001**, 84, 1081.

[36]. S. S. A. A. H. Rashid, Y. M. Sabri, A. E. Kandjani, C. J. Harrison, R. K. C. Balasubramanyam, E. D. Gaspera, M. R. Field, S. K. Bhargava, A. Triconli, W. Wlodarski, S. J. Ippolito, ACS Appl. Mater. Interfaces **2019**, 11, 29255.

[37]. S. Vempati, F. Kayaci-Senirmak, C. Ozgit-Akgun, N. Biyikli, T. Uyar, RSC Adv. **2015**, 5, 82977.

3.3.7 Supporting Information

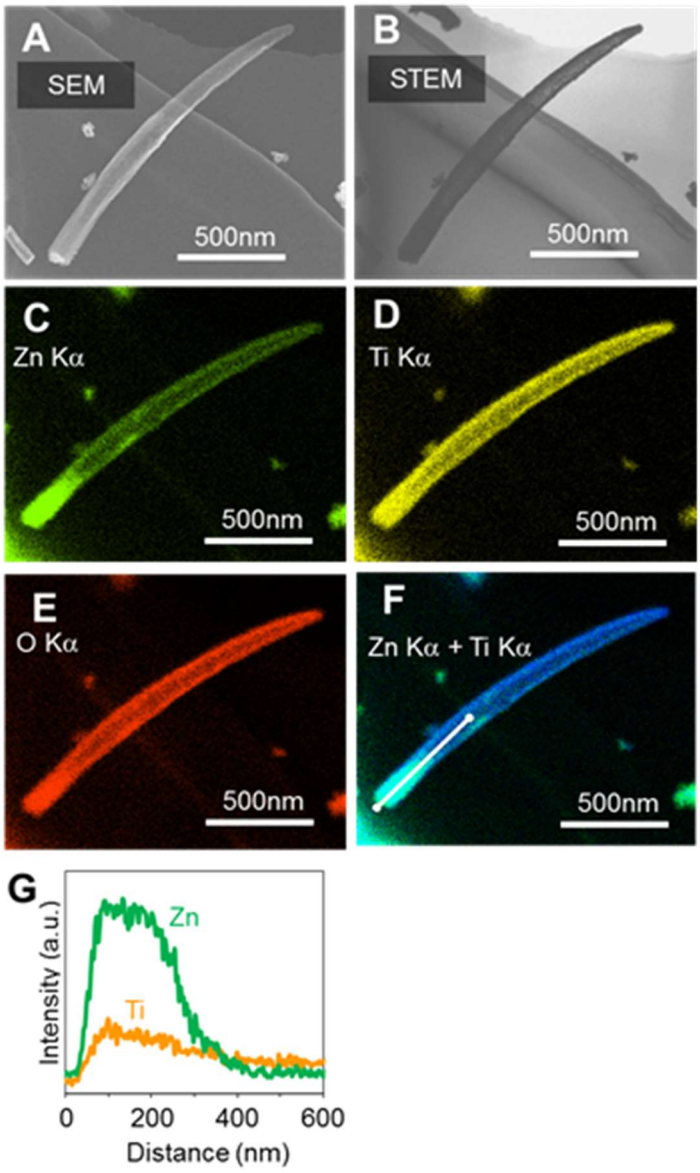

Figure S1. *(A) SEM image, (B) STEM image, (C-F) EDS mappings for (C) Zn K□, (D) Ti K□, (E) O K□, (F) Zn K□ + Ti K□ and (G) EDS line profiles for a ZnO-titanate core-shell nanowire fabricated with 3 nm thick support layer. The line profiles are obtained from the area indicated in (F).*

3.4 Design of Surface Acidity on Metal Oxide Nanowire by Acid Treatment Approach

3.4.1 ABSTRACT

Catalytic molecular sensing using solid nanostructures inherently requires two conflicting characteristics including a molecular reactivity and an ease of molecular desorption of products from a solid surface. Here, we demonstrate that a simple surface treatment using strong acids creates such two conflicting properties on WO_3 nanowire surfaces to enhance the electrical molecular sensing of aldehydes (nonanal). To reveal the underlying mechanism of surface treatments, we monitor the surface molecular transformation behaviors by performing mass-spectrometric and spectroscopic measurements. Mass-spectrometric measurements reveal that the surface treatment substantially promotes both the oxidization of nonanal and the desorption of products-nonanoic acid from the surfaces at lower temperatures. Spectroscopic and structural measurements combined with numerical simulations identify the two different adsorption structures of carbonyl groups on the surface, of which molecules directly bound to surface tungsten ions preferentially proceed to the catalytic oxidization reaction and subsequent desorption process. Thus, a monitoring of catalytic surfaces will support a better understanding of complex molecular transformations on various nanostructured metal-oxide surfaces to further tailor their sensor performances

KEY WORDS: WO_3 nanowire, surface treatment, molecular sensing, aldehyde, catalytic oxidation

3.4.2 INTRODUCTION

Electrical molecular sensing of various chemical species recently offers new scientific and industrial approaches to understand inherently complex systems (biological activity, chemical processing, human metabolism and others) via analyzing collected chemical big-data, which can be further combined with available existing data using physical sensors[1-7]. Among various molecular sensing methods, a molecular sensing utilizing catalysts is particularly promising for such electrical molecular sensing devices[8-12]. This is because such catalytic effects on solid surfaces exhibit the molecular transformations with the electron transfers, which enhance the molecular sensitivity and selectivity in recorded electrical signals[13-15]. Despite of such superior characteristics of catalytic molecular sensing, there are inherently two conflicting requirements to enhance the catalytic effects, which are a molecular reactivity and an ease of molecular desorption of products from a solid surface[16-21]. In terms of the molecular behavior, these two requirements are clearly conflicting. Because a molecular reactivity essentially requires to capture molecules on a solid surface, which is completely conflicting to a molecular desorption from a surface[22,23]. Thus, satisfying above two conflicting requirements is essential to design catalytic molecular sensing devices. For example, noble metal nanostructures, which are an important class of materials that used for the chemical bonds activation of the reactant molecules, are usually supported on the surface of solids to increase the surface reaction coefficient[24-26]. Besides, heterogeneous catalysts that constructed with different type of semiconductors also could enhance the molecular-solid reaction due to the built-in electric field in heterojunction interfaces can boost the charge exchange with the molecules and facilitate the charge transfer after reaction[27-30]. However, no matter for the noble metal or nonmetal surface coupling, a proper matching of electronic band structure among the heterogeneous catalysts generally required, otherwise it is difficult to realize the two conflicting requirement.

In this study, we show that a simple surface treatment using strong acids offers an effective route to satisfy two conflicting requirements on WO_3 nanowire surfaces for the catalytic molecule sensing of aldehydes (nonanal). Mass-spectrometric measurements show that the surface treatment substantially promotes both the oxidization and desorption of nonanal on WO_3 nanowire surfaces at lower temperatures. Spectroscopic and structural measurements combined with numerical simulations reveal the critical roles of surface molecular transformation pathways on the catalytic molecular sensing performances.

3.4.3 EXPERIMENTAL

Fabrication of WO_3 nanowire. *h*-WO_3 nanowires were fabricated by two steps which including the polytungstic acid sol synthesis and the nanowires growth.[31] For polytungstic acid (H_2WO_4) sol synthesis, first, 4 g of tungsten powder (W) was dissolved in 30 g of hydrogen peroxide solution (H_2O_2, 30 wt. % in H_2O) with an ice bath under stirring. After the W powder completely dissolved, a transparent solution was obtained. Then, Pt foil was immersed in the solution to catalytically remove the excess H_2O_2. As no bubble generated, the as-synthesized polytungstic acid sol were diluted by the distilled water to 100 g. Afterward, 50 g of polytungstic acid sol (10.88 mM) was transferred to a 100 mL capacity of autoclave. Then, 0.5625 g (6.25 mM) oxalic acid ($H_2C_2O_4$) were added to the mixture and NaOH solution (1 mol/L) was used to adjust the pH of the mixture solution to 1.68. Finally, sealed the Teflon-lined high-pressure autoclave and transferred to the sintering furnace and maintained at 200 ºC for 24 hours. Finally, WO_3 Nanowires were obtained after centrifugation of the products and washed by distilled water to remove the excess ions.

Acid and annealing treatment of WO_3 nanowire. Here, concentrated sulfuric acid (H_2SO_4) was utilized to dehydrate the *as-grown* WO_3 nanowire. The *as-grown* WO_3 nanowires were mixed with 50mL H_2SO_4 and stirred at 90ºC with different time (1, 2, 4, and 8 hours). Then, the samples were washed by distilled water for ten times to remove residual H_2SO_4. Annealing treatment was conducted at 400ºC in air for 1h.

Structure Characterization. Scanning electron microscopy (SEM) images were obtained using a JEOL JSM-7610F microscope. Transmission electron microscopy (TEM) images were acquired using a JEOL, JEM-ARM300F. X-ray diffraction (XRD) patterns were recorded with a Rigaku SmartLab diffractometer (Cu Kα, λ = 1.5406 Å, 45 kV, and 40 mA). Fourier transform infrared spectroscopy (FT-IR) spectra were measured using a Nicolet iS50 FT-IR spectrometer (Thermo Fisher Scientific) equipped with an MCT detector.

Desorbed gas analysis using Gas chromatography-mass Spectroscopy (GC-MS). A Shimadzu GCMS-QP 2010 Ultra instrument (equipped with a high polar InertCap FFAP capillary column and an OPTIC-4 inlet temperature control system) was used to analyze the desorbed compounds at each temperature. Firstly, as-grown and acid treatment WO_3 nanowires (The amount of nanowires were controlled at ~20 mg) were loaded on a silicon substrate with 0.2 cm × 2.0 cm and drying at 100 ºC for 1 hour to remove the liquid water. In the same time, nonanal liquid (4 µL) was dropped in a 25 mL closed bottle and kept for 30 min to vaporize the

nonanal gas. Then, the sample was placed in a bottle filled with nonanal gas for a fixed time (10 min.) and immediately transferred into the inlet port of the GC-MS instrument for further measurements. The inlet temperature was rapidly heated (60 ºC/s) to a given temperature (25-400 ºC with step of 25 °C) and maintained for 10 min, then immediately cooled to 25 °C. The desorbed gas at each temperature was analyzed by mass spectroscopy. The measurements for each temperature were conducted sequentially without removing the sample from the inlet port. The detailed temperature program is shown in Figure S5.

FT-IR monitoring of molecular adsorption progress. Firstly, as-grown and acid treatment WO_3 nanowires (The amount of nanowires were controlled at ~50 mg) were loaded on a silicon substrate with 2 cm × 2.0 cm and drying at 100 ºC for 1 hour to remove the liquid water. In the same time, nonanal liquid (20 μL) was dropped in a 100 mL closed bottle and kept for 30 min to vaporize the nonanal gas. Then, the sample was placed in a bottle filled with nonanal gas for a fixed time (10 min.) and immediately transferred into the FT-IR chamber for further measurements. The nonanal-adsorbed WO_3 nanowires were heated at a given temperature (25-400 ºC with step of 25 °C) for 10 min and cooled to room temperature. The FT-IR spectra of the nanowires were then recorded at room temperature on a Thermo Fisher Scientific Nicolet iS50 FT-IR spectrometer equipped with a MCT detector.

X-ray absorption spectroscopy. XANES and EXAFS analyses of W L_3-edge were performed in transmission mode at the BL 06 (Kyushu University beamline) of the SAGA-LS (Saga, Japan) with a storage ring operating at the energy of 1.4 GeV. A monochromator with two Si (111) crystals was used to scan the energy of the X-ray beam. The photon flux was 2×10^{10} photons/second. The intensities of the fluorescence X-rays were monitored by a silicon drift detector. Powder samples of the standard W, WO_2, and WO_3, and WO_3 nanowire samples were diluted with boron nitride to provide the optimum concentration and then pressed into a tablet with a diameter of 1 cm. The spectra of the prepared pellet samples were measured in the transmission mode. XANES data processing and *r*-space fitting of XAFS data were carried out by Athena and Artemis included in the Ifeffit package. Detailed fitting processes are shown in Supporting Information.

Fabrication of single nanowire device and molecular sensing measurement: Nanowire suspension was prepared by mixing the fabricated nanowire samples with 2-propanol with light sonication. Then, the dispersed nanowires were transferred on a 100 nm thickness of SiO_2 coated Si (100) substrate with pre-patterned contact Pt electrodes. Electron beam (EB) lithography (Elionix, ELS-S50YND) was performed at accelerating voltage of 50 kV to make

the electrode patterns for bridging a single nanowire with contact electrodes using ZEP520A-7 (ZEON) as a resist. A 800 nm layer of Pt was then deposited by RF sputtering (SEINAN) in an Ar 0.4 Pa atmosphere. Afterward, lift-off (*N*, *N*-dimethylformamide) and acetone cleaning processes were conducted to complete the device fabrication. The gap size of bridged nanowire was designed to be 1 μm and the nanowires with ca. 300-400 nm diameter were chosen for all fabricated device to eliminate the variation of electrical properties caused by the device geometry. The sensing performance to nonanal was carried out by a self-made chamber combined with the Keithley 4200A-SCS Parameter Analyzer (TEKTRONIX, INC.). Resistance of the WO_3 nanowire device under N_2 was recorded as baseline (R_{N2}). The resistance upon exposure of nonanal gas (produced by bubbling liquid nonanal solution) was noted as R_{gas}, and sensing response was defined as R_{N2}/ R_{gas}. The recovery time was defined as the time required for the recovery of the resistance to 90% of R_{N2} for the desorption process. All the sensing tests were carried out under a DC bias voltage of 1V. Nonanal gas was produced by bubbling liquid nonanal solution with high pure N_2, and its concentration was calibrated by the GCMS (Shimadzu GCMS-QP2010 Ultra) with temperature control system (GL Sciences, OPTIC-4). The flow rate of dry air and the nonanal gas were controlled at 200sccm during the sensing performance tests and the testing temperature was set to vary from 25 to 250 °C. The bubbling nonanal gas was diluted 400 times to ppb level for the sensing test. 10-15 devices were fabricated for each sample to obtain statistical data.

3.4.4 RESULT AND DISCUSSION

First, we show the effect of surface treatment using H_2SO_4 on the electrical response data of WO_3 nanowire sensor. Figure 1a and 1b show the schematic image and scanning microscope image (SEM) of fabricated sensor device composed of a single WO_3 nanowire and Pt electrodes. The transmission electron microscopy (TEM) and selected area electron diffraction (SAED) images of a WO_3 nanowire (Figure S1) show that the *as-grown* nanowire is hexagonal phase structure and sidewall surface is composed of well-defined (100) crystal planes. The open-top gap between electrodes was designed to be 1 μm. The details of sensor device fabrication processes can be seen in Method section. We performed a surface treatment for *as-grown* WO_3 nanowires using H_2SO_4 for 4 hours. Figure 1c and 1d show the comparison between 1) sensor device using *as-grown* WO_3 nanowire and 2) sensor device using H_2SO_4-surface treated WO_3 nanowire on the electrical response data when introducing a nonanal with 2.67 ppm. The

nonanal concentration dependent molecular sensing performances of WO_3 nanowire device are shown in Supporting Information (Figure S2). It is found that the acid treated WO_3 nanowire still present an excellent electrical response when the nonanal concentration diluted as low as 6.7 ppb. The operating temperatures was 200 ºC and temperature dependent (25 to 250 °C) molecular sensing results are shown in the Supporting Information (Figure S3). As can be seen, the surface treatment significantly enhances the sensor electrical response and recovery rate even at lower temperatures down to 25 ºC. To further confirm the effect of surface acid treatment, the surface treatment time dependence on the sensor properties (sensor response ratio and recovery time data) was examined, as shown in Figure 1e. Clearly, increasing the surface acid treatment time improves the sensor properties (*i.e.* increasing the sensor response and decreasing the sensor recovery time). Thus, the simple surface treatment using H_2SO_4 significantly alters the electrical response behaviors of WO_3 nanowire sensors.

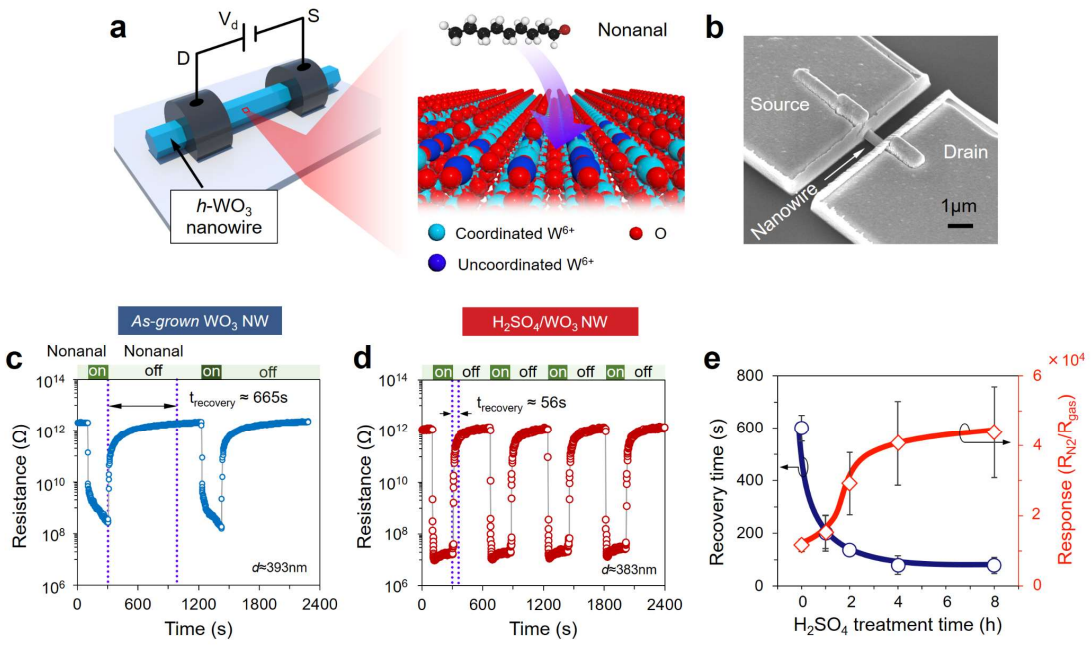

Figure 1. *Effect of acid treatment on the electrical sensing response and recovery rate of h-WO_3 single nanowire sensor. (a) and (b) Schematic illustrations and SEM images of single h-WO_3 nanowire sensor device. (c) and (d) are dynamic resistance response of the as-grown and H_2SO_4-surface treated h-WO_3 nanowire sensor devices to 2.67 ppm of nonanal under alternating flow of pure N_2 and nonanal bubbling gas at 200 °C. Recovery time is defined as the time required to obtain the 90% original resistance value after the sample was exposed to nonanal for 200 seconds and then exposed to pure N_2 flow. (e) Recovery time and sensing response of the WO_3 single nanowire device that varied with the H_2SO_4 treatment time at 200 °C. The dynamic resistance response curves are shown in Figure S4.*

Since the observed electrical response in Figure 1 is inherently determined by the surface chemical reaction events, we performed temperature-programmed desorption/gas chromatography mass spectrometry (TPD-GCMS) to analyze chemical composition of the desorbed gas from nonanal-adsorbed WO_3 nanowires. (Figure 2a, b). The temperature-dependent chromatograms show that not only nonanal (Figure S6) but also nonanoic acid (Figure S6) are contained in the desorbed gas, which elucidate the progress of nonanal oxidation on the WO_3 surface. Interestingly, there are several distinct differences in these oxidation and desorption behaviors between *as-grown* WO_3 nanowires and H_2SO_4-surface treated WO_3 nanowires. First, the temperature range which nonanoic acid detected in the chromatograms is much lower in the case of H_2SO_4-surface treated WO_3 nanowires (mainly at 25-75ºC), compared to *as-grown* WO_3 nanowires (mainly at 125-250ºC) (Figure 2c). Nonanal is almost fully converted into nonanoic acid below 50 °C on the H_2SO_4-surface treated WO_3 nanowires. It is contrast to the case of *as-grown* WO_3 nanowires, in which nonanal remain up to 250 °C (Figure 2d). These results highlight the superior oxidative activity of the surface treated WO_3 nanowires even at a low temperature. Second, at high temperature range (225-350 ºC), some carboxylic acids or olefins (Figure S7) with shorter alkyl chains are desorbed only from *as-grown* WO_3 nanowires. These compounds are considered to be formed by thermal decomposition of nonanoic acid, which remain adsorbed even in such a high temperature [31]. This result highlight that adsorption of the molecules is much stronger on the *as-grown* WO_3 nanowires than that of surface treated WO_3 nanowires. These identified trends of desorbed chemical species give an information as to surface chemical events related to the electrical sensor responses in Figure 1. *i.e.*, 1) the superior catalytic characteristics of surface treated WO_3 nanowires lowers the sensor operating temperatures, and 2) the residual compounds on *as-grown* WO_3 nanowire surface lengthen the recovery time even in the high temperature range.

Although above TPD-GCMS data identify the desorbed chemical compounds related to surface chemical reactions, they are not direct information of chemical events on sensor surfaces. For example, we cannot explain what kinds of molecular transformation pathways exist on the sensor surface, which are important to rationally design the sensor performance. Thus, we perform FT-IR spectroscopy measurements on the sensor surface to reveal more directly surface molecular structures. Figure 3a and b shows the comparison between *as-grown* WO_3 nanowires and H_2SO_4-surface treated WO_3 nanowires on the temperature dependent FT-IR spectra in the temperature range from 25 to 400ºC. Clearly, there are several distinct differences between the two spectra. First, the difference on two peaks (v_1 and v_2) in the

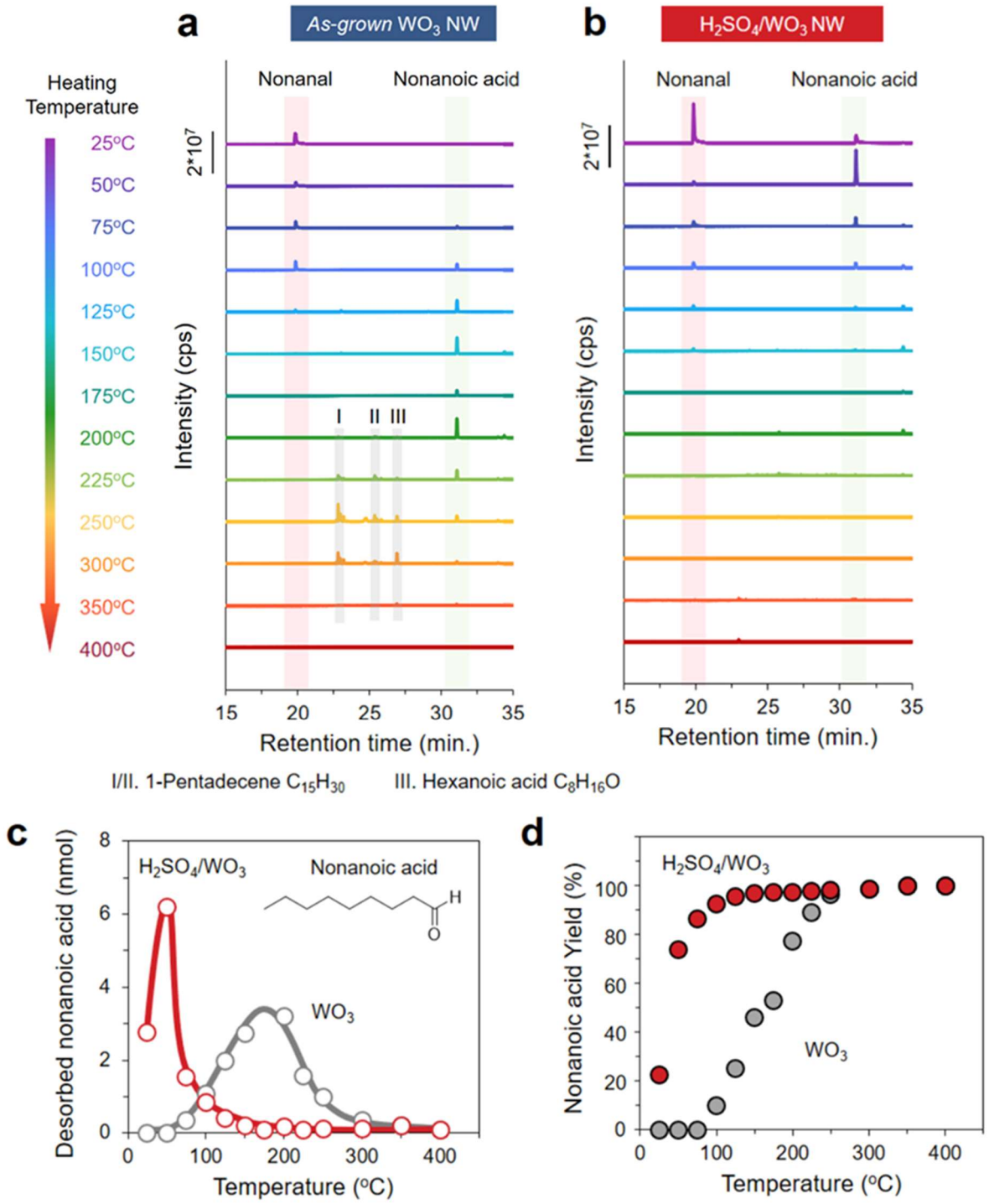

Figure 2. *TPD-GCMS analysis of chemical composition of the desorbed gas from nonanal-adsorbed WO_3 nanowires. (a) and (b) GC-MS spectra of desorbed gas from nonanal-adsorbed as-grown WO_3 nanowires and H_2SO_4-surface treated WO_3 nanowires upon heating from 25 - 400 °C. (c) Calculated concentration of desorbed nonanoic acid (nmol) from nonanal-adsorbed as-grown WO_3 nanowires and H_2SO_4-surface treated WO_3 nanowires. The nonanoic acid calibration curve is shown in Figure S8. (d) Comparison of desorbed nonanoic acid ratio between nonanal-adsorbed as-grown WO_3 nanowires and H_2SO_4-surface treated WO_3 nanowires.*

1660−1740 cm^{-1} region reveals two distinct adsorption states of carbonyl group, which depends on the surface acid treatment. The two peaks (ν_1-1710 cm^{-1} and ν_2-1668 cm^{-1}) are generally associated with the ν (C=O) vibration mode [32]. Compared to the FT-IR spectrum of liquid-phase nonanal (1726 cm^{-1}) [33], both ν (C=O) peaks (ν_1 (C=O) and ν_2 (C=O)) show distinct red shifts, implying decreases of C-O bond orders via Lewis acidic activation [33,34]. Consider the extent of the red shifts, the two ν (C=O) peaks are assigned to two different adsorption states of nonanal: ν_1 (C=O) is assigned to nonanal adsorbed via hydrogen bonding with a surface −OH, and ν_2 (C=O) to nonanal adsorbed by coordination to a surface W^{6+} (Figure 3c). The larger red-shift of the ν_2 (C=O) peak reflects the stronger Lewis acidity of W^{6+}, compared to that of −OH. As illustrated in Figure 3c, the present assignments of the ν_1 (C=O) and ν_2 (C=O) peaks are further supported by theoretical calculations based on density functional theory (DFT), and the peak wavenumbers are in good agreement with the theoretically calculated values. Based on these peak assignments, we discuss the effect of surface acid treatment on the ν_1 (C=O) and ν_2 (C=O) peaks. As can be seen in Figure 3a, at 25°C, *as-grown* WO_3 nanowires showed only ν_1(C=O) peak, whereas H_2SO_4-surface treated WO_3 nanowires exhibited mainly ν_2 (C=O) peak. This distinct difference can be reasonably interpreted in terms of above assignments of ν_1 (C=O) and ν_2 (C=O) peaks on the surface molecular structures. *i.e.* for H_2SO_4-surface treated WO_3 nanowires, the stronger Lewis acid cite (bare surface W ion) exists to show ν_2 (C=O) peak, whereas for *as-grown* WO_3 nanowires, OH terminated surface exists to exhibit ν_1(C=O) peak. Thus, these results highlight that the two distinct adsorption states of carbonyl group exist, which strongly depend on the history of surface acid treatment on WO_3 nanowires via the different surface adsorption cite.

Second, the broad peak in the 1550−1600 cm^{-1} region in Figure 3b, which appeared only for surface treated WO_3 nanowires, reveals the presence of carboxylate compounds on WO_3 nanowire surface [35,36]. Previous studies have reported that the broad peak in the 1550−1600 cm^{-1} region corresponds to an asymmetric stretching vibration mode: ν_{as} (COO) of carboxylate compounds, which strongly bound to solid surfaces [37,38]. This peak was not observable for *as-grown* WO_3 nanowires. In other words, such carboxylate compounds only exist on H_2SO_4 treated WO_3 nanowire surface. To further confirm the effect of H_2SO_4 treatment on the appearance of surface carboxylate compounds, we measured the temporal change of FT-IR spectra during H_2SO_4 treatment, as shown in Figure 3d. As can be seen, the peak intensity in the 1550−1600 cm^{-1} region tended to increase with the H_2SO_4 treatment time, revealing the significant effect of surface treatment on the appearance of surface carboxylate compounds.

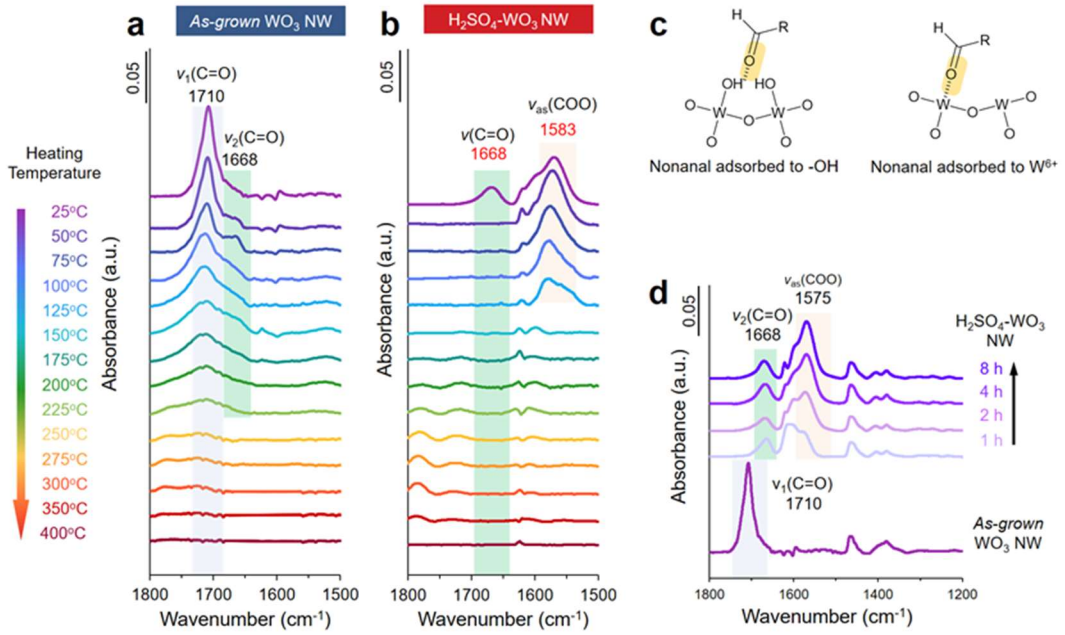

Figure 3. *FT-IR spectra of nonanal-adsorbed WO_3 nanowires after heating at various temperatures. (a) and (b) FT-IR spectra of nonanal adsorption on as-grown WO_3 nanowires and H_2SO_4-surface treated WO_3 nanowires upon heating from 25 - 400 °C. (c) Schematic structures of surface-adsorbed nonanal and corresponding DFT-calculated C=O frequencies (see the Supporting Information for details of the theoretical calculations). (d) FT-IR spectra of nonanal adsorption on WO_3 nanowires with different treatment time by H_2SO_4.*

In addition, the surface carboxylate compounds desorbed at relatively low temperatures below 125 ºC, which is consistent with the desorption profile of nonanoic acid for surface treated WO_3 nanowires in Figure 2c. On the other hand, ν_1 (C=O) peak for *as-grown* WO_3 nanowires remains at higher temperatures up to 225 ºC. These temperature dependences of carbonyl groups and carboxylate compounds on the spectroscopic data are in good agreement with TPD-GCMS data in Figure 2, revealing the detailed surface molecular transformation behaviors for the desorption process.

Above mass-spectrometric and spectroscopic results explain the effect of surface acid treatment on the sensing properties in terms of the surface molecular transformation phenomena on WO_3 sensor surface. However, we still cannot answer the following simple question, what are surface structures created by acid treatment, which improve the catalytic characteristics? To identify the mechanisms of catalytic surface structures, first we focus on the surface conditions before nonanal adsorption. Note that the spectroscopic data in Figure 3 do not contain any experimental trends as to water conditions on the sensor surface. This is because their spectra

are intentionally subtracted by a spectrum of sample before nonanal adsorption to exclude background moisture effects on the spectra. Figure 4a and 4b show the FT-IR spectra of *as-grown* WO_3 nanowires and H_2SO_4-surface treated WO_3 nanowires before nonanal adsorption. The annealing temperature effects on the spectra are also shown, since sensing experiments were performed at elevated temperatures up to 300°C. As can be clearly seen, there are distinct peaks of water, which are ranged at 3500-3700 cm^{-1}: a stretching mode of OH-ν_{OH}, and 1595-1650 cm^{-1}: a bending mode of OH- δ_{OH}. Clearly, increasing the annealing temperature decreases the amount of water, and the H_2SO_4 treatment further enhances the removal of a water from solid samples due to a strong hydration effect of SO_4^{2-} [39,40]. There is a difference of water content between *as-grown* WO_3 nanowires and H_2SO_4-surface treated WO_3 nanowires when introducing nonanal gas to sensor device. In addition, at elevated temperatures of sensing conditions, water related peaks almost disappeared for H_2SO_4-surface treated WO_3 nanowires, but not for *as-grown* WO_3 nanowires. In the 1595-1650 cm^{-1} region, there are two distinct peaks of *-OH*. The peak at 1595-1600 cm^{-1} is associated to *-OH* of WO_3, $2H_2O$, and the peak at 1620-1625 cm^{-1} can be assigned to *-OH_2* of WO_3, H_2O [41]. XRD measurements for these samples also show the presence of tungsten trioxide hydrates (WO_3, xH_2O) (Figure S9-S11) and the dehydration behaviors when annealing (Annealing treatment on the one hand would cause lattice water expelling, on the other hand, would cause phase transformation from hexagonal to monoclinic. Figure S12) and acid treatment were performed, as shown in Figure 4 c and d. Thus, results in Figure 4a-4d consistently indicate that H_2SO_4 surface treatment dehydrate WO_3 nanowires more than *as-grown* WO_3 nanowires at elevated temperature range of sensing conditions. This difference of water content in WO_3 nanowires should affect the absorption and desorption behaviors. First simple model to answer the questions 1) and 2) is based on the presence of surface water structures. This is because the presence of such surface water must hinder an interaction between a carbonyl group and a Lewis acid cite of surface W ion. As seen in the spectra of Figure 4, the thermal annealing alters the water content of WO_3 nanowires. Therefore, we can examine the effect of water content on the molecular transformation behaviors by using such annealed sample.

If the water content of WO_3 nanowires dominates surface molecular transformation behaviors of nonanal, the annealed WO_3 nanowires, which are dehydrated, should exhibit the catalytic and molecular behaviors similar to surface acid treated samples. Figure S shows the spectra of the nonanal adsorption on the annealed WO_3 nanowires. Contrary to above model

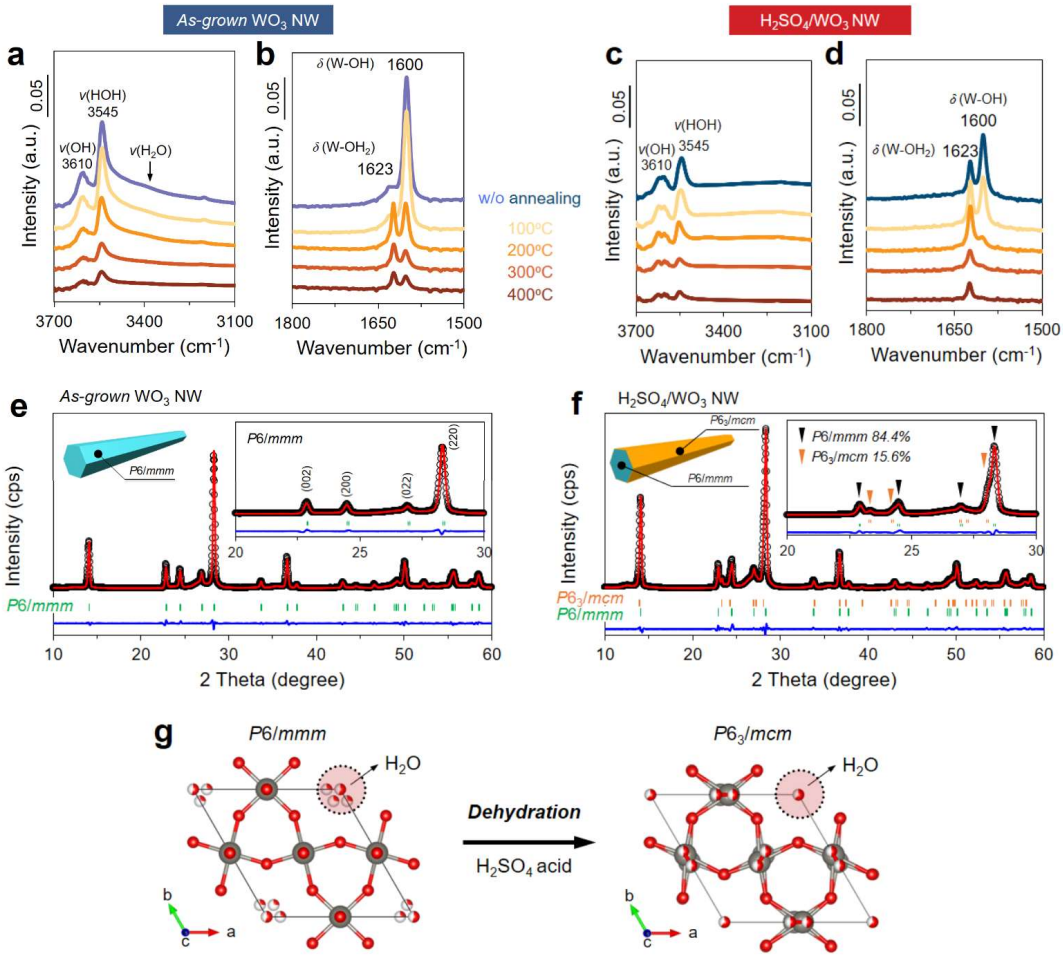

Figure 4. *Characterization of as-grown WO_3 nanowires and H_2SO_4-surface treated WO_3 nanowires before nonanal adsorption. (a) and (b) FT-IR spectra of as-grown WO_3 nanowires and H_2SO_4-surface treated WO_3 nanowires after thermally treated with different temperature. (c) and (d) X-ray diffraction (XRD) pattern and the Rietveld refinement of as-grown WO_3 hydrates and H_2SO_4-surface treated WO_3 nanowires. (g) the refined crystal structure unit of as-grown WO_3 hydrates and H_2SO_4-surface treated WO_3 hydrates, where the red sectors in water "dots" represent the probability of water's presence at the corresponding sites (other viewports are shown in Figure S10).*

prediction based on a surface water, the spectra are similar to that of *as-grown* WO_3 nanowires. Here, we consider an inherent difference between a surface acid treatment and a thermal annealing on a hydration process of WO_3 nanowires to clarify the mechanisms of surface acid treatment. Thermal annealing is performed to remove a water from a solid at elevated temperatures, whereas surface acid treatment chemically dehydrates solid WO_3 nanowires at relatively low temperatures by utilizing the strong hydration effect of SO_4^{2-} .[39,40] It is easily inferred that a high temperature operation of thermal annealing process creates a thermodynamically stable solid surface structure, while a low temperature operation of

chemical surface acid treatment might exhibit thermodynamically unstable solid surface structures, which is chemically active [42,43].

Extended X-ray absorption fine structure (EXAFS) analysis of a coordination structure of W ions can reveal such surface solid structure difference [44-46]. Figure 5a shows normalized W L_3-edge X-ray absorption near edge structure (XANES) of the WO_3 nanowire samples after H_2SO_4 surface treatment and thermal annealing treatment (400 °C). It is seen that the white line peaks of acid and thermal annealing treated WO_3 nanowire samples are consistent with the standard WO_3 (10218.5 eV), indicating oxidization states of W of the treated WO_3 nanowire samples have no change. This also supported by the XPS characterizations (Supporting Information, Figure S13). Further, the Fourier transform (FT) $k^3\chi(k)$ spectra of the WO_3 nanowire samples exhibit a dominant peak centered at 1.40 Å assignable to the W-O bond, and W-W bond peak centered at 3.60 Å (Figure 5b). In addition, the FT spectra of acid and thermal annealing treated WO_3 nanowire samples show that the W-W peaks undergo a downshift to 3.53 Å as compared to that of *as-grown* WO_3 nanowires, indicating that lattice contraction occurred due to the dehydration effect. Figure 5c shows the extracted coordination number of the first shell of W ion from the fitting of FT $k^3\chi(k)$ spectra. The analyzed coordination number of W ion tends to

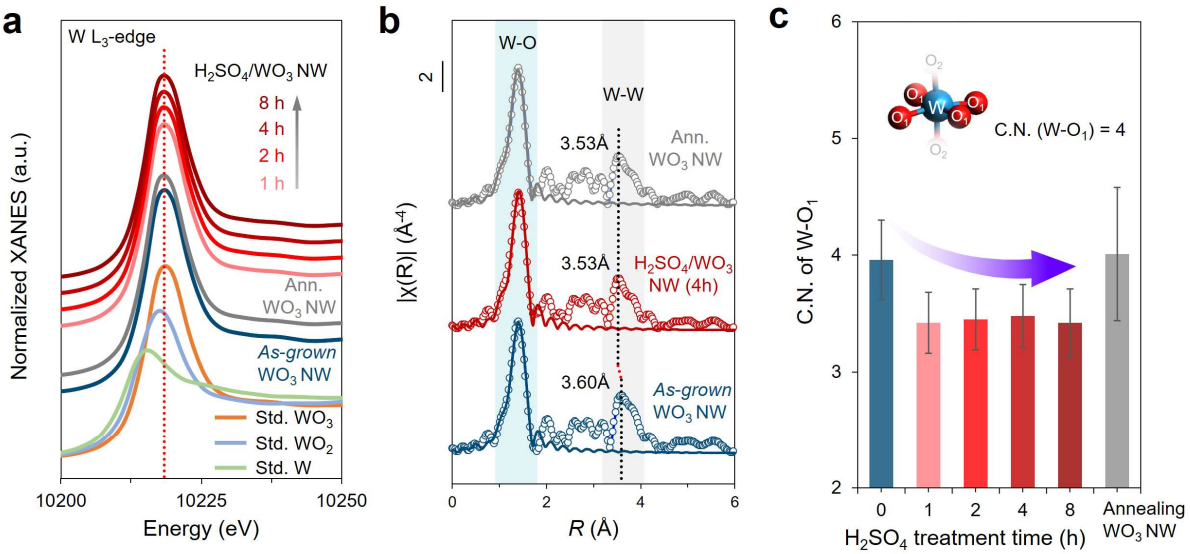

Figure 5. *XANES and EXAFS characterization of the WO_3 nanowires. (a) Normalized W L_3-edge XANES spectra of WO_3 nanowire samples and the standard W, WO_2 and WO_3 (Sigma Aldrich) as reference. (b) Fourier transformed k^3-weighted $\chi(k)$-function of the EXAFS spectra (circles) and first-shell fittings (line) of WO_3 nanowire samples. The detailed fitting processes are shown in the Supporting Information. (c) W coordination numbers (C.N.) of first shell extracted from Fourier transformed EXAFS curve fitting.*

decrease as the H_2SO_4-surface treatment time increases, while the annealing treatment has no effect on the coordination number of W. This result reveals the presence of coordination unsaturated W ions for H_2SO_4 surface treated WO_3 nanowires, but not for thermally annealed WO_3 nanowires. Thus, such surface structures created by surface acid treatment are responsible to provide the superior catalytic characteristics for nonanal.

3.4.5 CONCLUSION

In summary, we show that a simple surface treatment using strong acids creates such two conflicting properties on WO_3 nanowire surfaces to enhance the electrical molecular sensing of nonanal. To reveal the underlying mechanism of surface treatments, we monitor the surface molecular transformation behaviors by performing mass-spectrometric and spectroscopic measurements. Mass-spectrometric measurements reveal that the surface treatment substantially promotes both the oxidization of nonanal and the desorption of products-nonanoic acid from the surfaces at lower temperatures. Spectroscopic and structural measurements combined with numerical simulations identify the two different adsorption structures of carbonyl groups on the surface, of which molecules directly bound to surface tungsten ions preferentially proceed to the catalytic oxidization reaction and subsequent desorption process. Thus, a monitoring of catalytic surfaces will support a better understanding of complex molecular transformations on various nanostructured metal-oxide surfaces to further tailor their sensor performances.

3.4.6 REFERENCE

1. Shehada, N., Cancilla, J. C., Torrecilla, J. S., et al. Silicon nanowire sensors enable diagnosis of patients via exhaled breath. *ACS Nano* **10**, 7047-7057 (2016).
2. Lupan, O., Postica, V., Mecklenburg, M., et al. Low powered, tunable and ultra-light aerographite sensor for climate relevant gas monitoring. *J. Mater. Chem. A* **4**, 16723-16730 (2016).
3. Fahad, H. M., Shiraki H., Amani M., et al. Room temperature multiplexed gas sensing using chemical-sensitive 3.5-nm-thin silicon transistors. *Sci. Adv.* **3**, e1602557 (2017).
4. Iitani, K., Chien, P. J., Suzuki, T., et al. Fiber-optic bio-sniffer (biochemical gas sensor) using reverse reaction of alcohol dehydrogenase for exhaled acetaldehyde. *ACS Sens.* **3**, 425-431 (2018).
5. Arakawa, T., Suzuki, T., Tsujii, M., et al. Real-time monitoring of skin ethanol gas by a high-sensitivity gas phase biosensor (bio-sniffer) for the non-invasive evaluation of volatile blood compounds. *Biosens. Bioelectron.* **129**, 245-253 (2019).
6. Van den Broek, J., Abegg, S., Pratsinis, S. E., et al. Highly selective detection of methanol over ethanol by a handheld gas sensor. *Nat. Commun.* **10**, 4220 (2019).
7. Jian, Y., Hu, W., Zhao, Z., et al. Gas Sensors Based on Chemi-Resistive Hybrid Functional Nanomaterials. *Nanomicro. Lett.* **12**, 1-43 (2020).
8. Wetchakun, K., Samerjai, T., Tamaekong, N., et al. Semiconducting metal oxides as sensors for environmentally hazardous gases. *Sens. Actuator B-Chem.* **160**, 580-591 (2011).
9. Miller, D. R., Akbar, S. A., Morris, P. A. Nanoscale metal oxide-based heterojunctions for gas sensing: a review. *Sens. Actuator B-Chem.* **204**, 250-272 (2014).
10. Kim, H. J., Lee, J. H. Highly sensitive and selective gas sensors using *p*-type oxide semiconductors: Overview. *Sens. Actuator B-Chem.* **192**, 607-627 (2014).
11. Fu, Q., Bao, X. Surface chemistry and catalysis confined under two-dimensional materials. *Chem. Soc. Rev.* **46**, 1842-1874 (2017).
12. Dey, A. Semiconductor metal oxide gas sensors: A review. *Mater. Sci. Eng., B* **229**, 206-217 (2018).
13. Li, G. J., Zhang, X. H., Kawi, S. Relationships between sensitivity, catalytic activity, and surface areas of SnO_2 gas sensors. *Sens. Actuator B-Chem.* **60**, 64-70 (1999).
14. Cabot, A., Dieguez, A., Romano-Rodrıguez, A., et al. Influence of the catalytic introduction procedure on the nano-SnO_2 gas sensor performances: where and how stay the catalytic atoms? *Sens. Actuator B-Chem.* **79**, 98-106 (2001).
15. Kolmakov, A., Klenov, D. O., Lilach, Y., et al. Enhanced gas sensing by individual SnO_2 nanowires and nanobelts functionalized with Pd catalyst particles. *Nano Lett.* **5**, 667-673 (2015).
16. Korotcenkov, G. Metal oxides for solid-state gas sensors: What determines our choice? *Mater. Sci. Eng., B* **139**, 1-23 (2007).
17. Pan, J., Ganesan, R., Shen, H., et al. Plasma-modified SnO_2 nanowires for enhanced gas sensing. *J. Phys. Chem. C* **114**, 8245-8250 (2010).

18. Volanti, D. P., Felix, A. A., Orlandi, M. O., et al. The Role of Hierarchical Morphologies in the Superior Gas Sensing Performance of CuO-Based Chemiresistors. *Adv. Funct. Mater.* **23**, 1759-1766 (2013).
19. Kim, J. S., Yoo, H. W., Choi, H. O., et al. Tunable volatile organic compounds sensor by using thiolated ligand conjugation on MoS_2. *Nano Lett.* **14**, 5941-5947 (2014).
20. Long, H., Harley-Trochimczyk, A., Pham, T., et al. High surface area MoS_2/graphene hybrid aerogel for ultrasensitive NO_2 detection. *Adv. Funct. Mater.* **26**, 5158-5165 (2016).
21. Wang, X., Wang, Z., Zhang, J., et al. Realization of vertical metal semiconductor heterostructures via solution phase epitaxy. *Nat. Commun.* **9**, 3611 (2018).
22. Debecker D P, Delaigle R, Eloy P, et al. Abatement of model molecules for dioxin total oxidation on V_2O_5–WO_3/TiO_2 catalysts: The case of substituted oxygen-containing VOC. Journal of Molecular Catalysis A: Chemical, 2008, **289**: 38-43.
23. Hall R B. Pulsed-laser-induced desorption studies of the kinetics of surface reactions. Journal of Physical Chemistry, 1987, **91**: 1007-1015.
24. Cabot, A., Arbiol, J., Morante, J. R., et al. Analysis of the noble metal catalytic additives introduced by impregnation of as obtained SnO_2 sol–gel nanocrystals for gas sensors. *Sens. Actuator B-Chem.* **70**, 87-100 (2000).
25. Wang, X., Wang, W., Liu, Y. L. Enhanced acetone sensing performance of Au nanoparticles functionalized flower-like ZnO. *Sens. Actuator B-Chem.* **168**, 39-45 (2012).
26. Guo, J., Zhang, J., Gong, H., et al. Au nanoparticle-functionalized 3D SnO_2 microstructures for high performance gas sensor. *Sens. Actuator B-Chem.* **226**, 266-272 (2016).
27. Chen, W. Y., Jiang, X., Lai, S. N., et al. Nanohybrids of a MXene and transition metal dichalcogenide for selective detection of volatile organic compounds. *Nat. Commun.* **11**, 1302 (2020)
28. Park, S., Ko, H., Kim, S., et al. Role of the interfaces in multiple networked one-dimensional core–shell nanostructured gas sensors. *ACS Appl. Mater. Interfaces* **6**, 9595-9600 (2014).
29. Li, F., Gao, X., Wang, R., et al. Design of Core–Shell Heterostructure Nanofibers with different work function and their sensing properties to trimethylamine *ACS Appl. Mater. Interfaces* **8**, 19799-19806 (2016).
30. Han, Y., Huang, D., Ma, Y., et al. Design of hetero-nanostructures on MoS_2 nanosheets to boost NO_2 room-temperature sensing. *ACS Appl. Mater. Interfaces* **10**, 22640-22649 (2018).
31. Phuruangrat A, Ham D J, Hong S J, et al. Synthesis of hexagonal WO_3 nanowires by microwave-assisted hydrothermal method and their electrocatalytic activities for hydrogen evolution reaction. Journal of Materials Chemistry, 2010, **20**: 1683-1690.
32. Socrates, George. Infrared and Raman characteristic group frequencies: tables and charts. John Wiley & Sons, 2004.

33. Wang, C., Hosomi, T., Nagashima, K., et al. Rational method of monitoring molecular transformations on metal-oxide nanowire surfaces. *Nano Lett.* **19**, 2443-2449 (2019).
34. Raskó, J., Kiss, J. Adsorption and surface reactions of acetaldehyde on TiO_2, CeO_2 and Al_2O_3." *Appl. Catal. A* **287**, 252-260 (2005).
35. Patrono, P., La Ginestra, A., Ramis, G., et al. Conversion of 1-butene over WO_3-TiO_2 catalysts. *Appl. Catal. A* **107**, 249-266 (1994).
36. Staerz, A., Somacescu, S., Epifani, M., et al. WO_3 Based Gas Sensors: Identifying Inherent Qualities and Understanding the Sensing Mechanism. *ACS Sen.*, 2020.
37. Papageorgiou, S. K., Kouvelos, E. P., Favvas, E. P., et al. Metal–carboxylate interactions in metal–alginate complexes studied with FTIR spectroscopy. *Carbohydr. Res.* **345**, 469-473 (2010).
38. Bala, T., Prasad, B. L. V., Sastry, M., et al. Interaction of different metal ions with carboxylic acid group: a quantitative study. *J. Phys. Chem. A* **111**, 6183-6190 (2007).
39. JO'M, B., Gamboa-Aldeco, M., Szklarczyk, M. Ionic adsorption at the solid-solution interphase using three in situ methods. *J. Electroanal. Chem.* **339**, 355-400 (1992).
40. Wang, X. B., Sergeeva, A. P., Yang, J., et al. Photoelectron Spectroscopy of Cold Hydrated Sulfate Clusters, $SO_4^{2-}(H_2O)_n$ (n = 4-7): Temperature-Dependent Isomer Populations. *J. Phys. Chem. A* **113**, 5567-5576 (2009).
41. Daniel, M. F., Desbat, B., Lassegues, J. C., et al. Infrared and Raman study of WO_3 tungsten trioxides and $WO_3 \cdot xH_2O$ tungsten trioxide hydrates. *J. Solid State Chem.* **67**, 235-247 (1987).
42. Krüger, P., Koutiri, I., Bourgeois, S. First-principles study of hexagonal tungsten trioxide: Nature of lattice distortions and effect of potassium doping. *Phys. Rev. B* **86**, 224102 (2012).
43. Saha, D., Jensen, K. M. Ø., Tyrsted, C., et al. In Situ Total X-Ray Scattering Study of WO_3 Nanoparticle Formation under Hydrothermal Conditions. *Angew. Chem. Int. Ed.* **53**, 3667-3670 (2014).
44. Li, Y. H., Liu, P. F., Pan, L. F., et al. Local atomic structure modulations activate metal oxide as electrocatalyst for hydrogen evolution in acidic water. *Nat. Commun.*, **6**, 8064–8070 (2015).
45. Zhang, N., Li, X., Ye, H., et al. Oxide defect engineering enables to couple solar energy into oxygen activation. *J. Am. Chem. Soc.* **138**, 8928-8935 (2016).
46. Ren, Y., Zou, Y., Liu, Y., et al. Synthesis of orthogonally assembled 3D cross-stacked metal oxide semiconducting nanowires. *Nature Mater.* **19**, 203-211 (2020).

3.4.7 Supporting Information

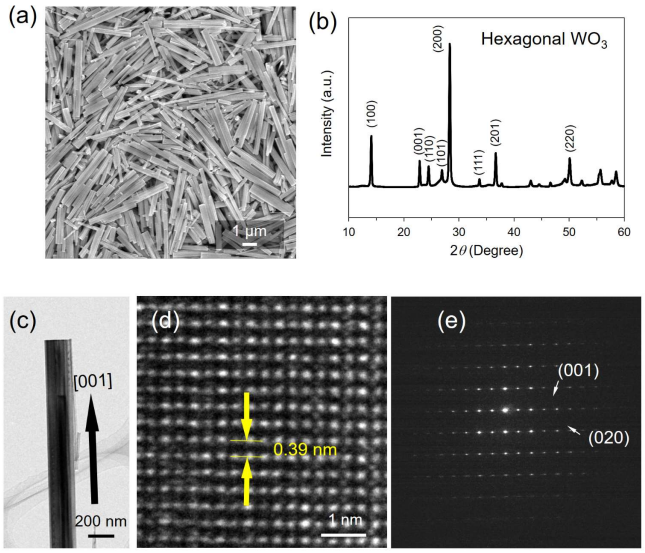

Figure S1. *(a) SEM image of as-grown WO_3 nanowire. (b) XRD pattern of as-grown WO_3 nanowire. (c) Low magnification TEM image of WO_3 nanowire. (d) High magnification TEM image of WO_3 nanowire and (e) selected area electron diffraction (SAED) pattern, indicating the [001] growth orientation.*

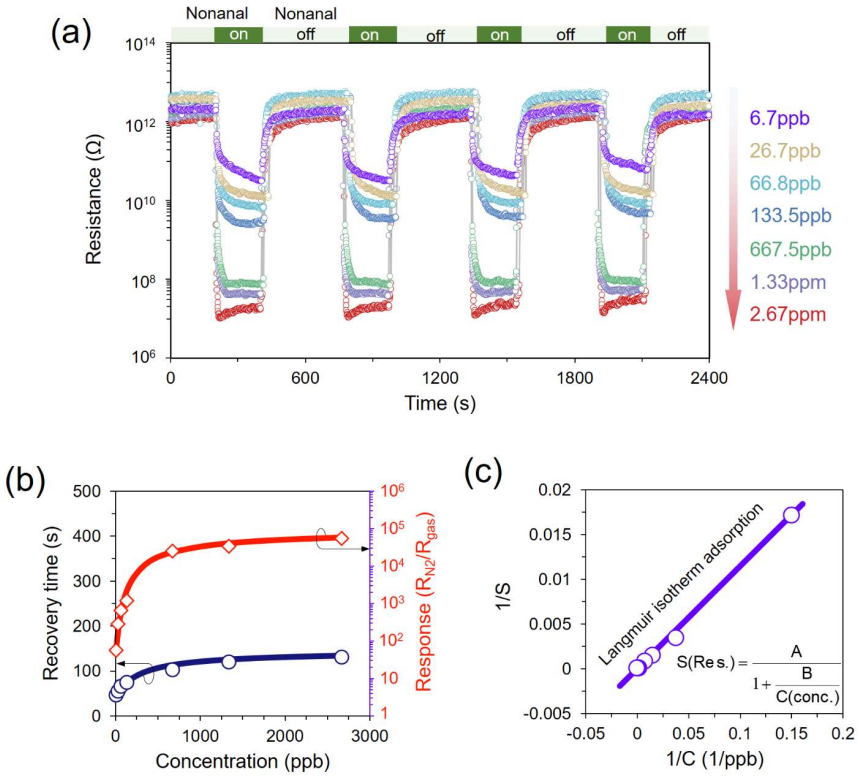

Figure S2. *(a) Dynamic resistance response of H_2SO_4-surface treated h-WO_3 nanowire sensor devices to various concentration (from 6.7 ppb to 2.67 ppm) of nonanal at 200 °C. (b) Sensing response and recovery time extracted from (a). (c) Fitting of 1/S (reciprocal of sensor response) vs. 1/C (reciprocal of nonanal concentration).*

The linear fitting of $1/S$ vs. $1/C$ has shown that the surface coverage of adsorbed molecules follows Langmuir isotherm.

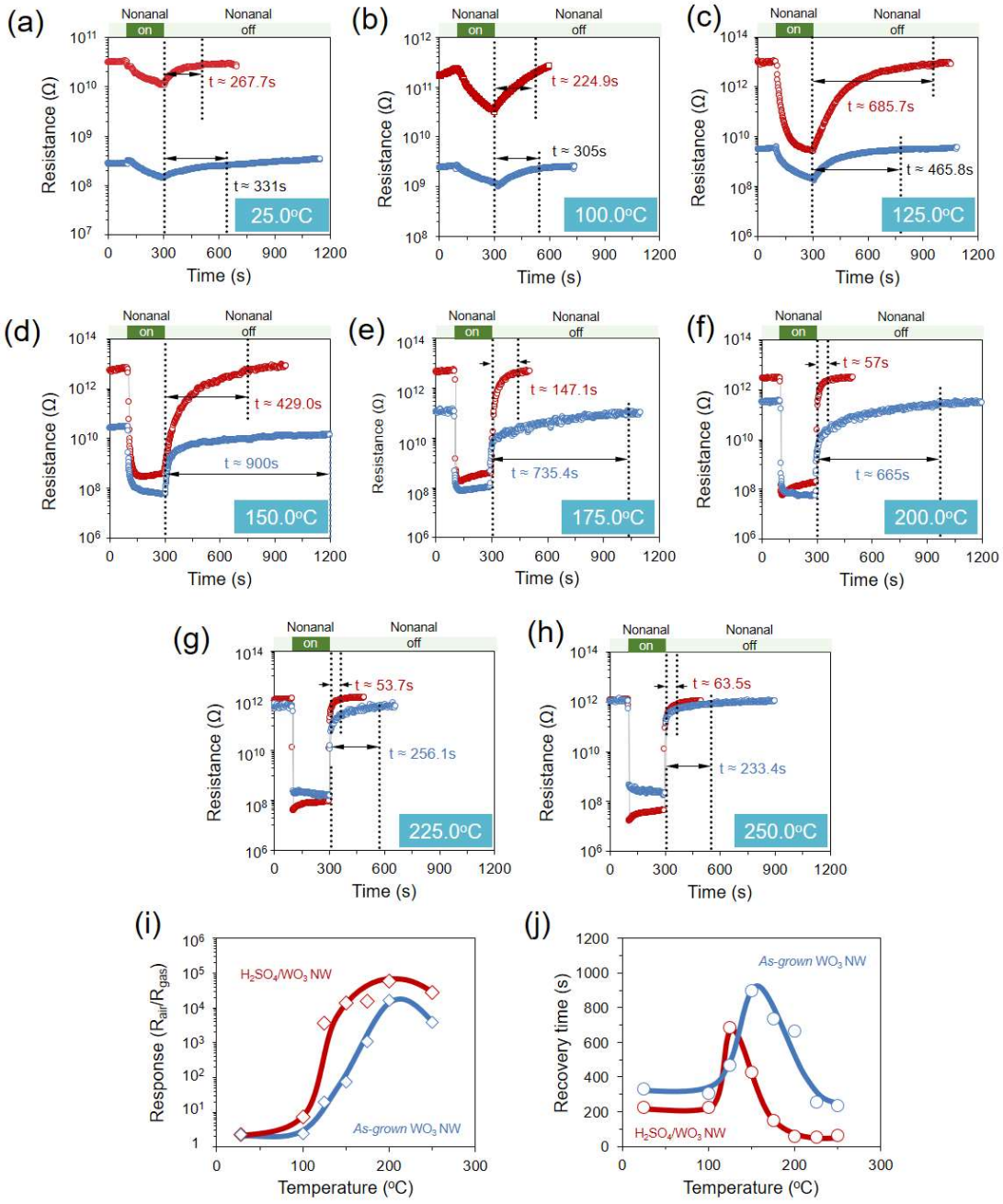

Figure S3. *(a) – (f) Dynamic resistance response of as-grown and H_2SO_4-surface treated h-WO_3 nanowire sensor devices working at different temperatures (25 – 250 °C) to 2.67 ppm nonanal. (b) Sensing response and (j) recovery time extracted from (a) to (f).*

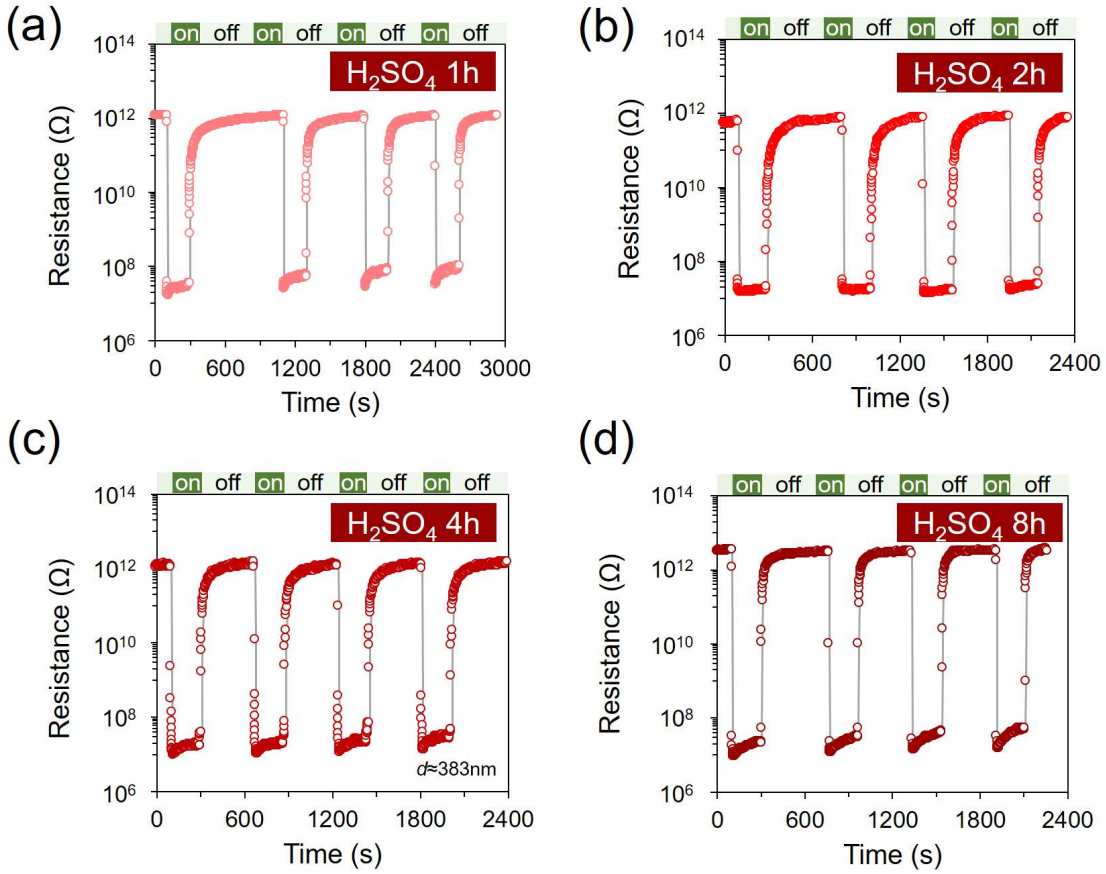

Figure S4. *(a) – (d) Dynamic resistance response of different time (1 – 8 h) treated h-WO_3 nanowire sensor devices to 2.67 ppm nonanal at 200 °C.*

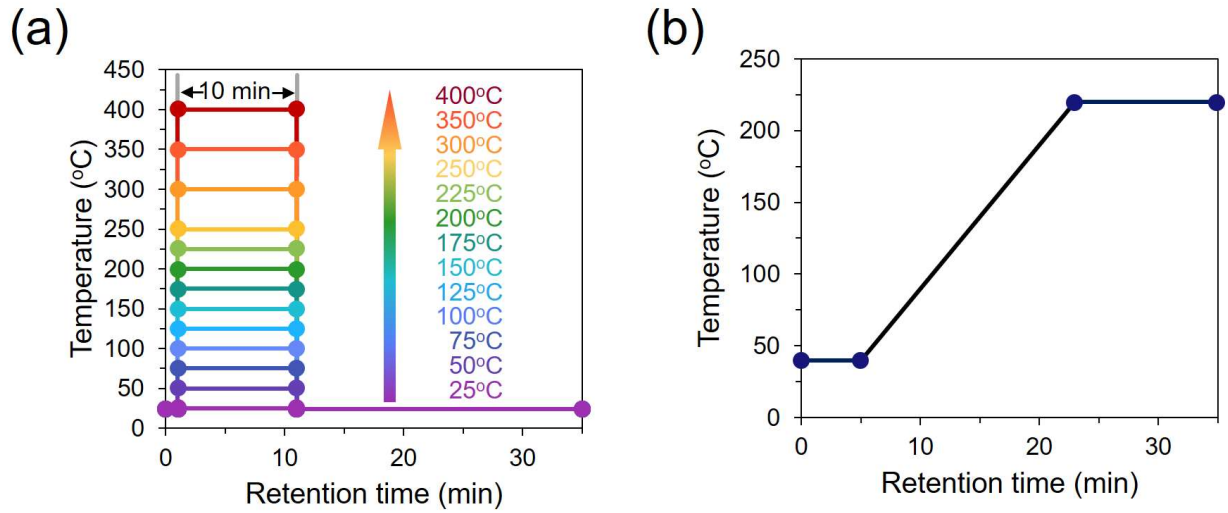

Figure S5. *The temperature program for desorbed gas analysis by GC-MS: (a) Inlet temperature; (b) Column temperature.*

The inlet temperature and column temperature were controlled with the program shown in Figure S5. The inlet temperature programs were sequentially executed for the condition of 25 °C, 50 °C, 75 °C, 100 °C, 125 °C, 150 °C, 175 °C, 200 °C, 225 °C, 250 °C, 275 °C, 300 °C, 350 °C and 400. The same column temperature program (Figure S5b) was used for each inlet-temperature condition.

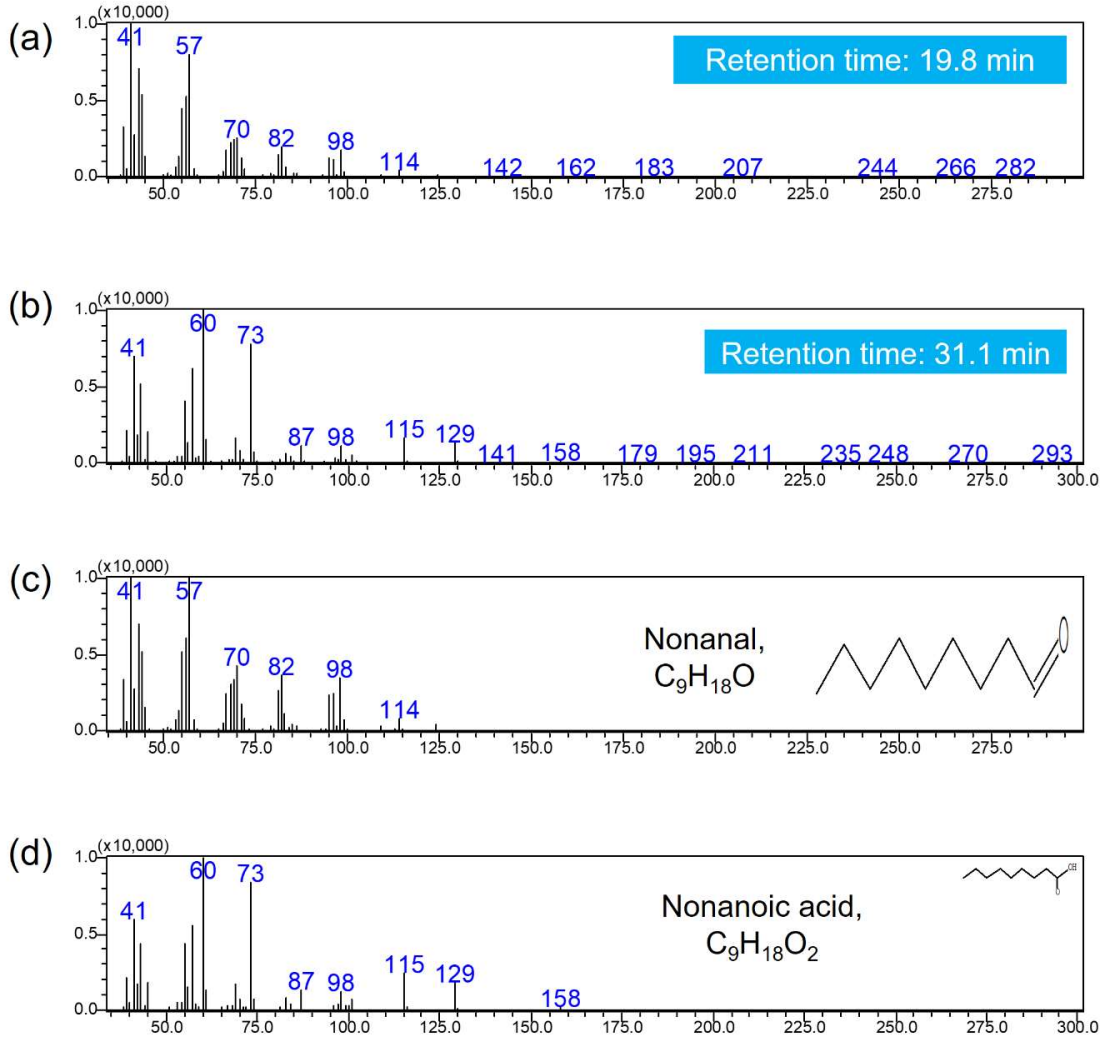

Figure S6 *The MS fragment pattern of the desorbed molecules from the nonanal-adsorbed WO_3 nanowire (as-grown and H_2SO_4-surface treated) at (a) retention time: 19.8 min and (b) retention time: 31.1 min. The library MS pattern of (c) nonanal and (d) nonanoic acid*

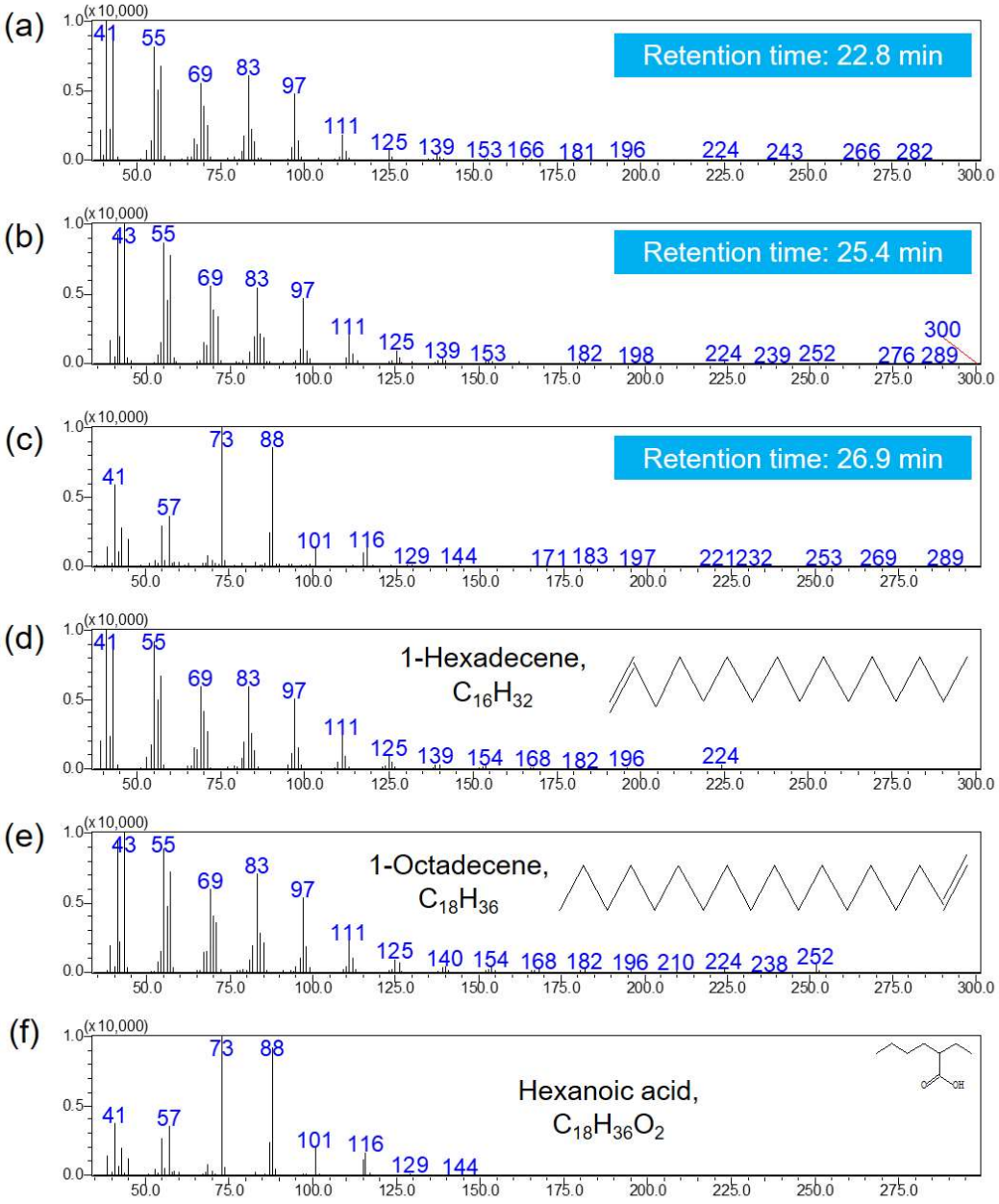

Figure S7*. The MS fragment pattern of the desorbed molecules from the nonanal-adsorbed WO_3 nanowire (as-grown) at (a) retention time: 22.8 min, (b) retention time: 25.4 min and (c) retention time: 26.9min above 200°C heating. The library MS pattern of (d) 1-Hexadecene, (e) 1-Octadecene and (f) Hexanoic acid.*

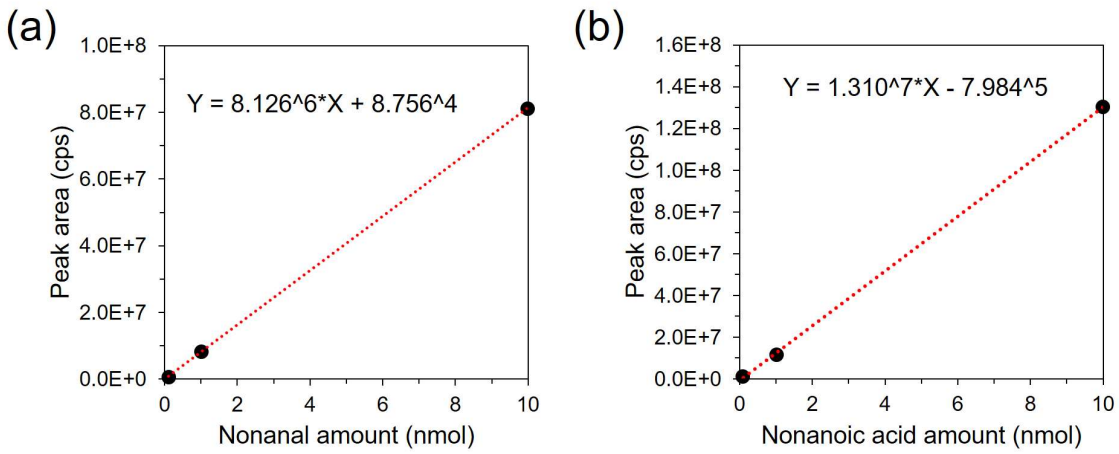

Figure S8. *(a) Nonanal and (b) nonanoic acid concentration calibration by GC-MS.*

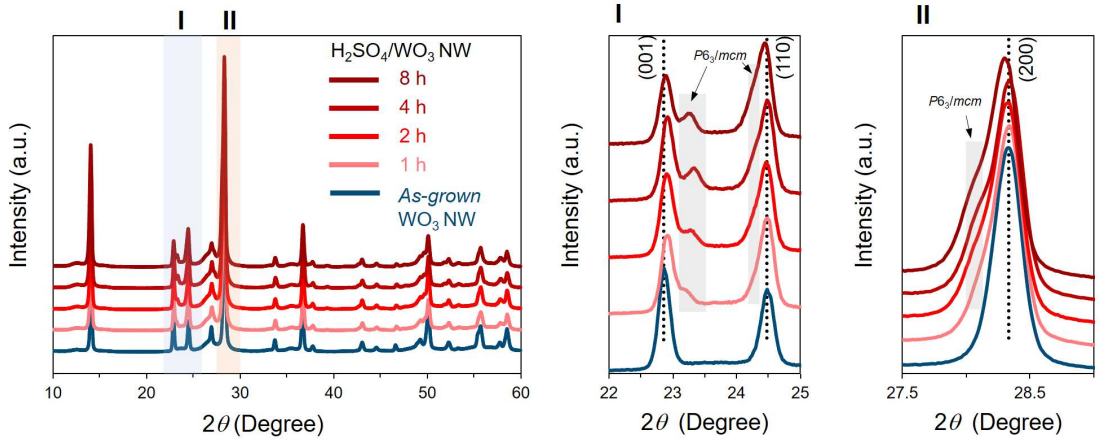

Figure S9. XRD patterns of *as-grown* and H_2SO_4-surface treated WO_3 nanowire samples.

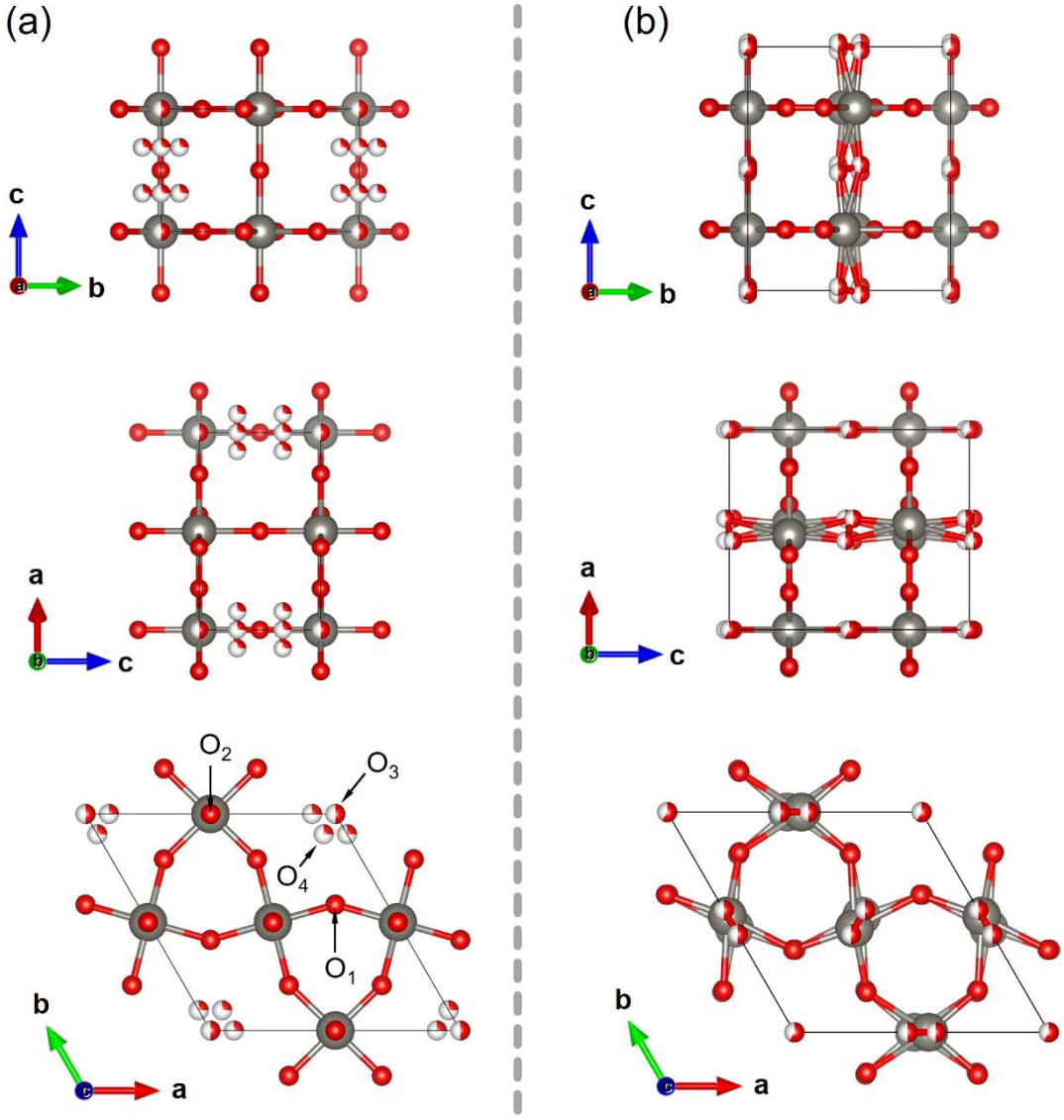

Figure S10. *The refined crystal structure of hexagonal tungsten hydrates with (a) P6/mmm (as-grown nanowire) and (b) P6$_3$/mcm (H_2SO_4-surface treated nanowire) space group, viewed along a, b and c (O_3 oxygen is positioned in the center of the dodecagon aligned with the tungsten, while O_4 oxygen offsets from the tungsten in the c axis slightly towards the O_2 oxygen. The red sectors in water "dots" represent the probability of water's presence at the corresponding sites.*

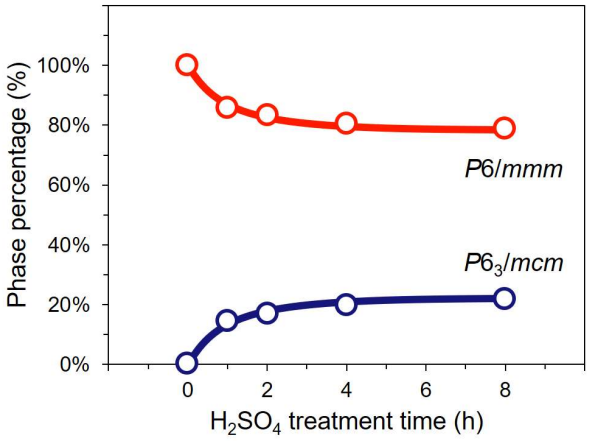

Figure S11. The structure percentage of hexagonal WO_3 nanowire that varied with the H_2SO_4-surface treatment time. These data are calculated from the Rietveld refinement of X-ray diffraction (XRD) patterns.

Table S1 Results of the refinement data of *as-grown* WO_3 nanowire in the Space Group P6/mmm

Space Group		Atom	x	y	z	Occupancy	Site	Symmetry
P6/mmm (100%)	1	W_1	0.50000	0.00000	0.00000	1.00000	3f	mmm
	2	O_1	0.50000	0.00000	0.50000	1.00000	6l	mm2
	3	O_2	0.20929	0.41865	0.00000	1.00000	3g	mmm
	4	O_3	0.00000	0.00000	0.00000	0.51840	1a	6/mmm
	5	O_4	0.09350	0.09350	0.31256	0.25144	12n	..m

Table S2 Results of the refinement data of H_2SO_4-surface treated (4h) WO_3 nanowire

Space Group		Atom	x	y	z	Occupancy	Site	Symmetry
P6/mmm (79.57%)	1	W_1	0.50000	0.00000	0.00000	1.00000	3f	mmm
	2	O_1	0.50000	0.00000	0.50000	1.00000	6l	mm2
	3	O_2	0.20929	0.41865	0.00000	1.00000	3g	mmm
	4	O_3	0.00000	0.00000	0.00000	0.51840	1a	6/mmm
	5	O_4	0.09350	0.09350	0.31256	0.25144	12n	..m
P6₃/mcm (20.43%)	1	W_1	0.00000	0.47200	0.250000	1.00000	3f	mmm
	2	O_1	0.18300	0.37500	0.75000	1.00000	6l	mm2
	3	O_2	0.00000	0.44500	0.01600	0.50000	3g	mmm
	4	O_3	0.00000	0.00000	0.00000	0.59856	1a	6/mmm
	5	O_4	0.09350	0.09350	0.31256	-0.30000	12n	..m

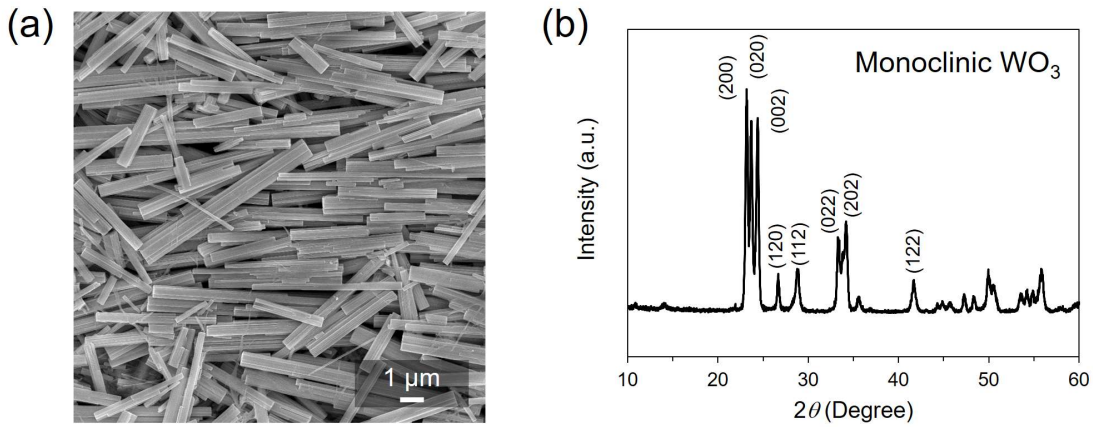

Figure S12. (a) SEM image and (b) XRD patterns of *as-grown* WO_3 nanowire after thermal annealing treatment (400°C) for 1h.

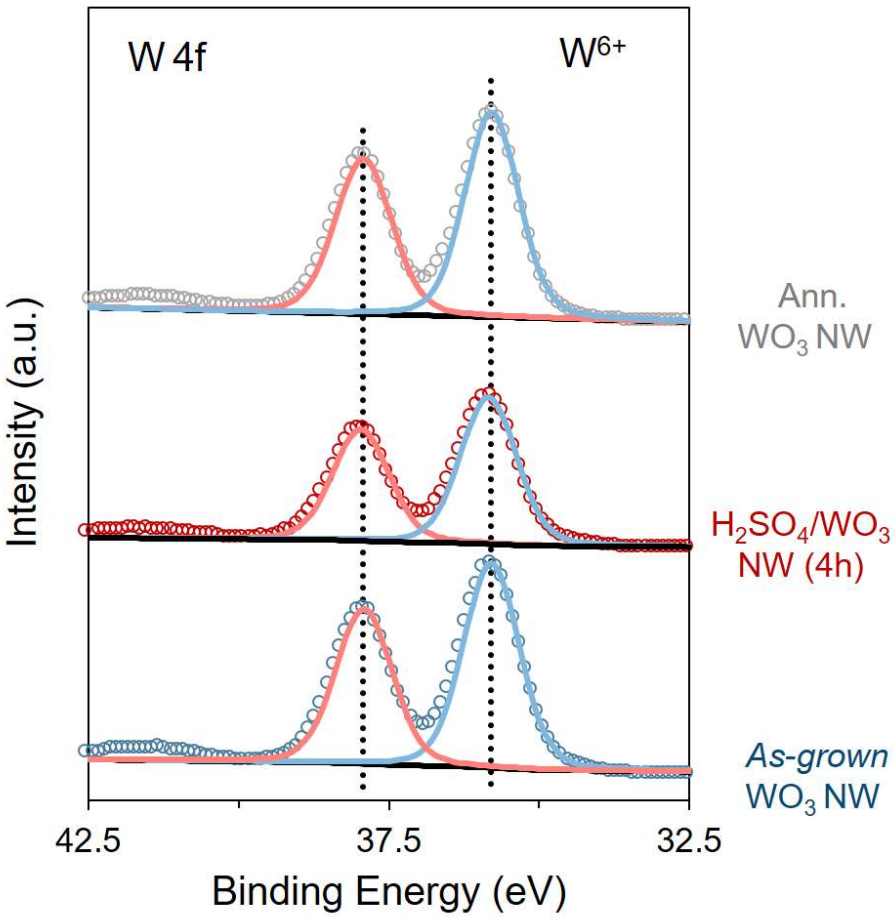

Figure S13. XPS W 4f spectra of as-grown WO_3 nanowire, H_2SO_4-surface treated (4 h) WO_3 nanowire and thermal annealing treated (400°C air, 1 h) WO_3 nanowire.

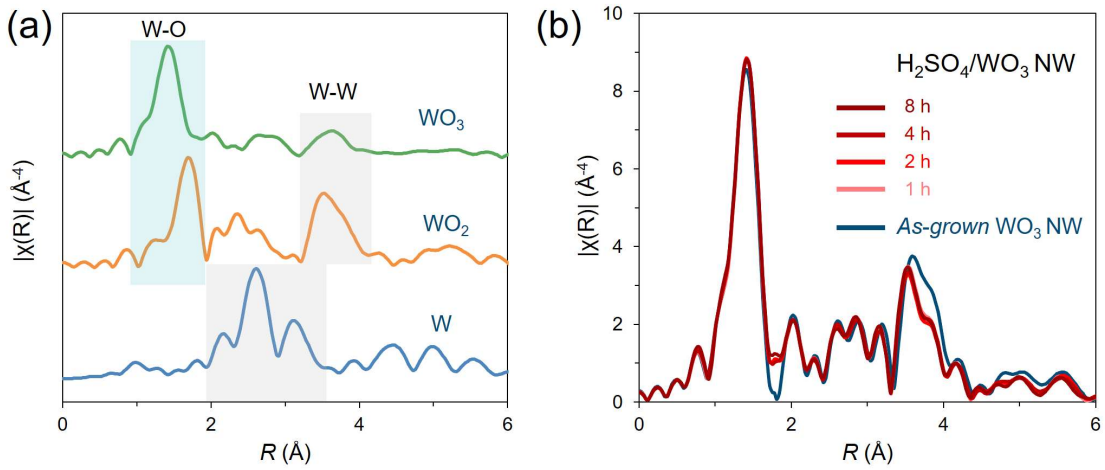

Figure S14. *(a) Fourier transformed k^3-weighted χ(k)-function of the EXAFS spectra of standard W, WO_2 and WO_3 powder samples. (a) Fourier transformed k^3-weighted χ(k)-function of the EXAFS spectra of as-grown and H_2SO_4-surface treated WO_3 nanowire samples.*

Table S3. EXAFS fitting parameters at the Cu K-edge various samples（S_0^2=0.67）

Sample	Path	[a]C.N.	[b]*R* (Å)	[c]$\sigma^2\times10^3$ (Å^2)	[d]ΔE_0 (eV)	R factor
W std	W-W	8*	2.74±0.01	2.6±1.7	12.0±1.1	0.001
	W-W	6*	3.15±0.01	3.1±0.2	11.0±2.0	
As-grown WO_3 NW	W-O_1	3.96±0.34	1.77±0.01	4.3±1.2	5.6±2.0	0.007
[e]TA_WO_3 NW	W-O_1	4.01±0.57	1.76±0.01	4.0±1.6	5.6±2.5	0.009
[f]S_WO_3 NW (1h)	W-O_1	3.42±0.26	1.76±0.02	3.4±1.8	4.9±2.8	0.015
S_WO_3 NW (2h)	W-O_1	3.45±0.26	1.76±0.02	3.6±1.9	4.8±2.8	0.009
S_WO_3 NW (4h)	W-O_1	3.48±0.29	1.76±0.02	3.6±1.9	5.0±2.8	0.008
S_WO_3 NW (8h)	W-O_1	3.42±0.34	1.76±0.02	3.5±2.0	4.8±3.0	0.010

[a]C.N.: coordination numbers; [b]*R*: bond distance; [c]σ^2: Debye-Waller factors; [d]ΔE_0: the inner potential correction; [e]TA: Thermal annealing treatment (Air, 400°C, 1h); [f]S: H_2SO_4-surface treatment. *R* factor: goodness of fit. * the experimental EXAFS fit of standard W powder by fixing C.N. as the known crystallographic value.

The obtained XAFS data was processed in Athena (version 0.9.25) for background, pre-edge line and post-edge line calibrations. Then Fourier transformed fitting was carried out in Artemis (version 0.9.25). The k^3 weighting, k-range of 3 - 15 $Å^{-1}$ and R range of 1 - 1.72 Å for 1 shell were used for the fitting. The model of bulk W and WO_3 were used to calculate the simulated scattering paths. The four parameters, coordination number, bond length, Debye-Waller factor and E_0 shift (CN, R, σ^2, ΔE_0) were fitted without anyone was fixed, constrained, or correlated.

CHAPTER IV

DESIGNED MOLECULAR RECOGNITION ADSORBTION SURFACE ON METAL OXIDE NANOWIRE WITH DISCRIMINATION AND CONCENTRATION PROPERTY

4.1 Thermally Engineered Formation of Molecularly Fingerprinted Metal Oxide Nanowires and Its Function on Molecular Discrimination

4.1.1 ABSTRACT

Nonanal ($C_9H_{18}O$) had been regarded as effective biomarker of lung cancer in human breath. For achieving the tiny amount detection from chaff interferences, a concept that nonanal pre-concentrator utilized prior to detection section shows its potential. To fabricate a novel material with good nonanal capability and discriminative recognition features, we synthesized nonanal imprinted TiO_2/ZnO nanowires. Nonanal adsorption amount displayed pre-heating formation temperature dependence property. 180 °C turned out to be the optimized condition for fabricating such imprinted nanowire. Residual products and their exist states after each pre-heating formation condition were also investigated and discussed for a better understanding of imprinted formation process. The target discriminative recognition property of nonanal imprinted functionalized nanowire was further demonstrated by amount comparison among adsorbed molecules from mixture. Not only nonanal adsorbed amount significantly enhanced, other interference molecule adsorption could also be depressed after imprint fabrication. This study provides a primary model for the further designing of molecule imprinted metal oxide with excellent target adsorption ability, even a discrimination property from complex atmosphere.

KEY WORDS: Nonanal recognition, pre-heating temperature, imprinted nanowire

4.1.2 INTRODUCTION

Nonanal, also called nonanaldehyde, pelargonaldehyde, or Aldehyde C-9, is one kind of alkyl volatile aldehyde containing a functional group with the structure −CHO, chemical formula is $C_9H_{18}O$. It is presented in several natural oils. Recent years, some researchers proved that nonanal contains in the breath of lung cancer patients, whose concentration is at the ppb level. [1-4] Since then, nonanal changed its identity as an effective biomarker for early lung cancer detection from exhale.[5-8] Numerous traditional (human sensory panel, canines etc.), and instrumental analytical methods mostly based on gas chromatography–mass spectrometer (GC–MS) were tested to detect tiny concentration nonanal,[9-12] those stated methods are efficient besides some limitations such as large size, high cost, complicated technical processing and large analysis time. Important challenges in the development of portable nonanal sensing device include improvements in sensitivity and selectivity, because it typically included in complex molecular atmosphere with a large variety of volatiles organic compounds (VOCs). A novel concept that utilizing a molecule collection device for recognizing, discriminating, trapping target, and then released in a short time, small space will be much easier to detect. Thus, developing a nonanal collection device with excellent nonanal adsorption and discrimination property is meaningful for realizing lung cancer diagnose from human breath.

The first and most important process of this strategy is the creation of a desirable functional surface character on which the nonanal capture should take place. Metal-oxide nanowire semiconductors are among the most suitable substrate materials for making functional surface due to their large surface and stability in air.[13-17] Some researches had proved its usability as pre-concentrator or separator for either volatile molecules or biomarker proteins. But it still necessary to improve the molecule discrimination property as well as robustness.[18-19] Nowadays molecule imprinted skill is considered to be a powerful approach to fabricate a molecular recognition space on material surface,[20] which means induce molecule as template and make cross-link around this template. After chemically and/or thermally treatment and remove the template molecule, a molecule trapped function is available. Therefore, combine the molecular imprinting technique onto metal-oxide nanowire surface would drastically enhance the molecule capability.

In this study, we fabricated a nonanal imprinted TiO_2/ZnO nanowire using titanium-oxide based material onto zinc oxide (ZnO) nanowires by introducing nonanal as template molecule.

The nonanal capability was evaluated by desorbed nonanal amount after keeping in the molecular atmosphere at a certain time. The nonanal imprinted cross-link formatted via a thermal pre-heating, and its temperature played as a crucial factor for enhancing the nonanal capability. Possibly reason of pre-heating temperature dependence for imprinted space formation explained by cross-link formation progress and stabilizing template bonding with metal-oxide. Based on the optimized formation condition, imprinted effect to molecule discrimination property can be demonstrated by discriminative ability in mixture of similar molecules.

4.1.3 EXPERIMENTAL

Fabricated of nonanal imprinted TiO_2/ZnO Nanowires

Hydrothermal method was utilized to grow ZnO nanowire array on Si (100) wafer. 5 nm Ti buffer layer was first sputtered on Si substrate, and then 100 nm ZnO thin film was sputtered as seed layer. 25 mM zinc nitrate hexahydrate ($Zn(NO_3)_2 \cdot 6H_2O$, Wako 99.0%), 25 mM hexamethylenetetramine (HMTA, $(CH_2)_6N_4$, Wako 99.0%), 2.5 mM polyethyleneimine (PEI, number average m.w. 1800, Aldrich 50 wt.% in H_2O), and 6 ml ammonia ($NH_3 \cdot 6H_2O$, Wako 28% in H_2O) were dissolved into 200 ml deionized (DI) water in sequence. The pre-prepared substrate was dipped into above solution and kept at 95 ℃ for 9 hours. After the growth, the samples were rinsed by DI water and dried by N_2 blow. An oxygen plasma treatment is operated for fully removing the surface organic of obtained nanowire.

After the nanowire growth, Ti layer was deposited by RF sputtering with a power of 50 W and an Ar pressure of 0.3 Pa for 30 min, followed by oxygen plasma treatment to form titanium oxide intermediate layer. Finally, the nonanal imprinted titanium oxide was formed onto the TiO_x coated ZnO nanowires by alkoxide based sol-gel technique. The sol was confected by mixing precursor-tetrabutyl titanate, dealcoholization catalyst agent-titanium (IV) chloride and template molecule-nonanal at 60 °C for 1 h. Then the sol was spin-coated on the nanowires with 4000 rpm of rotation speed for 1 min, and finally the sample was further baked at 500 °C for 1 h to completely remove the incorporated template molecules.

Characterization

The Scanning Electron Microscopy (SEM) images were obtained on a JEOL JSM-7610F microscope. Fourier Transform Infrared Spectroscopic (FT-IR) spectra were measured on a JASCO FT/IR-6700 spectrometer equipped with MCT detector. The nonanal adsorption capability experiments were conducted by gas chromatograph mass spectroscopy (GC-MS,

Shimadzu GCMS-QP2010 Ultra) with temperature control system (GL Sciences, OPTIC-4). To evaluate the amount of adsorbed molecule, we utilized the GC column (Intercap 1MS, length 60 m, inner diameter 0.32 mm). The sample was immediately heated up to 400 °C to fully desorb the adsorbed molecules.

4.1.4 RESULTS AND DISCUSSION

Nonanal imprinted TiO_x/ZnO nanowire synthesis procedure can be briefly described as following steps (The details conditions can be found in experimental section): Firstly, the ZnO nanowires are growth via hydrothermal method. Second, a titanium layer is deposited onto the ZnO nanowires by Ti sputtering and then oxygen plasma treatment. Third, spin-coating

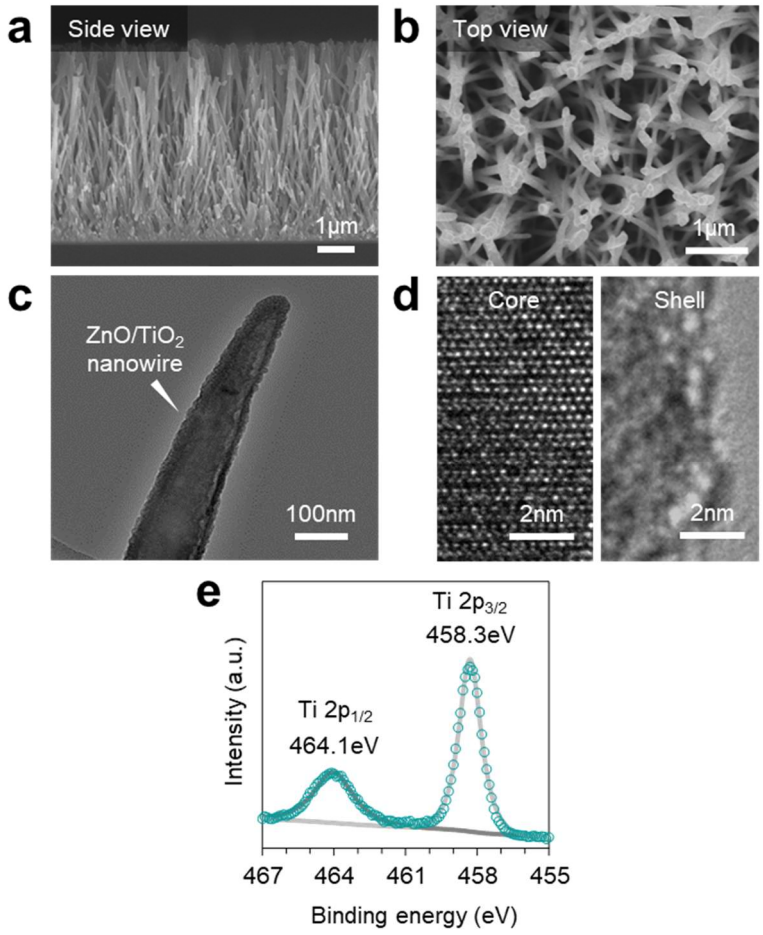

***Figure 1**. Imprinted TiO_2/ZnO nanowire synthesis. (a-b) Material morphology characterization by Scanning Electron Microscopy (SEM) of TiO_x sol-gel coating on ZnO nanowires from side view and top view, respectively; (c) Transmission Electron Microscopy (TEM) images of as-synthesis TiO_2/ZnO/ core-shell nanowires; (d) HRTEM images of ZnO core and TiOx outside layer; (e) X-ray photoelectron spectrum for titanium state confirmation.*

alkoxide titanium based sol-gel with nonanal as template onto this nanowires, a pre-heating treatment is conducted for promoting TiO_x skeleton formation. Finally, template nonanal is removal by annealing at high temperature. Nonanal imprinted TiO_x/ZnO nanowire was synthesized, the morphology comparison with bare ZnO nanowire is shown in Figure S1. Uniformly distribution ZnO nanowire provides a good substrate for sol-gel coating process, also expedites trapping, releasing, and transferring nonanal. Clearly surface coated by TiO_x can be observed after the sol-gel process, their morphology is shown in Figure 1a and b, SEM image from side view and top view, respectively. The imprinted layer already successfully costing, means as-synthesized TiO_x/ZnO nanowire can be further utilizing to evaluate nonanal capability. Detail crystal structure of as fabricated heterojunction material was observed under, transmission electron microscopy (TEM), the images in Figure 1 c and d illustrated such nanowire is consist of well-crystallized ZnO core and amorphous TiO_x outside layer. Titanium valence state was investigated by X-ray photoelectron spectrum (XPS), no other states exists except Ti^{4+}, [21-23] therefore, such nanowire would be defined as TiO_2/ZnO nanowires.

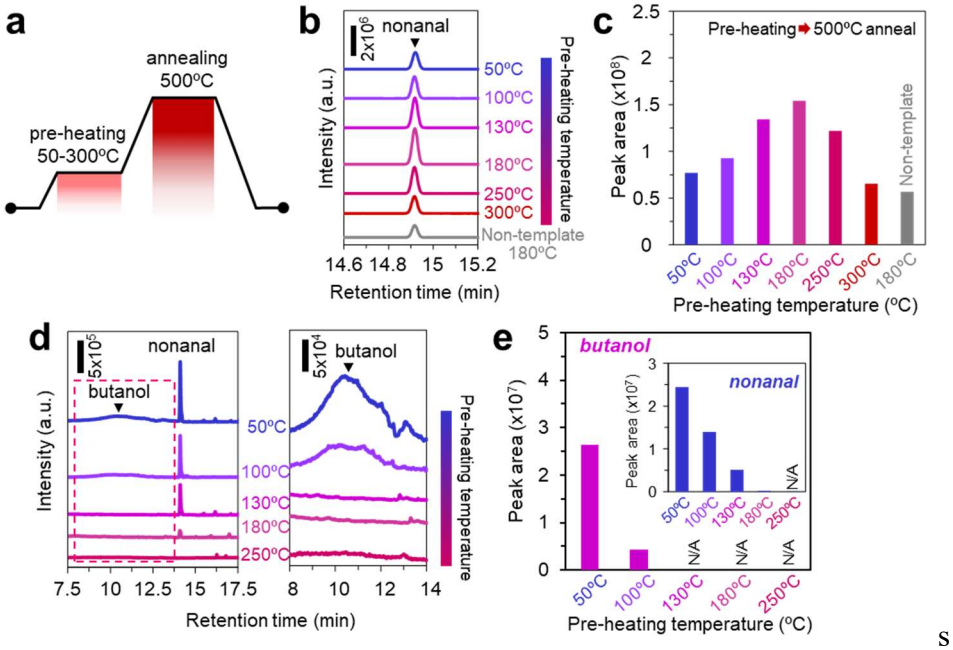

s

Figure 2. *(a) Two-steps thermal treatment illumination of imprinted nanowire formation process. (b) TIC spectra of desorbed products from GC-MS measurement by nonanal adsorbed imprinted TiO_2/ZnO nanowire samples synthesized at various pre-heating temperature, non-imprinted nanowire is also presented as comparison; (c) Nonanal peak area summarized from (c) to evaluate nonanal adsorption ability. (d) Residual molecules analysis by GC-MS from 400 ºC thermal desorption of imprinted TiO_2/ZnO nanowire synthesized at various pre-heating temperature. (e) Butanal (nonanal as insert) peak area summary from (d).*

Figure 2a presents the purpose of two thermal treatment process: relative low pre-heating is operated to facilitate TiO_x cross-link formation and high temperature annealing is aimed at completely remove template molecules. Imprinted TiO_2/ZnO nanowires synthesized under several pre-heating temperatures have been annealed for removing nonanal template, TIC spectra by GC-MS analysis by their nonanal adsorbed condition (after absorption in same concentration and duration) are shown in Figure 2b. Non-imprinted sample (synthesized by same process without template) is added as comparison. Due to molecular amount is liner associate with peak area of GC-MS results, Figure 1c summarized nonanal peak areas from Figure 1b and shows visually first increase and then decrease trend as pre-heating temperature rising. It presents the optimal performance at 180 °C pre-heating. In other words, nonanal adsorption capability of imprinted TiO_2/ZnO nanowire can be affected by pre-heating formation temperature. However, how the pre-heating temperature dependence happen is still unclear. There is one point need to note that all imprinted samples performed enhanced nonanal adsorption capability then non-imprinted. This exactly demonstrated our nonanal imprinted design is effective. For getting a detail understanding of the origin, from which nonanal capability trend with pre-heating temperature, residual molecules after various pre-heating temperature treatments are investigated by GC-MS. Figure 2d presents the TIC spectra via 400 ºC desorption analysis from unannealed imprinted TiO_2/ZnO nanowire after pre-heating at 50 ºC, 100 ºC, 130 ºC, 180 ºC and 250 ºC. Two species of molecule dominated the desorbed products, butanol and nonanal. In the case of butanol, (peak region has enlarged in Figure 2d), produced as by-product from the hydrolysis reaction of precursor-tetrabutyl titanate during TiO_x formation, can be regarded as criteria to judging the formation progress of cross-link. Butanol is unable to be detected as elevating pre-heating temperature above 130 ºC, indicated TiO_x cross-link completely formatted. But only unperfect TiO_x formation below 130 ºC pre-heating model is far from fully explanted for nonanal adsorption capability trend at higher pre-heating condition. Then discussion goes to nonanal origin from template we intensively involved, whose peak area is calculated and summarized in Figure 2e. It can be inferred that high pre-heating will cause template unexpected losing. At 180 ºC heating condition, nearly no peak belongs to template nonanal can be found. Here we wonder that if all the template nonanal is losing during pre-heating procedure, the nonanal capability should be continuously decrease until lost its imprint efficacy at 180 ºC pre-heating, while our result is opposite to such inference. Therefore, a hypothesis is proposed that template nonanal transforms to other exist states in the materials instead of losing directly.

To verify the above hypothesis, FT-IR measurement is conducted, and results present in Figure 3a. Interestingly, carboxylate bonding (COO) appears at 1400-1600 cm^{-1} region, which neither belongs to butanol nor nonanal,[24-27] peak height of asymmetric vibration also presents a first increase and then decrease trend (summarized in Figure 3b) as rising temperature. Such bonding state can tolerate the thermal temperature up to 500 ºC, demonstrate a stable exist state. Together with C-H bonding vibration of alkyl chain, our hypothesis can be proved that template nonanal strongly bonding with metal oxide surface through a carboxylate structure, this bonding structure formation can be facilitated by rising imprinted pre-heating temperature within a certain range. Over high pre-heating will destroy the alkyl-chain of template nonanal, results in failure of imprinting.

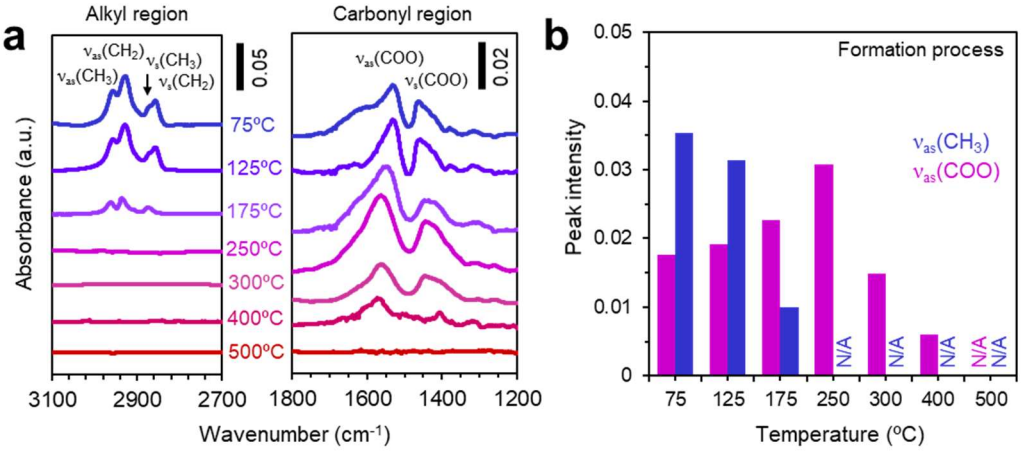

Figure 3. *Residual template nonanal bonding state with metal-oxide. (a) FT-IR spectra of imprinted ZnO/TiO_2 nanowires at a series heating treatment under continuously procedure without sample changing; (b) Peak height summary of antisymmetric vibration of carboxylate bonding (COO) from (a).*

Finally, nonanal imprinted function of TiO_2/ZnO nanowire at its optimized synthesized condition is demonstrated by target discriminate ability among mixture molecules with same aldehyde functional groups (cyclohexanal, benzaldehyde, p-tolualdehyde and nonanal). The measurement was taken by the GC-MS and relative adsorption was calculated by liquid molecule solution calibration. Considering the possible discriminative adsorption behavior difference between imprinted and non-imprinted nanowire, calculated amounts are further calculated by calibration curve (Figure S2) and shown in Figure 4. In this result, nonanal adsorption capability obviously enhanced after nanowire being imprinted (Figure 4a) compares with non-imprinted one. Even though non-imprinted nanowire also presents largest nonanal

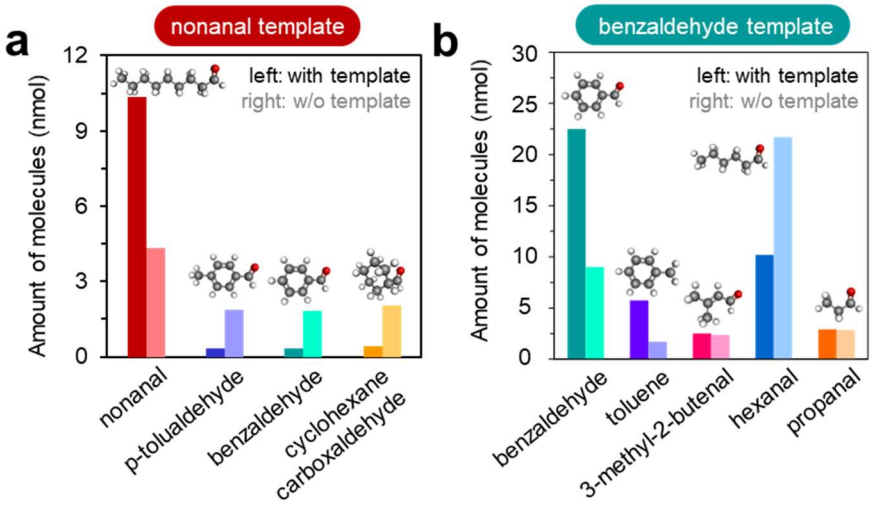

***Figure 4**. (a) Discriminative adsorption from mixture of similar chemical property molecules with aldehyde functional group (cyclohexanal, benzaldehyde, p-tolualdehyde and nonanal) comparison between nonanal imprinted and non-imprinted TiO_2/ZnO nanowires. (b) molecule discriminate ability of benzaldehyde imprinted TiO_2/ZnO nanowires among mixture of benzaldehyde, toluene, 3-methyl-2-butanal, hexanal and propanal.*

amount, this phenomenon is caused by nonanal intrinsic nature that relative higher vapor pressure at room temperature. In addition to nonanal, all other interference molecules adsorption amounts decreased, which major implies the suppression of interference molecule also devoted to successfully achieve good nonanal discrimination property by our imprinted TiO_2/ZnO nanowires. As an extend demonstration, discriminate ability of benzaldehyde imprinted is carried out in Figure 4b. Clearly aiming benzaldehyde adsorption amount enhancement in mixture of benzaldehyde, toluene, 3-methyl-2-butenal, hexanal and propanal after imprinted provides another powerful evidence for such molecular imprinted concept.

4.1.5 CONCLUSION

In summary, we reported a nonanal imprinted TiO_2/ZnO nanowire with enhanced target capability. Pre-heating temperature of its formation process is found as an important factor for optimizing the capability. At low pre-heating temperature, by-product butanol of cross-link TiO_x formation reaction regarded as criteria. When rising pre-heating temperature to it optimize value (180 ºC), cross-link TiO_x completely formation while nonanal template also strongly bonded, nonanal imprinted successfully. Template nonanal will be destroyed by over high pre-heating, caused the descent of target capability. Nonanal imprinted function was further

demonstrated by similar molecules adsorption capability comparison between with/without imprinted nanowire. This study provides detailed insight into molecule discriminative capture function formation process on metal-oxide nanowire surface, benefit the design for further applications as pre-concentrator to realize tiny nonanal detection from complex atmosphere.

4.1.6 REFENECES

[1]. Fuchs P, Loeseken C, Schubert J K, et al. Breath gas aldehydes as biomarkers of lung cancer[J]. International Journal of Cancer, 2010, 126(11): 2663-2670.

[2]. Vishinkin R, Haick H. Nanoscale sensor technologies for disease detection via volatolomics[J]. Small, 2015, 11(46): 6142-6164.

[3]. Hakim M, Broza Y Y, Barash O, et al. Volatile organic compounds of lung cancer and possible biochemical pathways[J]. Chemical reviews, 2012, 112(11): 5949-5966.

[4]. Darwiche K, Baumbach J I, Sommerwerck U, et al. Bronchoscopically obtained volatile biomarkers in lung cancer[J]. Lung, 2011, 189(6): 445-452.

[5]. Broza Y Y, Haick H. Nanomaterial-based sensors for detection of disease by volatile organic compounds[J]. Nanomedicine, 2013, 8(5): 785-806.

[6]. Peng G, Tisch U, Adams O, et al. Diagnosing lung cancer in exhaled breath using gold nanoparticles[J]. Nature nanotechnology, 2009, 4(10): 669.

[7]. Dent A G, Sutedja T G, Zimmerman P V. Exhaled breath analysis for lung cancer[J]. Journal of thoracic disease, 2013, 5(Suppl 5): S540.

[8]. Lim J H, Park J, Oh E H, et al. Nanovesicle‐Based Bioelectronic Nose for the Diagnosis of Lung Cancer from Human Blood[J]. Advanced healthcare materials, 2014, 3(3): 360-366.

[9]. Fu X A, Li M, Knipp R J, et al. Noninvasive detection of lung cancer using exhaled breath[J]. Cancer medicine, 2014, 3(1): 174-181.

[10]. Poli D, Goldoni M, Corradi M, et al. Determination of aldehydes in exhaled breath of patients with lung cancer by means of on-fiber-derivatisation SPME–GC/MS[J]. Journal of Chromatography B, 2010, 878(27): 2643-2651.

[11]. Munk S, Münch P, Stahnke L, et al. Primary odorants of laundry soiled with sweat/sebum: Influence of lipase on the odor profile[J]. Journal of Surfactants and Detergents, 2000, 3(4): 505-515.

[12]. Thriumani R, Zakaria A, Hashim Y Z H Y, et al. A study on volatile organic compounds emitted by in-vitro lung cancer cultured cells using gas sensor array and SPME-GCMS[J]. BMC cancer, 2018, 18(1): 362.

[13]. Zang J, Li C M, Cui X, et al. Tailoring zinc oxide nanowires for high performance amperometric glucose sensor[J]. Electroanalysis: An International Journal Devoted to Fundamental and Practical Aspects of Electroanalysis, 2007, 19(9): 1008-1014.

[14]. Liu C, Zapien J A, Yao Y, et al. High‐Density, ordered ultraviolet light-emitting ZnO nanowire arrays[J]. Advanced materials, 2003, 15(10): 838-841.

[15]. Lu C, Qi L, Yang J, et al. Hydrothermal growth of large-scale micropatterned arrays of ultralong ZnO nanowires and nanobelts on zinc substrate[J]. Chemical Communications, 2006 (33): 3551-3553.

[16]. Wang K, Chen J, Zhou W, et al. Direct growth of highly mismatched type II ZnO/ZnSe core/shell nanowire arrays on transparent conducting oxide substrates for solar cell applications[J]. Advanced materials, 2008, 20(17): 3248-3253.

[17]. Guan C, Wang X, Zhang Q, et al. Highly stable and reversible lithium storage in SnO2 nanowires surface coated with a uniform hollow shell by atomic layer deposition[J]. Nano letters, 2014, 14(8): 4852-4858.

[18]. Krivitsky V, Hsiung L C, Lichtenstein A, et al. Si nanowires forest-based on-chip biomolecular filtering, separation and preconcentration devices: nanowires do it all[J]. Nano letters, 2012, 12(9): 4748-4756.

[19]. Johnson K, Giordano B. Non-target analysis of vapor mixtures using silicon nanowire array sampling and thermal desorption[J]. Journal of Chromatography A, 2020: 460938.

[20]. Wulff G. Molecular imprinting in cross‐linked materials with the aid of molecular templates—a way towards artificial antibodies[J]. Angewandte Chemie International Edition in English, 1995, 34(17): 1812-1832.

[21]. Diebold U, Madey T E. TiO_2 by XPS[J]. Surface Science Spectra, 1996, 4(3): 227-231.

[22]. Reddy B M, Khan A, Yamada Y, et al. Structural characterization of CeO_2−TiO_2 and V_2O_5/CeO_2−TiO_2 catalysts by Raman and XPS techniques[J]. The Journal of Physical Chemistry B, 2003, 107(22): 5162-5167.

[23]. Zwijnenburg A, Goossens A, Sloof W G, et al. XPS and Mössbauer characterization of Au/TiO_2 propene epoxidation catalysts[J]. The Journal of Physical Chemistry B, 2002, 106(38): 9853-9862.

[24]. Mann A K P, Wu Z, Calaza F C, et al. Adsorption and reaction of acetaldehyde on shape-controlled CeO_2 nanocrystals: elucidation of structure–function relationships[J]. Acs Catalysis, 2014, 4(8): 2437-2448.

[25]. Zhang Q L, Du L C, Weng Y X, et al. Particle-size-dependent distribution of carboxylate adsorption sites on TiO_2 nanoparticle surfaces: insights into the surface modification of nanostructured TiO2 electrodes[J]. The Journal of Physical Chemistry B, 2004, 108(39): 15077-15083.

[26]. Dobson K D, McQuillan A J. In situ infrared spectroscopic analysis of the adsorption of aliphatic carboxylic acids to TiO_2, ZrO_2, Al_2O_3, and Ta_2O_5 from aqueous solutions[J]. Spectrochimica Acta Part A: Molecular and Biomolecular Spectroscopy, 1999, 55(7-8): 1395-1405.

4.1.7 Supporting Information

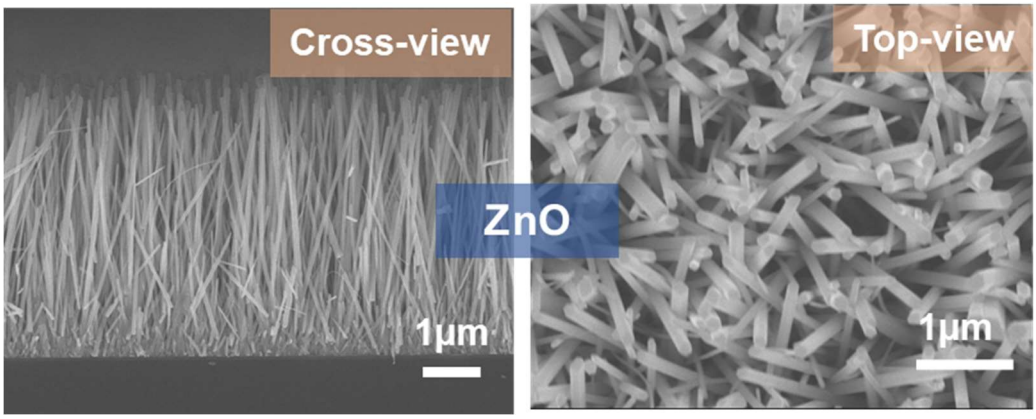

Figure S1. *SEM images of hydrothermal growth zinc oxide nanowires*

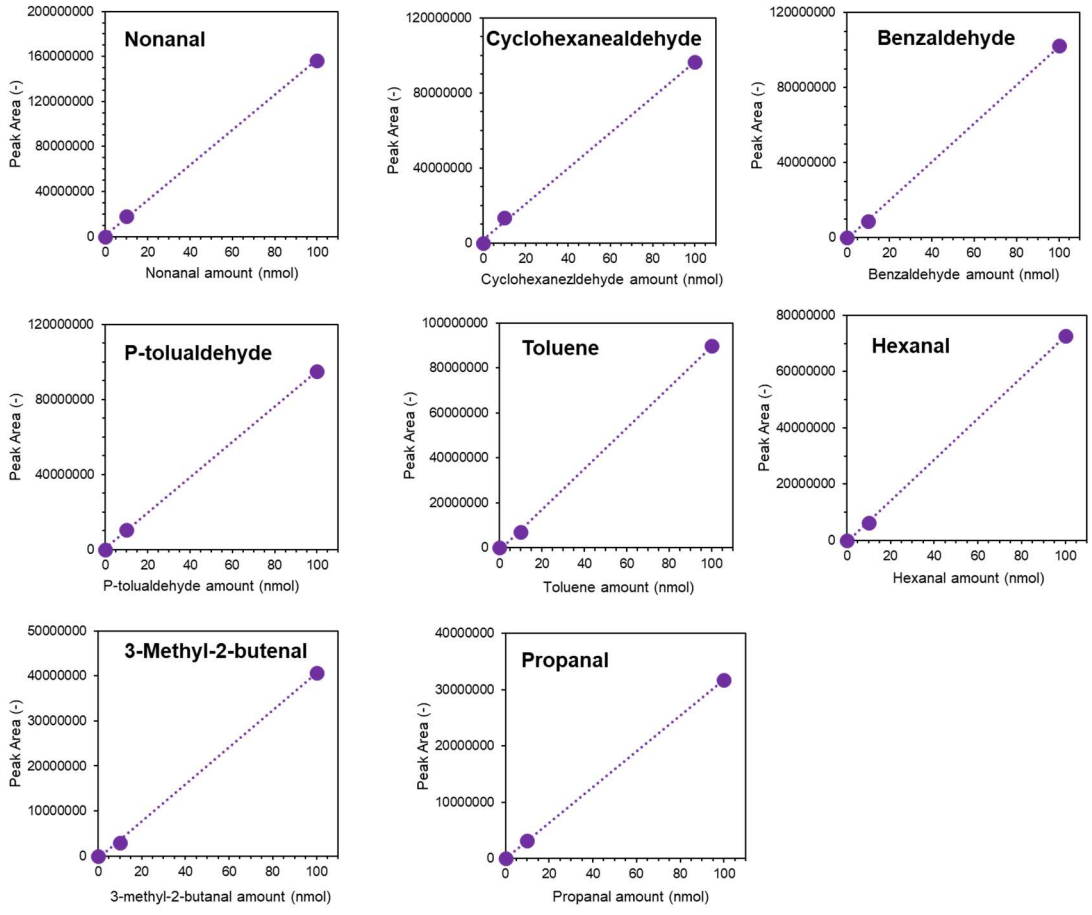

Figure S2. *Calibration curves of relationship between peak area (TIC spectrum) and molecular amounts utilized in the mixtures for TiO_2/ZnO nanowire to discriminate.*

4.2 Fundamental Principle and Design of Fingerprinted Metal Oxide Nanowire for Molecular Discriminated Adsorption from Mixture Volatiles

4.2.1 ABSTRACT

Here we demonstrate that a robust molecular fingerprinting of metal oxide nanowires selectively recognizes a target aldehyde molecule from volatile molecule mixture via discriminative adsorption. The metal oxide nanowires are composed of zinc oxide (ZnO) nanowires with molecularly fingerprinted titanium oxide shell. Interestingly, the aldehyde molecular fingerprint of oxide nanowires highly recognizes its target, and the molecular recognition property remained until 1000 cycles of heating treatment at 400 °C. The atomic-diffusion of zinc into the titanium oxide shell provides stronger bonding connection with metal atom during its formation process, which is benefit for template molecular being memorized without losing, so as to achieve the shape-recognition property from analogous structure mixtures. In addition, rich surface Zn amount of the molecular fingerprinted nanowire solidified its thermal robustness, allows us to repeatedly adsorb and thermally desorb aldehyde from surface. Based on the selectively adsorbed property, applying fingerprinted nanowire as pre-selector to a chemo-sensor, aldehyde (benzaldehyde as a model) can be selectively detected, even from imbalanced molecular ratio of tiny benzaldehyde. This methodology can provide an innovative approach to discriminate molecules, also a promising way to realize tiny molecule detection.

KEY WORDS: Molecular fingerprinted, nanowire, aldehyde discrimination, mixture volatiles, thermal robustness, functionalize mechanism

4.2.2 INTRODUCTION

Selectively discriminating a target molecule species from various volatile molecule mixture is an important challenge for precisely detecting poisonous materials, explosions, toxic gases and also biomarkers in exhaled human breath via electronic sensor devices toward forthcoming internet of things (IoT) technology based safe, comfortable and sustainably developing society. [1-3] To date, intensive efforts have been devoted to the development of various type of sensors for detecting various volatile molecules. [3-6] However, there is an inherent difficulty for the conventional sensors to selectively detect a target molecule species from volatile molecule mixture due to the fact that sensors gain electric signals via electrostatic and/or charge transfer interaction with functional groups of molecules and therefore the structurally and chemically analogous molecules are hardly discriminable. [7-10] In addition, the sensitivity of sensors is one of the crucial factors for the molecular discrimination. Since a noise signal tends to be marked accompanying with improvement of the sensor sensitivity, the selective discrimination of a target molecule from molecule mixture is quite difficult especially when the concentration of target molecule is much lower than those of other components. As such, a striking breakthrough is desired to selectively discriminate a target molecule species from volatile molecule mixture.

Molecular imprinting is a powerful approach to fabricate a molecular recognition space by introducing the molecule as a template during the material formation process. [11-12] Therefore, a discrimination performance of volatile molecule sensing would be drastically enhanced by combining the molecular imprinting technique to the sensor devices. [13-15] Fundamentally, the molecular recognition space is organized around a template molecule during the chemical synthesis mediated material formation process, [16] and a molecular recognition function is available after chemically and/or thermally removing the template molecule. [17] The molecular imprinting has been investigated mainly using polymers and siloxane based materials, [18-25] and lots of studies have focused on the improvement of molecular recognition property by modifying precursor, reactant, pH value and temperature conditions during the material formation process. [23-25] However, in general, the molecular recognition space is less effective to the volatile molecules with small number of recognition sites, and also the molecular recognition function tends to be degraded at appropriate operation temperature (200-400 ºC) of volatile molecule sensors due to the thermal instability

of polymer and siloxane based materials. [26-28] In fact, Dickert *et al.* reported the degradation of molecular recognition function in siloxane based molecularly imprinted material over 150 ºC. [28] These thermal instability of materials had limited the utilization of molecular imprinting technique to sensor devices. On the other hand, recent study demonstrated that the molecular imprinting utilizing titanium oxide based materials exhibited the excellent thermal robustness. [29-32] Nevertheless, the molecular recognition function of titanium oxide based material is substantially limited due to the lack of variety for molecular recognition space only via the metal-oxide binary system. Furthermore, in most cases, the molecular discrimination performance has been evaluated by comparing the adsorption property of individual molecule species and the molecular discrimination from mixed molecule species has been rarely seen especially for the volatile molecules, [33,34] while it is of crucial importance for the practical use of molecularly imprinted materials. Thus, synthesizing the thermally robust molecular recognition space with high performance molecular recognition and demonstrating the molecular discrimination from volatile molecule mixture are strongly needed to apply the molecular imprinting technique to the volatile molecule sensor devices.

Here we demonstrate '*molecularly fingerprinted*' metal oxide nanowires whose thermally robust molecular recognition space '*molecular fingerprint*' on nanowires highly discriminates a target volatile molecule species from volatile molecule mixture. The metal oxide nanowires are attractive nanomaterials for efficiently collecting the volatile molecule species due to their large surface and stability in air. In addition, the spatial selectivity of nanowire growth expands a flexibility of sensor design. [35-36] In this study, we fabricated a molecular fingerprint using titanium oxide based material onto zinc oxide (ZnO) nanowires by introducing aldehyde (nonanal/ benzaldehyde) as a template molecule which are known as typical lung cancer biomarker in exhaled human breath. [37-38] Atomic-diffusion of Zn from the ZnO nanowires to the titanium oxide shell drastically improved the recognition function for target molecule from mixture volatiles together with the thermal stability of molecular recognition at 400 ºC. Based on the selective adsorption and thermal robustness of molecularly fingerprinted oxide nanowires, we integrated for the first time a benzaldehyde sensing device utilizing such nanowire as selector prior to chemo-sensor. The isolation benzaldehyde sensing from volatile molecule mixture demonstrated our strategy to be a promising biomarker detection device in the near future.

4.2.3 EXPERIMENTAL

Synthesis and characterizations of molecularly fingerprinted oxide nanowires.

The molecularly fingerprinted oxide nanowires were synthesized by the following process. First, ZnO seed layer was deposited onto Si (100) (2 cm × 4 cm size) substrate by radio frequency (RF) sputtering with power of 100 W and Ar pressure of 0.3 Pa for 1 min. Then, the ZnO nanowires were grown from the seed layer by a hydrothermal growth technique. The nanowire growth solution was confected by dissolving 25 mM hexamethylenetetramine (HMTA), 25 mM zinc nitrate hexahydrate $Zn(NO_3)_2 \cdot 6H_2O$, 2.5 mM polyethyleneimine (PEI) into 150 ml deionized (DI) water and stirring for 5 min at room temperature. The sample was immersed into the growth solution with a manner of upside down to avoid a deposition of unintentionally formed ZnO nanocrystals during the nanowire growth. The ZnO nanowire growth was carried out after retaining in an oven at 95 ºC for 24 h. After the nanowire growth, Ti layer was deposited by RF sputtering with a power of 50 W and an Ar pressure of 0.3 Pa for 30 min, followed by oxygen plasma treatment with a power of 150 W and an O_2 pressure of 1 Torr for 10 min to form titanium oxide (TiO_x) intermediate layer. Compact TiO_x inter-layer as comparison was deposited by atomic layer deposition (ALD, Cambridge nanotech simply ALD), $Ti(NMe_2)_4$ and H_2O were using as precursors heated to 150 ºC and 75 ºC, respectively, and alternatively fed into the chamber with argon as a carrier gas with flow rate of 20 sccm. The thickness of TiO_x layer was controlled by changing deposition cycle numbers, growth rate was around 0.40 Å/cycle as deposited temperature was 150 ºC, 375 cycles were applied to obtain TiO_x layer thickness about 15 nm, oxygen plasma treatment was also used which was same as treating RF sputtering sample. Finally, the molecularly fingerprinted titanium oxide was formed onto the TiO_x coated ZnO nanowires by alkoxide based sol-gel technique. The sol was confected by mixing precursor-tetrabutyl titanate 67 µl, dealcoholization catalyst agent-titanium (IV) chloride 10 µl and template molecule-benzaldehyde (10 mg) /nonanal (13.4 mg) into 2-propanol solvent 970 µl at 60 °C for 1 h. Then the sol was spin-coated on the nanowires with 4000 rpm of rotation speed for 1 min and baked at 130 °C (benzaldehyde template) and 180 ºC (nonanal template) for 1 h. The sample was further annealed in oven at 400 °C for 1 h to completely remove the incorporated template molecules. For comparison to the molecularly fingerprinted nanowires, the template non-printed nanowires, the sol uncoated nanowires and their thin film forms were also prepared. For the thin film samples, TiO_x intermediate layers were coated onto Si substrates prior to the sol deposition without ZnO deposited. The

morphology and composition of the molecularly fingerprinted oxide nanowires were evaluated by 15 kV field emission scanning electron microscopy (FESEM, JEOL JSM-7610F) and 200 kV scanning transmission electron microscopy (TEM, JEM-ARM200F) equipped with energy dispersive x-ray spectroscopy (EDS).

Adsorption and desorption characterizations of volatile molecule analyses.

The adsorption of volatile molecule species was conducted into 20 ml vial bottle. For the single component adsorption, 2 μl of benzaldehyde was dropped at the bottom of 20 ml vial bottle and maintained for 20 min by capping the vial bottle to be a vapor equilibrium condition prior to the adsorption experiments. For the multi-component experiment, 2 μl of each reagent solution ((benzaldehyde, aniline, anisole, toluene, ethylbenzene) or (1-nonanal, 2-nonanaoe, 1-nonanol, nonane)) was dropped at the bottom of vial bottle and maintained for 20 min. Then the 2 mm×10 mm sized specimens were suspended in the vial bottle and the volatile molecules were adsorbed at room temperature for 5 min. The desorption experiments were conducted by gas chromatograph mass spectroscopy (GCMS, Shimadzu GCMS-QP2010 Ultra) with temperature control system (GL Sciences, OPTIC-4). The sample was immediately heated up to given temperature (400 °C was chosen to desorb all the molecules) with a rate of 60°C/sec to fully desorb the molecules. To evaluate the amount of adsorbed molecule, we utilized the GC column (Capillary Columns InertCap 1MS (length 60 m, inner diameter 0.25 mm)). The desorbed molecules were flown through the GC column by elevating the column temperature with a rate of 10 °C/min up to 280 °C with a constant He flow rate of 1 ml/min. The temperatures of GC/MS interface and ion source were set to be 200 °C. The measured m/z range was from 35 to 272. The amount of adsorbed molecules was estimated by GCMS peak area and calibrated by making curve of peak area as a functional with constant concentration solution (volatile molecule dissolve into isopropyl alcohol). The existence state of template molecule during the fingerprint formation process were heated at a given temperature for 10 min and cooled to room temperature, then evaluated by Fourier transform infrared spectroscopy (FTIR, Thermo Fisher Scientific, NICOLET iS50 with a mercury−cadmium-telluride (MCT) detector) at room temperature.

Scheme of molecule sensing system.

Fingerprinted oxide nanowire as mentioned above was synthesized on a size of 0.5 cm × 0.5 cm silicon wafer (100) with a snake-like Pt electrode on its upside which was making for the purpose of working as a heater to desorbed molecules from nanowire surface. This electrode was deposited by RF sputtering with power of 50 W for 40 min on snake-like mask concealed

silicon wafer, and its resistance turn out to be 83 Ω. Apply 25 V voltage on the electrodes, heating time can be controlled by PC program. Heating temperature was confirmed by thermographic camera. As for volatile molecules detecting and sensing, a 16-element chemo-sensitive sensor array was fabricate using blends of carbon black and gas chromatography (GC) stationary-phase materials preselected based on their sorption properties. Blends of the selected GC materials with carbon black particles were subsequently coated over chemo-sensitive sensor devices. Mix volatile compounds was pumped from 20 ml vial bottle with 2 μl of each reagent solution (benzaldehyde, aniline, anisole, toluene, ethylbenzene) into a chamber with fingerprinted nanowire and sensor in it. Nitrogen gas was used as fresh and background gas. The sensing response was calculated by

$$R=\frac{r(molecule)-r(background)}{r(N2)}\times 100\%$$

r(molecule) is the sensor resistance when detecting molecule; r(background) is the resistance when heating the nanowire without prior molecule adsorption, this value is utilized to eliminate the small influence by sensor temperature changing. r(N_2) is the resistance of nitrogen flowing situation.

4.2.4 RESULTS AND DISCUSSION

Figure 1a shows the schematic of molecularly fingerprinted metal-oxide nanowires which enables the discrimination of volatile molecules (benzaldehyde molecule as an example) from the mixed molecule species. Typical field emission scanning electron microscopy (FESEM) images from cross-section and top views of the molecularly fingerprinted oxide nanowires grown onto Si substrate are shown in Figure 1b. The nanowires are uniformly distributed on the substrate. The diameter, length and number density of nanowires are ca. 100 nm, 3 μm and 35 wires/μm^2, respectively. In this study, function molecules recognition and discrimination ability were evaluated by firstly adsorbed onto the nanowires at room temperature in vapor phase (The details can be seen in Method section), then the desorbed by thermally desorbing the molecules at 400 ºC in gas chromatograph mass spectroscopy (GCMS). The chromatographic peak area of a compound is considered linear with its content, on the basic of calibration curve (Supporting Information), molecules amount was displayed. To the knowledge of fragile molecular imprinted method by polymer, thermally robustness of as-prepared metal oxide fingerprinted nanowire was investigated by thermal treatment of 300-

1000 ºC for one hour, and their desorbed molecular amount as adsorbed in benzaldehyde vapor were shown in Figure 1c. Desorbed benzaldehyde amount present a rising at first and then decreasing trend with a top value at around 400 ºC annealing condition. The rising desorbed amount below 400 ºC was considered results from incompletely remove of template molecule, and structure collapse at high temperature treatment dominates the dramatically decrease after 500 ºC. Therefore, 400 ºC was chosen as annealing temperature for a thermal robustness fingerprinted nanowire with functionalized discrimination ability. As comparisons to the molecularly fingerprinted nanowires (denoted as 'Fingerprinted-NW'), no template printed nanowires (Non printed-NW) was taken into consider demonstrating the so-called molecularly fingerprint effect to the molecule discrimination ability from mixture volatiles. Such discrimination ability is evaluated by the desorbed molecules after mixture volatile adsorption and their relative amount calculated from obtained GC-MS spectra. It can be seen from Figure 1d, fingerprinted nanowires with benzaldehyde as template present an obvious benzaldehyde amount enhancement (2.6 times) than no-template nanowires from the vapor mixture volatile of benzaldehyde, aniline, anisole, toluene and ethylbenzene, which have same benzene-ring, the various comes from molecular functional group. Similar molecule enhancement (2.1 times) occurs to nonanal template molecularly fingerprint nanowires (Figure 1e) from mixture of nonanal, 2-nonanone, 1-nonanol and nonane, those also structure semblable with different functional group molecular species. Although other non-target molecules amount ratio also changed, it exactly right to demonstrate the surface template-involved molecularly fingerprinted nanowires had been functionalized, in other words, such nanowire makes designed molecule recognition possible. Benzaldehyde collection of series samples molecularly fingerprinted (Fingerprinted-NW), no template printed nanowire (No-template NW), Sol-gel uncoated nanowires (Control-NW), molecularly fingerprinted thin film (Fingerprinted TF), no template printed thin film (Non-printed TF) and sol uncoated thin film (Control-TF) were also examined and result was normalized by desorbed benzaldehyde from Fingerprint NW in Figure 1f. Note that for the thin film samples the sol-gel oxide layers were deposited onto titanium oxide (TiO_x) coated Si substrates without ZnO layer. The desorbed amounts of benzaldehyde compared with that from the molecularly fingerprinted nanowires are 22.2 % for the no template printed nanowires, 2.9 % for the sol uncoated nanowires, 1.4 % for the molecularly fingerprinted thin film, 0.6 % for the no template printed thin film and 0.5 % for the sol uncoated thin film, respectively. Remarkably, the benzaldehyde recognition

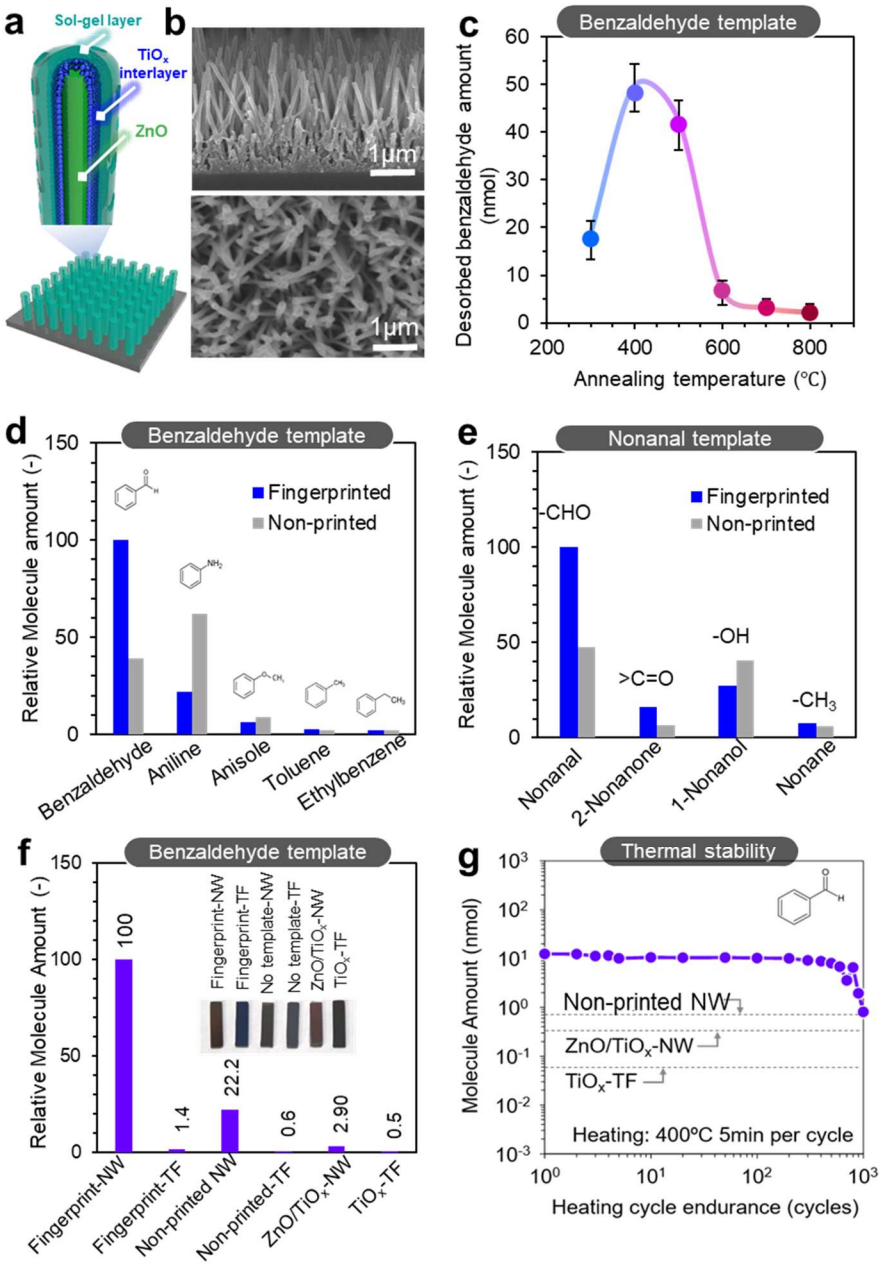

Figure 1. *Molecule recognition and discrimination properties of molecular fingerprinted nanowires. (a) Schematic illustration of the robust molecularly fingerprinted oxide nanowires which enables the discrimination of volatile molecules from the mixed molecule species; (b) Typical SEM images of the molecularly fingerprinted oxide nanowires from side-view and top view; (c) Benzaldehyde collection ability of benzaldehyde template fingerprinted nanowire by pre-treatment annealing temperature of 300 to 1000 ºC; (d) Molecules discrimination ability comparison between benzaldehyde template fingerprinted nanowire and no-template nanowire from mixture (benzaldehyde, aniline, anisole, toluene and ethylbenzene) and (e) comparison between nonanal template fingerprinted nanowire and no-template nanowire from mixture (nonanal, 2-nonanone, 1-nonanol and nonane) by calculating*

molecules desorbed amount from peak area of GC-MS spectra; (f) Benzaldehyde collection of series samples (molecularly fingerprinted nanowires (Fingerprinted-NW) and thin film (Fingerprinted-TF), the target non-fingerprinted nanowires (Non printed-NW) and thin film (Non printed-TF), and the sol uncoated nanowires (Control-NW) and thin film (Control-TF). The used temperature for the benzaldehyde desorption was 400 ºC; (g) The thermal endurance property for benzaldehyde recognition of the molecularly fingerprinted nanowires. The heating treatment was performed at 400 ºC for 5 min per each cycle.

function of the molecularly fingerprinted nanowires is ca. 200 times higher than the sol uncoated thin film, which is much larger value than the surface area ratio of nanowires (S_{NW}) to thin film (S_{TF}), S_{NW}/S_{TF}=17.5. This indicates a critical role of the molecular fingerprints on the benzaldehyde recognition of the molecularly fingerprinted nanowires. Next we examined the thermal stability of the molecular recognition function of the molecularly fingerprinted oxide nanowires. Figure 1g shows the thermal endurance property for benzaldehyde recognition of the molecularly fingerprinted nanowires. Each heating treatment was carried out at 400 ºC for 5 min. The molecular recognition function of the molecular fingerprints remaining until 1000 cycles of heating treatment, which has not been attainable by the thermally unstable polymers or the siloxane based molecular recognition space. [27,28]

Here we discuss the molecular recognition function of the molecularly fingerprinted nanowires. Firstly, we consider the effect of surface area since the large nanowire surface might facilitate the benzaldehyde collection. When we compare the sol uncoated nanowires and thin films, the nanowire sample showed 5.8 times higher molecular recognition function than the thin film sample. The relatively smaller value to the surface area ratio of nanowires to thin film (17.5 times) might be due to the limitation of vapor diffusion to the bottom side of nanowires. Next, we consider the effect of molecular imprinting on the benzaldehyde recognition. The molecular recognition function was improved by only 2.3 times with the molecular imprinting, as can be seen in the comparison of the molecularly fingerprinted thin film and the no template printed thin film. Therefore, the drastic improvement on the molecular recognition function of the molecularly fingerprinted nanowires cannot be solely interpreted by the surface area effect and the molecular imprinting on titanium oxide. Here we consider the effect of atomically diffused Zn on the molecular recognition function. Since the molecularly fingerprinted thin film does not contain ZnO, the prominent molecular recognition function of the molecularly fingerprinted nanowires might be caused by the introduction of Zn atoms during the formation

of the molecular fingerprint. To confirm the effect of Zn atoms on the molecule recognition, we fabricated the molecularly fingerprinted nanowires by atomic layer deposition (ALD) coated TiO_x intermediate layer with compact atom accumulation to control the Zn diffusing to shell-layer since the ALD layer is formed by a layer-by-layer growth mechanism. Figure 2a shows the Zn and Ti elemental mapping TEM images and the elemental line profiles of the molecularly fingerprinted nanowires with the sputtering coated TiO_x intermediate layer and the atomic layer deposition (ALD) coated TiO_x intermediate layer. From the slope comparison of Zn elemental line profiles, we find that the sputtering coated TiO_x intermediate layer fingerprinted nanowires present higher slope, which means more Zn content at near-surface place. To prove this result, XPS surface atom ratio (Zn and Ti) of those two kinds fingerprinted nanowires were measured, sputtering TiO_x inter-layer nanowire with 45.3% Zn atom at its surface, while ALD inter-layer nanowire is 14.8%, corresponding to the elemental mapping result, Zn diffusion suppressed fingerprinted nanowire during the sol-gel process was successfully by using the ALD coated forming the defect free TiO_x inter-layer. Then we investigated the relationship between molecule recognition and surface Zn amount, Figure 2b shows the normalized desorbed amount from benzaldehyde and nonanal adsorbed on the molecularly fingerprinted nanowires with the use of sputtering coated intermediate TiO_x layer and the ALD coated intermediate TiO_x layer. Interestingly, the benzaldehyde recognition function of the benzaldehyde fingerprinted nanowires was drastically deteriorated (8.5 times) by using ALD coated TiO_x layer. Same phenomenon happens to nonanal recognition by its fingerprinted nanowires. By blending sputtering and ALD depositing TiO_x-interlayer, fingerprinted nanowires with several surface Zn ratio was prepared. In Figure 2c, benzaldehyde recognition ability evaluated by desorbed benzaldehyde amount trend to increase with surface Zn ratio of nanowires. All these results draw a conclusion that the diffused Zn plays an important role on the enhancement of molecule recognition ability.

Until here, molecule recognition ability enhancement of fingerprint nanowires is considered from material surface functionalized by template molecule being involved and remove. Herein, further investigations towards discriminating the specified molecule from mixture volatile molecule species are necessary to identify the features of fingerprinted nanowires with rich diffused Zn. We proposed an assumption that molecule discrimination can be realized by the shape of recognition sites, and rich Zn atom at fingerprinted nanowires surface can benefit memorizing template. To verify this shape-recognition assumption, molecules with deformity

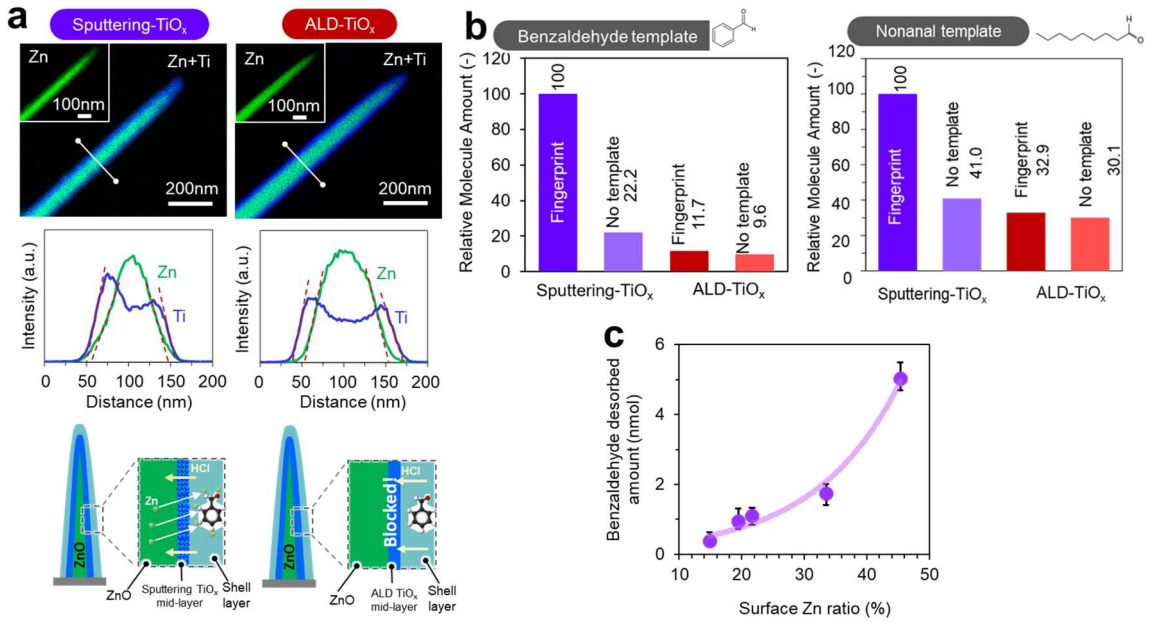

Figure 2. *Zn atom-diffused effect to molecule recognition property of fingerprinted nanowires. (a) EDS elemental mappings (Zn K and Ti K) and line profiles of fingerprinted nanowires with sputtering coated TiO_x intermediate layer and Atom Layer Deposition (ALD) coated TiO_x layer, the insets in mapping images are the elemental mapping only for Zn; (b) Relative molecule amount (normalized by sputtering TiO_x-interlayer fingerprinted nanowire of each template molecule) calculated from GC-MS spectra for benzaldehyde and nonanal collection abilities assessment by consistent-templated fingerprinted nanowire; (c) Benzaldehyde desorbed amount various with surface Zn ratio of fingerprinted nanowires.*

shapes were chosen as templates and mixture contents for fingerprint nanowires discriminating. Benzaldehyde fingerprinted nanowires for mixture consists of benzaldehyde, toluene, cyclohexanealdehyde and anisole discrimination result is shown in Figure 3a, unless something unexpected, largest benzaldehyde amount desorbed, other molecular amount is normalized by benzaldehyde amount. While cyclohexanealdehyde fingerprinted nanowires for same mixture vapor discrimination result in Figure 3b as a comparison. Cyclohexanealdehyde has a twisted structure at its ring part, means a different shape to benzaldehyde. An obvious desorbed molecule amount ratio changed when template alter to cyclohexanealdehyde. Even though the discrimination performance is not perfect due to the same aldehyde group, our shape-recognition assumption can be preliminary vitrificated. Those mixture molecules discriminated performance performed by fingerprinted nanowires with suppressed Zn diffusion were added in Figure S8, almost no desorbed molecule amount change by molecularly fingerprinted.

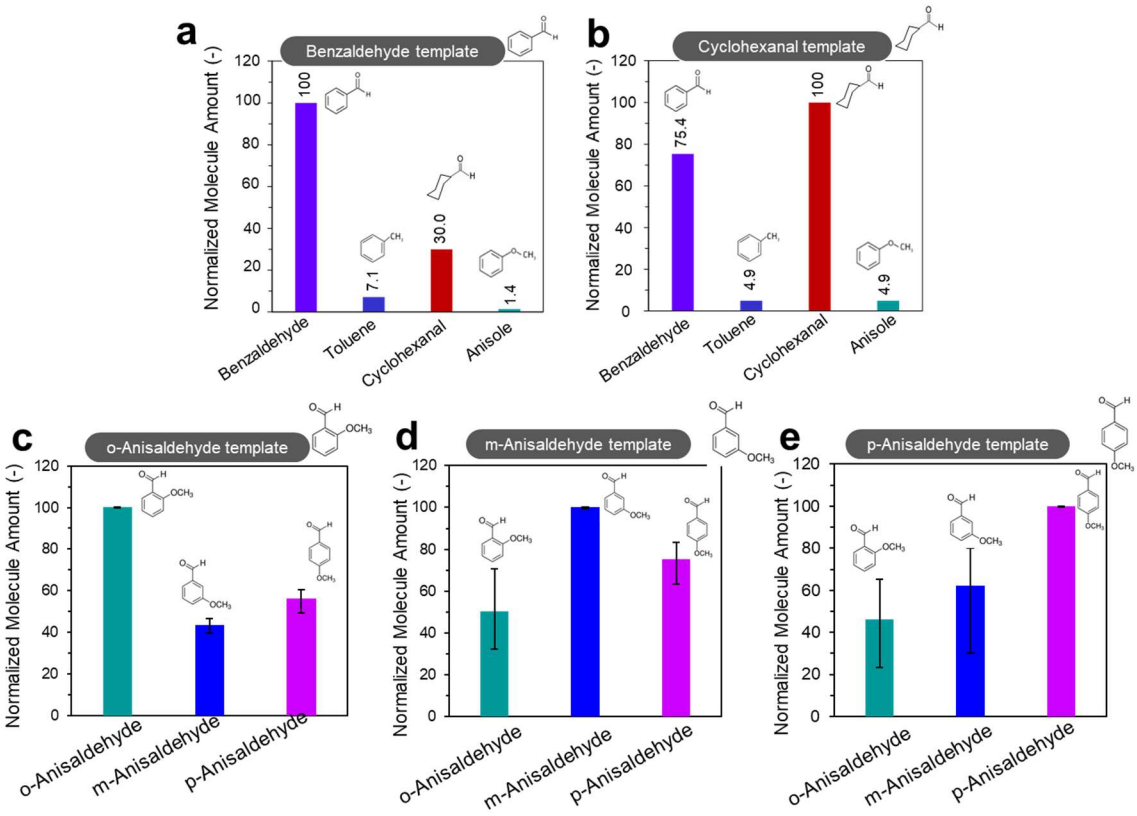

Figure 3. *Molecule discrimination by fingerprinted nanowires from similar shape mixture volatiles. (a) Normalized desorbed molecule amount calculated from GC-MS spectra of benzaldehyde template and (b) cyclohexanealdehyde template molecularly fingerprinted nanowires from the mixture (benzaldehyde, toluene, cyclohexanealdehyde and anisole) adsorption; Normalized desorbed molecule amount calculated from GC-MS spectra of (c) o-anisaldehyde template (d) m-anisaldehyde template and (e) p-anisaldehyde molecularly fingerprinted nanowires from the mixture (o-anisaldehyde, m-anisaldehyde and p-anisaldehyde adsorption) adsorption; Amount is normalized by the highest desorbed molecule amount after adsorption in each mixture.*

This exactly right demonstrated Zn diffusion is crucial for shape-recognition molecules from mixture volatiles. Further molecules discrimination precision was investigated in a mixture with isomerise of o-anisaldehyde, m-anisaldehyde and p-anisaldehyde. Only different ether position on benzene ring of those molecules leads to extreme similar chemical properties and difficult to discriminate. Surprisingly, from the desorbed molecules amount ratio displayed in Figure 3c-e that obtained by immersing o-anisaldehyde, m-anisaldehyde and p-anisaldehyde fingerprinted nanowires in a vapor mixture of them, respectively. Slightly target molecule discrimination property can be realized, which reflected the correctness of our shape-recognition assumption. Considering a condition exist that of recognition site partially exposed

on nanowire surface, making molecularly shape-recognition unperfect and limited the discrimination precision from isomerise molecules. However, current discriminating result is already a step forward and our molecularly fingerprinted nanowires are worthy to study and be made promotion further.

Even molecule shape-recognition performance can be got by fingerprinted nanowires, we still cannot answer the following simple question, How Zn atom assist the shape-recognition property, which improve molecule discrimination characteristics? For providing an open-application, well-founded and designable functionalized material to facilitate the development of molecular discrimination devices, fingerprint mechanism was discussed in the following section. Since Zn diffused to fingerprinted nanowire shell-layer is necessary for aldehyde recognition, we assumed that the aldehyde recognition space is favourably created by the assistant of Zn atom during the molecular fingerprint formation process, therefore the aldehyde molecular shape can be memorized by the molecular fingerprint so that preferentially recognized from mixture volatiles. Fingerprinted formation can be divided to two processes, one is the synthesis of cross-material around template aldehyde at low temperature, the other is the template removal process by high temperature annealing. In such precondition, temperature dependence of desorbed products analysis and remained molecule bonding state with cross-material should be an appropriate way to identity the interaction of template aldehyde with metal-oxide during fingerprint formation. Herein, take the desorbed products at a series of formation temperatures by fingerprinted nanowire with different surface Zn ratio into first consideration, GC-MS spectra were carried out in Figure 4a and b, which successively conducted under 100-500 ºC without sample replacement by rich Zn (sputtering TiO_x-interlayer) and less Zn (ALD TiO_x-interlayer) nanowires, respectively. Butanol and nonanal (template aldehyde) dominating the desorbed products at comparatively low formation temperature (below 200 ºC). It is not hard to understand that butanol is a reaction product of cross-material formation around template because of the easy-hydrolysis property of precursor tetrabutyl-titanate. Close to same butanol desorption behaviour, limited effect to the cross-material formation proportion under each temperature by diffused Zn atom can be speculated. Then we analysed the desorbed tendency of template nonanal various with temperature. In terms of rich Zn fingerprinted nanowire, relative less nonanal amount was detected contrast to the case of with less Zn nanowires, especially at low temperature (100 ºC, even lower than the majority cross-material formation). The lapsed template nonanal molecule becomes the highly

possible factor that lead to fingerprint disabled. This result clearly signify the Zn atom has the capability to assist the maintenance of template aldehyde, not so easy to loss. Next, to identify the states of retained template nonanal, we perform FT-IR spectroscopy measurements to more directly monitored the carbonyl (C=O) state dynamic variations during the molecular fingerprinted formation processes. The FT-IR spectra of fingerprinted nanowires with rich and less Zn after treatment at various temperatures are shown in Figure 4c and d. Not as expected, no clearly peak relative to carbonyl is consistence with the FT-IR spectrum of liquid-phase nonanal (1726 cm^{-1}), [39] all spectra show two separated peaks in the 1650−1400 cm^{-1} region. It was frequently reported that carbonyl compounds bonding with metal oxides can be thermally oxidized to carboxylate bond, whose IR peaks appear around 1400-1550 cm^{-1}. [40-43] Therefore, the peak around 1550 cm^{-1} is assigned to the ν_{as} (COO) signal of carboxylate species, bigeminal peak around 1400-1450 cm^{-1} is ν_s (COO) signal. The intensity of these peaks increases first and then gradually decrease until disappear as raising the treatment temperature of fingerprint nanowire with both rich and less Zn. The first increasing phenomenon probably coming from transformation of transition state. Adequate thermal energy created by high temperature treatment break the carboxylate connection, and finally these two peaks fully eliminated. Notley, fingerprint nanowire with rich Zn present a stronger carboxylate bond because a higher template removal temperature (500 ºC) is necessary than less Zn case (400 ºC). For further analysis the carboxylate bonding state, the bonding structure is taken into consideration. Difference value ($\Delta\nu$) between antisymmetric and symmetric vibration wavenumbers in FT-IR spectrum is deemed to be a general way to identity carboxylic bonding structure. [44-47] Many researches had proved large $\Delta\nu$ (above 140 cm^{-1}) carboxylate state is classified into bridge structure, while small $\Delta\nu$ (below 140 cm^{-1}) is chelating structure. [48-51] In Figure 4e, rich Zn fingerprint nanowires with $\Delta\nu$ is 142 cm^{-1}, also less Zn fingerprinted nanowire with 99 cm^{-1} are calculated, following possibly bonding structures. Bridge structure is known as most stable bonding among other conceivable structure (eg. chelating, monodentate). Therefore, this bonding division result consistence well with the template aldehyde removal temperature. There is one point need to notice that $\delta(-CH_2)$ vibration mode generally shows its signal at around 1436 cm^{-1}, [52-53] which is somehow overlapped with ν_s (COO) signal. their peak positions at after 200 ºC treatment are adopted due to the completely removal of alkyl- chain. Based on the results of the mass spectrometry experiments and spectroscopy discussed above, we display a possible fingerprint formation mechanism schematic illumination in Figure4f. Since rich surface Zn atom shows the stronger bind, we

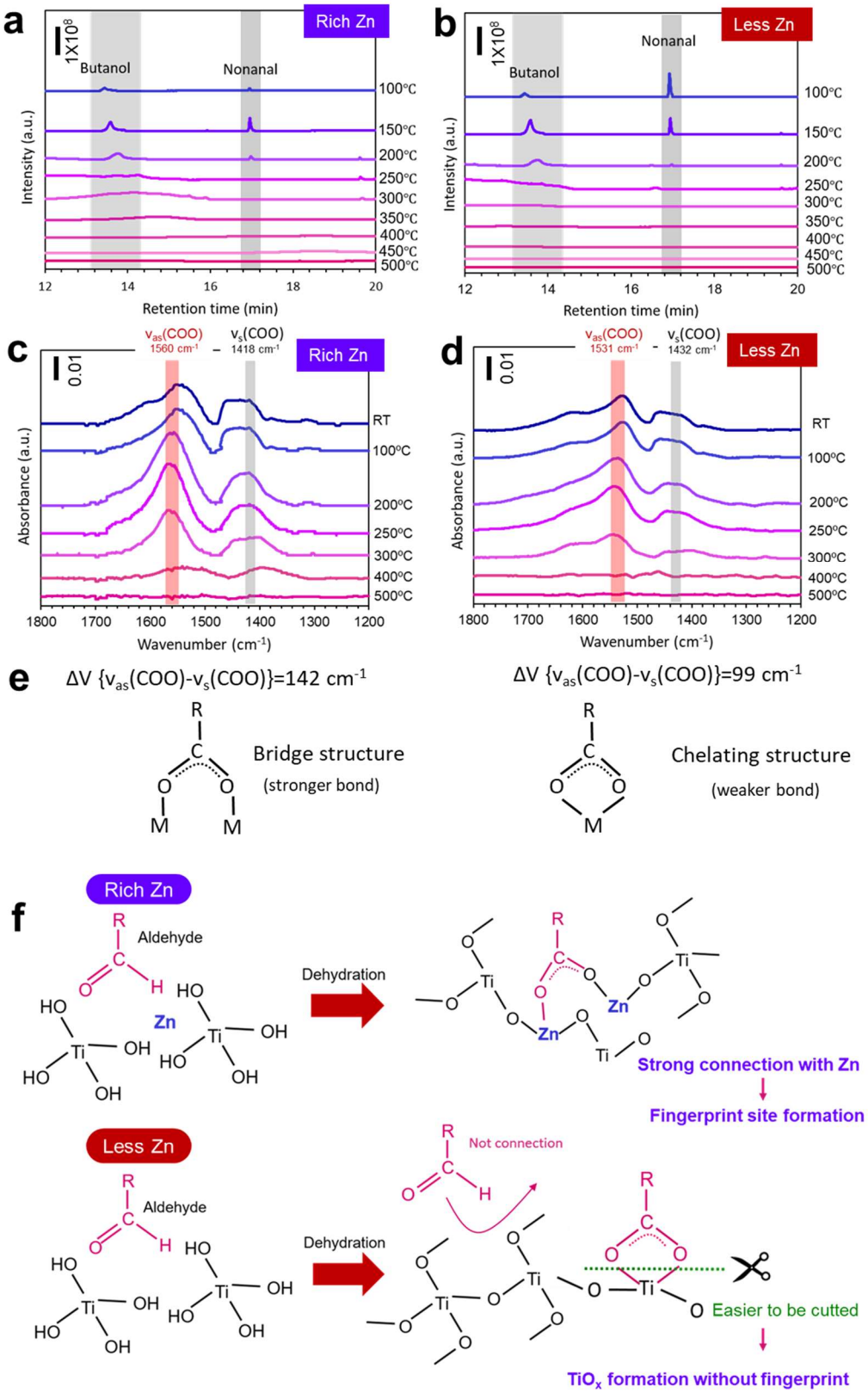
a
Rich Zn
1X10^8
Butanol
Nonanal
Intensity (a.u.)
100°C
150°C
200°C
250°C
300°C
350°C
400°C
450°C
500°C
Retention time (min)
b
Less Zn
c
Rich Zn
v_as(COO) 1560 cm-1
v_s(COO) 1418 cm-1
0.01
Absorbance (a.u.)
RT
Wavenumber (cm-1)
d
Less Zn
v_as(COO) 1531 cm-1
v_s(COO) 1432 cm-1
e
ΔV {v_as(COO)-v_s(COO)}=142 cm-1
Bridge structure
(stronger bond)
ΔV {v_as(COO)-v_s(COO)}=99 cm-1
Chelating structure
(weaker bond)
f
Rich Zn
Aldehyde
Dehydration
Strong connection with Zn
Fingerprint site formation
Less Zn
Not connection
Easier to be cutted
TiOx formation without fingerprint

Figure 4. *Molecular fingerprinted nanowire formation temperature denpendence. (a-b) Desorbed product analyze at a series of formation temperature (100-500 ℃) by GC-MS spectra and (c-d) FT-IR spectra between 1200-1800 cm^{-1} after the 10 min treatment under each formation temperature of sputtering TiO_x-interlayer (rich Zn) and ALD TiO_x-interlayer (less Zn) molecularly fingerprinted nanowires, respectively; (e) COO^- bongding structure hypothesis by the difference vibration of symmetic (V_s) and antisymmetic (V_{as}) from FT-IR spectra; (f) Posiblly molecularly fingerprint nanowire formation mechnism preconceived.*

supposed bridge structure is result in carboxylate bonding with Zn atom, chelating structure in less Zn case is bonding with Ti atom. A conclusion can be drawn that Zn atom keep template aldehyde from losing and provide a strong connection which ensure the memorized of molecular shape during fingerprint formation process.

On the basic of shape-recognition formation mechanism we proposed above, thermal stability of material structure is another fatal factor due to the destroyed possibility of shape-recognition sites by crystal structure transition during the template removal procedure. What's more, some researches had proved TiO_2 synthesised by sol-gel method has an amorphous to anatase phase transition temperature in the vicinity of 350-400 °C thermal treatment. Thus, it is necessary to consider the fine structure of fingerprint nanowire. Accurate measurements of the height and position of the pre-edge peak in Ti K-edge XANES (X-ray absorption near-edge structure) can offers a detailed and quantitative picture of the local structure around Ti atoms, which is particularly suited to assess changes in the local Ti coordination associated with different structures. The intensity of the transition is a good measure to evaluate the coordination environment of Ti atom. Higher pre-peak intensity because of the higher orbital mixing between Ti and O, means the more distortion/disorder from octahedral coordination. The three pre-peaks (see Figure 5), labelled as A1, A2, A3, correspond to transitions of the core electron to Ti 3d, 4p, 4s hybridized states. [54] In SI-Figure S10, the Ti K-edge XANES pre-edge region of sol-gel layer treated by a serious of temperatures. When treatment temperature up to 400 °C, intensity of A2 peak decreased gradually, means amorphous structure has been destroyed, obvious split three peaks lead to the assignment of TiO_2 anatase structure [55-56]. As for molecular fingerprinted nanowires, on account of Zn atom exist in outside sol-gel fingerprinted layer, the Ti coordination structure presents a different transition temperature. As shown in Figure 5a and b, which belong to rich Zn and less Zn fingerprinted nanowires at a range of treatment temperature (room temperature to 500 °C) during its formation procedure, the

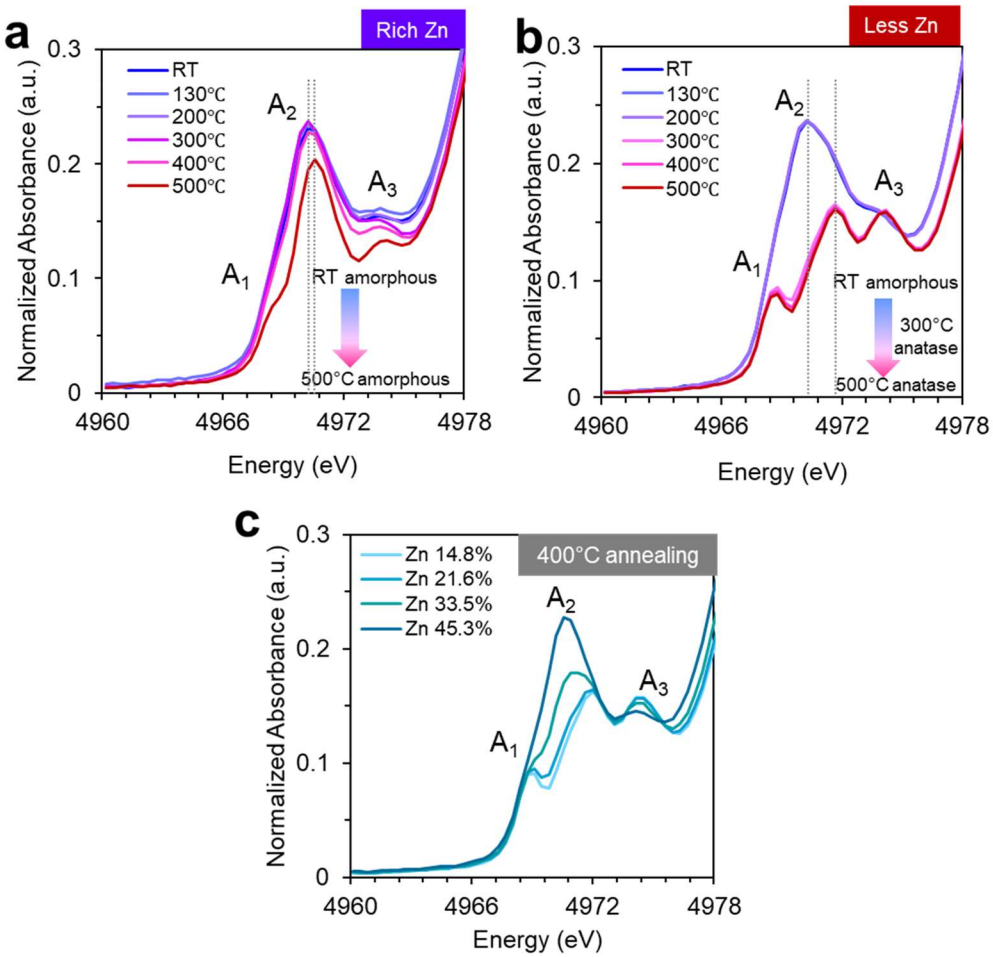

Figure 5. *Local structure around Ti atoms identification depended by fingerprinted formation temperature. (a) Normalized Ti pre-edge XANES spectra by sputtering TiO_x-interlayer and (b) ALD TiO_x-interlayer molecularly fingerprinted nanowires at a series of their fromation temperatures from room temperature to 500 ℃; (c) XANES spectra of 400 ℃ pre-annealing molecularly fingerprinted nanowires with various surface Zn ratio (14.8%; 21.6%; 33.5% and 45.3%).*

various difficulty of structure transition from amorphous to anatase between rich and less Zn amount can be found. Surprisingly, even under treatment temperature of 500 °C, amorphous structure still be kept in rich Zn fingerprinted nanowire case, much higher than less Zn fingerprinted nanowire with its transition temperature at 200-300 °C. In Figure 5c, XANES spectra of 400 °C pre-treated fingerprint nanowire with various surface Zn ratio are shown, visible peaks intensity decreases as Zn amount reduce provide a demonstration for rich Zn amount stabilized the fingerprinted layer. Therefore, we suppose rich Zn atom prevents the transport and rearrangement of Ti (IV) cations into larger crystalline units, directly result in the excellent thermally stability of molecule recognition by rich Zn fingerprinted nanowire.

Finally, we show the applicability of the fabricated molecular fingerprinted nanowires towards molecule-sensing devices with benzaldehyde discrimination functionality from mixture volatiles. As the model target molecules, we employ a benzaldehyde (as a typical biomarker in human breath). Benzaldehyde fingerprinted nanowire act before sensor for pre-selecting and releasing molecules, we named it as "selector" in the following discussion. Figure 6a shows the schematic of fabricated nanowire selector and chemo-sensor coupling device and its sensing procedure illumination. The detail of device fabrication process can be seen in the Experimental section. This methodology discriminates the benzaldehyde via selective benzaldehyde adsorption from mixture volatiles, constituent molecules is coincidence with benzaldehyde discrimination functions in Figure 1(d), containing aniline, anisole, toluene and ethylbenzene as structurally analogous analytes to benzaldehyde target molecule, note that all of these molecules are the components of exhaled human breath [57-62], following thermal desorption procedure and molecules transfer to sensor. A photograph of the as-integrated coupling device and its infrared thermography images which carried out to confirm the working temperature of current-controlled nanowire selector are shown in Figure 6b, 240 °C was chosen as thermal desorption temperature according to the desorbed molecule species and amount (SI-Figure S12): adequate thermal energy for benzaldehyde desorption and suppressed interference molecules that require more energy form desorption. Note that even short distance between nanowire selector and chemo-sensor, slight sensor temperature disturbed by operating nanowire selector at high temperature (SI Figure S13), such well-performance makes great contribution for the integration of miniature device. As the sketch of auto-control-program (Figure 6c), selectively benzaldehyde sensing from mixture volatiles can be described as below: Initially, the sensing system undergoes a fresh procedure by heating nanowire selector with N_2 as background flowing to get rid of surface molecular residues; Then proceed benzaldehyde selectively adsorption through flowing mixture volatiles for 3 min without heating and N_2 flowing; Once adsorption procedure is over, switch mixture to N_2 flow to remove redundant molecules in sensing chamber; Next ventilate mixture once again for 20 seconds in order to get sensing signal caused by all molecules; The last step conducted benzaldehyde sensing by thermal benzaldehyde desorption from selector surface and sensing for 12 seconds. A mini pump is operating continuously for molecule transferring and flow rate controlling. For a better understanding of benzaldehyde selector application effect, especially tiny benzaldehyde in complicate atmosphere, intensively adjusted benzaldehyde ratio in mixture is considered as an efficient path. Prior to mixture volatiles ventilating, vapor

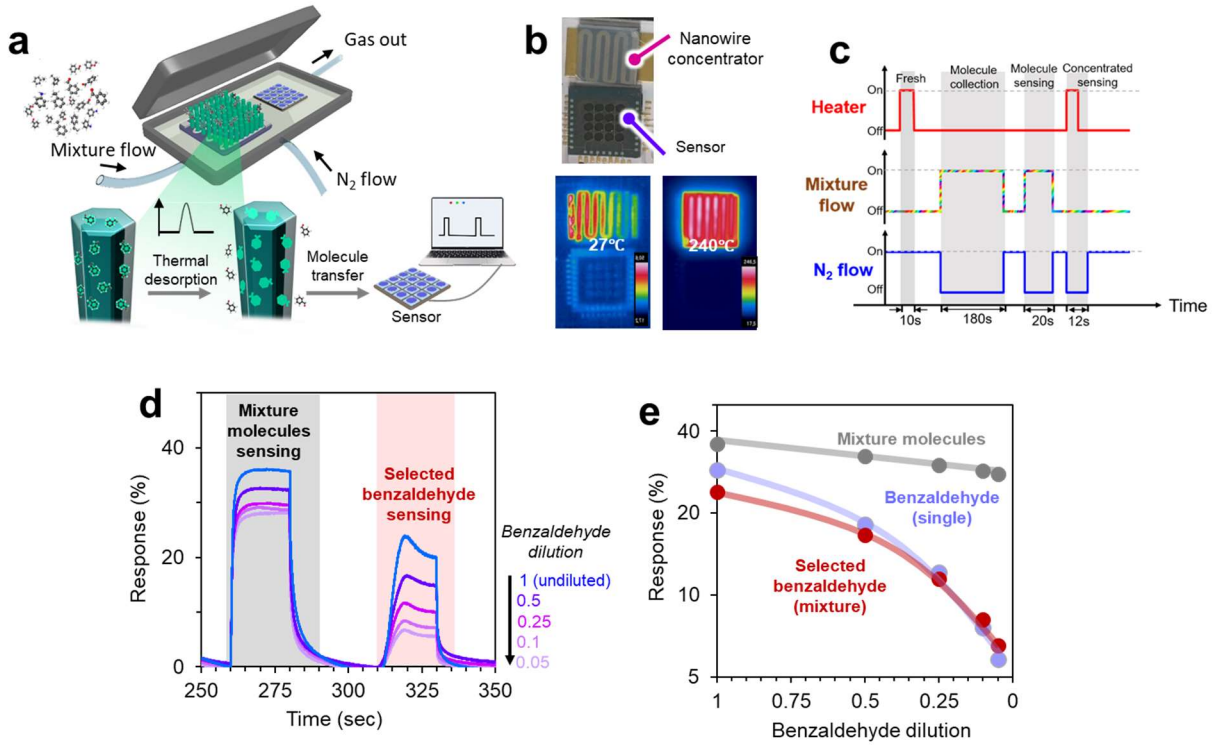

Figure 6. *Nanowire selector integrated with sensor for benzaldehyde discrimination from mixture volatiles. (a) Schematic illustration of integrated sensing device consists of nanowire-selector and chemo-sensor for benzaldehyde discrimination from volatile mixture. This methodology discriminates the benzaldehyde via selective benzaldehyde adsorption and the following thermal desorption procedure. (b) Infrared thermal images of temperature-controllable molecularly fingerprinted nanowires selector; (c) Controlling profile of desorption temperature by heater, mixture volatile molecules flow and background nitrogen flow for benzaldehyde selective detection procedure; (d) Dynamic sensing response curves in mixture with different benzaldehyde component, first sensing response belong to mixture molecules sensing, and second response curve is desorbed benzaldehyde molecules sensing through thermal desorption; (e) Sensing response comparison from (d).*

pressure difference lead to various concentration of each species at naturally balance evaporated at room temperature (SI-Figure S14), although benzaldehyde concentration being at lower level compares with others, molecules adsorbed amount from each benzaldehyde ratio mixtures (SI-Figure S12) exactly prove significance of preferentially benzaldehyde adsorbed onto the nanowires performance by addition of molecular fingerprint. Further thermal desorption manipulated at 240 °C was designed for restricting the release of majority obstructive molecules, thus, more precise benzaldehyde sensing signal can be observed even from quit limited benzaldehyde ratio mixture Figure 6d shows response curves obtained from

adsorption in mixture volatiles with various benzaldehyde ratio to other species. Nearly square response curves not only signify excellent response and recovery properties, also demonstrate the successful of molecule transfer from nanowire selector to chemo-sensor, which is crucial for realizing benzaldehyde selective sensing. Summarized response percentage values in Figure 6e exhibit increase trend as benzaldehyde ratio rising, either all molecules sensing or benzaldehyde sensing. However, obvious slope distinction of the trend curve can be found, which demonstrates more effective and accuracy benzaldehyde sensing. So as to evident such sensing response is result from desorbed benzaldehyde, responses from single component benzaldehyde at various concentration were summarized together as a comparison. Initially, similar response values by mixture volatiles adsorption and single benzaldehyde at each concentration condition was expected. Nevertheless, beyond our expected, sensing from single benzaldehyde has a slightly higher response value than mixture, we considered it might be due to the excessive molecular free movement somehow prevent benzaldehyde from adsorption. Therefore, desorbed molecules were confirmed by GC-MS spectra (SI-Figure S16), from which selectively benzaldehyde sensing is able to be limited in benzaldehyde-diluted mixture by 20 times (ratio 0.05), anisole initiates to dominate the sensing from absorbed in ulterior diluent can be speculated. While completely response trend obtained by only chemo-sensor without the application of benzaldehyde nanowire selector (SI-Figure S17) demonstrate unrealized benzaldehyde sensing, further implying the importance of nanowire selector application. To the best of our knowledge, on account of the intrinsically difficulty for suppressing the unintentional adsorption of other analyte molecules, selectively discriminating the benzaldehyde target molecule from the volatile molecule mixture is quite hard by the vast majority of sensing device, thus successfully extract benzaldehyde from mixture with such low target ratio is a great breakthrough for the development of molecular discrimination device.

Based on the above analyses, aldehyde collection capability enhancement from mixture by molecularly fingerprinted nanowires with Zn atom assisting its formation suggests a new promising strategy for discriminating structurally analogous molecules through “shape-recognition” character. To the best of our knowledge, such selectively adsorption molecule volatiles has rarely been achieved so far due to the difficulty of imprinting micro-molecules and intrinsic similar chemical interaction property with materials. Despite only aldehyde discrimination is valid in this research, the possible mechanism of fingerprinted formation we proposed in Figure 4f provides a basis model for further realizing the discrimination of else

functional group molecules by a better understanding between chemical features and metal-atom.

4.2.5 CONCLUSION

In this study, we demonstrated that a robust molecular fingerprinting of metal oxide nanowires selectively and repeatedly discriminates a target aldehyde molecule from structurally and chemically analogous volatile molecule mixture via cognitive adsorption. The metal oxide nanowires were composed of zinc oxide (ZnO) nanowires with molecularly fingerprinted titanium oxide shell. Interestingly, the molecularly fingerprinted of oxide nanowires can highly recognize aldehyde and remained its molecular recognition property until around 800 cycles of 400 °C heating treatment with rich atomic-diffusion of zinc into the titanium oxide shell. To a certain extend of structural isomer aldehyde discrimination performance by such fingerprinted nanowire, shape-recognition can be inferred. According to the results of the spectroscopy and mass-spectrometry experiments, a model of Zn atom assists the formation of molecule recognition function is proposed that rich surface Zn provides a stronger bridge carboxylate connection with template aldehyde, which prevents template from losing before fingerprinted formation at a heating procedure. Furthermore, thermal robustness character of the molecular fingerprinted nanowire is also owing to rich Zn atomic-diffusion stabilize amorphous TiO_x at high temperature treatment without crystal structure transition, allows us to utilize thermal molecular desorption strategy to transfer the selectively adsorbed aldehyde to electric signals of sensing device. The present selective-adsorption and sensing concept is successfully demonstrated by integrating benzaldehyde fingerprinted nanowire as a pre-selector with chemo-sensor. It is worthy to note that even dilution benzaldehyde component in mixture volatiles (limited to 0.05 ratio to initial undiluted), the selective sensing can also be achieved. Further applications of the molecularly fingerprinted nanowire presented here is a prospected for designed aiming molecular detection from complex atmosphere, on which very limited achievement is available within the molecular sensing and discriminating fields.

4.2.6 REFERENCES

[1]. Fahad, H. M., Shiraki, H., Amani, M., Zhang, C., Hebber, V. S., Gao, W., Ota, H., Hettick, M., Kiriya, D., Chen, Y.-Z., Chueh, Y.-L. & Javey, A. Room temperature multiplexed gas sensing using chemical-sensitive 3.5-nm-thin silicon transistors. Sci. Adv. 3, e1602557 (2017). DOI: 10.1126/sciadv.1602557

[2]. Vishinkin, R. & Haick, H. Nanoscale sensor technologies for disease detection via volatolomics. Small 11, 6142-6164 (2015). DOI: 10.1002/smll.201501904

[3]. Szulczyński, B. & Gębicki, J. Currently commercially available chemical sensors employed for detection of volatile organic compounds in outdoor and indoor air. Environments 4, 21 (2017). DOI: 10.3390/environments4010021

[4]. Broza, Y. Y. & Haick, H. Nanomaterial-based sensors for detection of disease by volatile organic compounds. Nanomedicine 8, 785-806 (2013). DOI: 10.2217/NNM.13.64

[5]. Tsuboi, O., Momose, S. & Takasu, R. Mobile sensor that quickly and selectively measures ammonia gas components in breath. FUJITSU Sci. Tech. 53, 38-43 (2017).

[6]. Meng, G., Zhuge, F. W., Nagashima, K., Nakao, A., Kanai, M., He, Y., Boudot, M., Takahashi, T., Uchida, K. & Yanagida, T. Nanoscale thermal management of single SnO2 nanowire: pico-Joule energy consumed molecule sensor. ACS Sens. 1, 997-1002 (2016). DOI: 10.1021/acssensors.6b00364

[7]. Nallon, E. C., Schnee, V. P., Bright, C., Polcha, M. P. & Li, Q. Chemical discrimination with an unmodified graphene chemical sensor. ACS Sens. 1, 26-31 (2016). DOI: 10.1021/acssensors.5b00029

[8]. Paska, Y., Stelzner, T., Christiansen S. & Haick, H. Enhanced sensing of nonpolar volatile organic compounds by silicon nanowire field effect transistors. ACS Nano 5, 5620-5626 (2011). DOI: 10.1021/nn201184c

[9]. Cho, S.-Y., Koh, H.-J., Yoo, H.-W., Kim, J.-S. and Jung, H.-T. Tunable volatile-organic-compound sensor by using Au nanoparticle incorporation on MoS2. ACS Sens. 2, 183-189 (2017). DOI: 10.1021/acssensors.6b00801

[10]. Su, S. & Hu, J. Ultrasound assisted low-concentration VOC sensing. Sens. Actuators B: Chem. 254, 1234-1241 (2018). DOI: 10.1016/j.snb.2017.07.175

[11]. Wulff, G. Molecular imprinting in cross-linked materials with the aid of molecular templates—A way towards artificial antibodies. Angew. Chem. Int. Ed. Engl. 34, 1812-1832 (1995). DOI:10.1002/anie.199518121

[12]. Haupt, K. & Mosbach, K. Molecularly imprinted polymers and their use in biomimetic sensors. Chem. Rev. 100, 2495-2504 (2000). DOI: 10.1021/cr990099w

[13]. Debliquy, M., Dony, N., Lahem, D., Tang, X., Zhang, C., Raskin, J.-P., Olivier, M.-G. Acetaldehyde chemical sensor based on molecularly imprinted polypyrrole. Proc. Eng. 168, 569-573 (2016). DOI: 10.1016/j.proeng.2016.11.527

[14]. Hussain, M., Kotova, K. & Lieberzeit, P. A. Molecularly imprinted polymer nanoparticles for formaldehyde sensing with QCM. Sensors 16, 1011 (2016). DOI:10.3390/s16071011

[15]. Liu, C., Wyszynski, B., Yatabe, R., Hayashi, K. & Toko, K. Molecularly imprinted sol-gel-based QCM sensor arrays for the detection and recognition of volatile aldehydes. Sensors 17, 382 (2017). DOI: 10.3390/s17020382

[16]. Holthoff, E. L. & Bright, F. V. Molecularly imprinted xerogels as platforms for sensing. Acc. Chem. Res. 40, 756-767 (2007). DOI: 10.1021/ar700087t

[17]. Holthoff, E. L. & Bright, F. V. Molecularly templated materials in chemical sensing. Anal. Chim. Acta 594, 147-161 (2007). doi:10.1016/j.aca.2007.05.044

[18]. Vasapollo, G., Sole, R. D., Mergola, L., Lazzoi, M. R., Scardino, A., Scorrano, S. & Mele, G. Molecularly imprinted polymers: present and future prospective. Int. J. Mol. Sci. 12, 5908-5945 (2011). DOI: 10.3390/ijms12095908

[19]. Chen, W., Ma, Y., Pan, J., Meng, Z., Pan, G. & Sellergren, B. Molecularly imprinted polymers with stimuli-responsive affinity: progress and perspectives. Polymers 7, 1689-1715 (2015). DOI:10.3390/polym7091478

[20]. Kubo, T., Hosoya, K. & Otsuka, K. Molecularly imprinted adsorbents for selective separation and/or concentration of environmental pollutants. Anal. Sci. 30, 97-104 (2014). DOI: 10.2116/analsci.30.97

[21]. Lofgreen, J. E. & Ozin, G. A. Controlling morphology and porosity to improve performance of molecularly imprinted sol-gel silica. Chem. Soc. Rev. 43, 911-933 (2014). DOI: 10.1039/c3cs60276a

[22]. Holthoff, E. L., Stratis-Cullum, D. N. & Hankus, M. E. A nanosensor for TNT detection based on molecularly imprinted polymers and surface enhanced Raman scattering. Sensors 11, 2700-2714 (2011). DOI:10.3390/s110302700

[23]. Kupai, J., Razali, M., Buyuktiryaki, S., Kecili, R. & Szekely, G. Long-term stability and reusability of molecularly imprinted polymers. Polym. Chem. 8, 666 (2017). DOI: 10.1039/c6py01853j

[24]. Chen, L., Xu, S. & Li, J. Recent advances in molecular imprinting technology: current status, challenges and highlighted applications. Chem. Soc. Rev. 40, 2922-2942 (2011). DOI: 10.1039/c0cs00084a

[25]. Naklua, W., Mahesh, K., Chen, Y. Z., Chen, S., Roongnapa, S. Molecularly imprinted polymer microprobes for manipulating neurological function by regulating template-dependent

molecular interactions. Proc. Biochem. 51, 124-157 (2016). DOI: 10.1016/j.procbio.2015.11.002

[26]. Tominaga, Y., Kubo, T., Yasuda, K., Kato, Keita & Hosoya, K. Development of molecularly imprinted porous polymers for selective adsorption of gaseous compounds. Micropor. Mesopor. Mater. 156, 161-165 (2012). DOI: 10.1016/j.micromeso.2012.02.020

[27]. Bunte, G., Hürttlen, J., Pontius, H., Hartlieb, K. & Krause, H. Gas phase detection of explosives such as 2,4,6-trinitrotoluene by molecularly imprinted polymers. Anal. Chim. Acta 591, 49-56 (2007). DOI: 10.1016/j.aca.2007.02.014

[28]. Mujahid, A., Lieberzeit, P. A. & Dickert, F. L. Chemical sensors based on molecularly imprinted sol-gel materials. Materials 3, 2196-2217 (2010). DOI: 10.3390/ma3042196

[29]. Lieberzeit, P. A., Afzal, A., Glanzing, G. & Dickert, F. L. Molecularly imprinted sol-gel nanoparticles for mass-sensitive engine oil degradation sensing. Anal. Bioanal. Chem. 389, 441-446 (2007). DOI: 10.1007/s00216-007-1274-3

[30]. Mujahid, A., Afza., A., Glanzing, G., Leidl, A., Lieberzeit, P. A. & Dickert, F. L. Imprinted sol-gel materials for monitoring degradation products in automotive oils by shear transverse wave. Anal. Chim. Acta 675, 53-57 (2010). doi:10.1016/j.aca.2010.07.005

[31]. Li, X., Wang, J., Li, M., Jin, Y., Gu, Z., Liu, C. & Ogino, K. Fe-doped TiO2/SiO2 nanofibrous membranes with surface molecular imprinted modification for selective photogradation of 4-nitrophenol. Chin. Chem. Lett. in press (2017). DOI: 10.1016/j.cclet.2017.09.007

[32]. Han, D., Li, Y. & Jia, W. Preparation and characterization of molecularly imprinted SiO2-TiO2 and photo-catalysis for 2, 4-dichlorophenol. Adv. Mat. Lett. 1, 188-192 (2010) DOI: 10.5185/amlett.2010.7137

[33]. Zhang, Y., Liu, Q., Zhang, J., Zhu, Q. & Zhu, Z. A highly sensitive and selective formaldehyde gas sensor using a molecular imprinting technique based on Ag-LaFeO3. J. Mater. Chem. C 2, 10067-10072 (2014). DOI: 10.1039/c4tc01972e

[34]. Chen, B., Liu, C. Ge, L. & Hayashi, K. Localized surface plasmon resonance gas sensor of Au nano-islands coated with molecularly imprinted polymer: Influence of polymer thickness on sensitivity and selectivity. Sens. Actuators B 231, 787-792 (2016). DOI: 10.1016/j.snb.2016.03.117

[35]. Wu, W., Wen, X. & Wang, Z. L. Taxel-addressable matrix of vertical-nanowire piezoelectric transistors for active and adaptive tactile imaging. Science 340, 952-957 (2013). DOI: 10.1126/science.1234855

[36]. Yasui, T., Yanagida, T., Ito, S., Konakade, Y., Takeshita, D., Naganawa, T., Nagashima, K., Shimada, T., Kaji, N., Nakamura, Y., Thiodorus, I. A., He, Y., Rahong, S., Kanai, M., Yukawa, H., Ochiya, T., Kawai, T. & Baba, Y. Unveiling massive numbers of cancer-related urinary-

microRNA candidates via nanowires. Sci. Adv. 3, e1701133 (2017). DOI: 10.1126/sciadv.1701133

[37]. Borganonkar, H. V., Raverkar, S. R. & Chandalia, S. B. Liquid phase oxidation of toluene to benzaldehyde by air. Ind. Eng. Chem. Prod. Res. Dev. 23, 455-458 (1984). DOI: 10.1021/i300015a026

[38]. Ligor, M., Ligor, T., Bajtarevic, A., Ager, C., Pienz, M., Klieber, M., Denz, H., Fiegl, M., Hilbe, W., Weiss, W., Lukas, P., Jamnig, H., Hackl, M., Buszewski, B., Miekisch, W., Schubert, J. & Amann, A. Determination of volatile organic compounds in exhaled breath of patients with lung cancer using solid phase microextraction and gas chromatography mass spectroscopy. Clin. Chem. Lab Med. 47, 550-560 (2009). DOI: 10.1515/CCLM.2009.133.

[39]. Wang C, Hosomi T, Nagashima K, et al. Rational Method of Monitoring Molecular Transformations on Metal-Oxide Nanowire Surfaces[J]. Nano letters, 2019, 19(4): 2443-2449.

[40]. Papageorgiou S K, Kouvelos E P, Favvas E P, et al. Metal–carboxylate interactions in metal–alginate complexes studied with FTIR spectroscopy[J]. Carbohydrate research, 2010, 345(4): 469-473.

[41]. Xiong G, Pal U, Serrano J G, et al. Photoluminesence and FTIR study of ZnO nanoparticles: the impurity and defect perspective[J]. physica status solidi c, 2006, 3(10): 3577-3581.

[42]. Mazzeo R, Prati S, Quaranta M, et al. Attenuated total reflection micro FTIR characterisation of pigment–binder interaction in reconstructed paint films[J]. Analytical and bioanalytical chemistry, 2008, 392(1-2): 65-76.

[43]. Gershevitz O, Sukenik C N. In situ FTIR-ATR analysis and titration of carboxylic acid-terminated SAMs[J]. Journal of the American Chemical Society, 2004, 126(2): 482-483.

[44]. Liu W, Sarofim A F, Flytzani-Stephanopoulos M. Complete oxidation of carbon monoxide and methane over metal-promoted fluorite oxide catalysts[J]. Chemical engineering science, 1994, 49(24): 4871-4888.

[45]. Li C, Sakata Y, Arai T, et al. Adsorption of carbon monoxide and carbon dioxide on cerium oxide studied by Fourier-transform infrared spectroscopy. Part 2.—Formation of formate species on partially reduced CeO_2 at room temperature[J]. Journal of the Chemical Society, Faraday Transactions 1: Physical Chemistry in Condensed Phases, 1989, 85(6): 1451-1461.

[46]. Zhang Q L, Du L C, Weng Y X, et al. Particle-size-dependent distribution of carboxylate adsorption sites on TiO2 nanoparticle surfaces: insights into the surface modification of nanostructured TiO2 electrodes[J]. The Journal of Physical Chemistry B, 2004, 108(39): 15077-15083.

[47]. Saw E T, Oemar U, Ang M L, et al. High-temperature water gas shift reaction on Ni–Cu/CeO_2 catalysts: effect of ceria nanocrystal size on carboxylate formation[J]. Catalysis Science & Technology, 2016, 6(14): 5336-5349.

[48]. Deacon G B, Phillips R J. Relationships between the carbon-oxygen stretching frequencies of carboxylato complexes and the type of carboxylate coordination[J]. Coordination Chemistry Reviews, 1980, 33(3): 227-250.

[49]. Nakamoto K. Infrared and Raman Spectra of Inorganic and Coordination Compounds[J]. Handbook of Vibrational Spectroscopy, 2006.

[50]. Manhas B S, Trikha A K. Relationships between the direction of shifts in the carbon-oxygen stretching frequencies of carboxylato complexes and the type of carboxylate coordination[J]. Journal of the Indian Chemical Society, 1982, 59(2): 315-319.

[51]. Martini D, Pellei M, Pettinari C, et al. Synthesis, spectroscopic and structural characterization of Cu (II) derivatives of tris (pyrazol-1-yl) methanes[J]. Inorganica chimica acta, 2002, 333(1): 72-82.

[52]. Li Z, Jiang W T, Hong H. An FTIR investigation of hexadecyltrimethylammonium intercalation into rectorite[J]. Spectrochimica Acta Part A: Molecular and Biomolecular Spectroscopy, 2008, 71(4): 1525-1534.

[53]. Urlaub R, Posset U, Thull R. FT-IR spectroscopic investigations on sol–gel-derived coatings from acid-modified titanium alkoxides[J]. Journal of non-crystalline solids, 2000, 265(3): 276-284.

[54]. Brydson R, Sauer H, Engel W, et al. Electron energy loss and X-ray absorption spectroscopy of rutile and anatase: a test of structural sensitivity[J]. Journal of Physics: Condensed Matter, 1989, 1(4): 797.

[55]. Farges F, Brown G E, Rehr J J. Ti K-edge XANES studies of Ti coordination and disorder in oxide compounds: Comparison between theory and experiment[J]. Physical Review B, 1997, 56(4): 1809.

[56]. Paris E, Mottana A, Della Ventura G, et al. Titanium valence and coordination in synthetic richterite; Ti-richterite amphiboles; a synchrotron-radiation XAS study[J]. European Journal of Mineralogy, 1993, 5(3): 455-464.

[57]. Fuchs, P., Loeseken, C., Schubert, J. K. & Miekisch W. Breath gas aldehydes as biomarkers of lung cancer. Int. J. Cancer 126, 2663-2670 (2010). DOI: 10.1002/ijc.24970

[58]. Liu, H., Wang, H., Li, C., Wang, L., Pan, Z. & Wang L. Investigation of volatile organic metabolites in lung cancer pleural effusions by solid-phase microextraction and gas chromatography/mass spectroscopy. J. Chromatogr. B 945-946, 53-59 (2014). DOI: 10.1016/j.jchromb.2013.11.038

[59]. Peng, G., Tisch, U., Adams, O., Hakim, M., Shehada, N., Broza, Y. Y., Billan, S., Abdah-Bortnyak, R., Kuten, A. & Haick, H. Diagnosing lung cancer in exhaled breath using gold nanoparticles. Nat. Nanotechnol. 4, 669-673 (2009). DOI: 10.1038/nnano.2009.235

[60]. Filipiak, W., Sponring, A., Filipiak, A., Ager, C., Schubert, J., Miekisch, W., Amann, A. & Troppmair, J. TD-GC-MS analysis of volatile metabolites of human lung cancer and normal cells in vitro. Cancer Epidemiol Biomarkers Prev. 19, 182-195 (2010). DOI: 10.1158/1055-9965.EPI-09-0162

[61]. Mochalski, P., Sponring, A., King, J., Unterkofler, K., Troppmair, J. & Amann, A. Release and uptake of volatile organic compounds by human hepatocellular carcinoma cell (HepG2) in vitro. Cancer Cell Int. 13, 72 (2013). DOI: 10.1186/1475-2867-13-72

[62]. Trefz, P., Koehler, H., Klepik, K. Moebius, P., Reinhold, P., Schubert, J. K. & Miekisch, W. Volatile emissions from Mycobacterium avium subsp. paratuberculosis mirror bacterial growth and enable distinction of different strains. PLoS One 8, e76868 (2013). DOI: 10.1371/journal.pone.0076868

4.2.7 Supporting Information

4.2.7.1 Concept schematic illumination

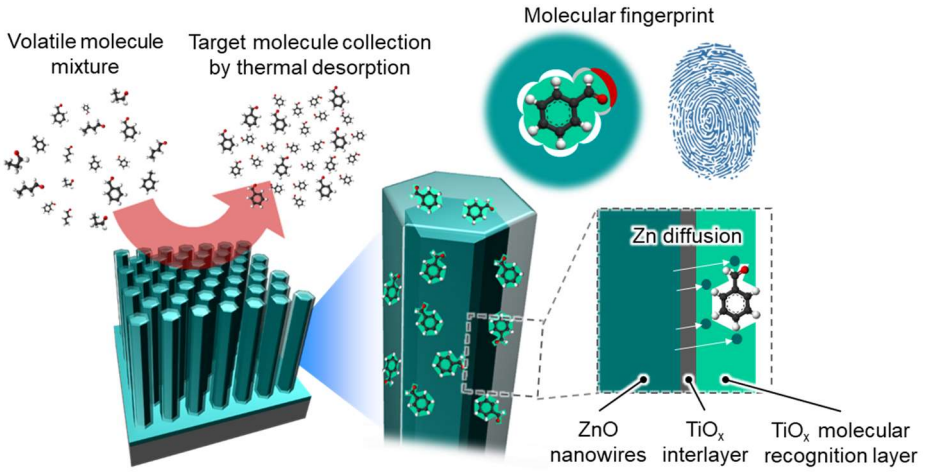

Figure S1. *Schematic illumination of metal-oxides molecular fingerprinted nanowire*

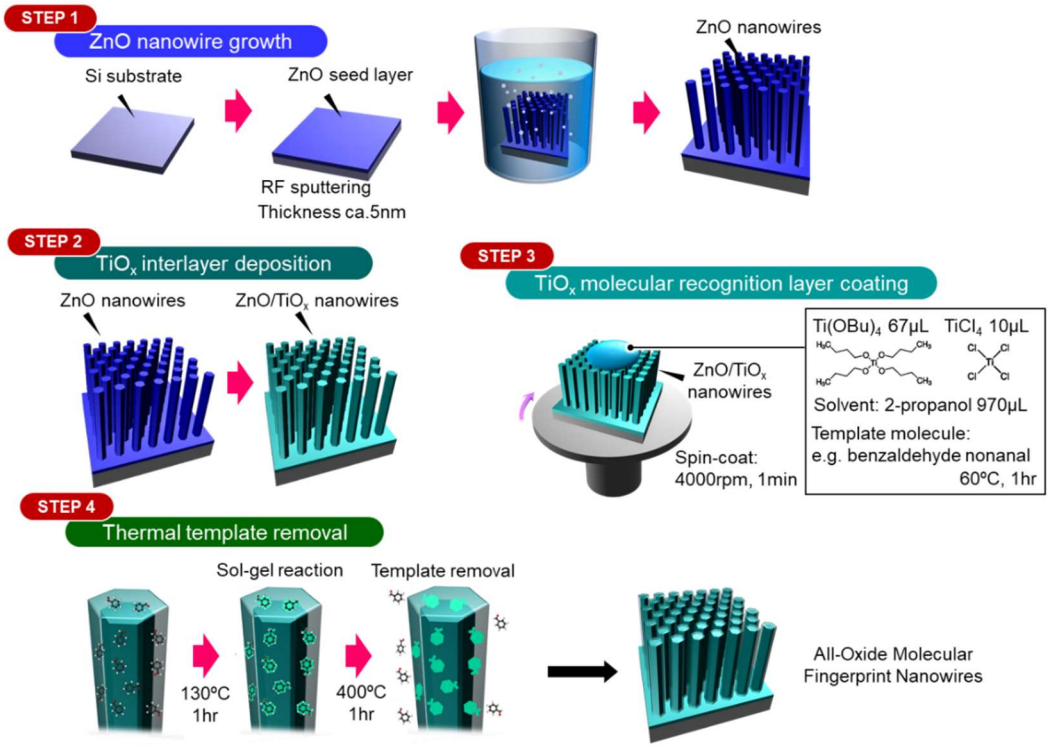

Figure S2. *Molecularly fingerprinted metal-oxide nanowires formation process*

4.2.7.2 Molecularly fingerprinted nanowire structure characterization

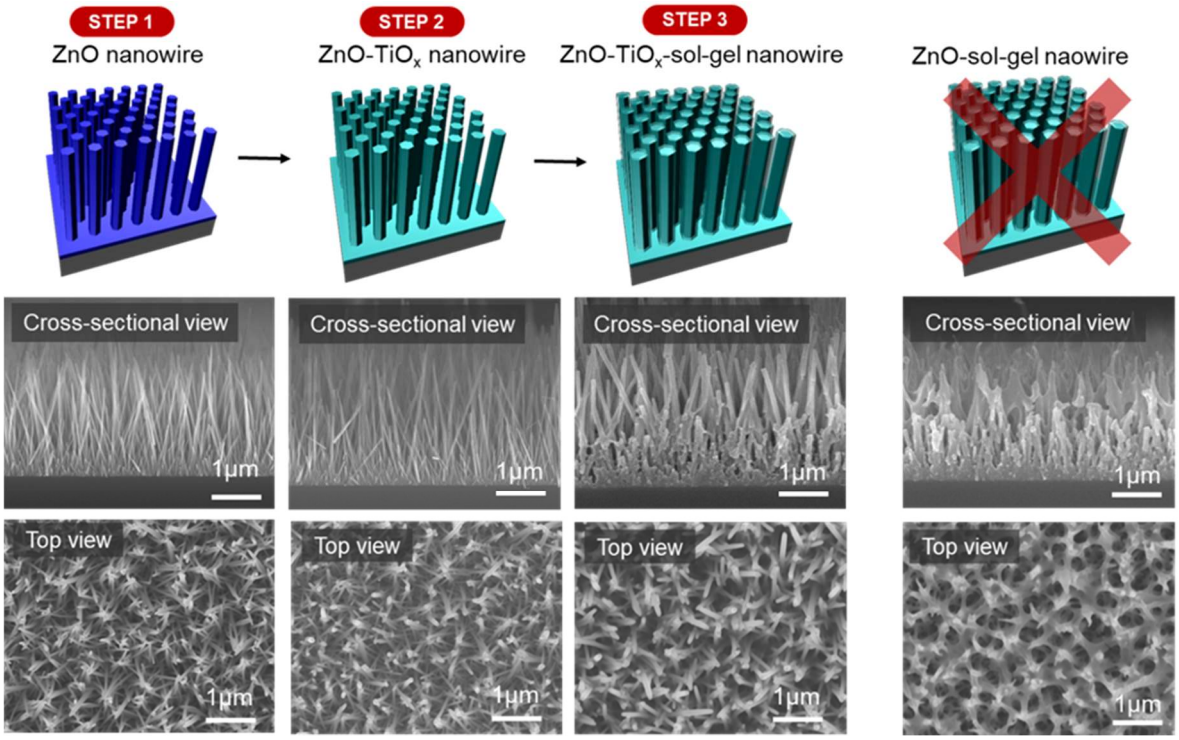

Figure S3. *FE-SEM images after each fingerprinted nanowire synthesis step. TiO_x-interlayer is necessary for preventing nanowire from being etched by hydrochloric acid, which is produced by sol-gel layer formation.*

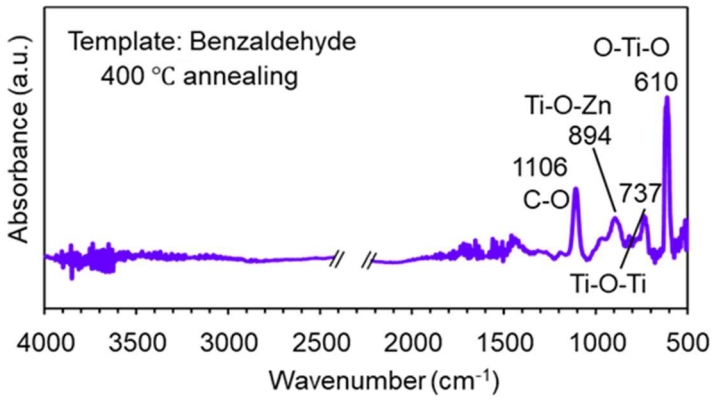

Figure S4. *Thermally template removal process confirmation by FT-IR. Template benzaldehyde can be completely remove at 400 ℃ annealing for 1 hour.*

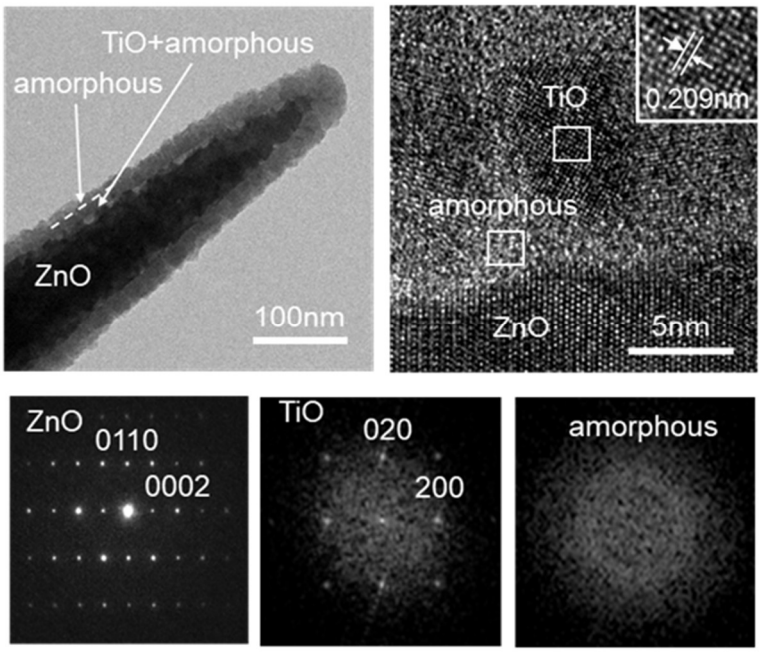

Figure S5. *TEM and SAED images of a molecularly fingerprinted nanowire pre-treated 1 hour at 400 °C for crystal structure conformation.*

4.2.7.3 Desorbed molecule analyses by GC-MS

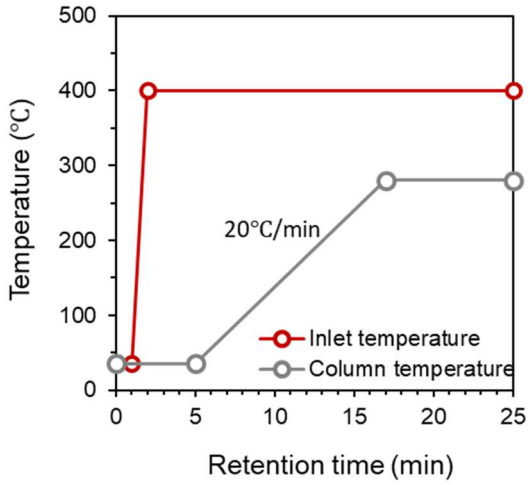

Figure S6. *The temperature program: (Inlet temperature and column temperature) for desorbed gas analysis by GC-MS.*

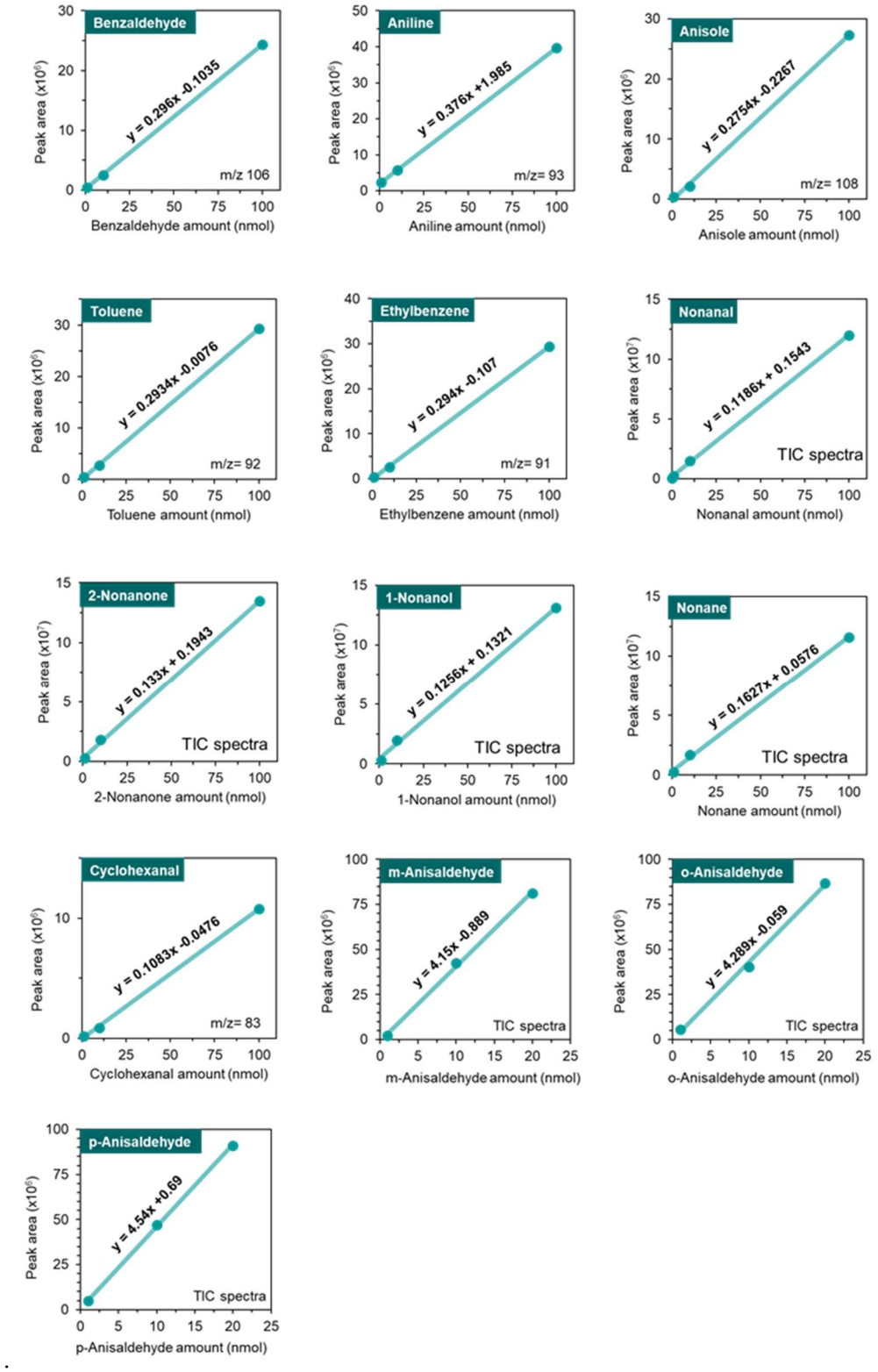

Figure S7*. Calibration curves for desorption amount calculation of every kinds of molecules involved in this research.*

4.2.7.4 Molecule recognition property of molecularly fingerprinted nanowires

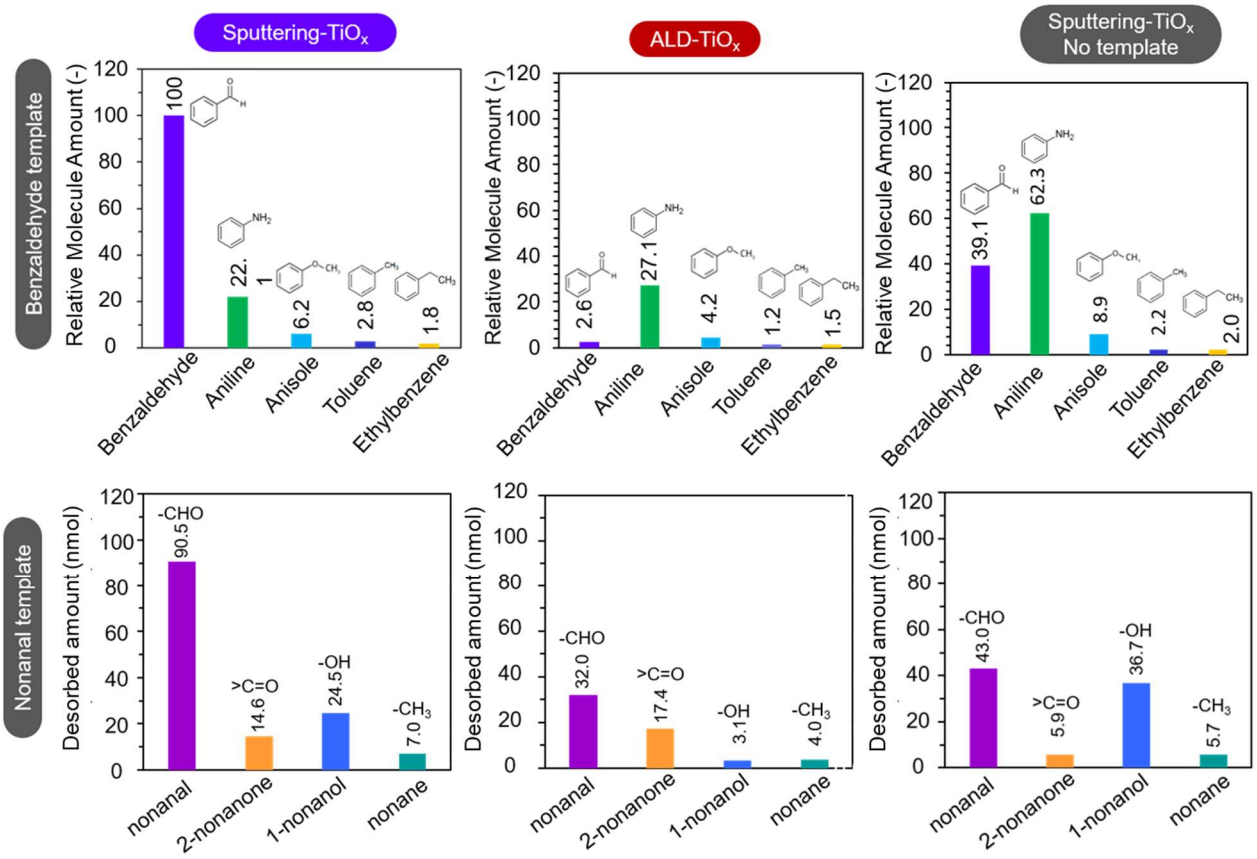

Figure S8. *Desorbed molecules amount from mixture volatiles adsorption. Benzaldehyde fingerprinted nanowires adsorbed in a mixture of benzaldehyde, aniline, anisole, toluene and ethylbenzene, nonanal fingerprinted nanowires adsorbed in a mixture of nonanal, 2-nonanone, 1-nonanol and nonane. Atom Zn diffused to shell-layer is considered as a crucial factor for the target molecule recognition property.*

4.2.7.5 Molecule Recognition property of molecularly fingerprinted formation mechanism

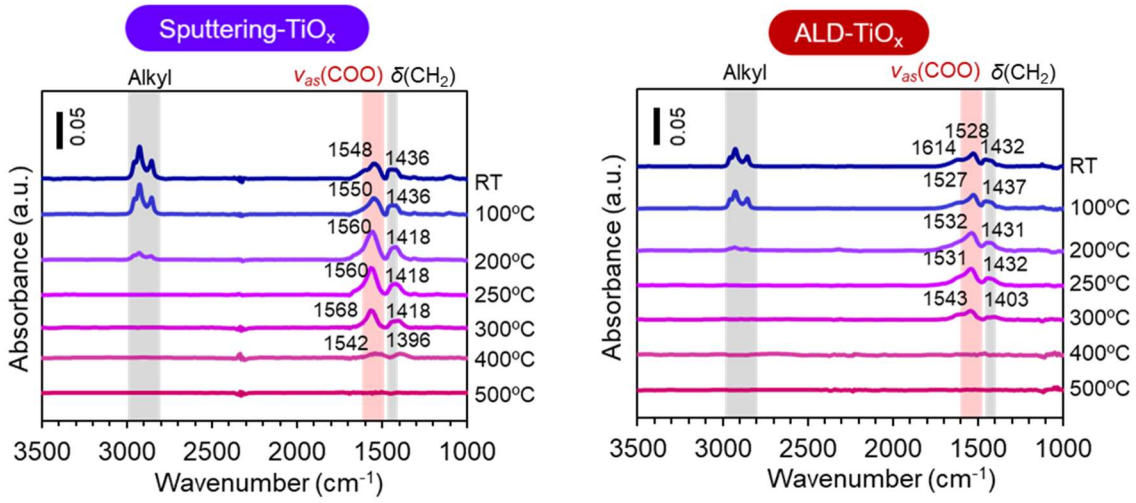

Figure S9. *FT-IR spectra of template aldehyde exist states in metal-oxide (C-H and C-O areas together) during fingerprint formation procedure at a series elevated temperature for picking symmetric COO vibration wavenumber out from C-H bending vibration.*

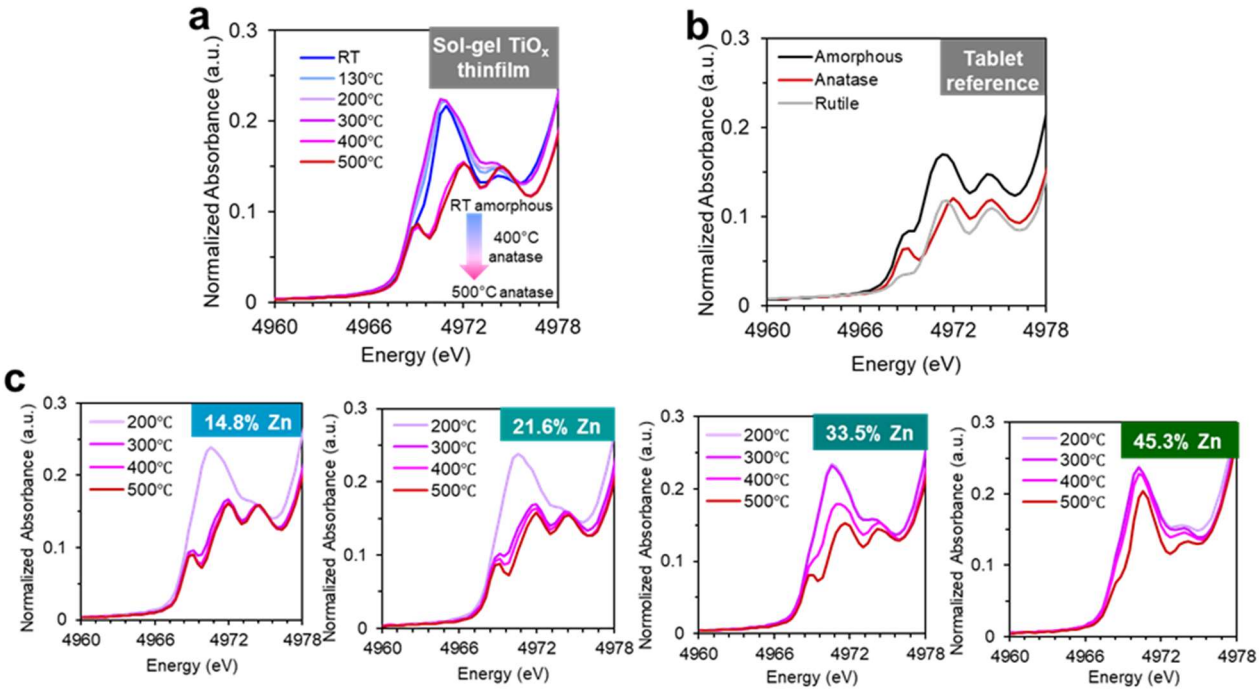

Figure S10. *Local structure around Ti atoms identified by XANES. (a) Sol-gel TiO_x thinfilm pre-treated from room temperature to 500 ºC; (b) Standard TiO_x (amorphous, rutile and anatase crystal structure) as references;(c) Surface Zn atom component effected to the structure transformation temperature of fingerprinted nanowires.*

4.2.7.6 Validation of model using ketone & alcohol molecules

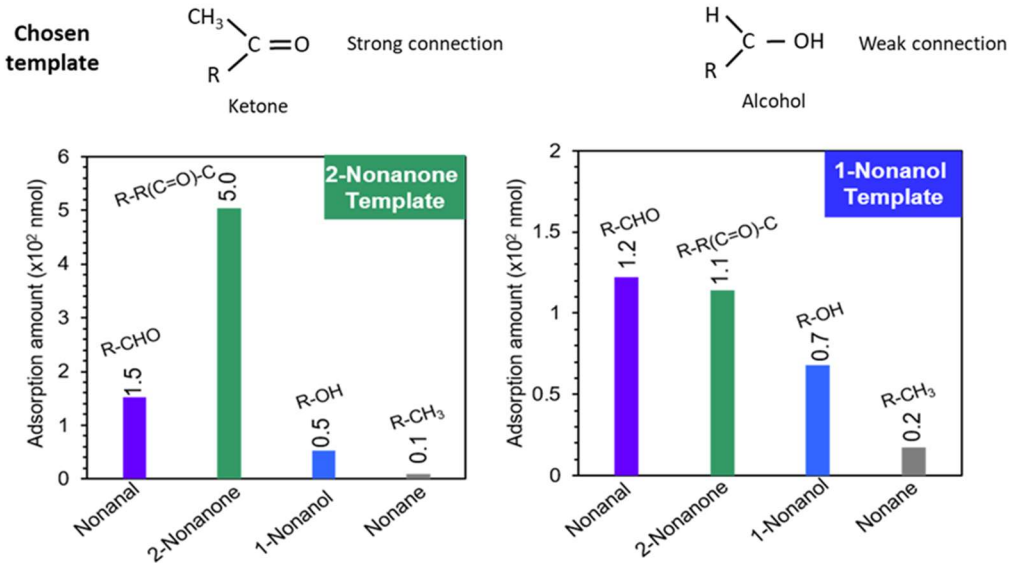

Figure S11. *Target molecule recognition property by ketone (left) and alcohol (right) fingerprinted nanowires for the model validation.*

4.2.7.7 Aldehyde molecule discriminating sensing from mixture volatiles

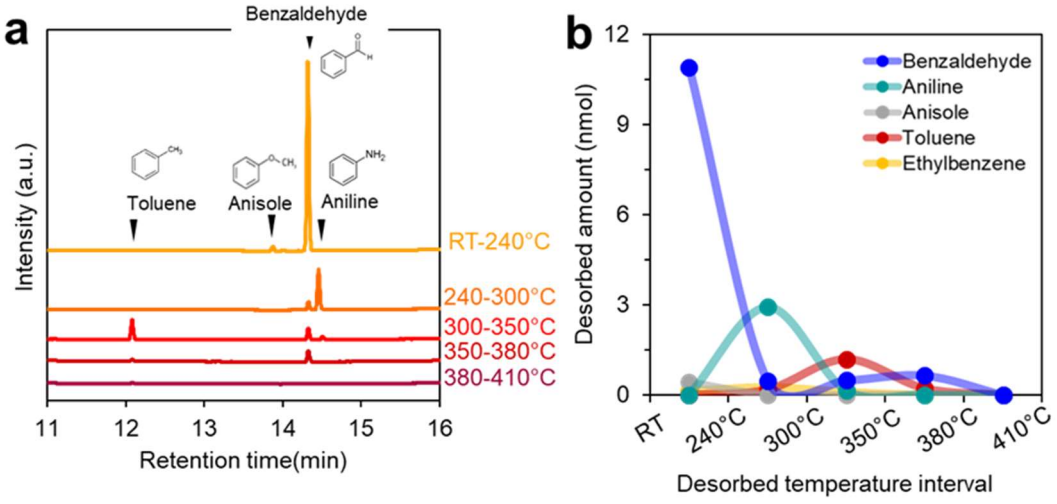

Figure S12. *Desorbed molecules analysis by mixture adsorption (benzaldehyde undiluted). (a) TIC spectra from GC-MS analysis by a continuously temperature evaluated measurement without taking sample out. (b) Molecules desorbed amount calculated from (a).*

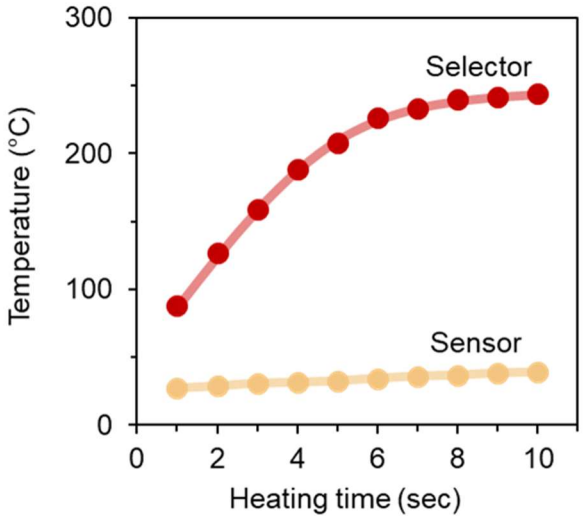

Figure S13. *Temperature interference between selector and sensor at different selector heating time condition. Selector and sensor temperature are collected together at every condition by thermally graphic.*

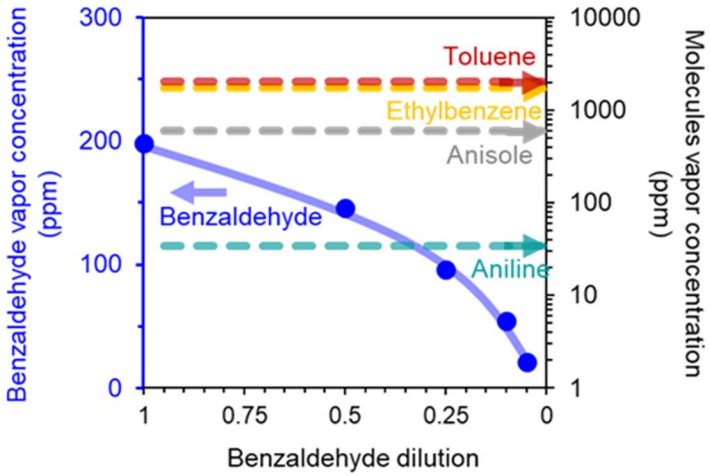

Molecules	Vapor pressure
Benzaldehyde	0.13@26°C
Aniline	0.083@25°C
Anisole	0.59@25°C
Toluene	2.79@25°C
Ethylbenzene	1.16@25°C

Figure S14. *Molecules concentration calculated by GC-MS from their naturally room temperature vapor. Only benzaldehyde is gradatim diluted (undiluted defined as 1) in every mixture condition.*

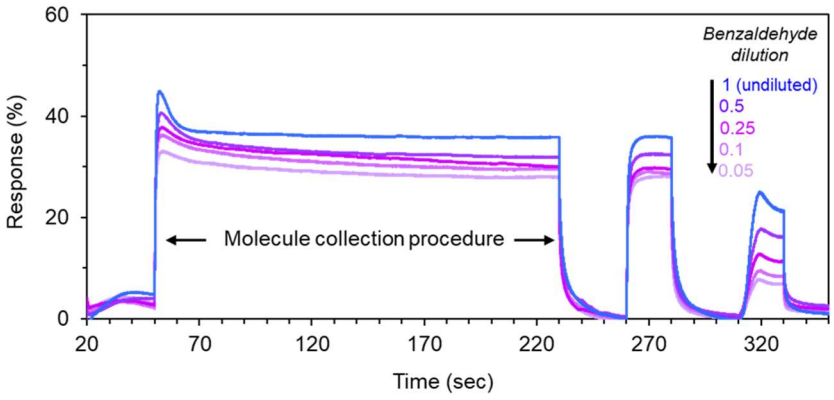

Figure S15. *Whole dynamic sensing response curve of every adsorption in mixture with various benzaldehyde component.*

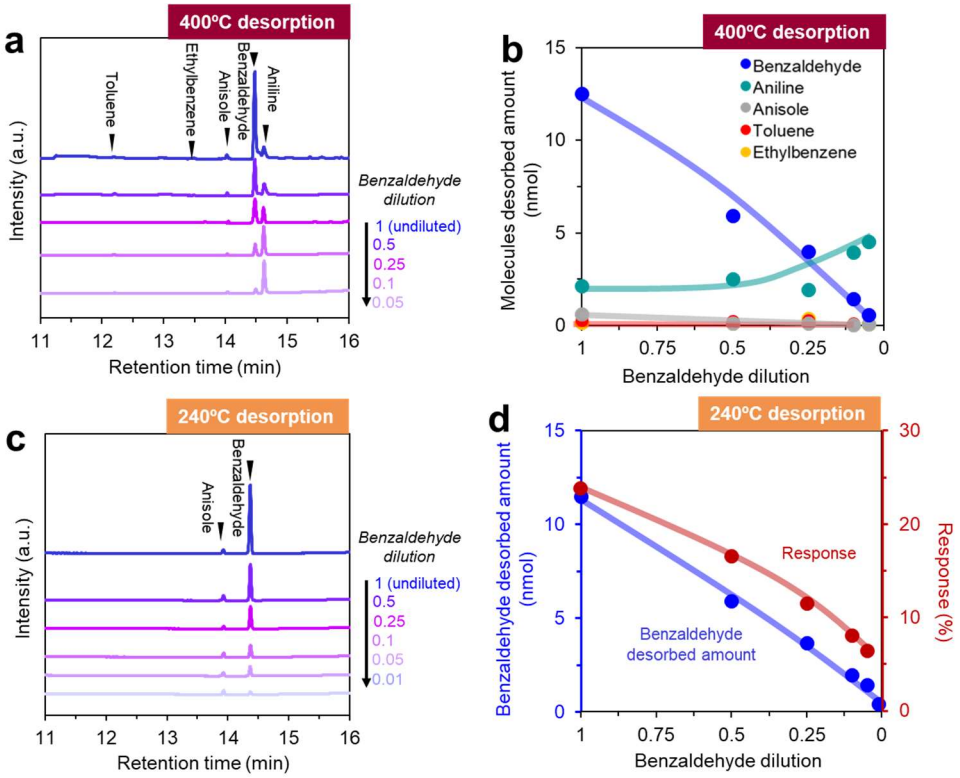

Figure S16*. Desorbed molecules analysis from mixture with various benzaldehyde component adsorption. (a) 400 ℃ desorbed TIC spectra and (b) related calculated molecule amount. (c) 240 ℃ desorbed TIC spectra and (d) related calculated molecule amount together with sensing response for demonstrating the benzaldehyde selected sensing.*

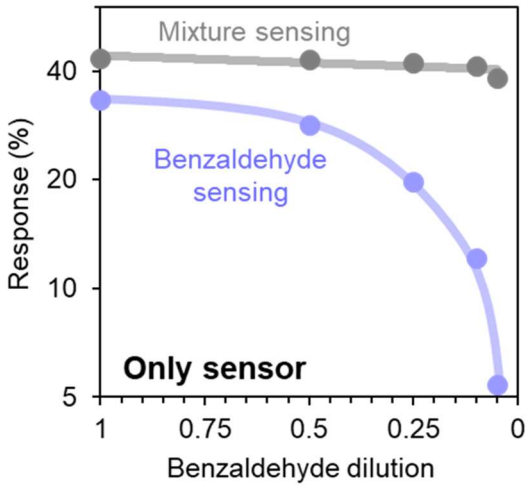

Figure S17*. Single benzaldehyde sensing and mixture sensing by only sensor in various benzaldehyde component atmosphere.*

4.3 Sub-ppb Nonanal Sensing by Thermally Robust Nanowire Molecular Preconcentration Platform

4.3.1 ABATRACT

The demand for trace nonanal detection by portable electronic device improved since it been proved as an effective biomarker of lung cancer from breath. Here, ultra-low nonanal molecules detection is accomplished using a rational micro-system through integrating a nonanal pre-concentrator based on metal oxide nanowire for nonanal molecule collection, with a sensitive gas sensor in a package together. Such nanowire concentrator is preponderate for its high nonanal collection ability caused by the recognition space inventively produced and good thermal stability of titanium oxide recognition layer. A significantly sensitivity enhancement (about 200 times) successfully achieved by applying this pre-concentrator. More worthy to mention is even exposure to sub-ppb level nonanal, obvious sensing response can be observed. It is the first time to realize such ultra-low nonanal sensing and this micro-system has the potential to realize early detection of lung cancer by simple human breath monitoring approach.

KEY WORDS: Nonanal sensing, preconcentration platform, metal oxide nanowire, thermally robust, low detection limit

4.3.2 INTRODUCTION

Lung cancer has been regarded as a horrible disease due to the high possibility of being in post-stage once examined and low survival rate [1-3]. Some meaningful researches about human breath reported that the breath of lung cancer patients includes higher concentration aldehydes such as nonanal, can be an effective lung cancer biomarker [4-7], therefore it is vital importance to develop one kind of simple exhaled breath monitoring system with noninvasive and safe screening, diagnosis, and follow-up of nonanal detection. Molecule detection methods, such as nano-mechanical sensor [8-9] and semiconductor gas sensor [10-11] can be used to detect nonanal molecule with-out expensive and time-consuming analytical measurements. In spite of a fact that patients' breath contains larger nonanal amount, parts per billion (ppb) level nonanal trace is too small to be tracked and until now, it is still beyond the detect limitation for portable sensing device [12-13]. Under this conditions, adding a nonanal concentration stage (pre-concentrator) prior to sensitive gas sensor probably be a potential solution. In such expected technique, gas concentration is increased temporarily by releasing molecules through controlled heating the concentrator material, which adsorbing molecules over a definite period of time, making sensing easier.

Several options can be chosen as pre-concentration material, such as metal-organic frameworks (MOF), mesoporous SiO_2 powders materials, carbon nanotubes and so on [14-17], they have been successfully used for some species of volatile organic compounds (benzene, acetone) concentrating and detecting at low concentration level [18-20]. Apart from them, nanowire structure with remarkable feature of surface-to-volume ratio with defined crystal planes and good thermal conductivity make it a priority choice [21-22], which means relatively large quantities of nonanal molecules can be concentrated on its surface and quickly desorbed when suitably heating. For the purpose of further enhancing nonanal concentrated ability of nanowire structure, our strategy is developing a fingerprint oxide layer on nanowire surface. Fingerprint oxide is defined from fabricating a molecular recognition space by introducing the molecule as a template during the oxide material formation process. The molecular recognition space is organized around a template molecule as chemical synthesis mediated material formation, and a molecular recognition space turns out to be available after removing the template molecule. Theoretically, molecule adsorption and recognition of nanowire pre-concentrator would be enhanced.

In this study, a sensing micro-system integrated by nonanal pre-concentration and sensitive gas sensor was designed to the end of sub-ppb level nonanal detection. Molecular fingerprint nanowire fabricated from ZnO/TiO_2 core-shell nanowires was chosen as pre-concentrator material due to their fascinating conductive properties and thermal stability [23-24]. Our strategy offers an effective nonanal sensing approach towards sub-ppb level concentration, which had not been achievable previously.

4.3.3 EXPERIMENT

Nonanal pre-concentrator fabrication.

The fabrication process of nonanal pre-concentrator (Figure S1) is described as following: The nonanal concentrator consisted of a heater on the surface of Si (100) wafer (0.7 cm × 0.7 cm) substrate and molecularly fingerprinted oxide nanowires were growth over the heater. Heater on the substrate can be obtained by RF sputtering method to deposit Pt (50 W for 40 min) directly onto serpentine mask concealed silicon wafer. Prior to the nanowire growth, ZnO seed layer was deposited onto this substrate by RF sputtering (50 W power for 3 min), it is necessary for the following hydrothermal method nanowire growth. A solution for the hydrothermal reaction was prepared by dissolving equimolar ratio of 25 mM zinc nitrate hexahydrate ($Zn(NO_3)_2 \cdot 6H_2O$) and hexamethylenetetramine (HMTA, $(CH_2)_6N_4$) into 150 mL deionized water mixed with 2.0 g branched polyethylenimine (PEI, Mn=1800) solution. All materials were analytical grade and used without further purifications. Dipped the substrate into the solution and kept at 95 °C for 12 h, ZnO nanowire structure can be obtained. Before making the fingerprint layer on the nanowire structure, a titanium oxide (TiO_x) intermediate layer was deposited onto the ZnO nanowires by Ti sputtering (50 W for 30 min) and oxygen plasma treatment (150 W power for 10 min) for the purpose of preventing ZnO nanowires being destroyed by hydrogen chloride, which was a by-product of the after-mentioned sol-gel process. Next fingerprinted layer was formed onto such nanowires by alkoxide based sol-gel technique. Spin-coating the sol-gel solution which was string at 60 °C for 1 hour with the composition of 67 µl tetrabutyl titanate alkoxide precursor, 10 µl titanium (IV) chloride catalyst agent, 970 µl 2-propanol solvent and intensively induced 13.4 mg nonanal template molecule. Then, the substrate was baked at 180 °C for 1 hour to form the titanium oxide shell and at the same time, interactions between the nonanal template molecule and the titanium oxide skeleton can be formed. Finally, the fingerprinted oxide nanowires were annealing at 500 °C for 1 hour to completely remove template nonanal molecule, thereby nonanal pre-concentrator can be

obtained. For the nonanal molecule collection ability comparison, the non-imprinted nanowire pre-concentrator was prepared by similar method of the fingerprint nanowire pre-concentrator, except that the template didn't present in the sol-gel solution. Thin-film making was prepared only through RF sputtering (50 W for 30 min).

Characterization of fingerprint nanowire pre-concentrator

Field Emission Scanning Electron Microscope (FESEM) images were acquired conducted on a JEOL JSM-7610F instrument. Transmission electron microscope (TEM) images, Selected Area Electron Diffraction (SAED) patterns and Energy Dispersive X-ray Spectroscopy (EDS) were collected on a JEOL ARM-200F microscope. X-ray Photoelectron Spectroscopy (XPS) measurements were employed on a Kratos AXIS-165 spectrometer. Surface charging effects were corrected with a C 1s peak at 284.6 eV as a reference.

Sensing microsystem of the nonanal pre-concentrator integrated with sensor

The sensing system consisted of gas control system and a sensing device. Nonanal gas was controlled by gas dilution equipment and nitrogen was flowing as the background gas to dilute nonanal gas. Concentration control by adjusting flow rate of nonanal and nitrogen. A 16-element chemo-sensitive sensor array was used for performing nonanal sensing response, it was fabricated by coating gas chromatography (GC) stationary-phase materials and blends of carbon black on to chemo-sensitive sensor devices (Figure S2). In this study, the sensing data was collected by only one sensor of such 16-element chemo-sensitive sensor array, this sensor is fabricated by automatic spotting machine (customize machine, Musashi Engineering, Inc., Tokyo, Japan) using needle syringe to dropped the sensing material (10 mg/mL PEG 4000 and 7.5 mg/mL carbon black fully mixed water solution) onto the sensor device substrate. Details of the sensor can be find in the publication of Panasonic [39]. Nonanal pre-concentrator and sensor were integrated on a sensor chip [40]. The heating temperature were confirmed by temperature monitor (APISRE corporation FSC-2000).

Molecule collection ability confirmation

Flow nonanal into the sensing system and let pre-concentrator adsorbed nonanal molecules for 3 min, nonanal collection amount was then calculated by the peak area in the spectrum got from Gas Chromatography–Mass Spectrometry (Shimadzu GC-MS-QP 5050A instrument) equipped with a Supelco SLB-IL60 capillary column and an OPTIC-4 inlet temperature control system. To analyze the desorbed compounds, 240 °C, 300 °C, 350 °C, 380 °C and 410 °C were

used and hold for 1 second to simulate the desorption temperature of pre-concentrator at different heating time (see the Figure S2). For the desorption temperature measurement of adsorbed molecules, we utilized a fused silica capillary tube with salinized surface modification (length 1 m, inner diameter 0.1 mm) equipped on the GC-MS, the inlet temperature increase from 35 ℃ to 400 ℃ with a rate of 0.5 ℃ /s. The temperatures of GC/MS interface and ion source were set to be 200 °C.

4.3.4 RESULTS AND DISCUSSION

Sensing micro-system structure illumination

Our proposed methodology using micro-system by a fingerprint nanowire pre-concentrator integrated with sensor enabled us to detected ultra-low concentration nonanal, which are undetectable in convention methods. Figure 1 provides the schematic diagram illustrating the operation of our micro-system. The fingerprint nanowire traps nonanal when kept at a moderate temperature (e.g., room temperature) over a certain time, and then a rapid thermal desorption when suitably heated to generate a high gas concentration for a short period, which make ultra-low concentration gas detection become possible.

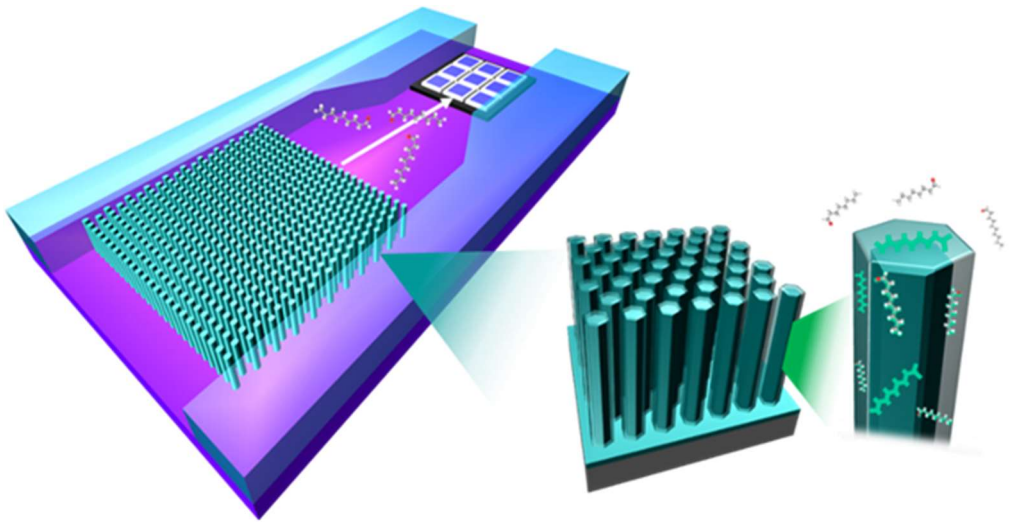

Figure 1. *Schematic illustration of sensing micro-system by fingerprint nonanal nanowire pre-concentrator integrated with gas sensor*

Characterization and nonanal collection ability of fingerprint nanowire

A typical FESEM image in Figure 2a presents the side view of fingerprinted oxide nanowires grown on Si substrate. The details of growth conditions are described in Experimental Section and figure caption. Most nanowires are grown vertically and uniformly onto the substrate with average length about 3 μm. Detail structure analyzed by TEM image (Figure 2b) displays a single molecular fingerprinted oxide nanowire with diameter around 100 nm. Core-shell structure is confirmed by magnificent TEM image (Figure 2c), together with which shown out the HRTEM images of ZnO core and TiO_2 shell layer areas. The Selected Area Electronic Diffraction (SAED) pattern displays a certainly single crystalline ZnO core with a lattice spacing of 0.28 nm that can be assigned to hexagonal structure. As for the shell layer, both single crystal and amorphous structure exist, which indicates that anatase titanium monoxide (TiO_2) nanoclusters with a lattice spacing of 0.35 nm embeds in amorphous shell. The surface elemental composition analysis of such nanowire (Figure S2) is characterized by EDS. Titanium and zinc elements distribution separately, obvious boundary illustrates TiO_2 distributes outside the ZnO nanowire. XPS spectrums (Figure S3) confirm $Zn^{2+}$and Ti^{4+} states [25-26] in fingerprint nanowire. In order to investigate the nonanal collecting ability, we focus on comparing the desorbed nonanal amount of as-obtained nanowire by peak area of spectrums exported from GC-MS analyzing after collection. Nonanal amount is calculated based on calibration curve (Figure S4). At the first consideration, nonanal collection ability can be, to a large extent, affected by pre-treatment temperature. Apply several annealing temperatures (300 °C to 1000 °C) to pretreat the nanowire, further nonanal adsorption amount in 90 ppm nonanal atmosphere are carried out in Figure 2d. A tendency of nonanal desorbed amount increase at first and then decrease as rising the annealing temperature. The reason for the first increase was taken for incomplete removal of template nonanal molecule. Existence state of template nonanal molecule (Figure S5) backs up this explanation. And excessive temperature will destroy the sites purposely made for nonanal adsorption. A maximum amount at annealing temperature of 500 °C, therefore further experiments are all pre-treated using this annealing temperature. Furthermore, such fingerprint nanowire presents a good nonanal recognition ability from mixture similar molecules with different functional group (nonanal, 2-nonanone, 1-nonanol and nonane) and repeatability by 500 °C pre-treatment (Figure S6). Molecule recognition of siloxane based molecularly imprinted material reported by Dicker et al. showed degradation phenomenon over 150 °C treatment [27], and polymer based imprinted material

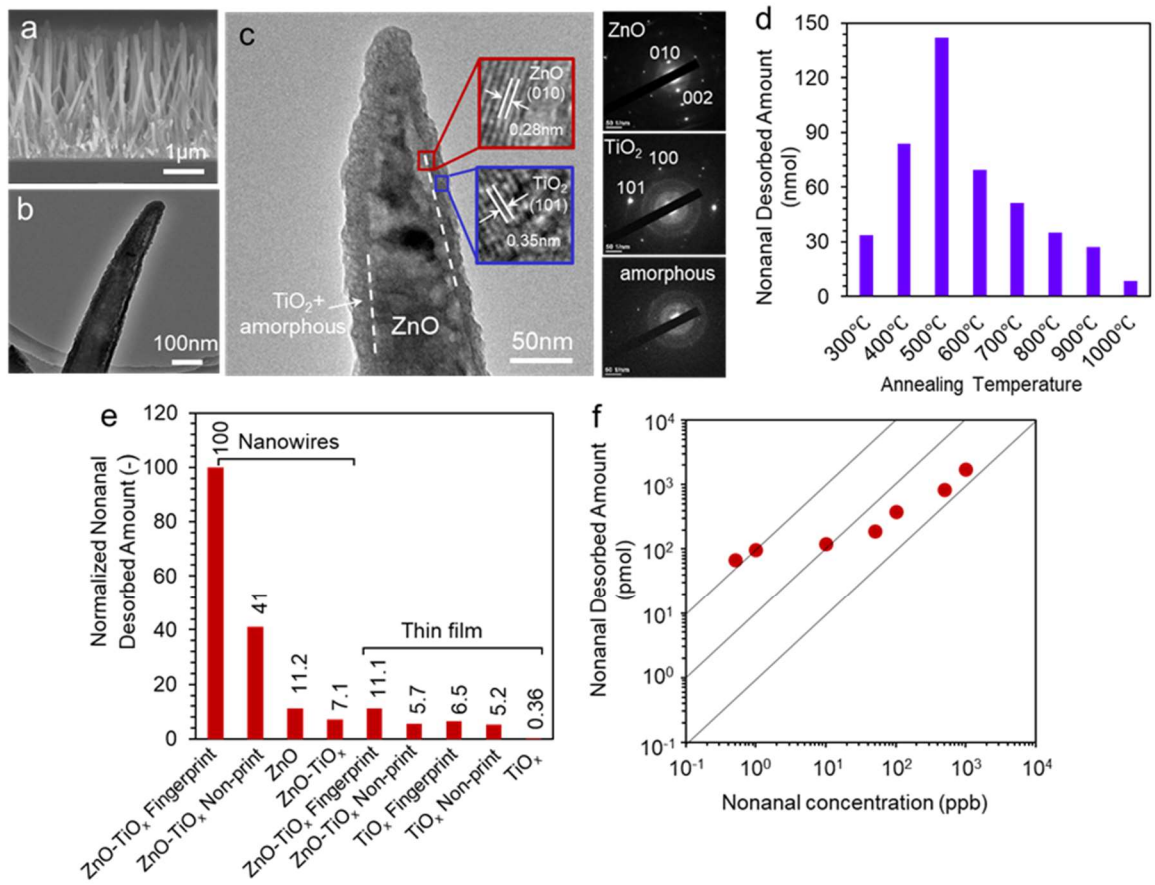

Figure 2. *(a) FESEM image from the side view of fingerprinted oxide nanowires; (b-c) TEM images; HRTEM images; SAED images of fingerprinted oxide nanowires; Nonanal desorbed amount of (d) various annealing temperature pre-concentrator in 90 ppm nonanal atmosphere; (e) comparison among several pre-concentrators fabricated by different surface materials and structures; (f) fingerprint nanowire when exposure to different nonanal concentration.*

working limited to 200 °C [28-30], therefore our titanium oxide based nanowire with fingerprint recognition layer is benefited for thermal stability as concentrated material. Nonanal collection ability comparison in Figure 2e is evaluated by molecule desorption amount using similar materials and different structures, result evidences the highest nonanal collection ability by ZnO/TiO_2 fingerprint nanowire structure. Those desorbed amounts are displayed by normalized amount, which means the highest amount being counted as 100, and others are counting from this standard. Compared with thin film structure, nanowire structure is more adaptive due to excellent nonanal collection performance. Fingerprint nanowire (100) shows 2.4 times nonanal amount enhancement to non-print nanowire one (41). Similar phenomenon also appears when measuring ZnO/TiO_2 thin film fingerprint (11.1) and non-print (5.7). It thus can be said that fingerprint layer plays a crucial role for enhancing nonanal collection ability.

Consequently, both fingerprint layer and nanowire structure are necessary for getting good nonanal collection material. Nonanal desorption amount exposure to 500 ppt ~1000 ppb condition (Figure 2f) are carried out to investigate the nonanal collection ability of fingerprint nanowire at low concentration range. Nonlinear rise dependence demonstrates the gradation of collection ability. Worthy of mention is that fingerprint nanowire presents better performance at especially low condition (sub-ppb level), it is more easy be observed after three auxiliary lines being draw onto the figure. Such good collection ability at low nonanal concentration make it have the potential to realize the effective detection towards sub-ppb level nonanal once integrated with sensor.

Microsystem sensing device integrated by fingerprint nanowire and sensor

To assess the effect of nonanal concentrated by fingerprint nanowire, a micro-system sensing device was integrated by fingerprint nanowire as pre-concentrator and sensitive sensor which fabricated from carbon and GC material (Figure 3a). To gain a rapidly molecule desorption

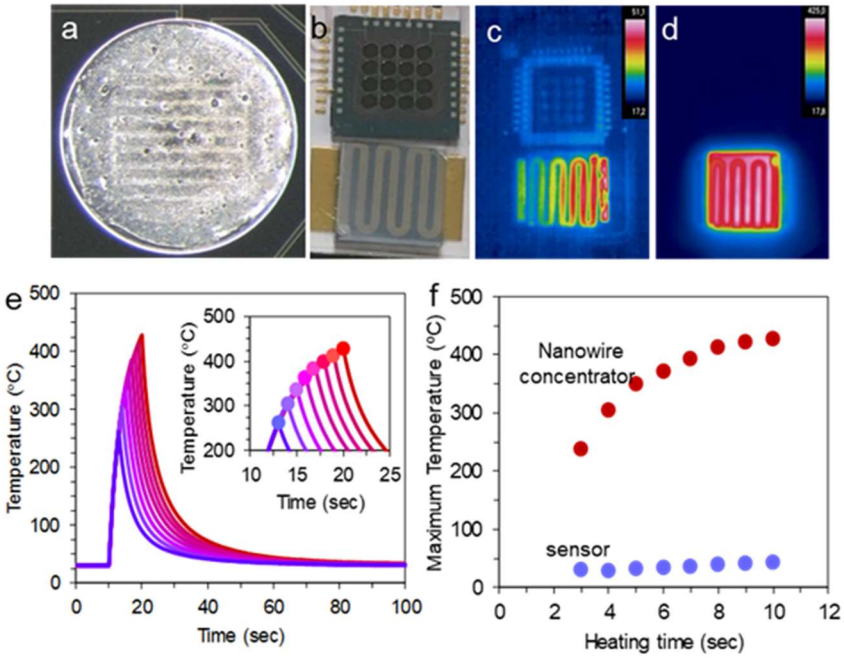

Figure 3. *(a) Sensor image; (b) Image of sensing device integrated by pre-concentrator and sensor; (c-d) infrared thermal images of such device as heater off/on. (e) Heating temperature various with heating time of pre-concentrator and sensor; (f) Maximum temperature summarized from (e).*

performance from concentrator surface, a heater at the bottom of nanowire was prepared. Such micro-system sensing device structure is shown in Figure 3b. Temperature can be recorded from thermal graphs as room temperature and applying 25 V voltage onto the heater (Figure

3c and d). Temperature curves as a function of time at different heating time condition (Figure 3e) present an increasing trend of both highest heating temperature and thermally energy (estimated by area under curve in Figure S7) as prolonging heating time. And the highest temperature of pre-concentrator and sensor at different heating time condition (Figure 3f) demonstrates even heating the pre-concentrator temperature up to 200-400 °C, sensor temperature keeping at nearly same value. Nevertheless, background sensing is needed for further eliminating the temperature effect to the sensing response, which means without molecule collection, the response caused by tiny temperature increase should be subtracted.

Nonanal sensing performance

As a proof of concept, nonanal sensing by as-obtained micro-system sensing device is conducted under a dynamic sensing system (Figure 4a). During sensing response measuring process, nitrogen gas flowing as background gas. Before gas collection, heating the concentrator for 6 s (highest temperature reached to 371 °C) at the meantime flowing nitrogen gas, aims at getting rid of surface-residual molecule through flashing the pre-concentrator. Then the nonanal collection process starts after naturally cooling the pre-concentrator to room temperature, simultaneously switched off nitrogen flow and on nonanal flow for 180 s. Finally, nonanal sensing in an enclosed chamber without any gases flowing. Transport collected nonanal molecules to sensor by heating the concentrator for several seconds. Intuitively response change can be found in relative dynamic sensing response curve obtained by 7s heating (Figure 4b), and the following dynamic sensing behavior of the only sensor (Figure 4c) displays as a contrast. Excellent sensing performance can be observed with the contribution of pre-concentrator application. As long as molecule desorption started, intact response curves show up, even to 500 ppt nonanal gas, sensing response rapidly rising and reached to the highest value within 10 s. After each sensing, sensor response recovered by purging nitrogen. Response was reversible because only several seconds required for recovering to initial level. Sensing performance towards various nonanal concentrations is shown in Figure 4d. As expected, sensing response raising as concentration increasing. What mentionable is by comparison among 3s, 5s and 7s heating, sensing response enhanced as heating time being prolonged. A possible factor is considered that short heating time provides insufficient thermal energy that can’t cast off all collected nonanal molecules. Desorbed product from 90 ppm nonanal-adsorbed pre-concentrator surface is analyzed by GC-MS spectrum (Figure S10) for verifying our hypothesis. Spectrum contains not only nonanal molecule peak, also aldol condensation

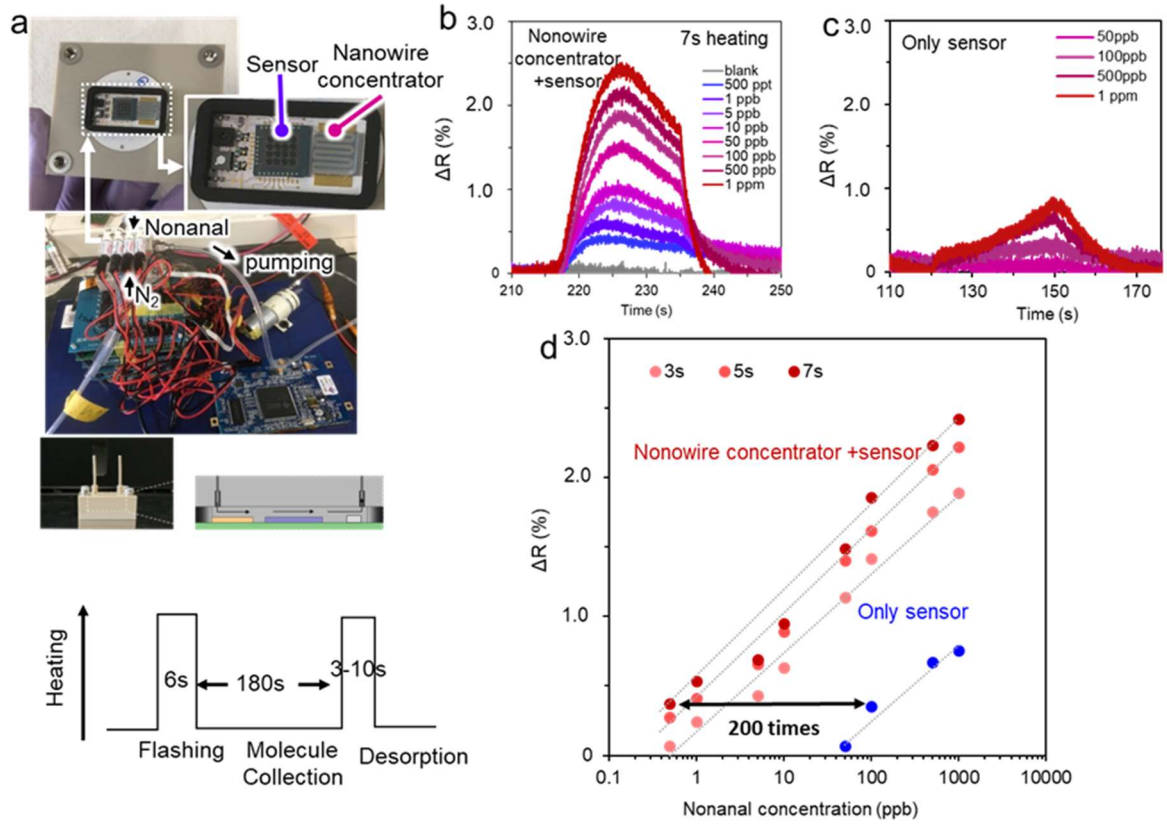

Figure 4. *(a) Device structure of pre-concentrator integrated with sensor and the sensing system; (b) Dynamic response curve at various concentration by 7s heating; (c) Dynamic response of only sensor at various nonanal concentration; (c) Sensing response various with nonanal concentration at 3s, 5s, 7s heating time;*

product 2-heptyl-2-undecenal peak, production process of this molecule has already been investigated by our previous work in detail [31]. Nonanal molecule amount keep a stable value, unaffected by desorbed temperature, but 2-heptyl-2-undecenal molecule amount gradually increase as desorbed temperature going up. Such result provides a convictive explain for sensing response enhancement by prolonging heating time that 2-heptyl-2-undecenal molecule transport to sensor can further improve sensing performance. By heating concentrator for 7s, nearly same response value can be obtained when expose to 500 ppt nonanal with only sensor to 100 ppb nonanal gas, about 200 times sensing ability strengthened by utilizing fingerprint nanowire pre-concentrator, significantly reduced the nonanal detecting limitation. From above analysis, sub-ppb level nonanal gas can be successfully detected based on the excellent sensing performance, such concentration even in the recommended human breath reach.

Nonanal sensing breakthrough

To show the novel advantage of our micro-system sensor, we summarize the best sensing detection limit reported from literatures [32-38] (Figure 5). Nonanal concentration as low as 50 ppb can be successfully detected until now by several sensor structures include metal oxide semiconductor gas sensor, sensor array, quartz crystal microbalance (QCM) and so on. But as far as we know, not a research had achieved sub-ppb level nonanal sensing. Herein, an amazing ultra-low level of 500 ppt nonanal sensing obtained by present micro-system is the best nonanal sensing performance so far, which shows a breakthrough towards nonanal sensing.

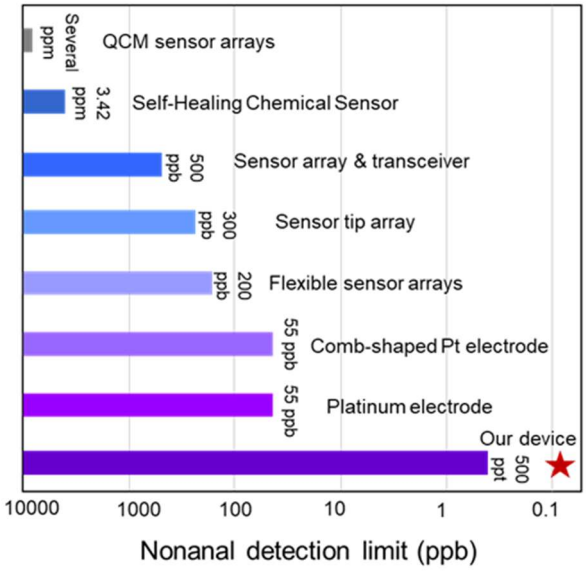

Figure 5. *Nonanal sensing limit of several type sensors based on previous researches*

4.3.5 CONCLUSION

In summary, we successfully fabricated one kind of thermal robust fingerprint nanowire with high-efficient nonanal collection ability as pre-concentrator material, and developed a micro-system sensing device contains of it with a sensitive sensor. Excellent nonanal sensing performance can be obtained by such micro-system. Application of fingerprint pre-concentrator can dramatically enhance sensing response about 200 times by comparing with only sensor. Even in ultra-low nonanal concentration atmosphere (500 ppt), obvious sensing response can be observed. The present results that can't be realized before provides an application prospect for human breath nonanal detection, so far as to realize the conceive of lung cancer early diagnose.

4.3.6 REFERENCE

[1] Smith R A, von Eschenbach A C, Wender R, et al. American Cancer Society guidelines for the early detection of cancer: update of early detection guidelines for prostate, colorectal, and endometrial cancers: Also: update 2001—testing for early lung cancer detection[J]. CA: a cancer journal for clinicians, 2001, 51(1): 38-75.

[2] K. Gross, A. Wronski, A. Skibinski, S. Phillips, C. Kuperwasser, Cell fate decisions during breast cancer development, J. Dev. Biol. 4 (2016) 4.

[3] Dominioni L, Imperatori A, Rovera F, et al. Stage I nonsmall cell lung carcinoma: analysis of survival and implications for screening[J]. Cancer, 2000, 89(S11): 2334-2344.

[4] Fuchs P, Loeseken C, Schubert J K, et al. Breath gas aldehydes as biomarkers of lung cancer[J]. International Journal of Cancer, 2010, 126(11): 2663-2670.

[5] Xue R, Dong L, Zhang S, et al. Investigation of volatile biomarkers in liver cancer blood using solid-phase microextraction and gas chromatography/mass spectrometry[J]. Rapid Communications in Mass Spectrometry: An International Journal Devoted to the Rapid Dissemination of Up-to-the-Minute Research in Mass Spectrometry, 2008, 22(8): 1181-1186.

[6] Hakim M, Broza Y Y, Barash O, et al. Volatile organic compounds of lung cancer and possible biochemical pathways[J]. Chemical reviews, 2012, 112(11): 5949-5966.

[7] De Zwart L L, Meerman J H N, Commandeur J N M, et al. Biomarkers of free radical damage: applications in experimental animals and in humans[J]. Free Radical Biology and Medicine, 1999, 26 (1-2): 202-226.

[8] Mandal S, Goddard J M, Erickson D. A multiplexed optofluidic biomolecular sensor for low mass detection[J]. Lab on a Chip, 2009, 9(20): 2924-2932.

[9] Bargatin I, Myers E B, Aldridge J S, et al. Large-scale integration of nanoelectromechanical systems for gas sensing applications[J]. Nano letters, 2012, 12(3): 1269-1274.

[10] Tricoli A, Righettoni M, Teleki A. Semiconductor gas sensors: dry synthesis and application [J]. Angewandte Chemie International Edition, 2010, 49(42): 7632-7659.

[11] Akbar S, Dutta P, Lee C. High‐temperature ceramic gas sensors: a review[J]. International journal of applied ceramic technology, 2006, 3(4): 302-311.

[12] Pereira J, Porto-Figueira P, Cavaco C, et al. Breath analysis as a potential and non-invasive frontier in disease diagnosis: an overview[J]. Metabolites, 2015, 5(1): 3-55.

[13] Amal H, Shi D Y, Ionescu R, et al. Assessment of ovarian cancer conditions from exhaled breath[J]. International journal of cancer, 2015, 136(6): E614-E622.

[14] Ueno Y, Horiuchi T, Tomita M, et al. Separate detection of BTX mixture gas by a microfluidic device using a function of nanosized pores of mesoporous silica adsorbent[J]. Analytical chemistry, 2002, 74(20): 5257-5262.

[15] Pijolat C, Camara M, Courbat J, et al. Application of carbon nano-powders for a gas micro-preconcentrator[J]. Sensors and Actuators B: Chemical, 2007, 127(1): 179-185.

[16] Camara E H M, Breuil P, Briand D, et al. A micro gas preconcentrator with improved performance for pollution monitoring and explosives detection[J]. Analytica chimica acta, 2011, 688(2): 175-182.

[17] Ni Z, Jerrell J P, Cadwallader K R, et al. Metal− Organic frameworks as adsorbents for trapping and preconcentration of organic phosphonates[J]. Analytical chemistry, 2007, 79(4): 1290-1293.

[18] Leidinger M, Rieger M, Sauerwald T, et al. Integrated pre-concentrator gas sensor microsystem for ppb level benzene detection[J]. Sensors and Actuators B: Chemical, 2016, 236: 988-996.

[19] Duran C, Vilanova X, Brezmes J, et al. Thermal desorption pre-concentrator based system to assess carbon dioxide contamination by benzene[J]. Sensors and Actuators B: Chemical, 2008, 131(1): 85-92.

[20] Rydosz A, Maziarz W, Pisarkiewicz T, et al. A gas micropreconcentrator for low level acetone measurements[J]. Microelectronics Reliability, 2012, 52(11): 2640-2646.

[21] Bertuna, A.; Faglia, G.; Ferroni, M.; Kaur, N.; Arachchige, H. M. M. M.; Sberveglieri, G.; Comini, E. Sensors 2017, 17, 1000.

[22] Pan H, Sun H, Poh C, et al. Single-crystal growth of metallic nanowires with preferred orientation[J]. Nanotechnology, 2005, 16(9): 1559.

[23] Minami T, Yamamoto T, Miyata T. Highly transparent and conductive rare earth-doped ZnO thin films prepared by magnetron sputtering[J]. Thin Solid Films, 2000, 366(1-2): 63-68.

[24] Breckenridge R G, Hosler W R. Electrical properties of titanium dioxide semiconductors[J]. Physical Review, 1953, 91(4): 793.

[25] Wang Z, Helmersson U, Käll P O. Optical properties of anatase TiO_2 thin films prepared by aqueous sol–gel process at low temperature[J]. Thin Solid Films, 2002, 405(1-2): 50-54.

[26] Mar L G, Timbrell P Y, Lamb R N. An XPS study of zinc oxide thin film growth on copper using zinc acetate as a precursor[J]. Thin Solid Films, 1993, 223(2): 341-347.

[27] Mujahid, A., Lieberzeit, P. A. & Dickert, F. L. Chemical sensors based on molecularly imprinted sol-gel materials. Materials 3, 2196-2217 (2010). DOI: 10.3390/ma3042196

[28] Kupai J, Razali M, Buyuktiryaki S, et al. Long-term stability and reusability of molecularly imprinted polymers[J]. Polymer chemistry, 2017, 8(4): 666-673.

[29] Liu X Y, Guan Y, Ding X B, et al. Design of temperature sensitive imprinted polymer hydrogels based on multiple-point hydrogen bonding[J]. Macromolecular bioscience, 2004, 4(7): 680-684.
[30] Pfeiffer K, Bleidiessel G, Gruetzner G, et al. Suitability of new polymer materials with adjustable glass temperature for nano-imprinting[J]. Microelectronic Engineering, 1999, 46(1-4): 431-434.
[31] Wang C, Hosomi T, Nagashima K, et al. Rational Method of Monitoring Molecular Transformations on Metal-Oxide Nanowire Surfaces[J]. Nano letters, 2019, 19(4): 2443-2449.

[32] Toshio Itoh, Takaomi Nakashima, Takafumi Akamatsu, Noriya Izu, Woosuck Shin. Sensors and Actuators B 187 (2013) 135–141

[33] Yoshitake Masuda, Toshio Itoh, Woosuck Shin & Kazumi Kato, Scientific Reports volume 5, Article number: 10122 (2015)

[34] Chuanjun Liu, Bartosz Wyszynski, Rui Yatabe, Kenshi Hayashi, Kiyoshi Toko. Sensors 2017, 17, 382

[35] Tan-Phat Huynh, Muhammad Khatib, Rawan Srour, Marian Plotkin, Weiwei Wu. Adv. Mater. Technol. 2016, 1, 1600187

[36] Masuda Y, Kato K, Kida M, et al. Selective nonanal molecular recognition with SnO2 nanosheets for lung cancer sensor[J]. International Journal of Applied Ceramic Technology, 2019.

[37] Han Jin, Tan-Phat Huynh, Hossam Haick. Nano Lett. 2016, 16, 4194−4202

[38] Sunshine S A. Sensor arrangement: U.S. Patent 7,040,139[P]. 2006-5-9.

[39] Wyszynski B, Yatabe R, Nakao A, et al. Array of Chemosensitive Resistors with Composites of Gas Chromatography (GC) Materials and Carbon Black for Detection and Recognition of VOCs: A Basic Study[J]. Sensors, 2017, 17(7): 1606.

[40] Shunori A, Yatabe R, Wyszynski B, et al. Multichannel Odor Sensor System using Chemosensitive Resistors and Machine Learning[C]//2019 IEEE International Symposium on Olfaction and Electronic Nose (ISOEN). IEEE, 2019: 1-3.

4.3.7 Supporting information

1. Schematic illumination of fingerprint nanowire formation process

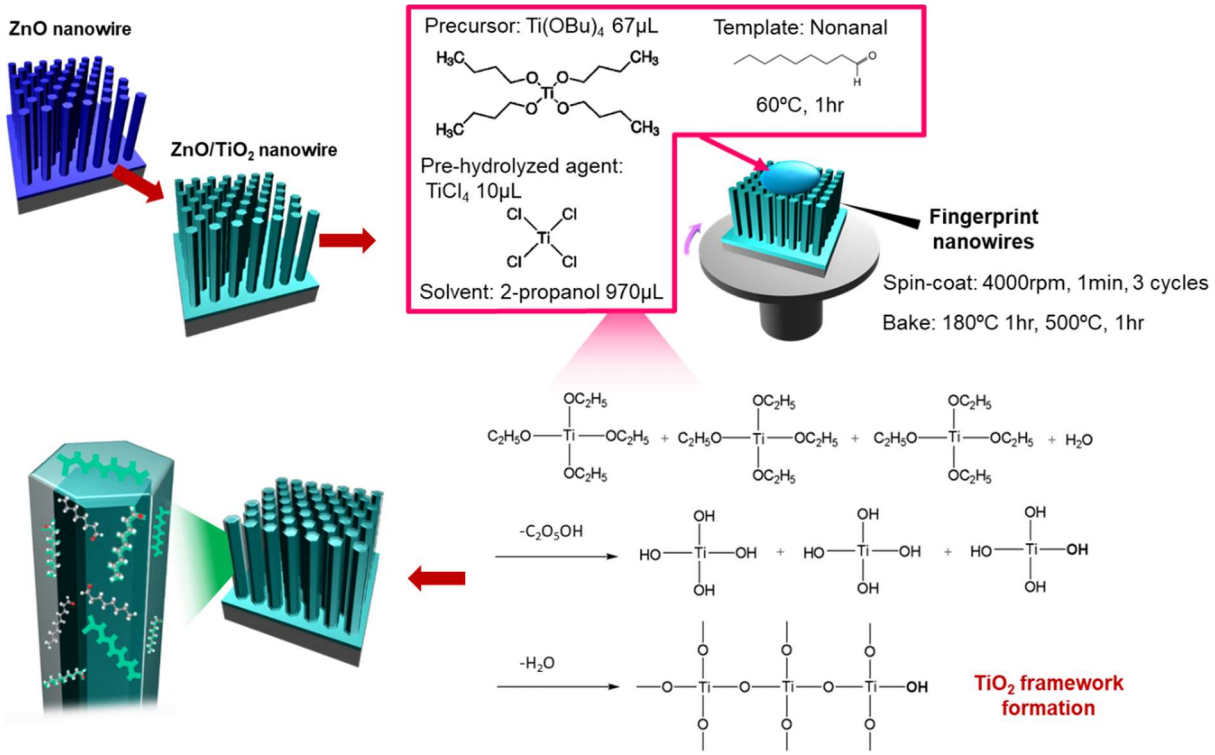

Figure S1. *Fingerprint nanowire formation process and TiO_2 framework formation mechanism*

2. Structure characterization

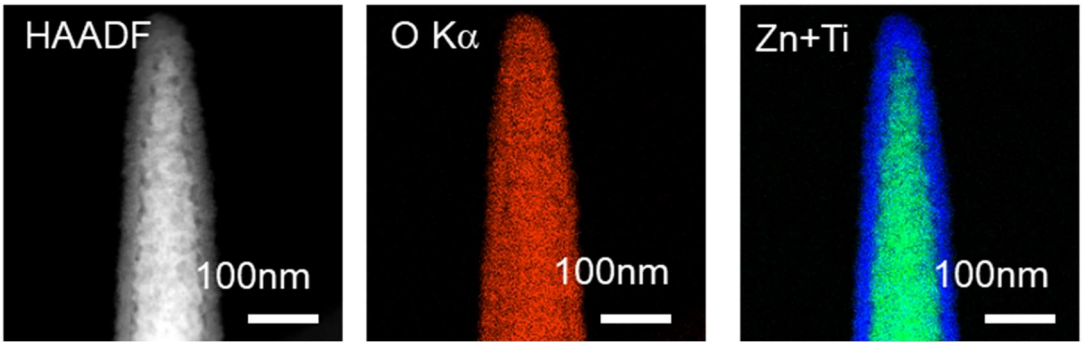

Figure S2*. EDS mapping of fingerprint nanowire.*

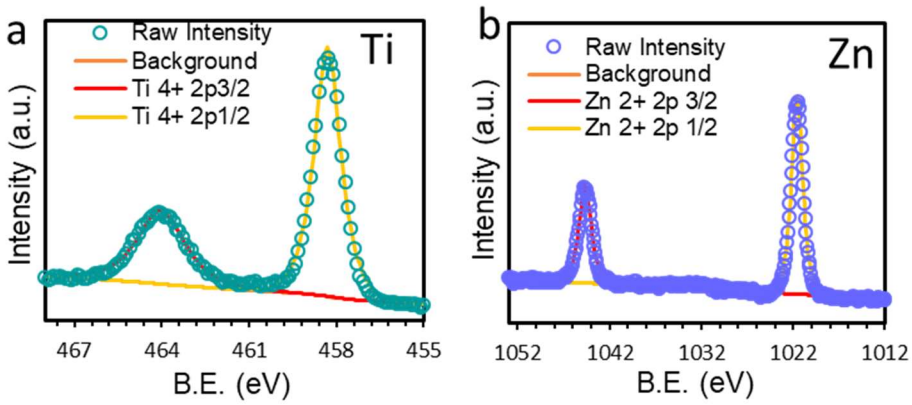

Figure S3. *XPS spectrum of fingerprint nanowire.*

3. Nonanal collection ability of fingerprint nanowire

3.1 nonanal collection amount calculation

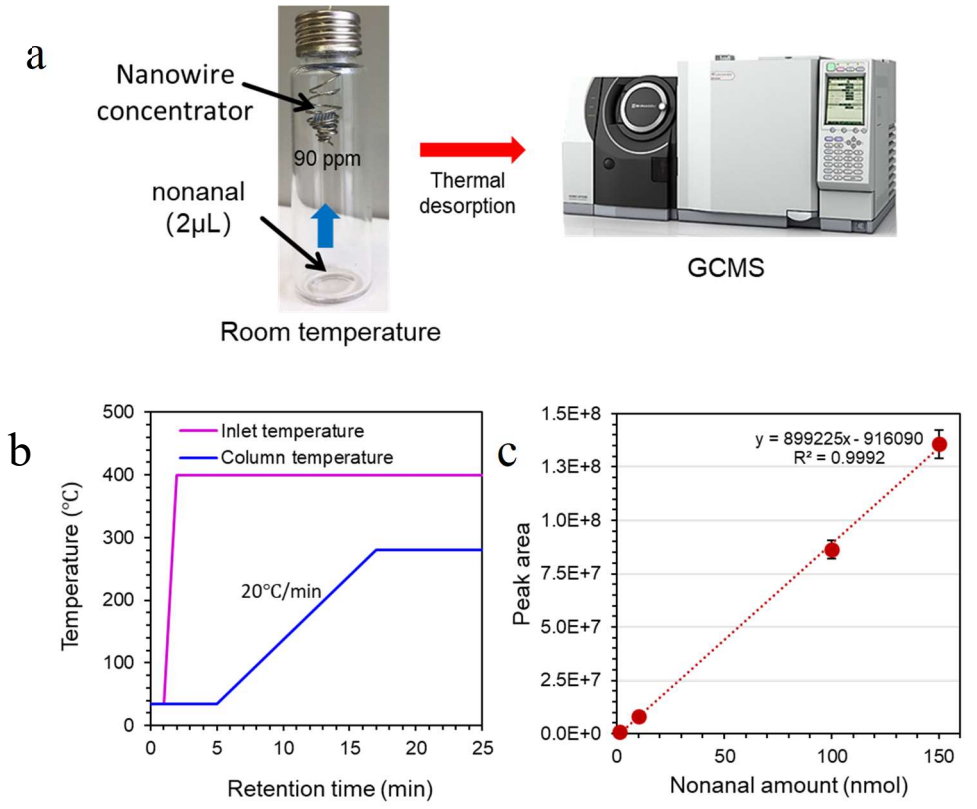

Figure S4. *(a) Nonanal collection in 90 ppm gas by nanowire concentrator and desorbed into GC-MS to analyze; (b) The temperature program for desorbed amount analysis by GC-MS; (c) Calibration curve for nonanal amount calculation from peak area of GC-MS spectrum.*

Earliest nonanal collection was conducted in a 20 mL bottle by injecting 2 μL nonanal liquid at the bottom of this bottle and let it vapor naturally for 20 min at room temperature. The concentration of such vapor was about 90 ppm which was calculated by GC-MS peak area based on the calibration curve described in the following process. Nanowire concentrator was suspended in the bottle as shown in Figure S4(a) for 5 min to collect nonanal molecule. The inlet temperature and column temperature were controlled with the program shown in Figure S4(b). The inlet temperature program was raising to 400 °C immediately for molecule desorption. Calibration curve was obtained by inject a certain volume of nonanal solution whose concentration was controlled and known into GC-MS, calculated peak area from GC-MS spectrum as amount calibrated standard. Same process for low nonanal calibration in Figure S6(b) and 2-hyptyl-2-undecenal calibration curve in Figure S9.

3.2. FT-IR analyses for template nonanal molecule eliminating process

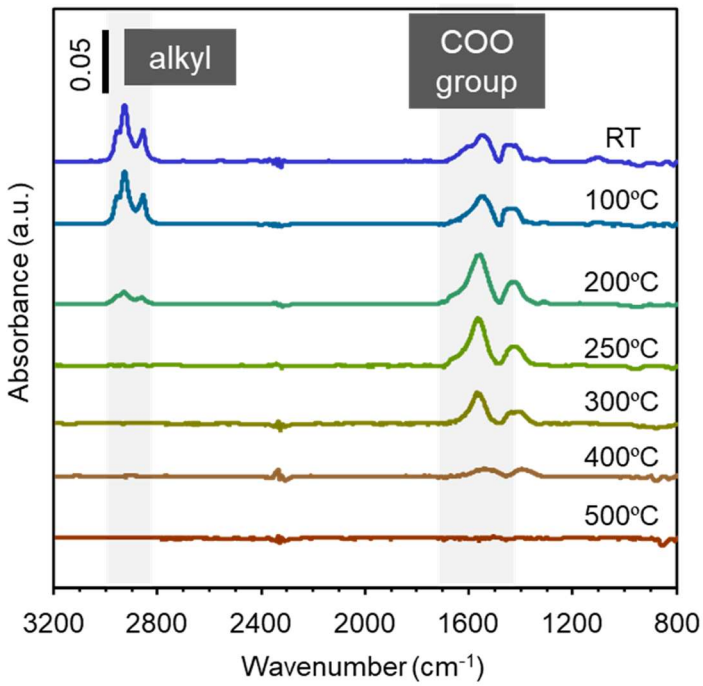

Figure S5. *FT-IR spectrum of nonanal template at various annealing temperature*

Peaks at 2800-3000 cm^{-1} belongs to alkyl vibration (-CH_2- and –CH_3), and they can be completely eliminated at 250℃ annealing. COO^- bond exist at 1500-1700 cm^{-1}, 500℃ is necessary for fully eliminating this group on account of the stronger connection with metal atom. Here we considered alkyl of template nonanal molecule can be cutted after 250 ℃, further increase the annealing temperature, COO^- will desorbed as CO_2.

3.3 Selectively molecule recognition

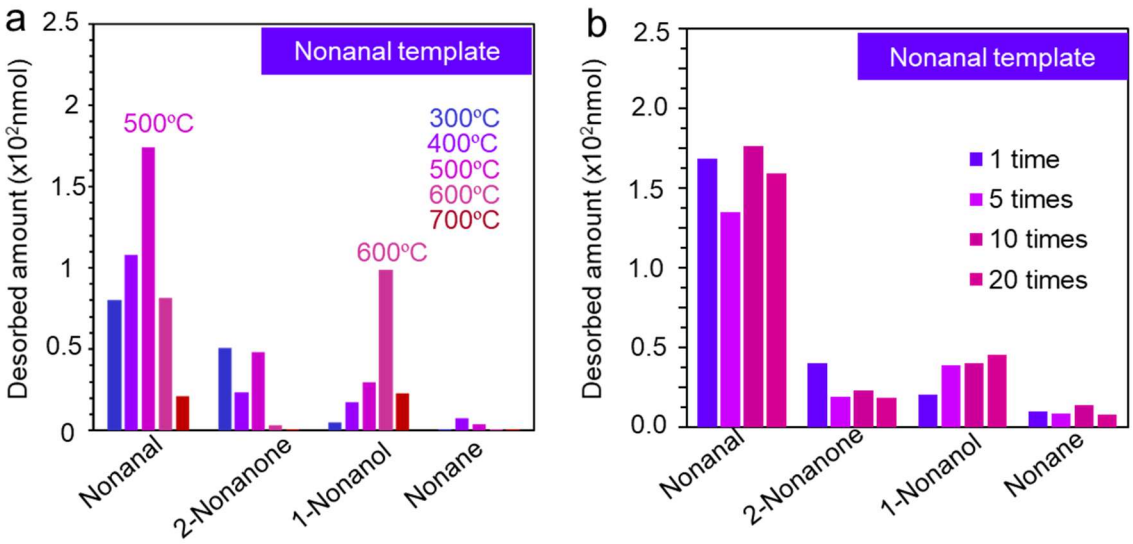

Figure S6. *(a) Selectively molecule recognition ability from mixture (nonanal, 2-nonanone, 1-nonanol and nonane) by annealing temperature from 300 to 700°C. (b) Repeatability of molecule recognition ability.*

4. Integrated sensing device structure

4.1 Sensor electrodes structure

Figure S7*. Structure of chemo-sensor substrate.*

4.2. Thermal energy provide by concentrator heater

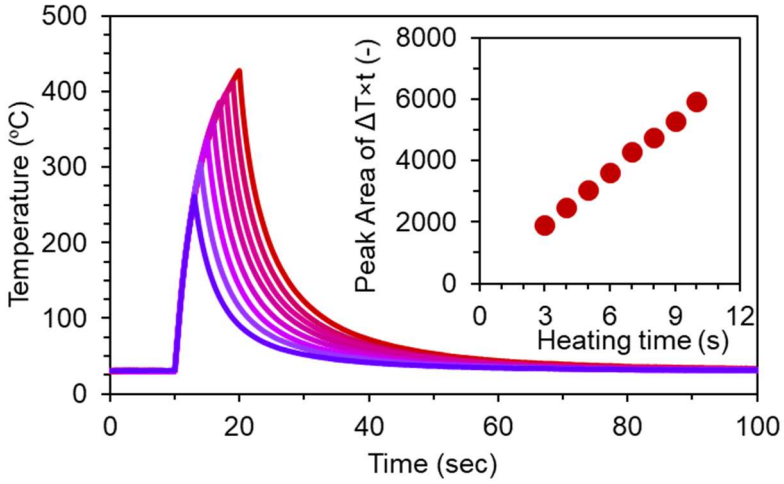

Figure S8. *Peak area calculated as a thermal energy illumination of nanowire concentrator.*

5. Nonanal sensing property measurement

5.1. Concentration controlling and of flowing nonanal gas

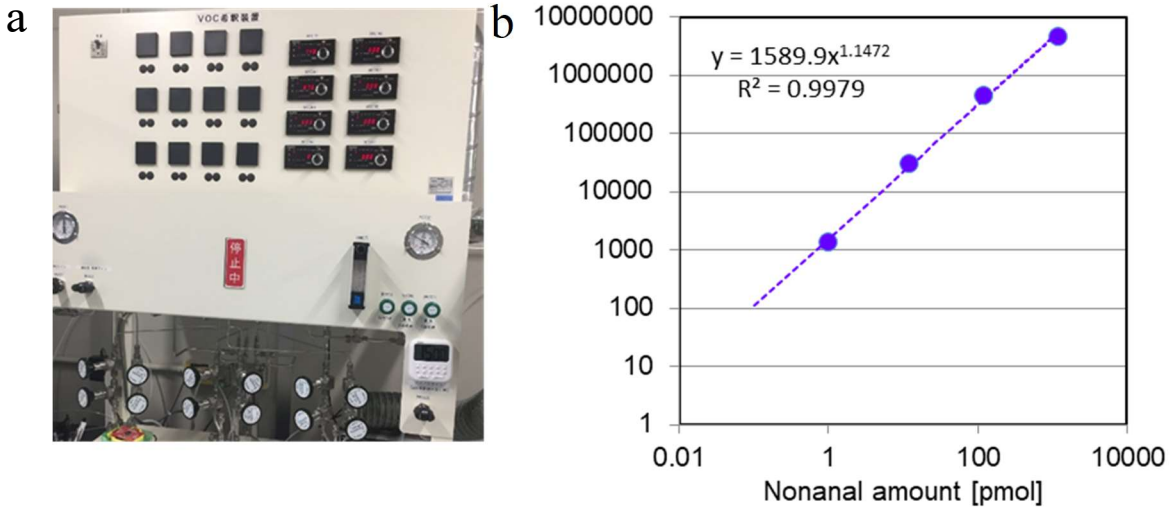

Figure S9. (a) Low concentration gas generation system; (b) Calibration curve for nonanal concentration confirmation.

Nonanal sensing part was conducted under flowing nonanal gas condition, nonanal gas was diluted by nitrogen. The concentration was obtained by inject a certain volume of gas into GC-MS and calculated by the calibration curve.

5.2. Desorbed product analysis by GC-MS

5.2.1 Desorbed product

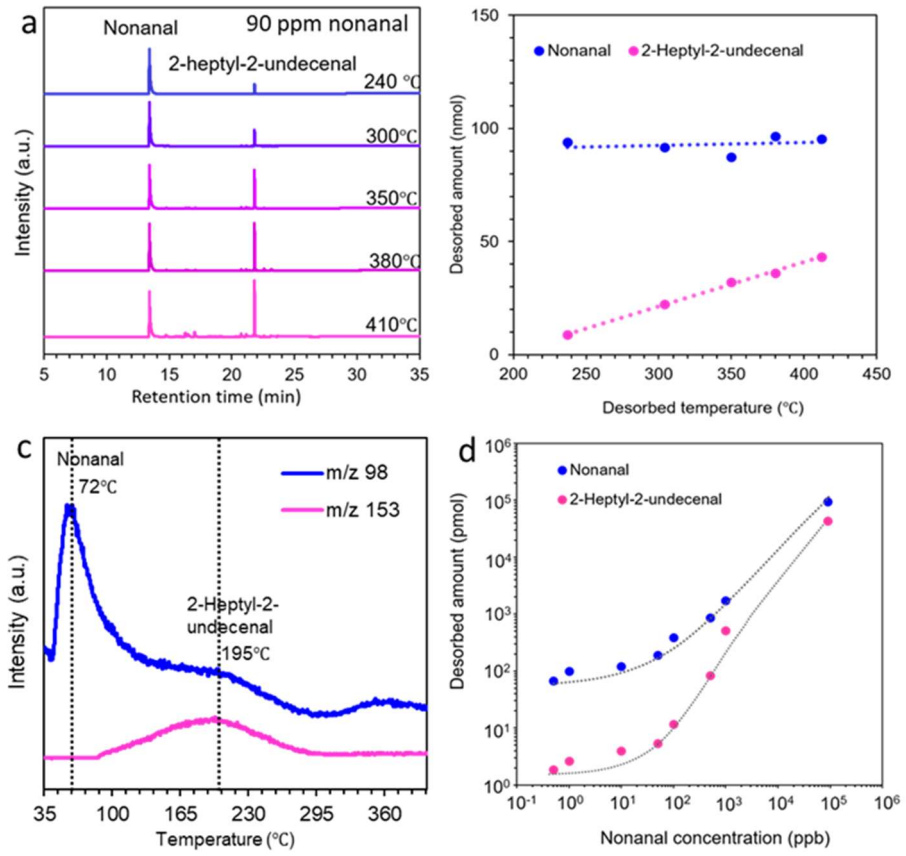

Figure S10. *(a) Desorbed product analysis from 90 ppm nonanal-adsorbed pre-concentrator surface by GC-MS at various desorbed temperatures (240, 300, 350, 380 and 410 ℃); (b) Desorbed amount calculate from (a); (c) TPD/MS profiles of 90 ppm nonanal-adsorbed pre-concentrator; (d) Calculated molecule desorbed amount plotted against nonanal collection concentration.*

By analyzing typical mass fragment pattern of TPD/MS desorption profiles (Figure S10-c), nonanal (m/z=98) desorbed peak exist at around 72 °C, much lower than 2-heptyl-2-undecenal (m/z=153) at 195 °C. Therefore, the conclusion can be drawn that fast heating process by the concentrator heater can provide enough thermal energy for nonanal desorption, even only heat for 3 seconds, but insufficient for completely desorbing 2-heptyl-2-undecenal by short heating time. 2-heptyl-2-undecenal can also contribute to sensing response as thermal energy being promoted by extending heating time. Desorbed molecules amount in 500 ppt rising to 90 ppm

nonanal collection in Figure 5d presents a monotonically increasing trend of both nonanal and 2-heptyl-2-undecenal. And that 2-heptyl-2-undecenal amount trend to be larger in high nonanal concentration, which is not difficult to understand based on our previous result [31] that high nonanal density on material surface gives more opportunity for aldol condensation happen. Even though aldol condensation reaction rate is limited in extremely rare nonanal condition, 2-heptyl-2-undecenal molecules still exist, and can be utilized to further improve sensing response.

5.2.2 The condition of desorbed molecule analyses

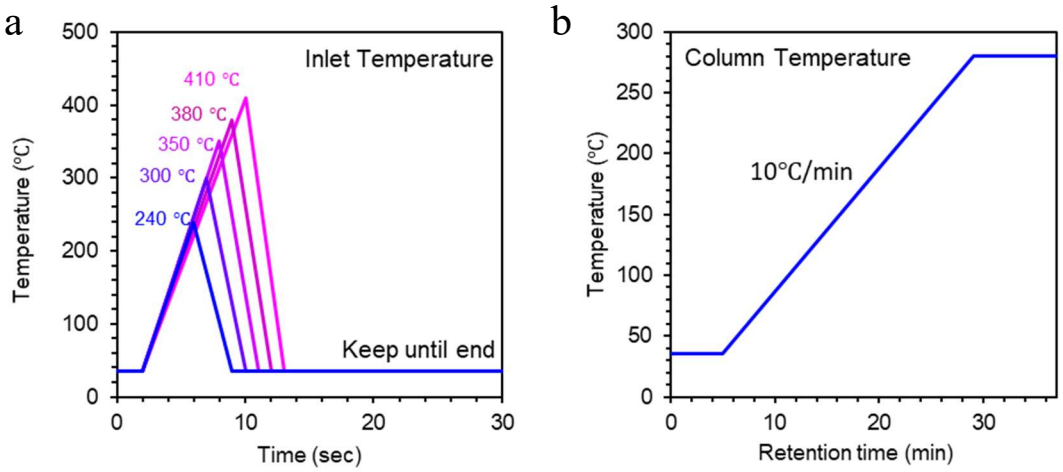

Figure S11. *The temperature program for desorbed gas analysis by GC-MS: (a) Inlet temperature; (b) Column temperature.*

The inlet temperature program in Figure S11(a) was set inlet temperature respectively raised to 240 °C, 300 °C, 350 °C, 380 °C, and 410 °C immediately and terminated heating once target temperature reached, keep at room temperature until the program finished (in total 37 min) when analyzing the desorbed product.

5.2.3 Aldol condensation product 2heptyl-2-undecenal amount calculation

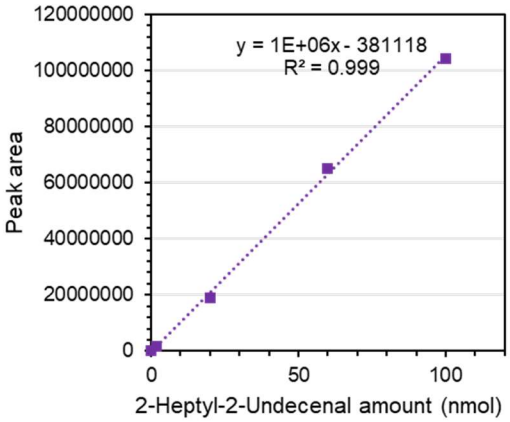

Figure S12. *Calibration curve of aldol condensation product -2heptyl-2-undecenal.*

5.2.4 The condition of Temperature-programed desorption gas analyses

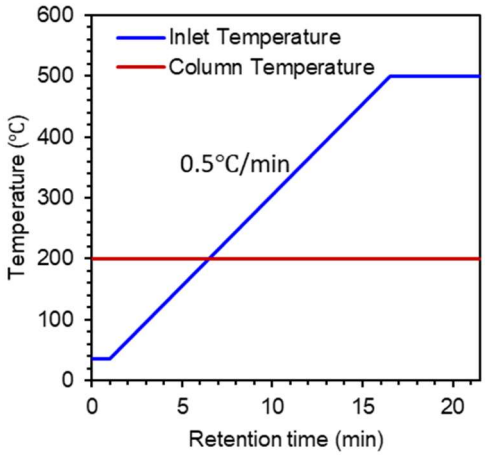

Figure S13*. The temperature program for desorption gas analysis by TPD.*

CHAPTER V

MOLECULAR DISCCRMINATIVE SENSING VIA DESORPTION FROM METAL OXIDE NANOWIRE SURFACE

5.1 Thermally Manipulated Selective Desorption on Nanowire Surface of Novel Molecular Sensing Platform

5.1.1 ABSTRACT

Here we demonstrate a novel molecular sensing platform for electrical discrimination of molecules via thermally manipulated desorption on metal oxide nanowire surface. Co-adsorbed nonanal and (E)-2-hepthyl-2-undecenal on zinc oxide (ZnO) nanowire surface are used as a model. Entropy-involved numerical simulation anticipates that these adsorbed molecules on ZnO nanowire surface can be discriminated by thermal desorption. This is because the undesired probabilistic desorption of molecules, which is caused by continuous heating, is effectively suppressed by controlling the heating period below the residual time of molecules adsorbed on nanowire surface. According to this implication, we successfully discriminate nonanal and (E)-2-hepthyl-2-undecenal via a pulse heating. A hybrid device composed of nanowire molecule collector and chemoresistive sensor array further demonstrates the capability of electrical molecular discrimination by the present methodology. Our nanowire-sensor hybrid sensing system has a potential for drastically improving the performance of electrical discrimination of molecules especially for molecular mixture, which had hardly been realized in previous sensor technology.

KEY WORDS: Thermally desorption, discriminate sensing, nanowire platform, residual time, hybrid sensing system

5.1.2 INTRODUCTION

Molecular sensors have received considerable interest over the past decade owing to their tremendous promise for the ever-increasing advancement demand in monitoring the environment surroundings, health condition of individuals and communication technologies of modern smart objects, which brings with it an opportunity to take part in new era of application development for Internet of Things (IoT), Big Data, Chemical data and Monitoring.[1-5] Although the generalized detection of molecules has generally employed for sensors, the discrimination of compounds within a given molecule mixture remains a challenging goal due to similar chemical property of contained molecules.[6-9] Previous some approaches and technologies for sensor development to overcome the molecules discrimination hinder have been employed. For examples, sensor arrays, theoretically, increasing the number of the sensors in the array might lead to some improvements in the discrimination properties. Nevertheless, it also increases the power consumption and complicates the device circuitry.[10-12] Additionally, the higher the number of the sensing elements, the higher the risk of overfitting toward the analysed data, particularly in cases where the sample size is limited. [13-14] Artificial Intelligent/ Principal Component Analysis are also effective ways for molecules discrimination, but incapability reflection of concentration variation impeded its development. [15-18] Recently, an interesting research presented a detector successfully discriminated analytes between methanol and ethanol which belong to same chemical family by utilizing a separation column prior to sensing part, the least of perfection is down scaling such column filter-sensor system is difficult. Thus, technical breakthrough for electrically discriminating molecule mixture is strongly required.

Considering the sub-size, low power consumption and easy integration demand of sensor, on this basic, for further pursuing the desire of molecule discrimination, a concept came up that thermally manipulate molecule desorption from material surface and time-separate molecule sensing based on the variation of molecule-to-surface connection properties. To realize such concept, one of the essential points emphasized here is the heating temperature and time control for molecule desorption from surface. Theoretically, controlling the heating period below the residual time of molecules adsorbed on material surface effectively suppressed the undesired probabilistic desorption of molecules, in other words, pulse heating is more suitable for this concept than continuous heating. Beyond that, pulse heating not only benefit for molecules

separating desorption, also sharply falling the power consumption down. As we know, the major drawback of traditional oxide-based resistive-type gas sensors is their rather high energy consumption required to heat the device because the reversible oxygen adsorption and reactions occur only at high temperatures around 300 °C. [19-22] Therefore, it is easier to make a type of molecule discrimination sensing device with pulse heating adopted on account of such designed concept battery-operable and portable.

In this study, we demonstrate a rational strategy for discriminating molecules by thermally manipulated desorption on solid surface. Furthermore, we propose a novel molecular sensing platform based on nanowire molecular collector-chemo-resistive sensor hybrid devices as schematically illustrated in figure 1. Unlike the previous study using column/filter connected sensor, the proposed methodology can be potentially miniaturized by semiconductor nanotechnology processing.

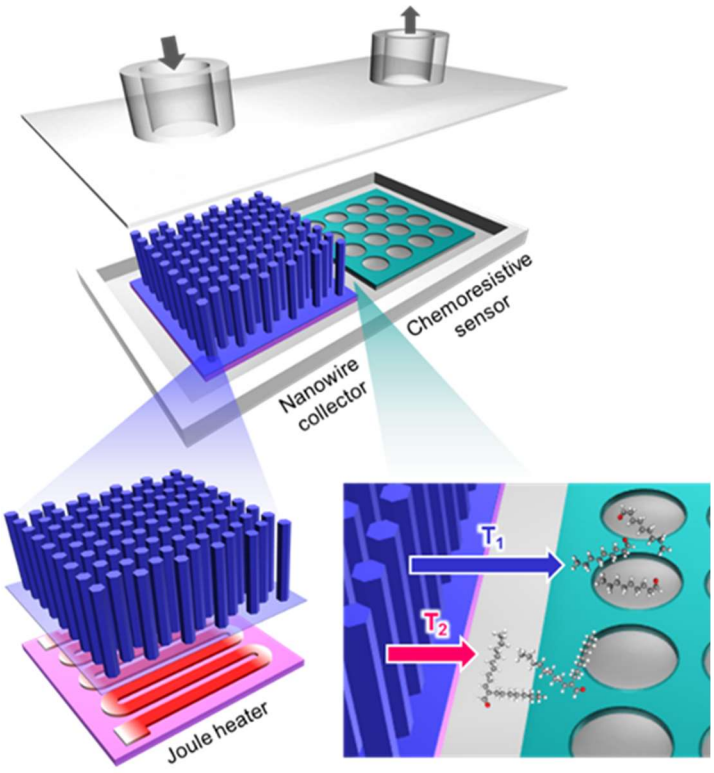

Figure 1. *Schematic illustration of a hybrid device composed of nanowire molecular collector and chemoresistive sensor array. The molecules discriminated by thermally manipulated desorption are transported to chemoresistive sensor array with different timing.*

5.1.3 EXPERIMENTAL

Heater-equipped ZnO nanowires fabrication.

For the purpose of thermal manipulation of molecular desorption, a Pt heater was firstly designed and constructed on a substrate. A 200 nm thick Pt layer was deposited directly on a 100 nm thick SiO_2 coated Si (100) substrate (0.5 cm × 0.5 cm size) by radio frequency (RF) sputtering method with a power of 50 W for 40 min using a serpentine-patterned metal mask. Next, a 5 nm thick ZnO seed layer was deposited on the substrate together with a 1 nm thick Ti buffer layer by RF sputtering (100 W, 1 min for Ti and 50 W, 3min for ZnO). ZnO nanowires were grown via hydrothermal method. The substrate was immersed into 300 ml aqueous solution containing 2.5 mM branched polyethylenimine (PEI, Mn=1800), 25 mM zinc nitrate hexahydrate ($Zn(NO_3)_2 \cdot 6H_2O$) and 25 mM hexamethylenetetramine (HMTA, $(CH_2)_6N_4$) in a manner of up-side down. All chemical reagents were analytical grade and used without further purification. The solution was then sealed, put into oven and kept at 95 ºC for 12 h for nanowire growth. After the growth, the substrate was taken out from the solution and rinsed by water. To fully remove organic contaminant from the fabricated nanowire surface, as-grown samples were annealed at 400 ºC for 1 h in air atmosphere. Consequently, the heater-equipped ZnO nanowires were obtained.

Characterization of nanowire and desorbed molecule analysis.

Morphology of fabricated nanowires was characterized by field emission scanning electron microscope (FESEM, JEOL JSM-7610F) at accelerating voltage of 15 kV. For desorbed molecules analysis, nonanal adsorption on ZnO nanowires surface was first conducted in a static condition. 2 μl liquid nonanal was placed at the bottom of 25 ml vial bottle and the bottle was sealed and kept for 30 min to vaporize nonanal. The suspended nanowire samples were inserted in the bottle filled with nonanal vapor, kept for 3 min and transferred to gas chromatograph-mass spectrometry (GC-MS, Shimadzu GCMS-QP2020 Ultra). The desorbed compounds were analyzed by GCMS equipped with an Inter-Cap 1MS capillary column (length 60 m, inner diameter 0.32 mm) and an OPTIC-4 inlet temperature control system. The temperatures of both GC/MS interface and ion source were set to be 200 °C. For the temperature dependent desorption compounds analysis, the samples were heated in the inlet port at a programmed temperature (75, 100, 150, 200, 250, 300, 350, 400 ºC), held for 1 s (pulse heating) and 3 min (continuous heating), and then immediately cooled down to 35 ºC. The

temperature dependent analysis was sequentially conducted without taking out the samples between the measurements.

Chemo-resistive sensor fabrication.

For molecular sensing, a 16-channel chemoresistive sensor array was used. Chemoresistive sensor used in this study was fabricated by a specially customized ink-jet printing system (Musashi Engineering, Inc.). Material ink composed of 10 mg/ml polyethylene glycol (PEG 4000) and 7.5 mg/ml carbon black in water was dropped by syringe needle onto an electrode-pattered chip (4 mm × 4 mm size). [23-24] The samples were dried for 3 days at room temperature in N_2 atmosphere and consequently the sensor chip was obtained.

Nanowire-sensor hybrid device fabrication and measurement.

Nanowire-sensor hybrid device was fabricated by integrating a heater-equipped ZnO nanowires and a 16-channel chemoresistive sensor array on a specially designed print-circuit board (PCB) in a side-by-side manner. Both of nanowire and sensor were electrically connected to PCB via Au wire bonding. Temperature control of ZnO nanowires was performed by Joule heating with applying direct current (DC) voltage bias to Pt heater underneath the nanowires. The temperature of nanowires was evaluated by infrared (IR) thermography camera (Apiste FSV-2000). Molecular sensing measurement was conducted at room temperature by 1 ppm nonanal in N_2 background. For the measurement, nonanal was flown for 3 min and collected on ZnO nanowire surface. Then nonanal and (E)-hepthyl-2-undecenal were sequentially desorbed from nanowire surface by applying 15 V for 2 s (corresponding to 103 ºC) and 25 V for 6 s (corresponding to 385 ºC) to Pt heater, respectively. The desorbed compounds were detected by chemoresistive sensor array with applied voltage of 2 V. Gas flow was controlled by mini-pump. The sensor response was characterized as $(R_g-R_a)/R_a\times100\%$, where R_a and R_g are the sensor resistances when exposed to N_2 and nonanal, respectively.

5.1.4 RESULTS AND DISCUSSION

Figure 2 (a) shows the schematic illumination of our material model used in this study, i.e. ZnO nanowires and co-adsorbed nonanal/(*E*)-2-hepthyl-2-undecenal molecules on their surface. Figure 2 (b) shows a typical cross-section field emission scanning electron microscopy (FESEM) image of ZnO nanowires. The ZnO nanowires with length of ca. 2.5 μm are vertically and uniformly grown on the substrate. In order to identify the desorbed compounds of nonanal-

adsorbed ZnO nanowires, we performed gas chromatograph-mass spectrometry (GC-MS) measurement in figure 2 (c). The measurement was conducted by heating the sample at 400 ºC for desorbing all compounds. Two distinct peaks are observed in the spectrum, which are assigned to nonanal and (*E*)-2-hepthyl-2-undecenal [25]. Thus this clearly confirmed the availability of our material model. Here we examine the feasibility of thermal desorption based discrimination for these co-adsorbed molecules on ZnO nanowires. Previous our study revealed that the desorption temperature of (*E*)-2-hepthyl-2-undecenal (ca. 230 ºC) is much higher than that of nonanal (ca. 115 ºC). This implies that these molecules interact with ZnO nanowire surface not only by carbonyl group (C=O) but also by their alkyl chains (figure 2 (d) and (e)). Therefore, we conducted the density functional theory (DFT) calculations for the nonanal and (E)-2-heptyl-2-undecenal molecules adsorbed on ZnO $(10\bar{1}0)$ plane by optimizing their intermolecular vibration, entropy, and Van der Waals forces. Figure 2 (f) presents the

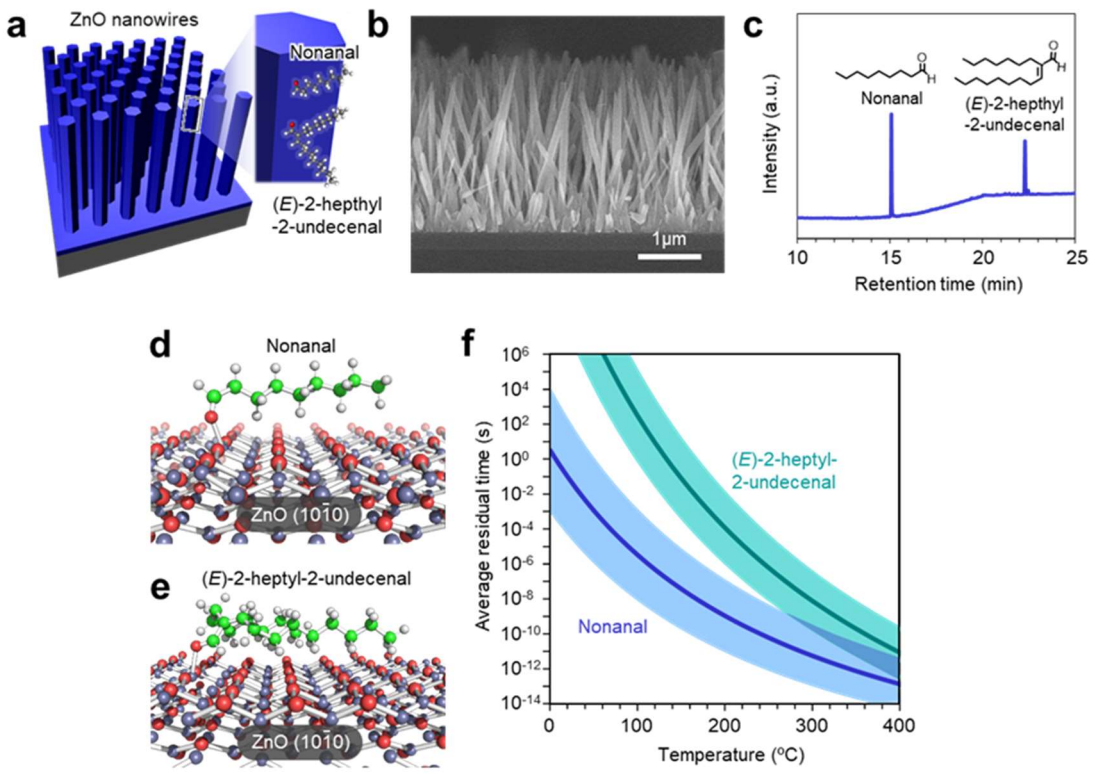

Figure 2. *(a) Schematic illustration of ZnO nanowires on a substrate and adsorbed molecules (nonanal and E-2-hepthyl-2-undecenal) on nanowire surface. (b) Cross-sectional FESEM image of ZnO nanowires (c) GC-MS spectrum for desorbed compounds from ZnO nanowire surface. (d) Schematic image and (e) simplified model for molecules (nonanal and E-2-hepthyl-2-undecenal) adsorbed on ZnO* $(10\bar{1}0)$ *crystal plane. (f) Temperature dependent average residual time of adsorbed molecules on ZnO crystal surface.*

simulation results of a relationship between each molecule average residual time and temperature. Two clearly separated curves strongly supported our concept that these co-adsorbed molecules on ZnO nanowire surface can be discriminated by thermal desorption by strictly controlling heating duration.

As a proof of concept, next we investigated the temperature dependent desorbed compounds of nonanal-adsorbed ZnO nanowires by means of pulse heating. Figure 3 (a) shows the temperature program used for this measurement. In this program, the sample temperature was elevated with a rate of 60 ºC/s, kept for 1 s at the objective temperatures and immediately cooled down. Figure 3 (b) shows the GC-MS spectra of pulse heating based desorbed compound analysis at various temperatures (75-400 ºC). Series of measurements were sequentially conducted without taking out the samples between the measurements. GC-MS spectra of such pulse heating based desorbed compound analysis (Figure 3b) and calculated peak area of desorbed molecules (nonanal and (E)-2-hepthyl-2-undecenal) at each programmed

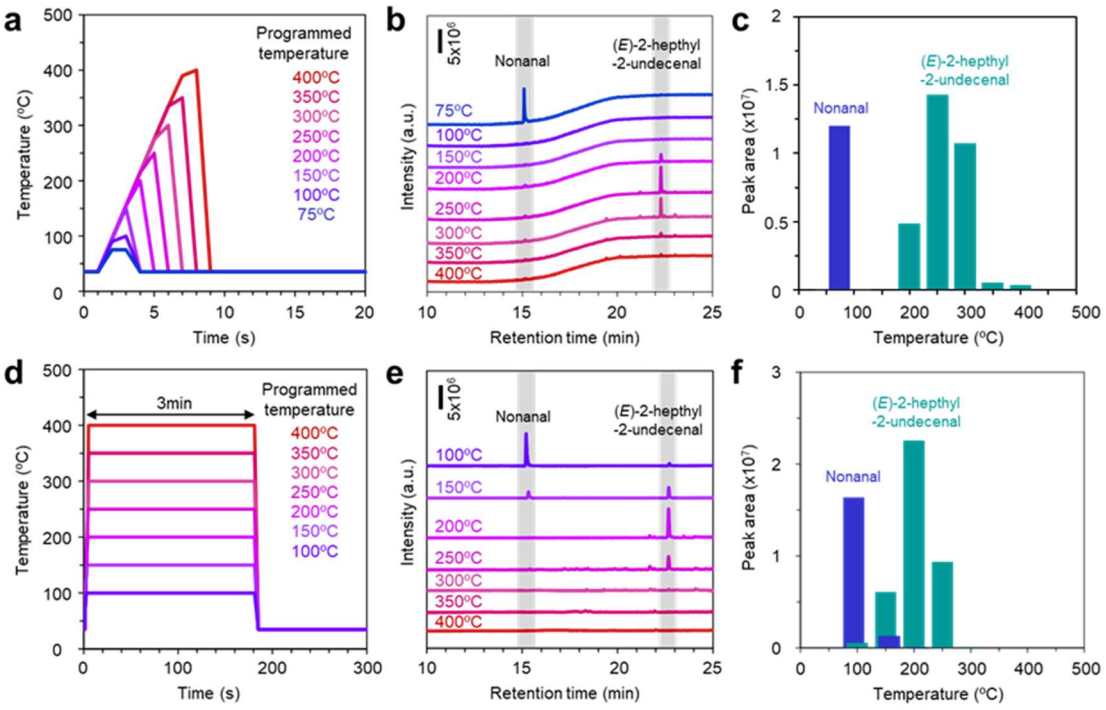

Figure 3. *(a) Temperature program and (b) GC-MS spectra of pulse heating based desorbed compound analysis. (c) Analyzed peak area of desorbed molecules (nonanal and (E)-2-hepthyl-2-undecenal) as a function of programmed temperature. (d) Temperature program and (e) GC-MS spectra of continuous heating based desorption compound analysis. (f) Analyzed peak area of desorbed molecules (nonanal and (E) -2-hepthyl-2-undecenal) as a function of programmed temperature.*

temperature (Figure 3c) present a fully separate desorption temperature. Nonanal molecule can be desorbed completely at 75 ºC pulse heating, while peaks belong to (E)-2-hepthyl-2-undecenal molecule appears from 200 ºC to 400 ºC. Wide desorption temperature rage (100 to 150 ºC) contains no molecule peaks makes the thermally manipulate the nonanal and (E)-2-hepthyl-2-undecenal desorption become possible. As a comparable demonstration, continuous heating program (heating at predefined temperature for 3min) and its desorption compound analysis were shown in Figure 3d-f. An overlap desorption temperature between nonanal (100-150 ºC) and (E)-2-hepthyl-2-undecenal (100-250 ºC) proves the necessity of constraining heating time for molecules separating. Lower (E)-2-hepthyl-2-undecenal desorption temperature by continuous heating implies molecules desorption can be effectively suppressed by controlling the heating period below the molecular residual time on material surface, which is corresponding to the simulation result.

To assess the concept of thermally manipulated desorption between nonanal and (E)-2-hepthyl-2-undecenal, an integrated sensing device composed of nanowire molecule collector and chemo-resistive sensor array was designed and fabricated. Its overview photograph and magnified image were shown in Figure 4 a and b, respectively. Pt heater at the bottom of nanowire was prepared as an essential of this thermally manipulated device. Temperature control was realized by applying voltage on the heater, temperature value of nanowire collector was recorded from IR thermography images, which are shown in Figure 4c. When applying V_{heat}=0 V (left), 15 V for 2 s (middle) and 25 V for 6 s (right) to Pt heater, nanowire temperature related to room temperature, 103 ºC and 385 ºC, respectively. According to the GC-MS analyse result, those heating setting reference can be utilized when performed sensing performance during molecule flowing (0 V) , nonanal desorption (15 V, 2 s) and €-2-hepthyl-2-undecenal desorption (25 V, 6 s). Temperature curves as a function of heating time at V_{heat}=15 V (Figure 4 d) and 25 V (Figure 4 e) conditions both present temperatures increasing trend with heating time. What's worthy mention is even heating the nanowire up to 200-400 °C, sensor temperatures remain at nearly same value, less temperature interaction effect between nanowire and sensor. Nevertheless, background sensing is needed for further eliminating the temperature effect to the sensing response, which means without molecule collection, the response caused by tiny temperature increase should be subtracted.

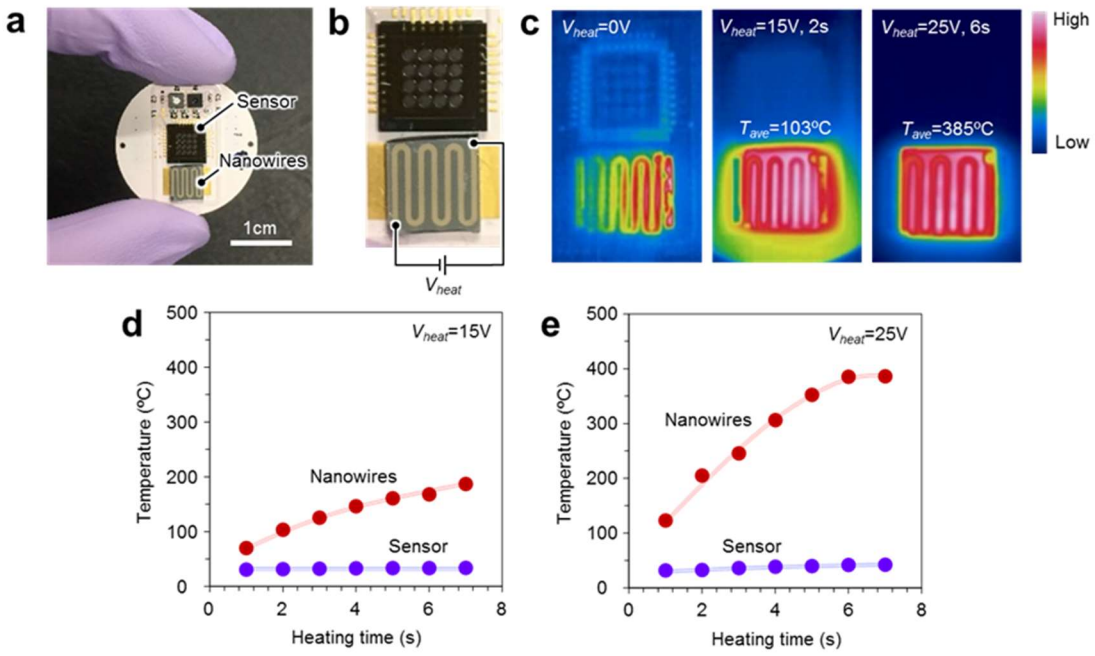

Figure 4. *(a,b) Photographs of nanowire-sensor hybrid device: (a) overview and (b) magnified image. (c) IR thermography images of hybrid device when applying V_{heat}=0 V (left), 15 V for 2 s (middle) and 25 V for 6 s (right) to Pt heater, respectively. (d,e) Measured temperatures of nanowires and sensor when applying (d) V_{heat}=15 V and € V_{heat}=25 V as a function of heating time.*

In the regards of desired working temperature can be realized by such temperature controllable nanowire, to demonstrate the molecules discrimination performance, dynamic sensing system was set up as the schematic in Figure 5a for molecule detection. N_2 gas and 1 ppm nonanal gas were flowing as the background gas and molecule collection, respectively. A pump at the other side of the sensor chamber was used for balancing gas flow rate. Temperature control program for molecular sensing measurement in Figure 5b provides a detail illumination of this procedure. When measurement started, 1ppm nonanal gas was flowing for 180 s as molecule collection procedure, following waiting 20 s to pump out molecules in the chamber. Then the first heating was set up to V_{heat}=15V, 2 s for nonanal desorption and sensing. Naturally down the temperature to room temperature by waiting for another 20 s, the second heating was carried out by V_{heat}=25 V, 6 s for (E)-2-hepthyl-2-undecenal desorption and sensing. Sensor response profile in Figure 5c is obtained from nonanal desorbed at lower temperature (103 ºC) and Figure 5d from (E)-2-hepthyl-2-undecenal desorbed at higher temperature. Short response and recovery time by nonanal sensing compare with slow response and recovery by (E)-2-hepthyl-2-undecenal sensing may cause by its longer residual time in chemo-resistance sensor. Figure 5e shows analysed sensing signal by voltage change value, it presents a same level

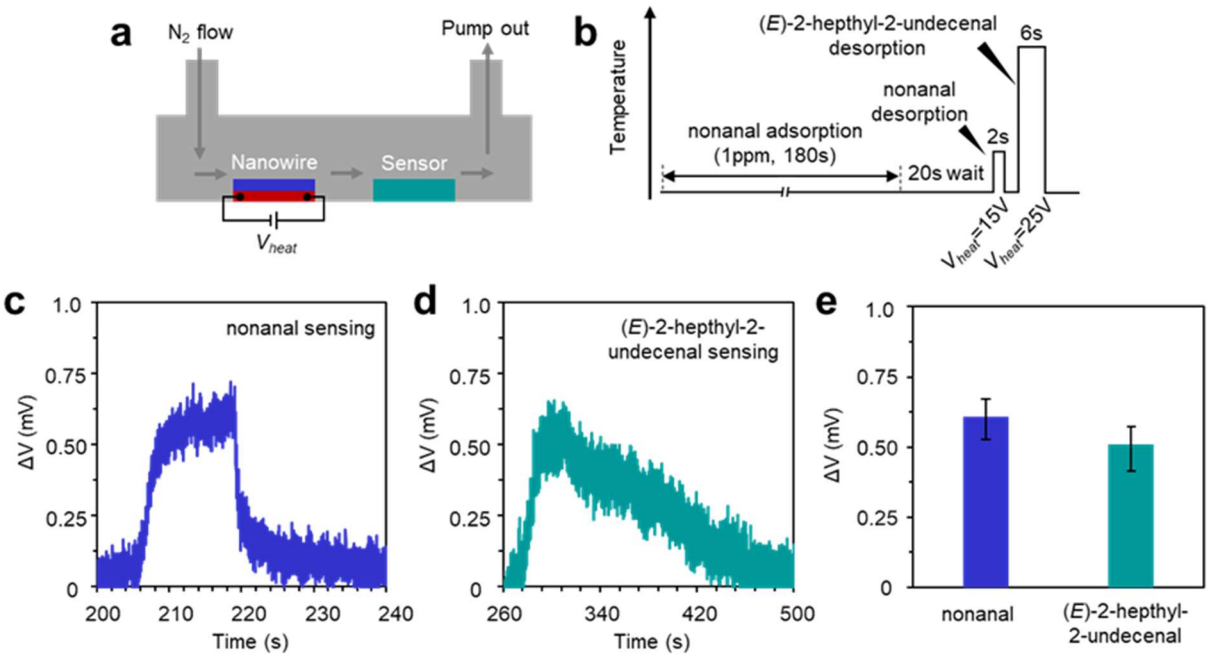

Figure 5. *(a) Schematic illustration and (b) program for molecular sensing measurement conducted by nanowire-sensor hybrid device. (c,d) Sensor response profiles for (c) nonanal desorbed at lower temperature and (d) E-2-hepthyl-2-undecenal desorbed at higher temperature, respectively. (e) Analyzed sensor response of nonanal and E-2-hepthyl-2-undecanal.*

sensing performance by two step heating, which means molecules separation sensing had been reached. Although desorbed products at low temperature and high temperature had been confirmed by GC-MS spectrum analysis, we further carried out a ZnCuO nanowire collector with limited aldol condensation reaction product (E)-2-hepthyl-2-undecenal, its depression mechanism can be get in our other study. Pulse heating desorption product by ZnCuO nanowire and its thermally manipulated sensing result are shown in Supporting Information Figure S2 and S3. Corresponding to pulse heating GCMS analysis molecules result, ZnCuO nanowire collector could provide a more effective low temperature desorption (nonanal sensing) signal and less signal by high temperature desorption molecule (E)-2-hepthyl-2-undecenal). Therefore, the obviously sensing signals change after the depression of aldol-condensation provide a powerful evidence for successful discrimination of nonanal and (E)-2-hepthyl-2-undecenal via a pulse heating by thermally manipulated hybrid device.

5.1.5 CONCLUSION

In conclusion, we proposed a novel molecular discriminate sensing platform by thermally manipulated desorption from metal oxide nanowire surface and separated sensing. A model of co-adsorbed nonanal and (E)-2-hepthyl-2-undecenal on zinc oxide (ZnO) nanowire surface is chosen to demonstrate our concept, and its feasibility was confirmed by entropy-involved numerical simulation. GC-MS analysis of desorbed molecules results supported a heating duration dependence molecules separation. Pulse heating below the residual time is more effective to depress the unexcepted desorption of molecules than continuous heating. Finally, the separate molecules sensing was successfully achieved by a nanowire-sensor hybrid device through thermal manipulated desorption. Such hybrid device concept shows its potential practicability as a supplementary mean for discriminating more complex mixture molecules contained atmosphere which can’t be realized by a simple sensing system.

5.1.6 REFERENCE

[1]. Takakusa H, Kikuchi K, Urano Y, et al. Design and synthesis of an enzyme-cleavable sensor molecule for phosphodiesterase activity based on fluorescence resonance energy transfer[J]. Journal of the American Chemical Society, 2002, 124(8): 1653-1657.

[2]. Cash K J, Ricci F, Plaxco K W. An electrochemical sensor for the detection of protein− small molecule interactions directly in serum and other complex matrices[J]. Journal of the American Chemical Society, 2009, 131(20): 6955-6957.

[3]. Huang B, Li Z, Liu Z, et al. Adsorption of gas molecules on graphene nanoribbons and its implication for nanoscale molecule sensor[J]. The Journal of Physical Chemistry C, 2008, 112(35): 13442-13446.

[4]. Baker B R, Lai R Y, Wood M C S, et al. An electronic, aptamer-based small-molecule sensor for the rapid, label-free detection of cocaine in adulterated samples and biological fluids[J]. Journal of the American Chemical Society, 2006, 128(10): 3138-3139.

[5]. Wang J, Qian X, Cui J. Detecting Hg2+ ions with an ICT fluorescent sensor molecule: remarkable emission spectra shift and unique selectivity[J]. The Journal of organic chemistry, 2006, 71(11): 4308-4311.

[6]. Wiskur, S. L.; Ait-Haddou, H.; Lavigne, J. J.; Anslyn, E. V. Acc. Chem. Res. 2001, 34, 963–972.

[7]. Bunz, U. H. F.; Rotello, V. M. Angew. Chem., Int. Ed. 2010, 49, 3268–3279.

[8]. Walker J M, Akbar S A, Morris P A. Synergistic effects in gas sensing semiconducting oxide nano-heterostructures: A review[J]. Sensors and Actuators B: Chemical, 2019, 286: 624-640.

[9]. Sysoev V V, Goschnick J, Schneider T, et al. A gradient microarray electronic nose based on percolating SnO_2 nanowire sensing elements[J]. Nano letters, 2007, 7(10): 3182-3188.

[10]. Taurino A M, Capone S, Siciliano P, et al. Nanostructured TiO_2 thin films prepared by supersonic beams and their application in a sensor array for the discrimination of VOC[J]. Sensors and Actuators B: Chemical, 2003, 92(3): 292-302.

[11]. Yang W, Wan P, Jia M, et al. A novel electronic nose based on porous In_2O_3 microtubes sensor array for the discrimination of VOCs[J]. Biosensors and Bioelectronics, 2015, 64: 547-553.

[12]. Cho S Y, Yoo H W, Kim J Y, et al. High-resolution p-type metal oxide semiconductor nanowire array as an ultrasensitive sensor for volatile organic compounds[J]. Nano letters, 2016, 16(7): 4508-4515.

[13]. Tomchenko A A, Harmer G P, Marquis B T, et al. Semiconducting metal oxide sensor array for the selective detection of combustion gases[J]. Sensors and Actuators B: Chemical, 2003, 93(1-3): 126-134.

[14]. Jin X, Huang Y, Mason A, et al. Multichannel monolithic quartz crystal microbalance gas sensor array[J]. Analytical chemistry, 2009, 81(2): 595-603.

[15]. Rakow N A, Sen A, Janzen M C, et al. Molecular recognition and discrimination of amines with a colorimetric array[J]. Angewandte Chemie International Edition, 2005, 44(29): 4528-4532.

[16]. Joy N A, Nandasiri M I, Rogers P H, et al. Selective plasmonic gas sensing: H2, NO2, and CO spectral discrimination by a single Au-CeO_2 nanocomposite film[J]. Analytical chemistry, 2012, 84(11): 5025-5034.

[17]. Frietsch M, Zudock F, Goschnick J, et al. CuO catalytic membrane as selectivity trimmer for metal oxide gas sensors[J]. Sensors and Actuators B: Chemical, 2000, 65(1-3): 379-381.

[18]. Suslick B A, Feng L, Suslick K S. Discrimination of complex mixtures by a colorimetric sensor array: coffee aromas[J]. Analytical chemistry, 2010, 82(5): 2067-2073.

[19]. Miller D R, Akbar S A, Morris P A. Nanoscale metal oxide-based heterojunctions for gas sensing: a review[J]. Sensors and Actuators B: Chemical, 2014, 204: 250-272.

[20]. Srivastava A K. Detection of volatile organic compounds (VOCs) using SnO2 gas-sensor array and artificial neural network[J]. Sensors and Actuators B: Chemical, 2003, 96(1-2): 24-37.

[21]. Yamazoe N. New approaches for improving semiconductor gas sensors[J]. Sensors and Actuators B: Chemical, 1991, 5(1-4): 7-19.

[22]. Yamazoe N, Sakai G, Shimanoe K. Oxide semiconductor gas sensors[J]. Catalysis Surveys from Asia, 2003, 7(1): 63-75.

[23]. Wyszynski B, Yatabe R, Nakao A, et al. Array of Chemosensitive Resistors with Composites of Gas Chromatography (GC) Materials and Carbon Black for Detection and Recognition of VOCs: A Basic Study[J]. Sensors, 2017, 17(7): 1606.

[24]. Shunori A, Yatabe R, Wyszynski B, et al. Multichannel Odor Sensor System using Chemosensitive Resistors and Machine Learning[C]//2019 IEEE International Symposium on Olfaction and Electronic Nose (ISOEN). IEEE, 2019: 1-3.

[25]. Wang C, Hosomi T, Nagashima K, et al. Rational Method of Monitoring Molecular Transformations on Metal-Oxide Nanowire Surfaces[J]. Nano letters, 2019, 19(4): 2443-2449.

5.1.7 Supporting information

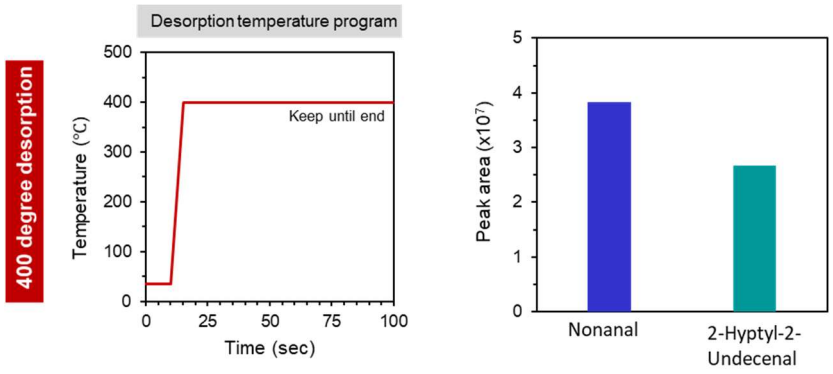

Figure S1. *One-step desorption product analysis from nonanal and (E)-2-hyptyl-2-undecenal co-adsorbed ZnO nanowire. (a) Inlet desorption temperature program; (b) relative peak area.*

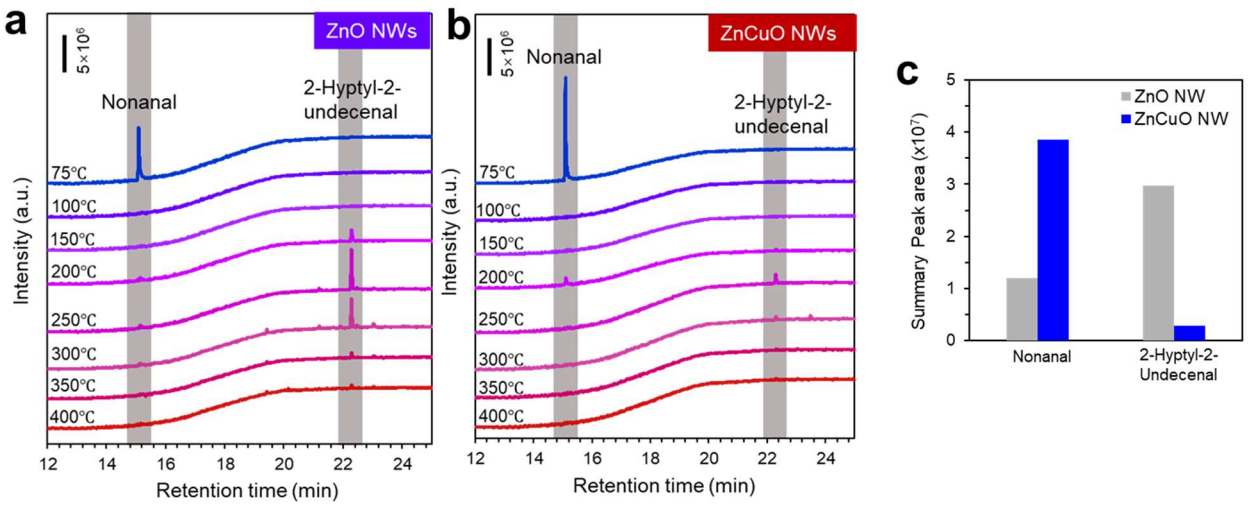

Figure S2. *Desorbed products from nonanal and (E)-2-hyptyl-2-undecenal co-adsorbed at a series of continuous temperature pulse heating. (a) ZnO nanowire; (b) $Zn_xCu_{1-x}O$ nanowire; (c) relative peak area comparison.*

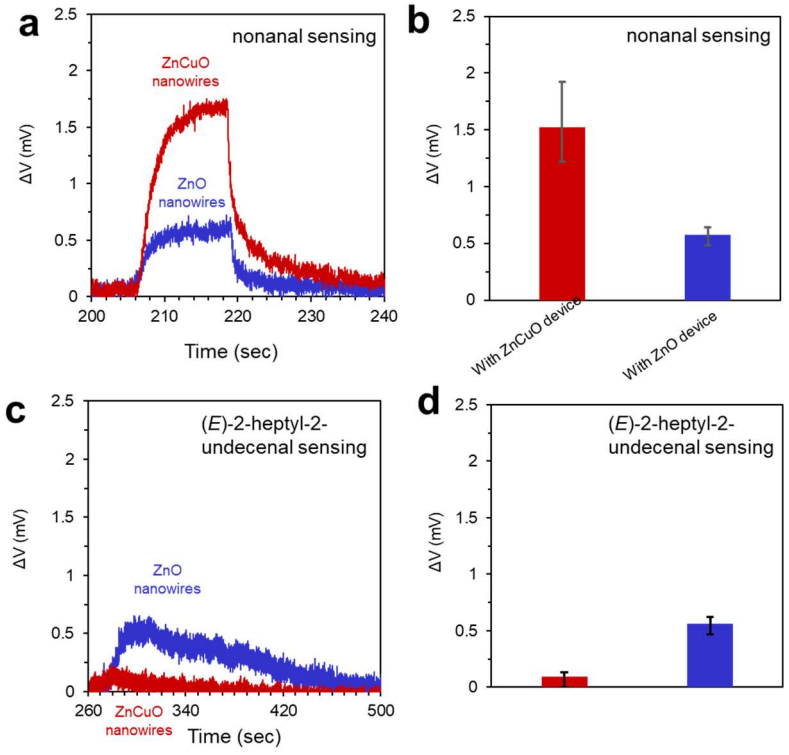

Figure S3. *Separated sensing performance. (a) Response curve of first-step nonanal sensing; (b) Response value comparison; (c) Response curve of second-step (E)-2-hyptyl-2-undecenal sensing; (d) Response value comparison between ZnO and* $Zn_xCu_{1-x}O$ *nanowire.*

CHAPTER VI

CONCLUSION AND OUTLOOK

As the most extensive applicated sensing material, metal oxide semiconductors have already been deeply exploited to catch the realistic requirement. But the major drawbacks of insufficient detection limit and poor selectivity still limited their development as powerful tools to detect various gas molecules. Based on the achievement of traditional molecule sensing improvement approaches such as metal element doping or material surface functionalized, and developing novel metal-oxide electronic devices, this thesis is organized by controllable synthesis of dopant nanowires, manipulating molecule-to-surface interaction and designing of novel sensor configuration in order to provide a fundamental knowledge in scientific and technological fields for reaching the goal of final practical sensor performance.

First, towards promoting the traditional metal-oxide semiconductor modification effect for obtaining excellent molecule sensing performance, both doping and surface regelation or treatment were performed in Chapter III. Prior to all, we demonstrated the morphology and the dopant distribution of hydrothermal zinc oxide nanowires critically determined by coordination structure of impurity metal ions on nanowire surface. Introduction of tungstate ions (WO_4^{2-}) significantly enhances a nucleation at sidewall $(10\bar{1}0)$ plane, while the dopant incorporation occurs only at (0001) plane unexpectedly. These conflicted face-selective behaviors lead to inhomogeneous dopant distribution in an individual ZnO nanowire. Even though this section highlights the essential importance to understand the coordination structure of metal ions for designing the hydrothermal metal oxide nanowire synthesis, but it failed to design the functional molecular sensing surface. In the following section, we employ a gradual modulation of cation composition in heterostructured $(Cu_x,Zn_{1-x})O$ nanowires to study the effect of surface cation composition (Cu/Zn) on the adsorption and chemical transformation behaviors of volatile carbonyl compounds, take the nonanal transformation behavior as a model. We found that a surface exposed copper significantly suppresses the adsorption of nonanal, meanwhile increasing Cu/Zn ratio on the nanowire surface systematically suppresses the aldol condensation reaction of nonanal. Nonanal sensing on such mixed cation composition nanowire surface obviously improved the durability and the recovery time without further increasing its working temperature. This discovery provides a potential approach to design energy-saving devices. Next, we demonstrated a facile methodology to create zinc titanate nanotubes via reaction-byproduct etching, allows us to form zinc titanate nanotubes at much lower temperature than the conventional solid-phase diffusion method, which will be a novel method for design nanotube surface. Except the surface design, we also revealed a mechanism of simple surface treatment using strong acids to remove surface covered water on WO_3

nanowire surfaces for enhancing the electrical molecular sensing of nonanal, as described in chapter V. Two different adsorption structures of carbonyl groups on the surface are founded, of which molecules directly bound to surface tungsten ions preferentially proceed to the catalytic oxidization reaction and subsequent desorption process. Surface treatment could raise the directly molecule-to-atom connection, thus tailor their sensor performances is achievable by controlling molecular oxidation transformations on metal-oxide surfaces.

Then, we explored a molecule imprinted surface for achieving the molecular discriminated adsorption in Chapter VI. After optimizing the formation process condition of TiO_x cross-link around template molecule, obviously aldehyde selective adsorption enhancement from volatile mixtures was obtained in the first section of this chapter. Deeper mechanism of functional recognition property formation was revealed in the next section through atomic-diffusion of zinc into the titanium oxide shell, which play a crucial role due to it provides stronger bonding of template connection with metal atom during its formation process, it is benefit for template molecular being memorized without losing, so as to achieve the shape-recognition property. What's more, good molecule recognition property still remained until 800 cycles of heating treatment at 400 °C, allows the practical of further applying as a selector by heating released adsorbed molecules prior to sensor. We realized this concept by design a novel nanowire-sensor hybrid device for molecules discrimination. Results turns out that aldehyde (benzaldehyde as a model) can be selectively detected, even from imbalanced molecular ratio of tiny benzaldehyde, which can't be reached by most currently sensing devices. To identify the detection limit of such functionalized nanowire surface in nanowire-sensor hybrid device, we conducted low concentrated nonanal sensing in the final section of this chapter, what surprising is that even exposure to sub-ppb level nonanal (500 ppt), obvious sensing response can be observed. It is the first time to realize such ultra-low nonanal sensing and this micro-system has the potential to realize early detection of lung cancer by simple human breath monitoring approach.

This nanowire-sensor hybrid device was designed on account of selective adsorption procedure, if applying selective adsorption together with this selective desorption design, more impressive molecules selective sensing can be expected. Therefore, A molecular discrinationg platform based on nanowire-chemosensor hybrid devises was proposed in Chapter V by manipulating the molecular desorption, take the co-adsorbed nonanal and its condensation product as an example, those molecules can be successfully separated sensing by two-steps

pulse heating. The feasible of this concept was confirmed by a DFT simulation of relationship between molecular surface residual time and temperature. Precisely control the heating time under residual time of undesired molecule, the discrimination among complex molecules atmosphere become possible.

However, there are still many hinders exist in the real application of metal oxide semiconductor gas sensors. The first thing is surrounding environment factors such as the temperature, humidity and ambient light influence on electrical characters can't be ignored. Especially for the application of biomarker detection in human breath, inaccuracy reflection doomed to occur because a certain degree of sensing response would be destroyed by moisture. Next problem is also the selectively detection aiming molecule from chaotic condition. The present thesis for solving such selectivity problem only focuses on aldehyde species. Specific sensing devices towards ketone or alcohol are also worthy to be exploited. In addition, the discrimination from same aldehyde group molecular mixtures is impossible due to the extremely analogous chemical properties. The last one is the portable and wearable feasibility, currently the excellent sensing performance always obtained by large scale detection system in the laboratorial level. Integrated devices with small size, simple analyzing system, real-time detection available is urgently necessary. Enormous work needed to be accomplished for new generation of semiconductor molecular sensor for reaching the commercial level. Luckily as the rapidly arousing of nanotechnical, confidence should be hold that successful application of perfect sensing device will coming in the near future.

LIST OF PUBLICATIONS

List of publications

【Scientific Journals】

1. Coordination Structure of Impurity Metal Ions Critically Determines Morphology and Dopant Distribution of Hydrothermal Zinc Oxide Nanowire.
   J. Liu, K. Nagashima, H. Yamashita, W. Mizukami, J. Uzhuhashi, T. Hosomi, M. Kanai, X. Zhao, Y. Miura, G. Zhang, T. Takahashi, M. Suzuki, D. Sakai, B. Samransuksamer, Y. He, T. Ohkubo, T. Yasui, Y. Aoki, J. C. Ho, Y. Baba and T. Yanagida
   査読中
2. Impact of Surface Copper of $(Cu_xZn_{1-x})O$ Heterostructured Nanowires on Adsorption and Chemical Transformation of Carbonyl Compounds.
   J. Liu, K. Nagashima, Y. Nagamatsu, T. Hosomi, C. Wang, W. Mizukami, G. Zhang, B. Samransuksamer, T. Takahashi, M. Kanai, T. Yasui, Y. Baba and T. Yanagida
   査読中
3. Facile Synthesis of Zinc Titanate Nanotubes via Reaction-Byproduct Etching.
   J. Liu, K. Nagashima, H. Yoshida, T. Hosomi, T. Takahashi, G. Zhang, M. Kanai, Y. He and T. Yanagida
   査読中
4. Novel Molecular Sensing Platform via Thermally Manipulated Selective Desorption on Nanowire Surface.
   J. Liu, K. Nagashima, W. Mizukami, T. Hosomi, A. Nakao, A. Shunori, G. Zhang, T. Takahashi, M. Kanai and T. Yanagida
   投稿準備中
5. Thermally Engineered Molecular Recognition Surface on TiO_2/ZnO Heterostructured Nanowires.
   J. Liu, K. Nagashima, T. Hosomi, T. Takahashi, G. Zhang, M. Kanai and T. Yanagida
   投稿準備中
6. Monitoring and Tailoring Catalytic Behaviors of WO_3 Hydrate Nanowires for Electrical Molecular Sensing.
   G. Zhang, T. Hosomi, W. Mizukami, **J. Liu**, K. Nagashima, T. Takahashi, M. Kanai, T. Yasui, Y. Baba, J. C. Ho and T. Yanagida
   投稿準備中

【Proceedings】

1. “Molecularly Fingerprinted Metal Oxide Nanowires for Discriminating Aldehyde from Volatile Organic Compound Mixture”

   J.Y. Liu, K. Nagashima, T. Yanagida,

   IEICES2018, Kyushu University, Fukuoka, Japan, 2018, pp116-117.

【Presentation】

1. “Molecular Imprinted Oxide Coated ZnO Nanowire Pre-concentrator for Separating Nonanal from Volatile Organic Compounds”

   J.Y. Liu, K. Nagashima, T. Yanagida

   4rd International Exchange and Innovation Conference on Engineering & Sciences (IEICES2018), Kyushu University, Fukuoka, Japan, 2018.10.18-19 (oral)

2. “Thermally robust molecularly imprinting on oxide nanowires discriminate nonanal from volatile organic compounds mixture” (Oral)

   J.Y. Liu, K. Nagashima, T. Hosomi, G. Zhang, T. Takahashi, M. Kanai and T. Yanagida

   The 3rd Asian Applied Physics Conference (Asian-APC), Fukuoka Univ., Fukuoka, Japan, 2018.12.8-9

3. “Thermal Discrimination of Volatile Organic Molecules by Molecularly Fingerprinted Metal Oxide Nanowires” (ポスター発表)

   J.Y. Liu, Kazuki Nagashima, Wenjun Li, Takuro Hosomi, Yong He, Mizuki Matsui, Guozhu Zhang, Tsunaki Takahashi, Hideto Yoshida, Masaki Kanai, Seiji Takeda, Takeshi Yanagida

   第 37 回電子材料シンポジウム, ホテル＆リゾーツ長浜, 滋賀, 2018 年 10 月 10-12 日

4. “高堅牢性分子指紋ナノワイヤを利用した揮発性分子群の形状/官能基認識及び選択的濃縮” (ポスター発表)

   長島 一樹, **J.Y. Liu**, 細見 拓郎, 高橋 綱己, Guozhu Zhang, 金井 真樹, 吉田 秀人, 竹田 精治, 安井 隆雄, 馬場 嘉信, 矢田部 塁, 都甲 潔, 柳田 剛

   ImPACT 宮田プログラム公開成果報告会, JP タワーホール＆カンファレンス, 東京, 2018 年 12 月 3-4 日

5. “Thermally Robust Molecular Fingerprint on Metal Oxide Nanowires Towards Volatile Biomolecular Analysis” (Poster)

K. Nagashima, **J.Y. Liu**, T. Hosomi, G. Zhang, T. Takahashi, M. Kanai and T. Yanagida

The Second International Workshop by the 174th Committee JSPS “Symbiosis of Biology and Nanodevices”, Kyoto Terrsa, Kyoto, Japan, 2019.1.29

【Patent】

1. 出願番号：特願 2020-055050

発明者：長島　一樹, **劉 江洋**, 柳田　剛, 中尾 厚夫, 花井 陽介, 中谷 将也

発明の名称：「検出システム」

出願人：パナソニック株式会社

出願日：2020 年 3 月 25 日

2. 出願番号：特願 2020-054511

発明者：長島　一樹, **劉 江洋**, 細見 拓郎, 高橋 綱己, 柳田　剛

発明の名称：「吸湿材及びその製造方法、除湿装置、並びに、ガスの乾燥方法」

出願人：九州大学

出願日：2020 年 3 月 25 日